THERMOMIGRATED JUNCTION ISOLATION OF DEEP REACTIVE ION ETCHED, SINGLE CRYSTAL SILICON DEVICES, AND ITS APPLICATION TO INERTIAL NAVIGATION SYSTEMS

A Thesis
Presented to
The Academic Faculty

By

Charles Choi Chung

In Partial Fulfillment
of the Requirements for the Degree
Doctor of Philosophy in the
College of Engineering

Georgia Institute of Technology
December, 2003

THERMOMIGRATED JUNCTION ISOLATION OF
DEEP REACTIVE ION ETCHED, SINGLE CRYSTAL SILICON DEVICES, AND
ITS APPLICATION TO INERTIAL NAVIGATION SYSTEMS

Approved by:

Dr. Mark G. Allen, Adviser

Dr. James Meindl

Dr. Gary May

Dr. Thomas Gaylord

Dr. Dennis Hess

Date Approved: December 1, 2003

TABLE OF CONTENTS

ACKNOWLEDGMENTS

There are many people without whom this work would never have completed. First, the many people in my research group who have answered countless questions, suggested countless solutions, and continuously shared and revitalized my interest in this work. In particular, I would like to thank Richard Shafer, who tirelessly kept our labs maintained, and delivered, installed, and helped me adapt the filament evaporator that allowed me to do much of the thermomigration work. I would also like to thank so many of my friends in the research group, including Dan Kercher, Florent Cros, Yong Kyu Yoon, Jennifer English, Brian English, Thierry Leichle, Oliver Brand, and David O'Brien. They have been an invaluable source of advice and expertise in the course of the research. But more importantly, they've been a constant source of laughter and fun. Without them, the work wouldn't have proceeded nearly as quickly or been nearly as much fun. Because we are all microsystems geeks, I look forward to decades of meeting at conferences and sharing research stories with them all.

Also, I would like to acknowledge the many friends that I have in the Georgia Tech Microelectronics Research Center, who daily insured that so many things were taken care of, so that I was able to concentrate on this work. In particular, I would like to thank Gary Spinner. If there ever was an argument for human cloning, it is this man. He single-handedly raises the quality and productivity of every research project in the MiRC by orders of magnitude. For me, he and his staff have demonstrated amazing patience and resolve in the constant repair and maintenance of the ICP-RIE that was used for the deep reactive ion etching work.

My adviser, Mark Allen, deserves special recognition in this work. He has been instrumental in so many ways. His was the original idea of employing thermomigration for creating deep junctions for electrical isolation. But even more that, when I first approached him, Dr. A. gave me a chance and accepted me into the group as an outsider and unknown. He has been exceptionally generous and reliable in securing funding, materials, and resources for this project. Dr. A.'s style of advising was ideal for me in many ways. He was always involved, but did not micro-manage the project. He respected the fact that I worked and thought about this research everyday, and always considered every suggestion, thought, and decision that I made. Most importantly, he preserved the sense of exploration and fun that originally inspired me to get involved in this research. I entered the program full of wonder and fascination for microsystems. I leave the program a bit more tempered and a bit wiser, but still very much enthused to be involved in such a cool field. I am very grateful and feel very lucky to have such a terrific adviser who made my Ph.D. experience such a gratifying experience.

I must also acknowledge Todd Kaiser and the MSSA group in Boston. Todd worked on a related project, the POGA, an accelerometer, whose design is related to the micro-gyroscope in this work. We spent many hours and many lunches together sharing not only our research, but many other topics. He has a roving, curious mind and an optimistic spirit that always made talking with him, and doing research with him, a pleasure. Even after Todd graduated, he was often the first person I considered consulting on the latest problems and challenges in the research. He knew better than just about anyone on the planet about this project. And, he's a cracking good researcher.

Most importantly, he was always incredibly generous with his advice and support with both the research and bigger life issues.

I know the MSSA guys through Dr. Allen and Todd. They are the ones that had the original idea for the gyroscope design. Ray Carroll, Bob Dauwalter, Joe Walsh, Joe Scopp, Dan Cardarelli, and Mike Sappupo. They know inertial navigation systems better than anyone, and their generosity with their expertise was invaluable.

I'd like to recognize Ron Pigate, whom I loved very dearly, and with whom I spent some very special moments. I feel lucky to have known him.

I would like to especially thank Sutton Edlich, who counseled me for countless hours, and who has given sage advice on many, many topics in my life, including the research. He is a true friend. I love him dearly, and I am blessed to know him.

Finally, I'd like to thank my family, my dad, mom, and brother. They all supported me, harangued me, and loved me. I could never have completed the degree without them.

Thanks to all…

-Chuck

LIST OF TABLES

LIST OF FIGURES

LIST OF SYMBOLS AND ABBREVIATIONS

DRIE – deep reactive ion etching

INS – inertial navigation system

MEMS – micro-electro-mechanical systems

SCS – single crystal silicon

TGZM – temperature gradient zone melting

SUMMARY

The introduction of deep reactive ion etching (DRIE) technology has greatly expanded the accessible design space for microscopic systems. Structures that are hundreds of micrometers tall with aspect ratios of 40:1, heretofore impossible, can now be achieved. However, this technology is primarily a forming technology, sculpting structures from a substrate. This work seeks to complement deep reactive ion etching by developing an electrical isolation technology to enable electro-mechanical function in these new deep reactive ion etched structures.

The objective of the research is twofold. The first is to develop and characterize an electrical isolation technology for DRIE, single crystal silicon (SCS) micro-electro-mechanical systems (MEMS) using temperature gradient zone melting (TGZM) of aluminum junctions for diodic isolation. The second is to demonstrate the utility of this electrical isolation technology in the design, simulation, fabrication, and testing of a MEMS device, i.e. a micro-gyroscope, in such a way that the benefits from junction isolated, deep reactive ion etched, single crystal silicon devices are preserved.

Chapter 1

Introduction & Previous Work

Single crystal silicon (SCS) bulk-micromachined micro-electro-mechanical systems (MEMS) enjoy a number of advantages. Silicon is well understood, well characterized, inexpensive, readily available, capable of integrating $>10^8$ transistors in a single die, and is supported by a multi-trillion-dollar infrastructure.

From a MEMS perspective, SCS furthermore enjoys a number of additional advantages. Because SCS is a single crystal material, there are no fatigue effects and no energy losses due to grain boundary shifts. And, because bulk-micromachined devices are sculpted out of the substrate, large thicknesses, up to the thickness of the wafer (typically hundreds of micrometers), are possible. Finally, the introduction of deep reactive ion etching (DRIE) technologies and, specifically, the Bosch silicon etching process [Larmer1999a] has greatly expanded the design space for bulk-micromachined single crystal silicon MEMS devices. SCS structures hundreds of micrometers thick with aspect ratios of over 40:1 can now be reproducibly fabricated.

Despite these advantages, SCS bulk-micromachined MEMS devices have not enjoyed as wide acceptance as surface-micromachined alternatives. One reason is that although fabricating mechanical structures out of SCS is relatively straightforward,

making these mechanical structures electro-mechanically functional has proven to be not-so-straightforward. The essential difficulty is that bulk-micromachined silicon devices are by definition etched out of one monolithic piece of silicon. Therefore, all of the components are electrically connected.

In the past, there have been three general approaches to electrically isolating electromechanical devices etched from bulk silicon: the bond/etch method, the etch/backfill method, and the SCREAM method.

The bond/etch approach involves physically separating each piece of silicon by etching gaps between voltage-distinct regions. Before the gaps are etched, the wafer is attached to a handle wafer to hold the microscopic parts in relative position to one another, [Larmer1999b, Najafi1995, Schmidt1995]. Figure 1 illustrates the bond/etch technique. This approach has been widely used; however, the handle wafer often presents difficulties in the final structure. For example, in devices that require symmetry, the handle wafer adds a great deal of mass to one side of the device, often resulting in undesired asymmetry that can cause non-ideal behavior, e.g., cross-axis sensitivity in accelerometers. For fluidic devices, the handle wafer can block the flow into and out of the device unless special ports are etched in the handle wafer. And, finally, for electromechanical devices on moving platforms, the additional bulk and mass of the handle wafer makes the platform slow and cumbersome.

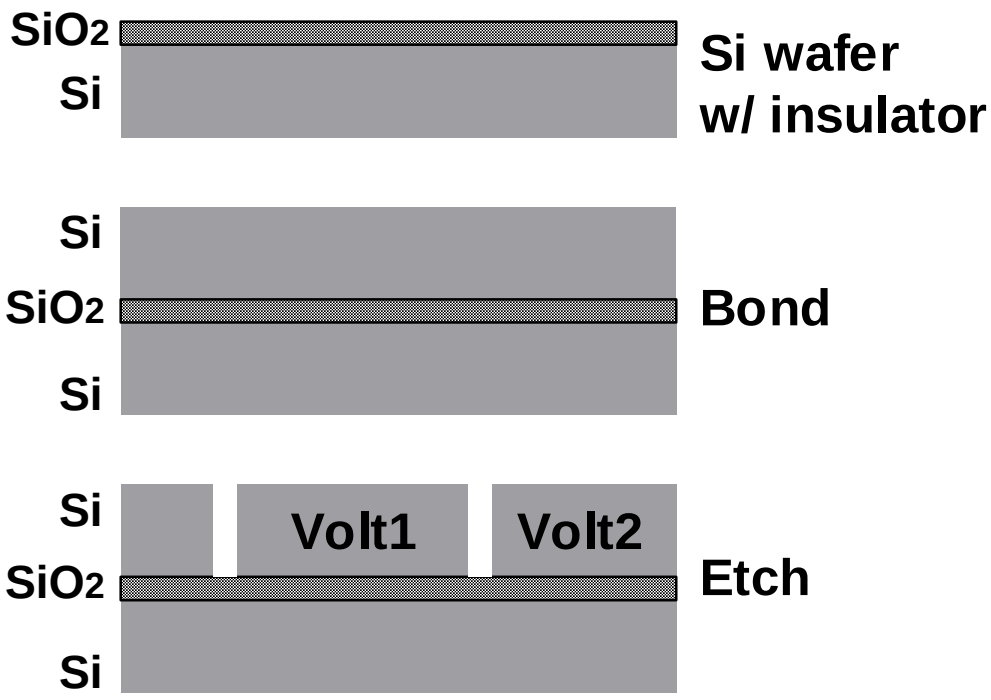

Figure 1 - The fabrication flow for the bond/etch approach to electrically isolate deep reactive ion etched, silicon MEMS devices.

The second approach, i.e. the etch/backfill approach, is similar in that the intervening silicon is removed to electrically isolate voltage-distinct regions; however, instead of leaving a gap, the etched volume is backfilled with an insulating material, typically silicon dioxide or polysilicon, to restore the mechanical integrity of the wafer [Elwenspoek1997, Howe1997]. This approach is illustrated in figure 2. The etch/backfill approach works well when applicable, however because of the addition of the backfill material, some of the inherent material advantages of single crystal silicon start to become lost. In most cases, the backfilled materials have poorer mechanical properties than the original silicon. In addition, the mechanical properties of the interface

between the silicon and the backfill material introduce new issues, such as adhesion. Finally, the etch/backfill method scales with difficulty with increasing thickness and aspect ratio of the device. The deeper the trench, the more time intensive the backfill process, and the more difficult it is to insure uniform material deposition throughout the trench while maintaining control of internal stress.

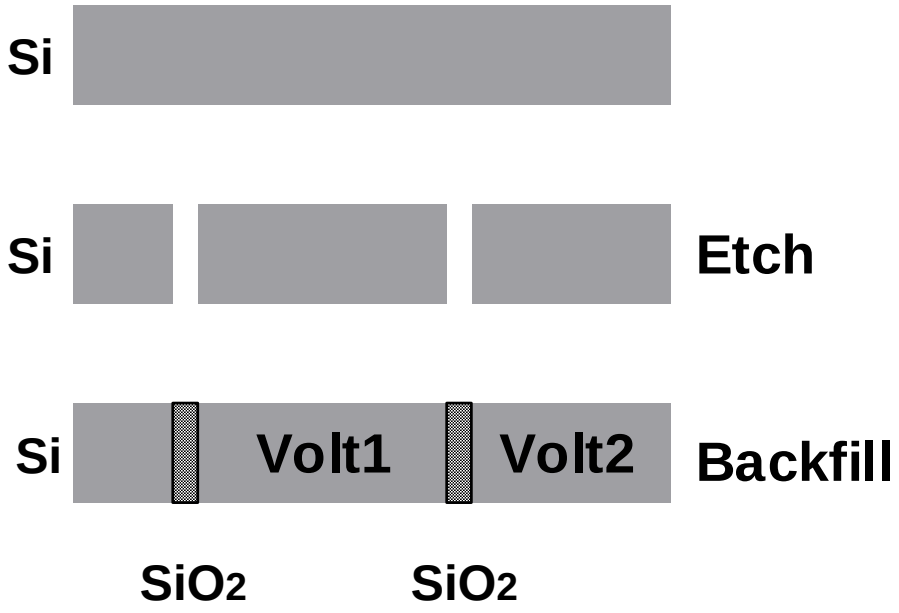

Figure 2 – The fabrication flow for the etch/backfill approach to electrically isolate DRIE, silicon MEMS devices.

The third approach is the SCREAM method, pioneered by Noel MacDonald's group at Cornell University. This approach uses the bulk-etched silicon as a mechanical material, and subsequently adds electrically isolated films on top of the silicon for the

electrical subsystem [MacDonald1994]. Figure 3 illustrates the SCREAM process. First, the microdevice is bulk-etched from the silicon. An insulating layer is either grown or deposited on the bulk-etched structure. Finally, to make the surface electrically active, conductive layers are deposited onto the sidewalls of the microstructure as well as on the top surface. Even though the mechanical structure remains one continuous piece of silicon, electrical isolation is achieved by the fact that the conductive layer is not continuous over the entire silicon substrate.

Although a widely used technique, the SCREAM approach requires deposition onto sidewalls, which becomes increasingly difficult with increasing aspect ratio and greater thicknesses. And, it is impossible to form electromechanically functional structures on moving platforms using this technique.

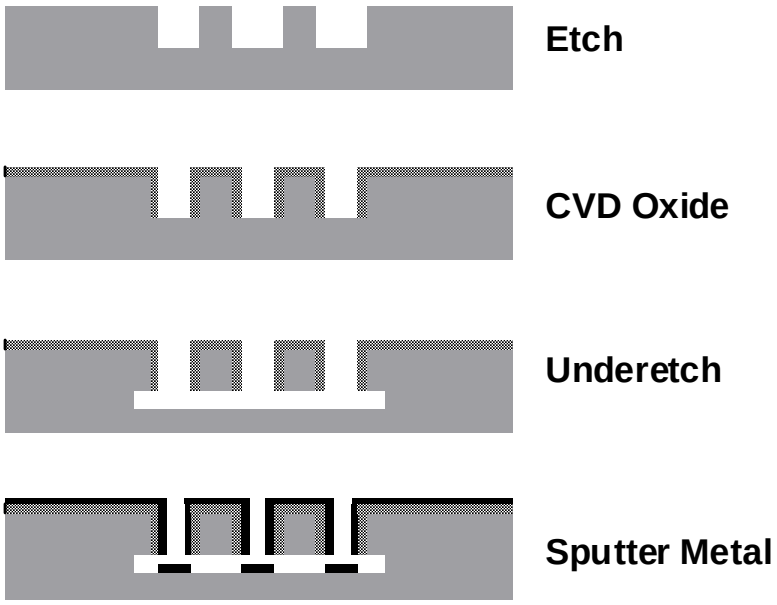

Figure 3 - Fabrication flow for the SCREAM process.

Junction Isolation

An alternative to these approaches is a technique widely used in microelectronics systems called "junction isolation" or "diodic isolation." This approach takes advantage of the semiconducting properties of silicon to electrically isolate with npn or pnp junctions. [Streetman1990, Sze1981] The npn or pnp regions act as two series-connected, back-biased diodes that block current flow from one voltage-distinct region to another (figure 4). With this technique, it becomes possible to electrically isolate various parts of the silicon while retaining the original mechanical integrity of the single crystal material.

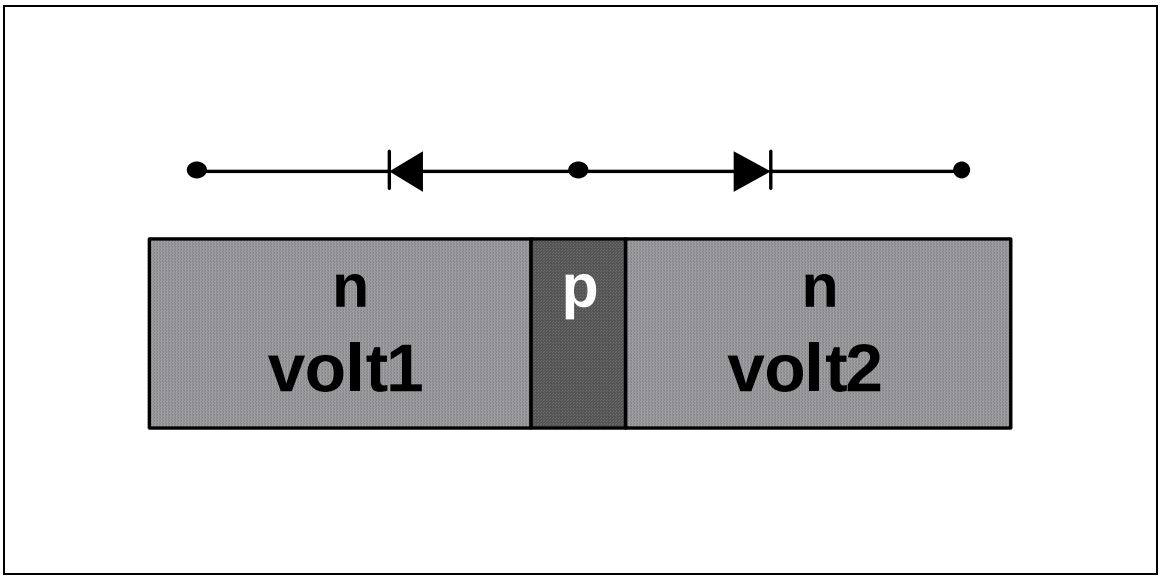

Figure 4 - electrical representation of npn junction diodic isolation.

Up to now, however, junction isolation has not been employed as an electrical isolation scheme for bulk silicon MEMS devices, primarily because in order to achieve isolation, it is necessary to dope the silicon through the entire thickness of the device, which may be hundreds of micrometers thick. The typical methods for doping silicon used in microelectronic devices, diffusion or ion implantation, are impractical to achieve such deep junction depths.

Temperature Gradient Zone Melting

The doping of silicon with junction depths on the order of hundreds of micrometers has been demonstrated in a process known as "temperature gradient zone melting (TGZM)" or "thermomigration." [Pfann1978] In this process, a thermal gradient is imposed through the thickness of the wafer, and dopants deposited on the cooler side propagate along the thermal gradient until the opposite face is reached or until the dopant material is exhausted. If this process is applicable to deep reactive ion etched, single

crystal silicon MEMS devices, then junction isolation may be a possible isolation scheme for thick, high aspect ratio, bulk-micromachined micro-electro-mechanical devices.

However at this point, TGZM has not been applied to the junction isolation of SCS bulk-micromachined MEMS devices. As a result, the limitations and possibilities of this approach are largely unexplored for MEMS systems. Outstanding questions exist such as, are the theoretical advantages of thermomigrated junction isolated, deep reactive ion etched, silicon MEMS devices in fact realizable? What are the practically achievable limits of TGZM fabricated junctions? What micromachining technologies is this approach compatible or incompatible with? What practical constraints are there in the realization of actual device?

In this research, the TGZM technique will be employed to electrically isolate thick, bulk-micromachined SCS wafers, in order to establish electromechanical functionality in MEMS devices. The fabrication limitations and opportunities will be investigated. The electrical isolation characteristics will be measured. And, finally, since so often "the devil is in the details" with engineering challenges, a useful MEMS device will be fabricated to demonstrate the utility of the TGZM technique.

A number of devices may be chosen for this vehicle; however an inertial sensor, specifically a gyroscope, is particularly interesting. The variety and breadth of applications for a small, compact, light navigation-grade system are enormous, and yet there is a complete lack of these systems. Thermomigrated junction isolation technology offers gyroscopes some inherent advantages while at the same time simplifying fabrication complexity. As a result, the demonstration of the isolation technique is interesting not only from an academic point of view, but also practically and

commercially, and may enable heretofore impractical applications.

Inertial Navigation

Navigation is one of humankind's oldest technologies. The many possible navigation techniques may be categorized in two ways: navigation by external reference and navigation by local reference. Navigation by external reference utilizes techniques that measure one's position and/or heading vis-à-vis an external reference, for example navigation by street signs, the North Star, the earth's magnetic field, or the Global Positioning System (GPS) satellite constellation. In contrast, navigation utilizing local references relies on measurements that may be done inside a "black box," i.e., without external reference, e.g., counting steps, measuring airspeed, or monitoring one's rate of turn.

External and internal navigation technologies are complementary technologies and are often used together. For example, although the GPS constellation is a convenient method to determine one's position and heading, it may be complemented by a local navigation method in situations where the system is unavailable, for example in a city where the view of the satellites may be blocked by buildings, or during conflict, when an enemy is intentionally jamming the signal, or perhaps simply due to bad weather.

Inertial navigation is a type of navigation by local reference. Specifically, this approach relies on local measurements of the changes in one's linear and angular momenta. As one collects a time history of the changes in momenta, the equations of motion may be integrated to calculate one's position, velocity, and heading relative to some previously known set of coordinates.

Inertial Micro-Devices

Miniaturized systems allow the possibility of small, light, low-power, low-cost devices, which in turn, enables heretofore impractical applications. Particular applications of low-volume inertial navigation systems (INS) include portable tracking capability such as navigating with a cell phone, or guiding individual fingers on a robotic hand. Low-mass INS systems may allow cost savings on spacecraft, where launch costs increase exponentially with mass. Low-power INS allows the possibility of a tracking system in a watch or PDA, where only a small battery is available. And, finally, low-cost INS systems allow these functions to be widely available.

Sensors that are low in volume, mass, power, and cost furthermore allow redundant INS systems and arrays of INS systems. In critical INS applications, multiple redundant sensors have the characteristic that failure of all devices diminishes probabilistically. A useful application of this may be to place multiple INS sensors on firepersons entering a burning building, or soldiers entering combat, or on a remote vessel exploring deep ocean crevasses. Finally, an array of INS sensors could return spatially varying information, or simply collect data over a wide area. This may be useful in the measurement of the vibration characteristics of an aircraft to identify maintenance needs, or to simply to track the location of a flock of migratory birds.

Thermomigrated Inertial Sensors

Although many angular rate microsensors have been fabricated, a highly sensitive device suitable for general navigation has yet to be demonstrated. The combination of thermomigration junction isolation and bulk silicon micromachining offers a way to

improve existing designs in several ways.

First, the sensitivity and noise characteristics of inertial sensors directly benefit from a large proof body, i.e. the inertial mass whose motion is measured to find changes in position or heading. For a given chip area, a bulk-micromachined silicon proof body can be as thick as the wafer itself, typically on the order of hundreds of micrometers. This allows a greater inertia in the proof body, and therefore a more sensitive and less noisy instrument.

Silicon bulk-micromachining is not the only way to fabricate structures with thicknesses on the order of hundreds of micrometers. However, a second attraction of bulk silicon devices is that it may be single crystal. Such materials are inherently free of the creep and fatigue found in poly-crystalline materials. Moreover, loss mechanisms resulting from shifts between grains are avoided, which allows high quality factor resonators, and therefore higher performing devices.

Among conventionally manufactured angular rate sensors, there are number of principles of operation and a number of possible designs. Among these designs, gyroscopes based on angular momentum conservation are among the highest performing devices. However, highly sensitive gyroscopes often require a complex set of electro-mechanical devices that are active on a gimbal, i.e. a freely rotating platform. Given the fabrication complexity, this design has largely been overlooked in favor of simpler designs. Because TGZM is able to electrically isolate bulk silicon through wafer, a rather elegant and straightforward method for realizing a gimbaled gyroscopic design is possible.

Because of all of these reasons, an angular rate sensor is chosen to demonstrate

and highlight the utility of the thermomigrated junction isolation technique.

Overall Structure of the Thesis

The thesis is composed of two halves. The first half is the development and characterization of the thermomigration fabrication technology coupled with deep reactive ion etching technology to enable junction isolation and electro-mechanical function in single crystal silicon devices. The second part is a demonstration of the utility of the TGZM junction isolation technique by the application of thermomigration towards the realization of a working micro-device.

The first half of the thesis is composed of the following sequence: the re-creation of the thermomigration process from the literature, the combination of thermomigrated junctions with deep reactive ion etching technology, and finally, demonstration and characterization of electrical isolation.

Whereas the first half of the thesis is a fabrication and feasibility oriented, the second half is device and practicability oriented. Not only must a working device be demonstrated, but additionally, this device must be fabricated in such a way that the benefits of a deep reactive ion etched, single crystal silicon device are preserved, batch fabrication compatibility is retained, and unusual and/or impractical fabrication measures are avoided. The sequence of the second half is as follows: first, a discussion of the working principle and the design/simulation of the gyroscope, then the fabrication of the device, and finally, the testing and characterization of the device.

Chapter 2

Thermomigration History, Theory and Process

Temperature Gradient Zone Melting (TGZM), or thermomigration, is a type of liquid epitaxy that is driven by a thermal gradient. This process occurs whenever two different materials are in contact in a temperature gradient, and the average temperature is above the eutectic point of the two materials, but below the melting point of the highest melting point material. Because the conditions for TGZM are so general, the phenomenon is ubiquitous, occurring in systems from the microscopic to the geographic.

History

Temperature gradient zone melting was first observed in icebergs. In 1926, Whitmann reported the motion of trapped brine in ice. He explained the phenomenon in terms of the temperature difference between the ocean and the air. [Whitmann1926]

TGZM was later independently rediscovered by Pfann in 1955, who was the first to apply the technique to semiconductors. Pfann used thermomigration to fabricate bipolar transistors in germanium. [Pfann1955] From 1973-1981, Anthony and Cline investigated this process for various solvent/solute systems [Cline1976a, Cline1976b]. Most notably, Anthony and Cline investigated the aluminum/silicon system with various silicon orientations and aluminum line directions. They reported thermomigrating aluminum lines through silicon wafers as thick as 1cm in 12 hours. More recently, TGZM has been applied to the fabrication of through wafer electrical vias for 3-D

integration of microelectronics [Little1989], electrical isolation of power electronics [Anceau2002], solar cells [Norskog1981], and intracortical electrode arrays [Normann1991, Normann1992a].

In addition to doping semiconductive materials, TGZM has been used for growing single crystals, joining materials, measuring diffusivities in liquids, and purification [Pfann1978]. Unintended thermomigration is also often cited in the literature as a failure mechanism for interconnects in microelectronics systems [Ru2000].

TGZM Theory

The process of thermomigration can be understood as a solvent/solute system, where a droplet of the solvent/solute is surrounded by solid solute. For the purposes of junction isolation, aluminum is chosen for the dopant/solvent and single crystal silicon is the solute. Aluminum is a p-type dopant and is chosen because of its high diffusion constant in silicon. When aluminum is thermomigrated through n-type silicon, pn junctions can be formed.

To understand thermomigration, first consider a uniform temperature field with a small droplet of aluminum inside solid silicon. If the temperature is above the eutectic temperature, but lower than the melting point of the highest melting point material, then a droplet of liquid aluminum/silicon will form inside the solid silicon.

If a thermal gradient is then imposed, the droplet will move. Because solid solubility is a function of temperature, the warmer side of the droplet will dissolve more silicon than the cooler side, establishing a concentration gradient. The concentration gradient drives the dissolved silicon toward the cooler side of the droplet. However, the

cooler side is already at its solid solubility limit, and consequently, the silicon and aluminum will solidify epitaxially, using the surrounding crystal as a seed. In this fashion, the droplet proceeds through the silicon much like an earthworm, with the hotter side following the thermal gradient and dissolving more silicon, and the cooler side depositing a trail of aluminum doped silicon behind it. The droplets continue to propagate either until the aluminum is exhausted or the edge of the silicon is encountered.

The velocity of propagation is described by the following relation:

$$V = D_o \frac{e^{-Q/RT}}{1-X} \frac{\partial X}{\partial T} \nabla T$$

where D_o is the diffusion coefficient of Al in Si (8×10^{-8} cm^2/s), Q is the heat of fusion of Si (49.62 kJ/g mol), R is the gas constant (0.008314 kJ/g mol K), T is the average temperature, X is the atomic fraction of silicon in liquid, dX/dT is the atomic fraction change with respect to temperature (1/K), and ∇T is the temperature gradient through the wafer [Normann1992b].

The velocity of propagation of the droplet is linearly proportional to the diffusion constant of the dopant. Although other dopant materials are possible, aluminum is chosen because of its high diffusion constant in silicon. A second reason aluminum/silicon system is chosen is because it is the most thoroughly researched solvent/solute system in the thermomigration literature.

Increased velocity of propagation also allows denser positioning of the Al thermomigrated regions. This is important because multiple junctions arranged in series have higher breakdown voltages. Denser positioning allows more npn junctions per given area, which in turn, allows higher operating voltages per given area.

It is experimentally observed that the droplets exit the wafer slightly randomly displaced from the original pattern on the cooler side of the wafer. The motion of the droplet may be divided into two components, one that is parallel to the thermal gradient and one that is orthogonal to the thermal gradient. The motion orthogonal to the thermal gradient is a random walk and is dependent on total time of propagation. The faster the droplets propagate through the wafer, the less distance the droplets randomly walk orthogonally. This allows more closely spaced npn junctions and higher breakdown voltages [Normann1992].

Increased propagation velocity may be increased with higher temperature and steeper thermal gradients, and the design of the thermomigration apparatus is directed by the optimization of these parameters.

The TGZM Process

The TGZM apparatus

In order to fabricate thermomigrated npn junctions, an apparatus capable of performing TGZM needed to first be constructed. The major requirements are that the thermomigration apparatus is able induce a thermal gradient through the wafer at a high average temperature in a controlled atmosphere.

Most thermomigration apparati impose a thermal gradient by radiatively heating one side of the wafer. A number of thermomigration apparati have been discussed in the literature. One method is to use a laser whose beam has been defocused to cover the surface of one side of the wafer. [Harrison1983] Another apparatus utilizes a rapid thermal processor (RTP) that heats the silicon wafer from one side with halogen bulbs.

[Dilhac1999] Yet another scheme uses an electron beam to heat a block of molybdenum, which in turn radiates to heat a silicon wafer. [Cline1976a, Cline1976b]

In all cases, the cooling is also radiative. Typically the colder side exchanges photons with a cool blackbody, typically either a water-cooled block or just simply allowing the photons to radiate into the void, typically modeled as a blackbody radiating at room temperature.

With the silicon/aluminum system, there is the additional requirement that the atmosphere be controlled. The primary problem is the presence of oxygen, which oxidizes both the silicon and the aluminum and impedes the thermomigration process. This can be prevented either by performing the TGZM process under vacuum [Cline1976a, Cline1976b] or in an inert gas. [D'Altroy1985]

Since the demands of thermomigration are quite general, a filament evaporator may be adapted to perform the thermomigration. A filament evaporator consists essentially of a vacuum chamber and a power supply to resistively heat a filament. The available filament evaporators are capable of sufficiently low pressures (0.1μTorr) to prevent oxidation of the silicon and aluminum, and also to prevent hydrogen poisoning of the tantalum filament. Figure 5 shows a photograph of the adapted filament evaporator.

Figure 5 - The filament evaporator adapted for thermomigration.

In order to adapt a filament evaporator for thermomigration, several things are needed. One is a sufficiently wide filament that may be resistively heated. Second, a cold body is needed for the cooler side of the wafer to exchange photons. The colder the body, the steeper the thermal gradient imposed across the wafer. Finally, since the heated wafer will radiate from the edge as well as from each face, a thermal compensation structure is needed to suppress a radial thermal gradient. The filament, wafer, and thermal compensation structure are shown in figure 6. Also seen in the figure 6 is a

reflector underneath the filament and the mechanical structure to suspend the wafer above the filament.

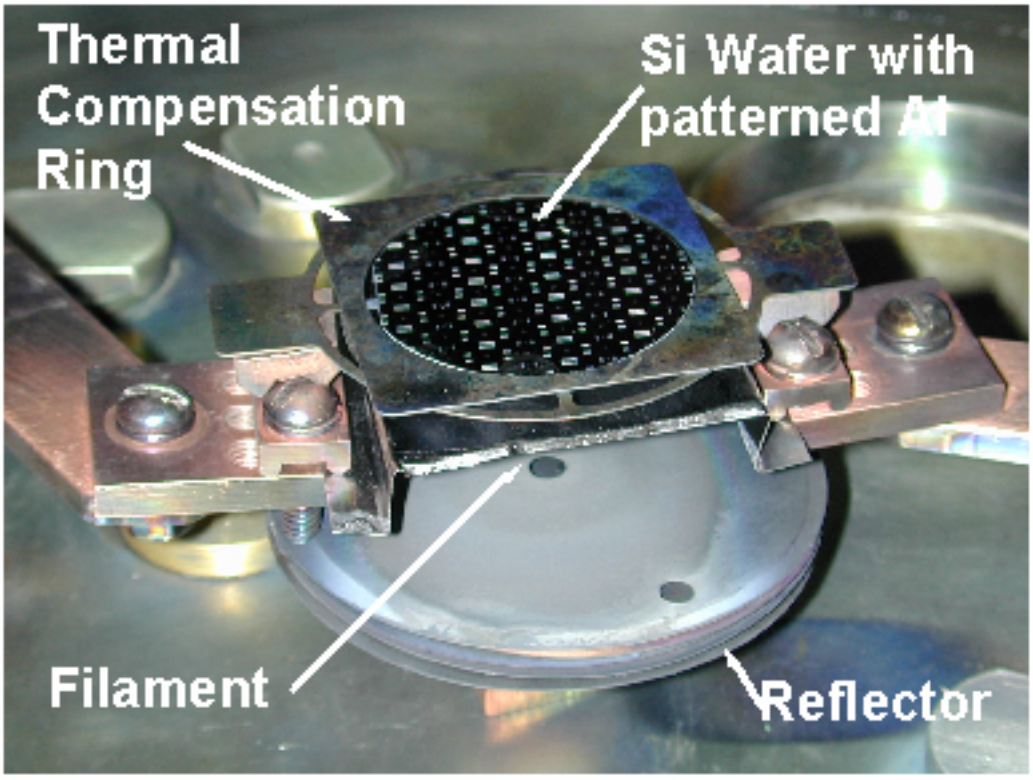

Figure 6 - The thermomigration filament, reflector, the wafer to be thermomigrated, and the thermal compensation ring. The filament is contacted to two copper arms that carry the current to heat the filament.

Filament Design

For the resistive heating element, a number of filament materials were investigated. Refractory metals are a logical choice since they can be resistively heated and have high melting points. Tungsten, molybdenum, and tantalum were considered, however, tungsten and molybdenum are less preferred than tantalum since when heated, the temperature of the tungsten and molybdenum filaments is visibly non-uniform. More

specifically, the shortest path between the contacts is visibly brighter than the rest of the filament. Since the droplets in the thermomigration process follow the thermal gradient, after thermomigration, the temperature non-uniformity in tungsten and molybdenum filaments can be seen in the thermomigrated aluminum. A tantalum filament, on the other hand, is uniform to the eye, and after thermomigration, no non-uniformity from the filament can be discerned in the thermomigrated pattern.

To maximize the temperature of the filament, and therefore the silicon wafer, the maximum power transfer into the filament is sought. For this particular filament evaporator, the power supply is a 2kW source. At the 5V setting, the maximum possible current is 400A. As a result, the filament is designed to be as close to 12.5mΩ resistance as possible.

The resistance as a function of geometry to first order is:

$$R = \rho \frac{L}{Area}$$

where R is the resistance of the filament, ρ is the resistivity of the filament material, $Area$ is the cross sectional area of the filament, and L is the length of the filament. The resistivity of tantalum at room temperature is 13μΩ-cm at room temperature and 66.5μΩ-cm at 1180C. [ESPI]

Foils of tantalum of adequate purity can be readily purchased in a variety of thicknesses, ranging from 0.1μm to greater than 1000μm. A thinner foil is desirable to increase the resistance; however, too thin a foil is mechanically fragile and typically

breaks from thermal expansion before the completion of the thermomigration in this work. In practice, the thinnest practically useful filament is found to be 125μm.

Another requirement is that the filament must be sufficiently wide in order to uniformly heat a wafer. 2" wafers were chosen since because they are readily available, have standard thicknesses of 280μm, and impose the least demanding width requirements on the filament. In order to uniformly thermomigrate wafers of this width, a 60mm wide filament is necessary for reasonable yields.

For a flat, planar filament, a 125μm thick, 60mm x 100mm tantalum filament is used in the filament evaporator. The 100mm figure is chosen since Ta is readily available at this length. This has a calculated resistance of 8.86mΩ which is low compared to the 12.5mΩ target. However, the contact resistance is significant compared to 8.86mΩ, and the observed output of the power supply with this filament is approximately 1600W.

Cooling Considerations

The temperature gradient that is needed in thermomigration is provided by allowing the heated wafer to radiatively cool. This is insured by placing a relatively cold, non-reflecting blackbody near the wafer. Many groups in the literature use a water cooled, black anodized aluminum block. However, for the available filament evaporator, this would have required feedthroughs to allow the water in and out of the vacuum. Instead, no special cool blackbody was used, and the heated wafer exchanged photons with the bell jar. During the thermomigration process, the bell jar would heat some, but would still be cool enough to touch, albeit with discomfort. A water cooled block would

have a temperature of approximately 20C while the bell jar is about 50C. Even if the bell jar were at a temperature of 100C, the temperature difference of a water cooled block and the bell jar is small compared to the average temperature of the wafer, which is about 1000C. In practice, the bell jar is an adequate cooling thermal sink for the thermomigration of 300μm deep Al-Si pn junctions.

Radial Thermal Gradient Suppression

Because of radiative cooling at the edge of the silicon wafer, there is a lateral, i.e. radial, component to the thermal gradient. This has two consequences. First, radial gradients result in angled npn junctions. Figure 7 shows a cross section of a wafer with a radial thermal gradient component. Second, overly large lateral gradients cause differential thermal expansion in the silicon, which stresses the substrate. After the wafer cools, this internal stress can persist, resulting in a fragile, fracture-prone wafer that is difficult to further process. If the lateral gradient is yet steeper, the differential thermal expansion causes the wafer to warp and become non-planar, causing a number of practical problems, ranging from proper contact with a spinner's vacuum chuck to imprecise imaging during photolithography. Because of these effects, the lateral thermal gradient must be suppressed as much as possible.

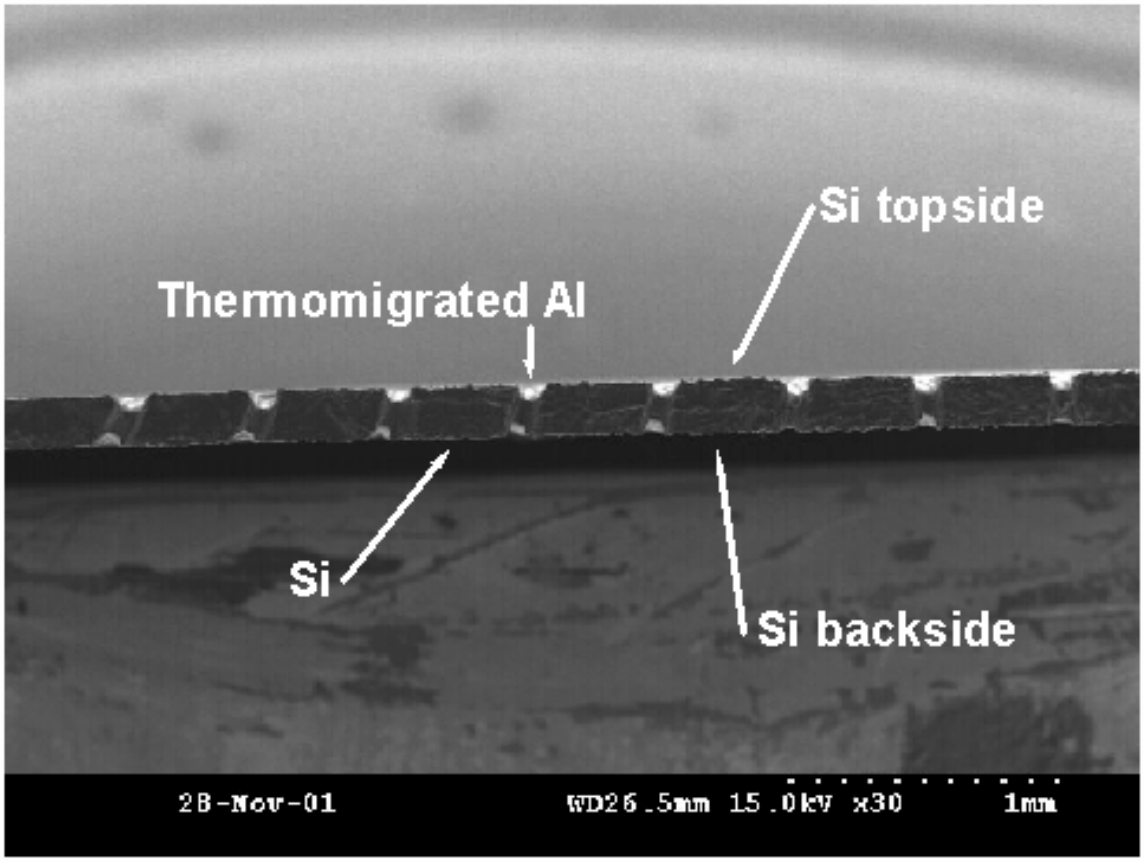

Figure 7 - Side view SEM of a thermomigrated wafer. The change in angle of the thermomigrated junctions from left to right show the effect of lateral cooling on the pn-junctions.

Angled npn junctions have a number of undesirable effects. First, non-vertical npn junctions have lower blocking voltages. More problematic is that fact that the path of the thermomigrated Al can move laterally into adjacent features, unintentionally changing characteristics. Additionally, Al doped silicon is harder to deep reactive ion etch. If the Al doped silicon shifts into a region between two mechanical free parts, it can be more difficult to etch through the material to free them. Figure 8 and 9 show a vertical and non-vertical junction after post-processing.

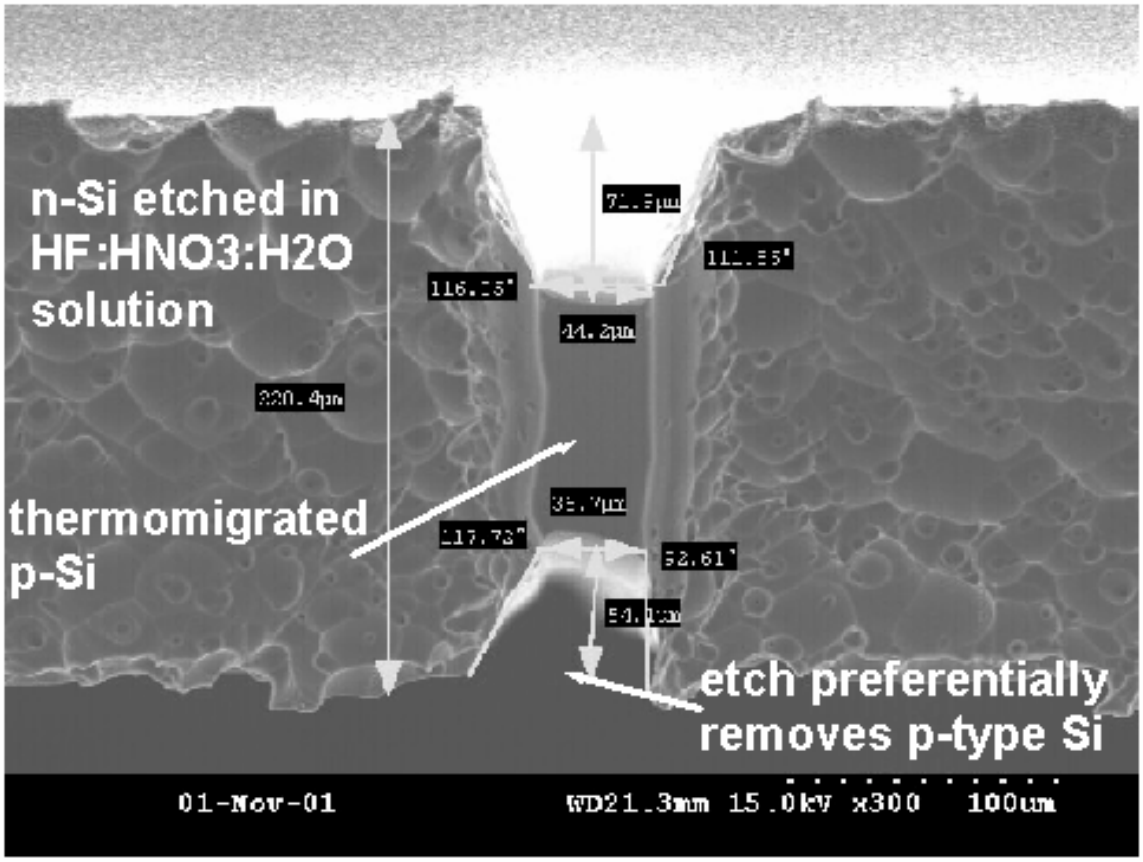

Figure 8 - Side view SEM of a vertical pn junction. The junction is post-processed to remove the excess Al and heat damaged Si.

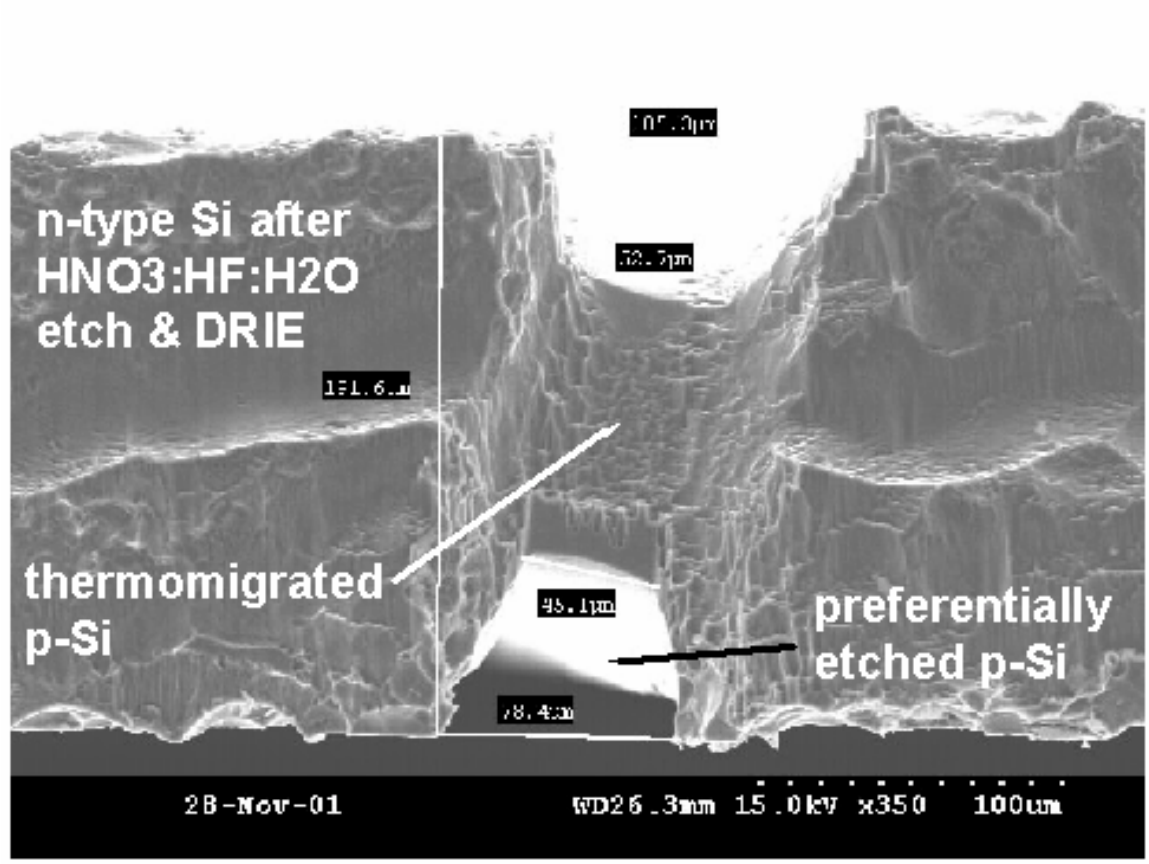

Figure 9 - Side view SEM of an angled pn-junction. Angled junctions typically have lower blocking voltages.

There are two known ways to discourage the formation of angled npn junctions. One is to increase spatial uniformity of the incoming thermal influx, and the second is to reduce lateral cooling.

From geometric relations, the amount of radiative energy captured by the silicon at each point on the wafer is a function of energy flux density seen by each part of the wafer. If the thermomigration heat source is on the order of the same size or smaller than the wafer, then, the amount of thermal influx varies greatly across the wafer. The simplest solution is to simply increase the size of the heat source so that it is large relative to the thermomigrated substrate, and the edge effects are reduced. Many of these

calculations were performed by Lord. [Lord1988] The problem with this approach is that it is power intensive. As the area increases, the power requirements to heat the filament increase quadratically. Given the temperatures required for thermomigration (~1000C at the substrate), the maximum power output of the source can be quickly reached.

As a result, it is necessary to also employ the second technique, which is to reduce the cooling that occurs laterally. Lateral cooling affects an entire 2 inch wafer and only a small area, approximately 1cm in diameter at the center of the wafer yields good die. This is an unacceptable loss for even a prototyping project. A thermal compensation ring may be used to transfer as much of this cooling affect to an outer mass.

If the wafer is modeled as a short cylinder, the majority of the silicon wafer's cooling will occur on the far face of the wafer from the heat source. However, because there is a thickness, photons will also radiate from the edge, causing an appreciable amount of cooling. To suppress this, a thermal compensation ring is placed around the silicon wafer.

This ring is simply a square piece of silicon with a hole in the middle to accommodate the silicon wafer. A picture of the ring with a silicon wafer is shown in figure 10. Both the wafer and the thermal ring are heated together, and the silicon wafer exchanges photons at the edge with the ring, while the ring exchanges photons with the cold body. The lateral cooling of the wafer is largely an edge effect, only practically important on the outer 1cm or so of the wafer. The thermal compensation ring simply shifts this effect from the wafer to the ring itself. A square shape is chosen to match the shape of the filament to capture a greater fraction of the emitted photons.

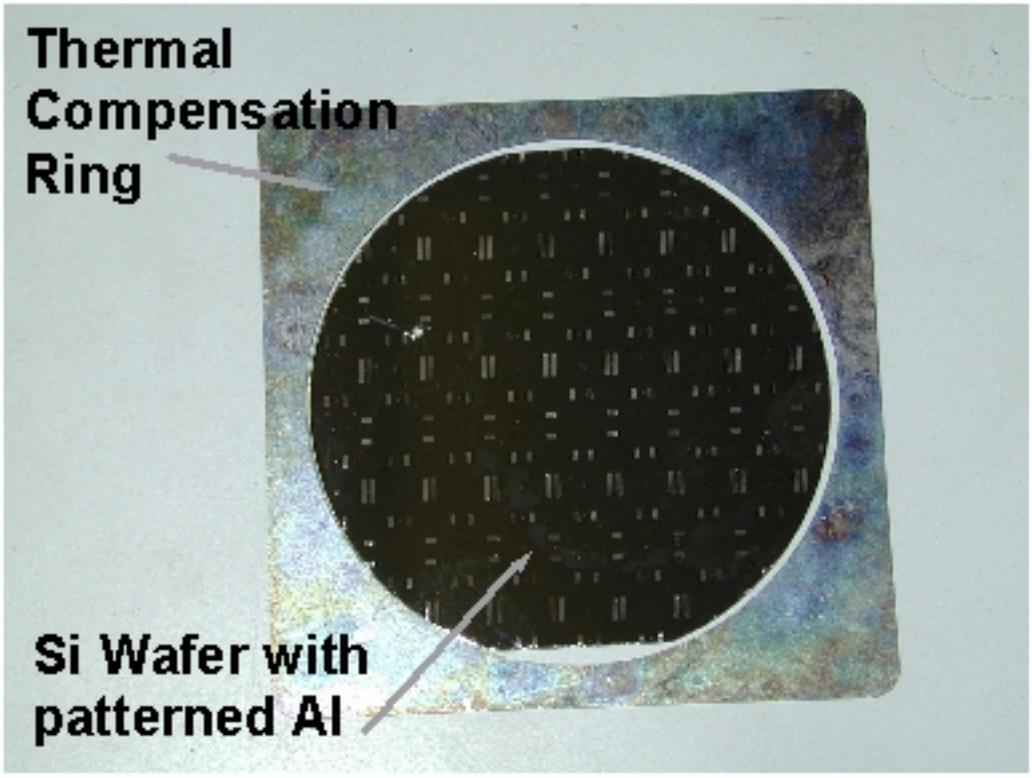

Figure 10 - Photograph of a silicon wafer to be thermomigrated inside a thermal compensation ring. The ring itself is square to match the shape of the filament to maximize captured energy.

The ring is fabricated by using an infrared laser to cut the silicon. A 6" diameter, 700μm thick wafer is chosen. The additional thickness increases the area that captures and exchanges photons with the silicon wafer to be thermomigrated. The parameters for the laser are in table 1.

Table 1 - The laser parameters used to fabricate the thermal compensation ring.

Laser Parameters for Thermal Compensation Ring	
wafer	Si, 6", 700um thick
wavelength	1026nm
transmission	80%
cut rate	0.75mm/s
pulse rate	1000Hz

Because the silicon is single crystal, it is prone to fracture along crystal planes. As a result, the pattern is laser cut into the silicon at an angle to the crystal planes. Furthermore, to gently separate the individual pieces, the silicon is etched in a dilute solution of $HF:HNO_3:H_2O$ at a ratio of 1:1:5 for 30 minutes. This preferentially etches the laser damaged silicon, and minimizes the amount of mechanical force necessary to separate the pieces. Finally, clever laser cut patterns will increase the yield of the fabrication of the ring. For example, instead of simply cutting a circle out of the silicon, pie shaped pieces are more easily separated. These pieces may be pressed in the center to release them. Also, if the outer circle has concentric circles with diameters 1mm and 2mm shorter, then the amount of energy transferred to the outer frame tends to be distributed over a larger area.

Thermomigration Post-processing

An excess of aluminum is initially deposited on cool side of the wafer to insure that the aluminum will not exhaust before reaching to the opposite face of the wafer. As a result, after thermomigration, an excess of aluminum resides on the opposite face of the

silicon. The excess aluminum can bridge the npn junctions and short the electrical isolation.

In addition, the heat of the thermomigration process can disrupt the single crystal silicon lattice, thus leaving dangling bonds and other non-idealities on the surface of the silicon, which lowers the breakdown voltage of the npn junction.

Both the excess aluminum as well as the heat-damaged silicon must be removed after thermomigration to insure electrical isolation. Most groups simply lap off the materials, and in cases when this is possible, it is recommended. However, for MEMS devices, this procedure may lap off previously fabricated structures. An alternative is to etch off the unwanted materials.

A dilute solution $HF:HNO_3:H_2O$ can be used in ratios of 15:35:50. This etch quickly removes both silicon as well as aluminum. Furthermore, a Cr mask can be used to protect structures from this etch. This etch preferentially removes either n- or p-type silicon doped in excess of $10^{19}cm^{-3}$. [Runyan&Bean1994a] The difference in etch rate can be mitigated by varying the ratio of the three etchants. A 2 minute etch removes about 40μm from each side of the wafer. Figure 11 shows a thermomigrated region through silicon after the post-processing.

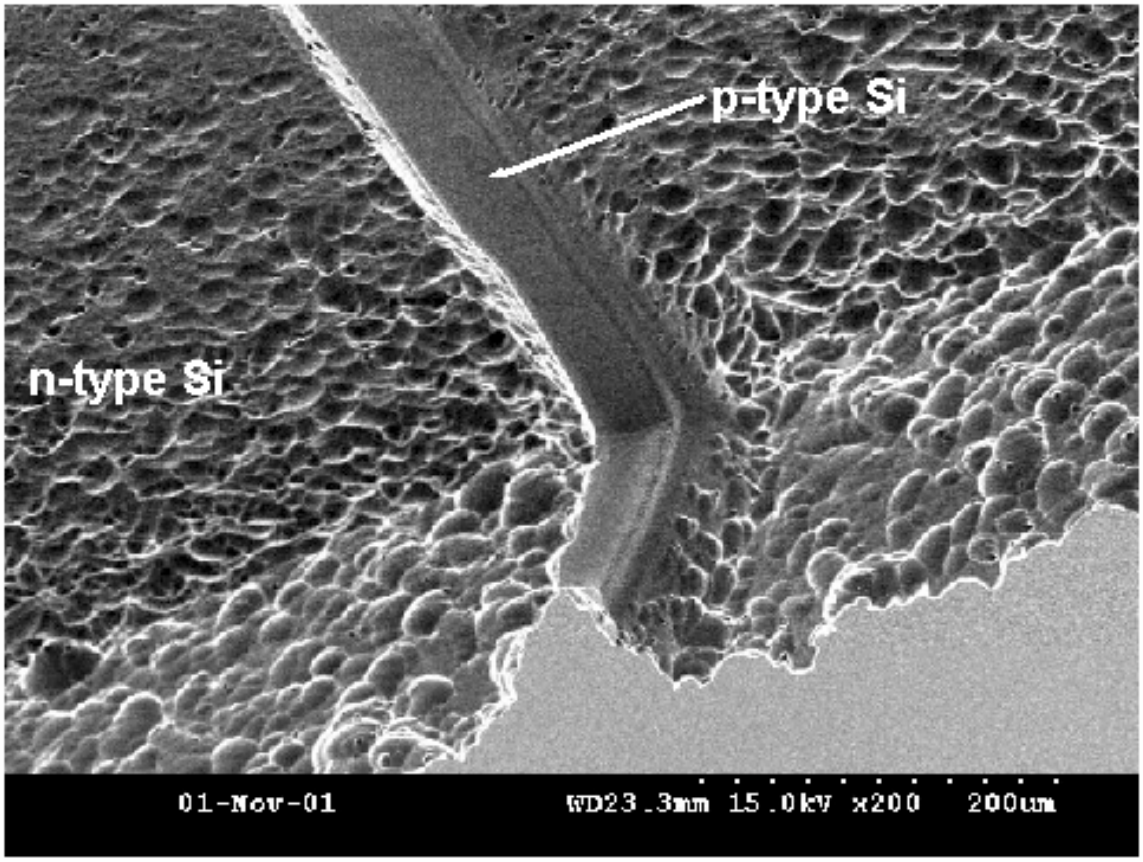

Figure 11 - SEM of a thermomigrated junction after post-processing. Note the additional material removed in the p-type silicon region.

Processing Particulars

At the temperatures and the pressures present during the thermomigration process, Al is an evaporable metal. Superior results are found when the Al/Si eutectic is allowed to thoroughly form. This is insured by heating the Al/Si to above the eutectic (577C) but below the melting point of Al (660C). This allows the Al to melt and dissolve the Si without evaporating. Too fast an increase in temperature results in much of the Al evaporating, often redepositing onto the wafer. Once the Al melts, dissolves the Si, and enters the bulk, the temperature may be ramped quickly, but must remain below the melting point of the silicon (1412C).

Fabrication Limits of Thermomigration for MEMS Devices

Given the particulars of the TGZM process, there are a number of limitations to thermomigrated junction isolation, such as allowable geometries, minimum size and range of doping levels.

In general, lines are more difficult to propagate than dots, primarily because the lines need to be aligned with the crystal orientation. Lines that are nonparallel tend to break up into several sections, each one aligned to the crystal plane, similar to aliasing in computer graphics. Such gaps allow current to go around the npn junction. It is possible to thermomigrate long lines; however, this requires care in alignment. [Cline1976c]

Because lines must be aligned to the crystal, arbitrary angles are not possible. The possible angles differ according to crystal orientation. <100> wafers allow rectilinear lines to be thermomigrated, i.e. along 0 and 90° directions. Other wafer orientations and allowable directions are shown in table 2. [Cline1976c] It should be noted that the thermal gradient must also be aligned with crystal plane in order for lines to stably thermomigrate through the wafer.

Table 2 - Possible orientations of the thermomigrated lines through wafers of different crystal orientations and planes.

Wafer Plane	Migration Direction	Stable Wire Directions
<100>	<100>	<011>
<110>	<110>	<110>
<111>	<111>	<011>
		<101>
		<110>
		<112>
		<211>
		<121>

In this work, the minimum npn junctions thermomigrated through 300μm wafers is approximately 50μm wide. Adjacent aluminum regions must also be separated by at least 50μm, otherwise, there is a risk of 2 adjacent aluminum regions random walking into each other, and merging, thus halving the overall breakdown voltage. Other groups have reported minimum geometries and separations of 35μm by increasing average temperatures and increasing the slope of the thermal gradient. [Normann1992b] Ultimate limits on minimum npn junction size seem to be limited mostly by equipment and time. Anthony and Cline demonstrated 50μm lines with 50μm spacings thermomigrated through 1cm of silicon. [Cline1976b]

There seems to be no maximum thickness for thermomigration. As stated before, Anthony and Cline report thermomigrating aluminum through 1cm thick silicon wafers in 12 hours. [Cline1976b]

Finally, the doping level of the aluminum in the silicon is rather inflexibly set by the solid solubility limit at the temperature of solidification. The doping level can be controlled to some degree by selecting the average temperature of thermomigration. From 700C to 1300C, the solid solubility limit only varies from $10^{19}cm^{-3}$ to $2x10^{19}cm^{-3}$. However, above 1300C to the melting point of silicon (1412C), the solid solubility limit

rapidly decreases two orders of magnitude from $2x10^{19}cm^{-3}$ to $4x10^{17}cm^{-3}$. In theory, a tightly temperature controlled thermomigration apparatus could vary the doping concentration through two orders of magnitude in this temperature region.

As a final note, in theory, because there is a thermal gradient, there is also a gradient of doping levels through the silicon. However, it is estimated that the temperature gradient through the thickness of the wafer is on the order of 1C, so although the doping concentration is non-uniform through the wafer, it is negligible for purposes of junction isolation.

The Thermomigration Recipe

1. Acquire n-type silicon wafers of higher resistivity. The higher the resistivity, the higher the final blocking voltages. For 1Ω-cm n-type wafers, a final blocking voltage of 184V is achievable.
2. Clean wafers using RCA clean
3. Deposit Al. Any deposition technique will do. The thicker the wafer, the more Al that is needed. For a 300μm thick wafer, 5μm of Al is adequate
4. Radiatively heat one side of the silicon wafer, and insure that the opposite side can radiatively cool. This must be done in either an inert atmosphere or in vacuum. The temperatures necessary are on the order of 1000C for thermomigration times on the order of an hour for a 300μm thick wafer. Perpendicularity of the thermomigration may be improved with thermal radiators on the side of the wafer.

5. Etch off heat damaged silicon and excess Al. This may be done either by lapping the wafer or etching the wafer. For etchant, a dilute solution of H_2O: HF:HNO_3 was used in ratios of 50:35:15. Etch time was approximately 2 minutes.
6. Proceed with subsequent fabrication

Chapter 3

Thermomigrated Junction Isolation and Its Application to MEMS

The fabrication of pn junctions hundreds of micrometers thick enables the possibility of junction isolating bulk-micromachined, single crystal silicon MEMS devices. However, the path from thermomigrated pn junctions to working MEMS devices is not well-mapped, and must encounter the following questions:

- Are the blocking voltages adequately high for MEMS device operation?
- Are the leakage currents sufficiently small?
- Are the thermomigrated junctions compatible with the deep reactive ion etching technologies that motivate this work?
- Are the thermomigrated junctions compatible with other technologies, such as surface micromachining and CMOS?
- Are there any other unforeseen issues that may or may not make this approach impractical?

Electrical Isolation

Spatial separation of voltage, i.e. the establishment of a voltage gradient, is the fundamental feature necessary to enable electrical and electro-mechanical functionality. This requires some sort of electrical isolation scheme. The ideal electrical isolation

would allow zero current flow regardless of the applied voltage. Unfortunately, no perfect electrical isolation method exists. Junction isolation deviates from the ideal by having a finite maximum voltage and a small leakage current. These non-idealities set a range for a number of operating parameters, such as operating voltage and power draw.

For the purposes of electrical isolation, npn junctions may be modeled as two series connected, back-biased diodes. While one diode is forward biased, the other is reverse biased, which prevents current flow regardless of the direction of the applied voltage. Since a diode in forward bias acts like a wire, the analysis of npn junctions for the purposes of electrical isolation reduces to a single pn junction in reverse bias.

Breakdown Voltage

Junction isolation has an upper limit to the amount of voltage that it is able to block, termed the breakdown voltage. There are several mechanisms for the voltage breakdown, however the dominant effect for thermomigrated junctions, where one side is heavily doped and the other is lightly doped, is avalanche breakdown.

The mechanism for avalanche breakdown is quite intuitive. As electrons are accelerated through the junction by the applied electric field, the electrons collide into the atoms of the lattice. Above a certain energy, i.e. above a certain voltage, the electron-lattice collision has enough energy to liberate electron-hole pairs. These electron-hole pairs, in turn, liberate more electron-hole pairs, and the current across the junction grows exponentially, to a point where the current flow electrically connects the two sides.

The breakdown voltage is inversely linear with doping concentration of the more lightly doped side. For TGZM fabricated npn junctions, the doping concentration of the

p-doped region is set by the solid solubility limit of aluminum in silicon at the thermomigration temperature. At an average temperature of 1000C, the solid solubility limit of Al in Si is approximately $2x10^{19}cm^{-3}$ which varies slowly up to 1300C. In contrast, the n-doped region is set by the silicon wafer's manufacture. Wafers with extremely light doping concentrations may be purchased, with resistivities exceeding 100Ω-cm. As a result, for aluminum thermomigrated junction isolation, the breakdown voltage is determined by the doping concentration of the n-type region.

The price increases rapidly for wafers with resistivities greater than approximately 30Ω-cm. Wafers with resistivities on the order of 1Ω-cm were purchased because they have an adequate breakdown voltage and are easily obtained. The particular wafers that were purchased had a range of resistivities, from 0.7Ω-cm to 1.4Ω-cm, measured with by 4 point probe, Veeco Instruments Inc., FPP5000.

From the resistivity (ρ), the doping concentration for n-type silicon can be found:

$$\rho = \frac{1}{q\left(n\mu_n + p\mu_p\right)} \approx \frac{1}{qn\mu_n}$$

where q is the electron charge, μ_n is the electron mobility and n is the doping concentration. Mobility is a function of both temperature and doping concentration. For Si at 300K, the mobility is approximately 1400 $cm^2/V\text{-}s$ for doping concentrations $<5x10^{16}cm^{-3}$ [Sze2002a].

Given this relation, at a resistivity of 1Ω-cm, the doping concentration is $4.45x10^{15}cm^{-1}$. From the concentration of the n-doped regions, the breakdown voltage for a pn junction may be calculated:

$$V_B = \frac{\varepsilon_{Si} E_c}{2q} (N_B)^{-1}$$

where V_B is the breakdown voltage, ε_{Si} is the dielectric constant for silicon which is 11.9 ε_o, E_c is the critical field, i.e. the electric field at breakdown, and N_B is the doping concentration of the more lightly doped side of the pn-junction. The critical field is a function of doping concentration. For 1Ω-cm resistivity n-type silicon, the critical field is approximately 5×10^5 V/cm. [Sze2002b] From this, the theoretical breakdown voltage is calculated to be 184V.

This voltage is adequately high to operate a range of devices. In many cases the supply voltage will be more limiting than the breakdown voltage. For the gyroscope, 184V is sufficiently high to achieve appreciable actuation. If this voltage is not adequate, then multiple npn junctions may be arranged serially to increase the overall breakdown voltage.

Leakage Current

Ideal pn-Junction Diode Model

At voltages less than breakdown, there is a small leakage. In current limited situations, the leakage current can be seen as another determinant in the maximum sustainable voltage difference across the junction. In non-current limited situations, the leakage current imposes a lower limit on the power draw of the device, and may set other operating ranges such as charge/drain times of capacitors.

The leakage current is also known as the pn junction's saturation current. The saturation current is due to generated carriers near the junction. These generated carriers are often either thermally or optically liberated electron-hole pairs. If the generated carrier is close enough, within one diffusion length, of a pn junction, the carrier may be swept across the junction resulting in a small current.

For the ideal diode, the saturation current may be calculated as:

$$J_S = \frac{qD_p p_{no}}{L_p} + \frac{qD_n n_{po}}{L_n} = qn_i^2 \left(\frac{1}{N_D}\sqrt{\frac{D_p}{\tau_p}} + \frac{1}{N_A}\sqrt{\frac{D_n}{\tau_n}} \right)$$

where D_p and D_n are the diffusion constants for holes and electrons respectively, p_{no} and p_{po} are the equilibrium hole concentration in the n and p regions respectively, and L_p and L_n are the diffusion lengths for holes and electrons respectively, N_D and N_A are the donor concentrations on each side of the pn junction, and τ is the lifetime of each respective carrier.

If the following values are taken: $\tau_p = \tau_n = 5\text{x}10^{-7}$s, $D_n = 21\text{cm}^2/\text{s}$, $D_p = 10\text{cm}^2/\text{s}$, $n_i = 9.65\text{x}10^9\text{cm}^{-3}$, $N_D = 5\text{x}10^{-15}\text{cm}^{-1}$, and $N_A = 10^{22}\text{cm}^{-1}$, then the acceptor term is several orders of magnitude lower than the donor term, and may be dropped. The theoretical saturation current density is calculated to be $1.33\text{x}10^{-11}\text{A/cm}^2$. If we assume a 300μm thick silicon wafer and a square cross section, then the current is $1.20\text{x}10^{-14}$A. The ratio of breakdown voltage to leakage current is a useful figure of merit, which is a sort of "equivalent resistance," of $1.51\text{x}10^{16}\Omega$. This is comparable to the leakage current and resistance of thermally grown oxide. The measured resistivities of thermally grown

oxide range 10^{12}-10^{16} Ω-cm [Runyan&Bean1994], which for the same geometry as the TGZM junction, translates into a resistance of $5x10^{14}$-$5x10^{18}$Ω.

Diode in Reverse Bias

The previous derivation is for an ideal pn junction and assumes that the net generation-recombination rate in the depletion region is zero. However, in reverse bias, generation dominates recombination, since thermally generated pairs in the depletion region are quickly separated by the applied field. As a result, there is an additional contribution to the current across the junction.

For semiconductors such as silicon, the primary generation process is via electron-hole emissions through bandgap generation-recombination centers. For this effect, the expression for the current density is:

$$J_{Gen} \cong \frac{qn_iW}{\tau_g}$$

where J_{Gen} is the generation current in the depletion region, q is the electron charge, D_p is the diffusion constant for the holes in silicon, τ_p is the lifetime of the holes, n_i is the intrinsic carrier density, N_D is the donor dopant concentration, τ_g is the generation lifetime, and W is the width of the depletion region. [Sze2002]

Using the following expected values for a thermomigrated junction:

$q=1.602x10^{-19}C$ $\quad\quad$ $D_p=10cm^2/s$

$N_D=10^19cm^{-3}$ $\quad\quad$ $N_A=5x10^{15}cm^{-3}$

$n_i=9.65x10^{9}cm^{-3}$ $\tau_p=\tau_g=5x10^{-7}s$

The width of the depletion region is:

$$W=\sqrt{\frac{2\varepsilon_{Si}}{q}\left(\frac{N_A+N_D}{N_AN_D}\right)(V_{bi}+V)}$$

$$=\sqrt{\frac{2\varepsilon_{Si}}{q}\left(\frac{N_A+N_D}{N_AN_D}\right)\left(\frac{kT}{q}\ln\left(\frac{N_A+N_D}{n_i^2}\right)+V\right)}$$

$$=5.12\,x10^{-5}\sqrt{(1.017+V)}cm$$

Substituting this expression into the generation current yields:

$$J_{Gen}=\frac{qn_iW}{\tau_g}$$

$$=\frac{1.602x10^{-19}\times 9.65x10^{9}}{5x10^{-7}}\left(5.12x10^{-5}\sqrt{(1.017+V)}\right)\frac{A}{cm^2}$$

$$=1.590x10^{-7}\sqrt{(1.017+V)}\,\frac{A}{cm^2}$$

If the theoretical breakdown voltage for 1Ω-cm n-type silicon is substituted, 184V, and the cross-sectional area for a square 300μm thick junction, the generation current is:

$$I_{Gen} = 2.175x10^{-6}\frac{A}{cm^2}\times\left(300x10^{-4}\,cm\right)^2 = 1.958x10^{-9}\,A$$

The equivalent "resistance" that is the ratio of the breakdown voltage to the leakage current at breakdown is:

$$R = \frac{V_{br}}{I_{leak}} = \frac{184V}{1.958x10^{-9}\,A} = 93.99G\Omega \approx 100G\Omega$$

Characterization of TGZM Junction Isolation

To verify the theoretical results, a series of thermomigrated npn junctions that are deep reactive ion etched are fabricated, and their breakdown voltages and leakage currents are measured. In addition, since thermomigration is a batch fabrication technology, the time, materials, and labor to fabricate many junctions is the same as that for a single junction. It would be very interesting if multiple junctions arranged in series improve either the breakdown voltage or leakage current, but it is not apparent *a priori* if there is any benefit to this. To answer this question, both the blocking voltage and the leakage current are measured as a function of the number of npn junctions.

To measure these parameters, a structure with 12 thermomigrated junctions is fabricated. Each junction is 100μm wide and 300μm deep. The separation between

junctions is 500μm. Figure 12 shows a photomicrograph of the test structure. A ruler is in the background, with each division marking 1mm.

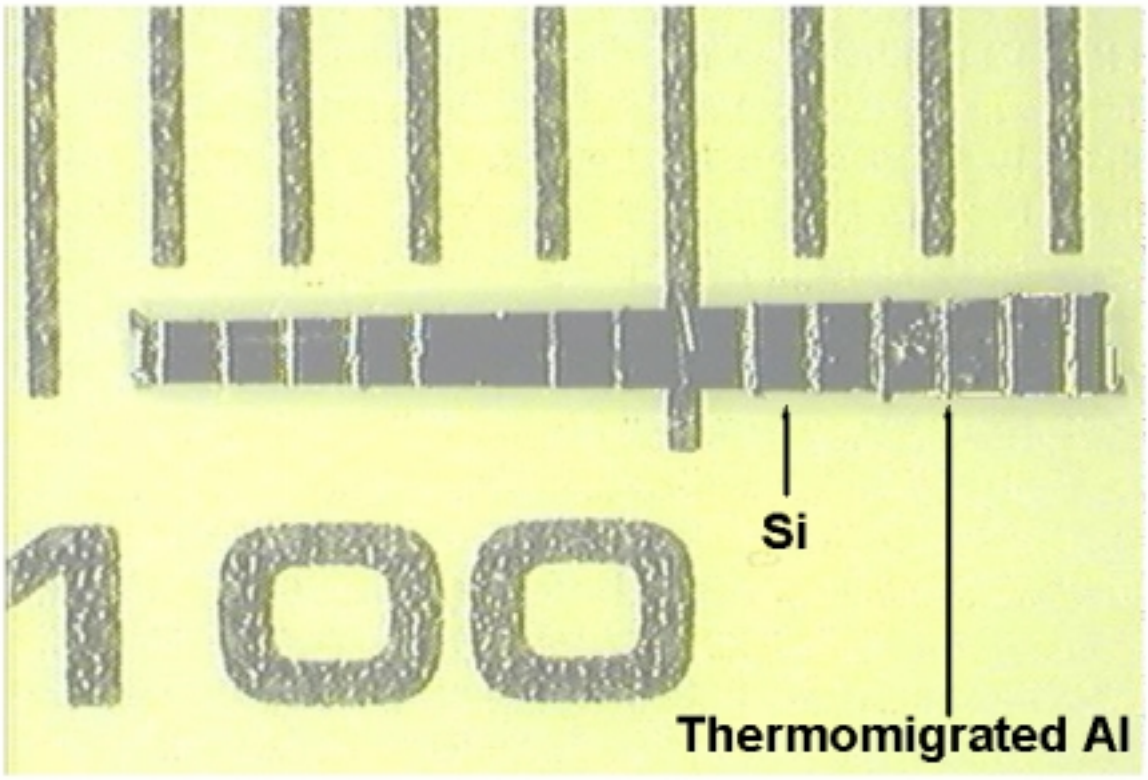

Figure 12 - Photograph of the blocking voltage/leakage current test structure for thermomigrated junction isolation. The thermomigrated lines are 100um wide and spaced 500um apart. The sample sits on a ruler. Each mark delineates 1mm.

Each npn junction is contacted on both sides of the Al line with tungsten probe tips. The tungsten probes are connected to a Tektronix 370A curve tracer to obtain the I-V curve of the npn junction. There is a Schottky diode that is formed at the contact between the Si and the tungsten probe. The breakdown voltage of the Schottky diode is less than 15V, above which the contact acts as a conductor. Since the breakdown voltage of the Schottky diode is significantly lower than the breakdown voltage of the npn

junction, for the purposes of measuring the breakdown of the junction, the presence of the Schottky diode may be treated as a lower order effect, and to first order is treated as a short.

The breakdown voltage is determined as the intercept of the low-resistance line, i.e. the I-V curve above breakdown, extended to the voltage axis. Some npn junctions have a classic npn junction profile; others had rather ragged looking features. An example of a junction with a non-standard profile is shown in figure 13. The I-V curve is asymmetric about the y-axis. Both breakdown voltages as well as leakage currents differ.

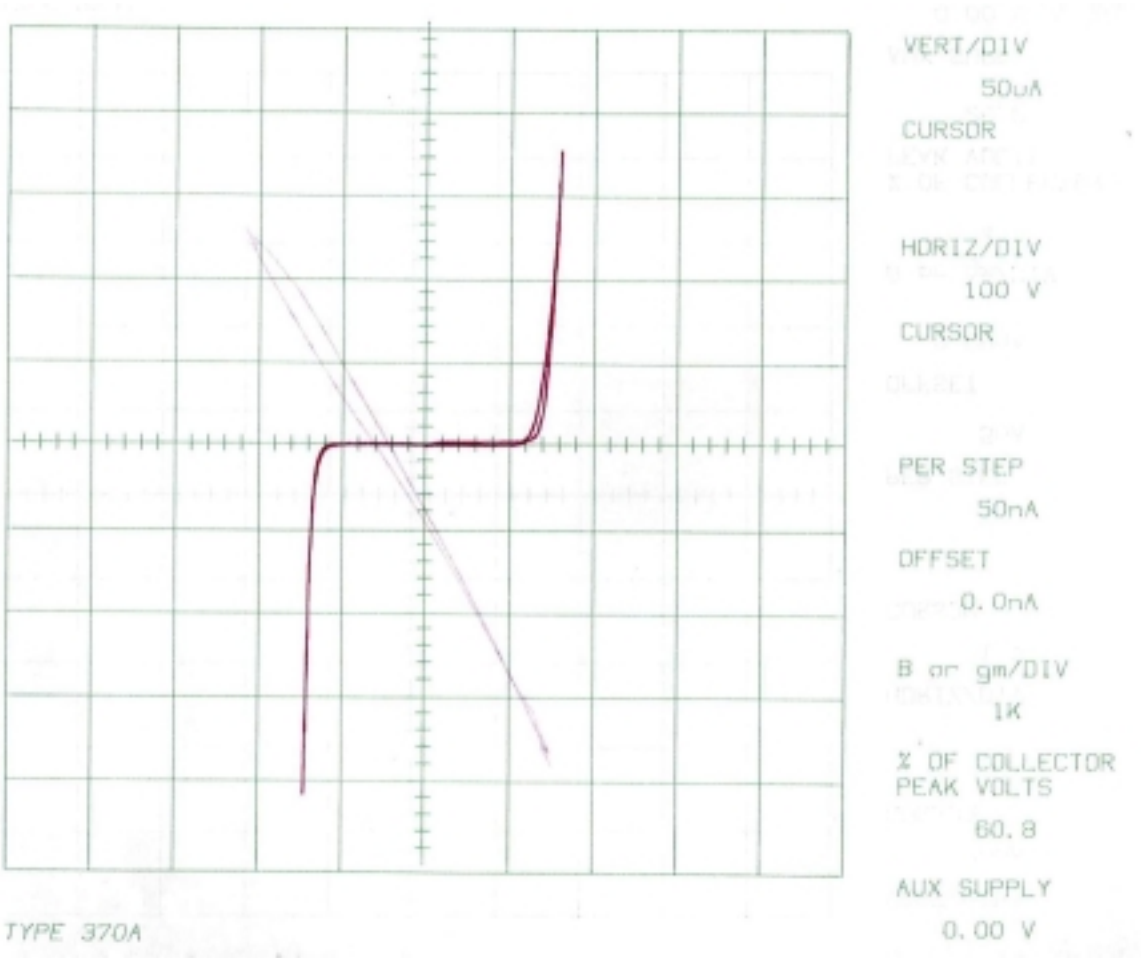

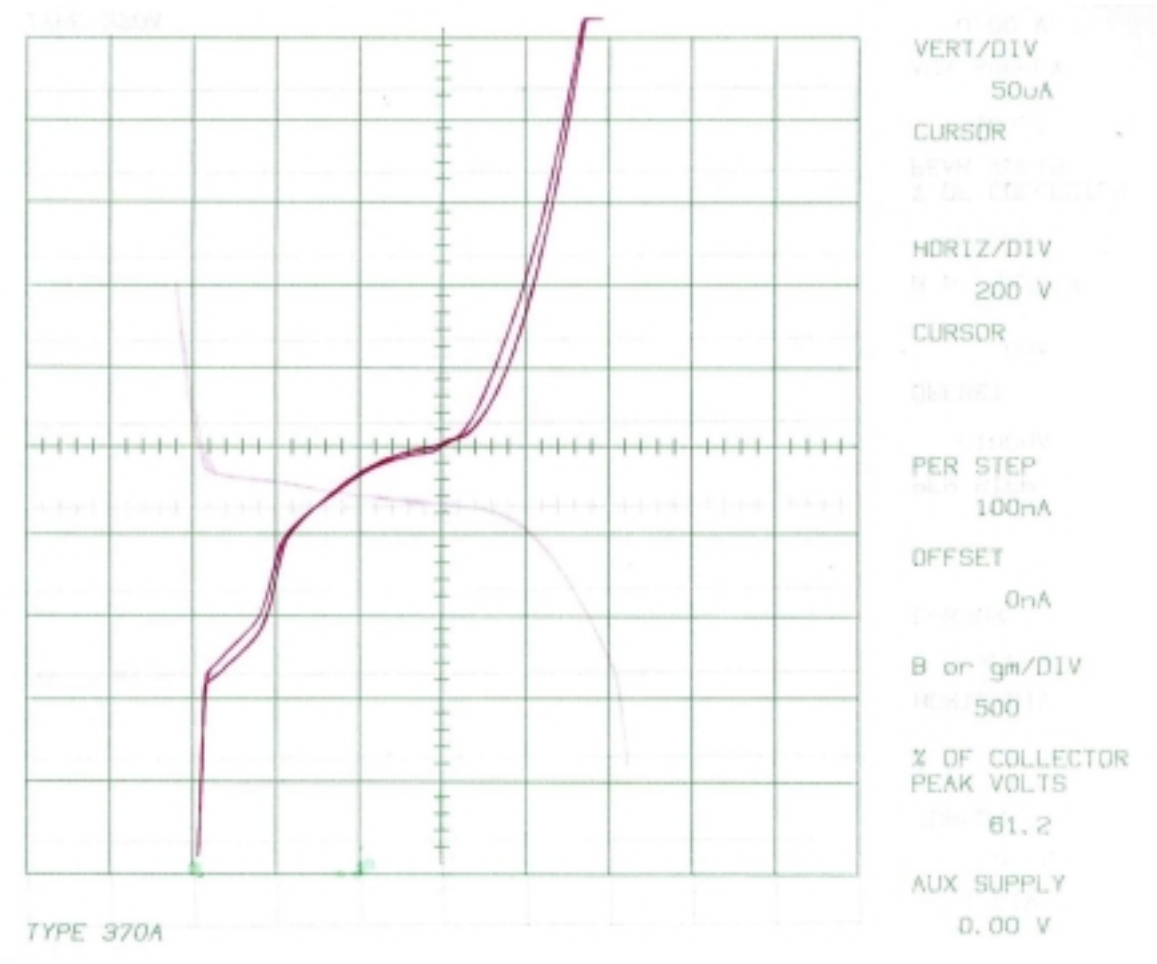

Figure 13 - I-V curve for a sample pn-junction.

The breakdown voltages for the 12 junction are shown in table 3. Using the above described method, the average blocking voltage of a single junction was measured to be 124.2V ± 55.34V with the voltage applied in one direction and 116.67±39.39 volts in the other direction. The average of the breakdown voltages in both direction is 120.4V±47.13V. The average leakage current at breakdown is less than 5μA.

Table 3 - Breakdown voltages for each junction of the test sample.

Junction Number	Breakdown V Forward	Breakdown V Reverse
1	140	170
2	190	180
3	180	150
4	180	130
5	90	110
6	140	120
7	80	90
8	80	110
9	170	100
10	40	110
11	40	30
12	160	100
average	**124.17**	**116.67**
stdev	**55.34**	**39.39**

For multiple junctions, arrangement of the npn junction in series is found to increase the overall blocking voltage while maintaining leakage current constant. The overall I-V curve is symmetric, resembling the I-V curve for a classic, standard single npn junction, albeit with higher blocking voltages and the same leakage current. Figure 14 shows the I-V curve for 12 npn junctions in series. The overall blocking voltage for the 12 junctions is 1550V in one direction and 1410 in the other. Leakage currents remained constant with overall current less than 20μA at 1500V.

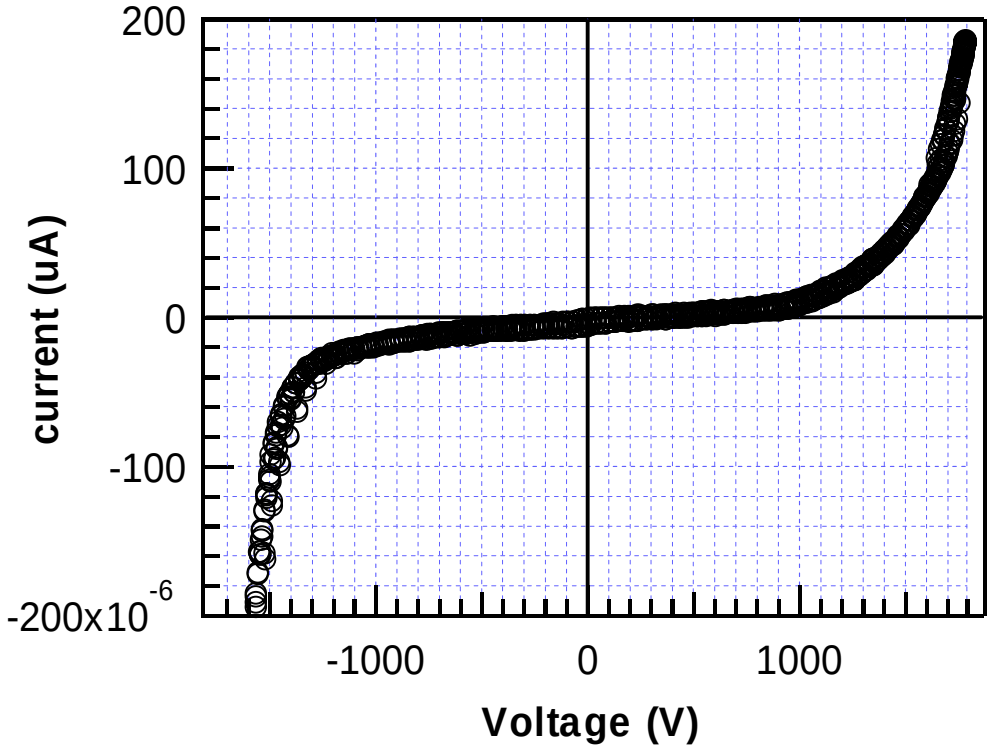

Figure 14 - Overall I-V curve for 12 npn junctions in series. The blocking voltages add, while the leakage current remains constant. The overall blocking voltage for 12 npn junctions exceeds 1500V.

The breakdown voltage increases linearly with the number of junctions. A plot of the overall breakdown voltage as a function of the number of junctions is shown in figure 15.

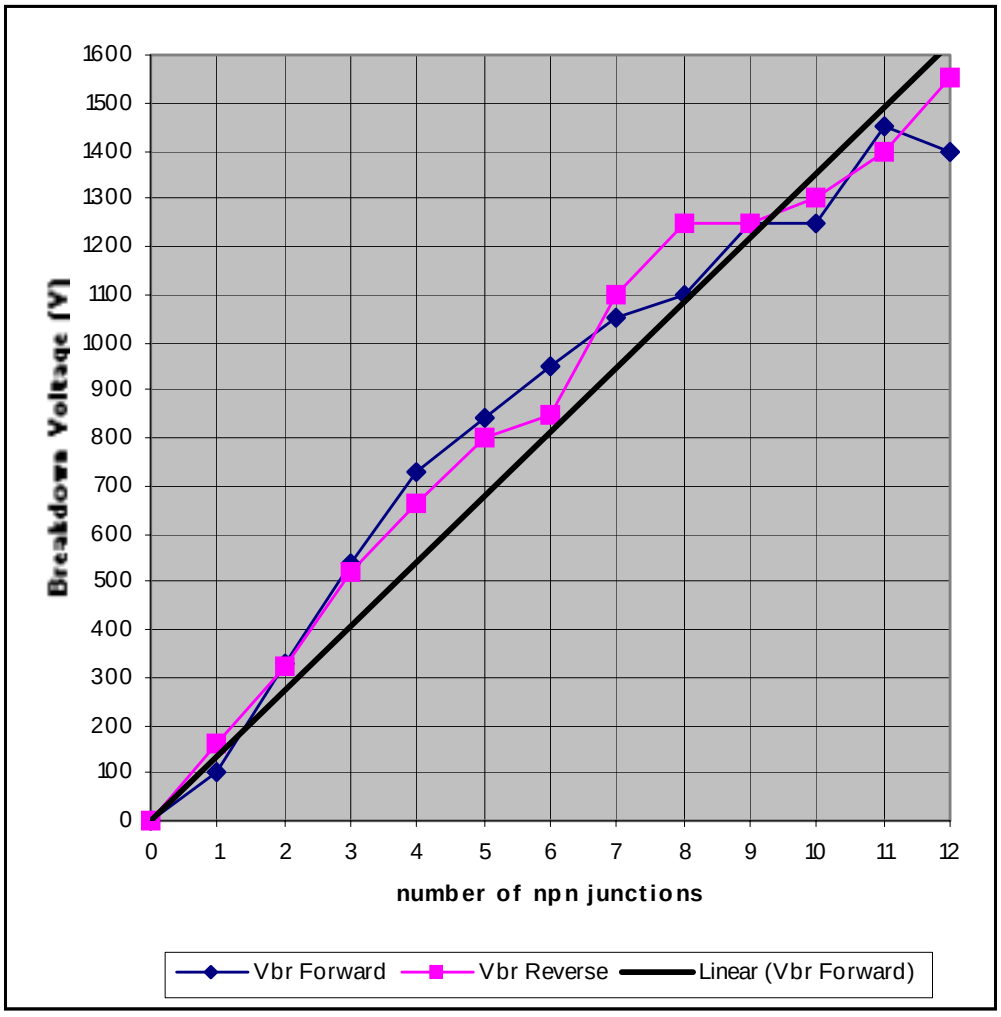

Figure 15 - Plot of the overall blocking voltage versus the number of npn junctions. The fit is linear with each junction contributing an average of 138V/jn to the overall breakdown voltage.

A linear fit of the plot reveals:

$$V_{block} = \left(138 \frac{V}{junction}\right)\left(number\_of\_junctions\right)$$

$$(R^2 = 0.9638)$$

Since this study was performed, the blocking voltages have steadily increased as a result of gradual optimization of the thermomigration process, e.g. complete removal of excess aluminum and heat damaged silicon and thermomigrated junctions that are more vertical. Now, blocking voltages greater than 180V per junction are routinely fabricated, which approaches the theoretical limit of 184V. I-V curves for 3 different devices are shown in figure 16. These blocking voltages are for 2 npn junctions in series. A table of blocking voltages is shown in Table 4.

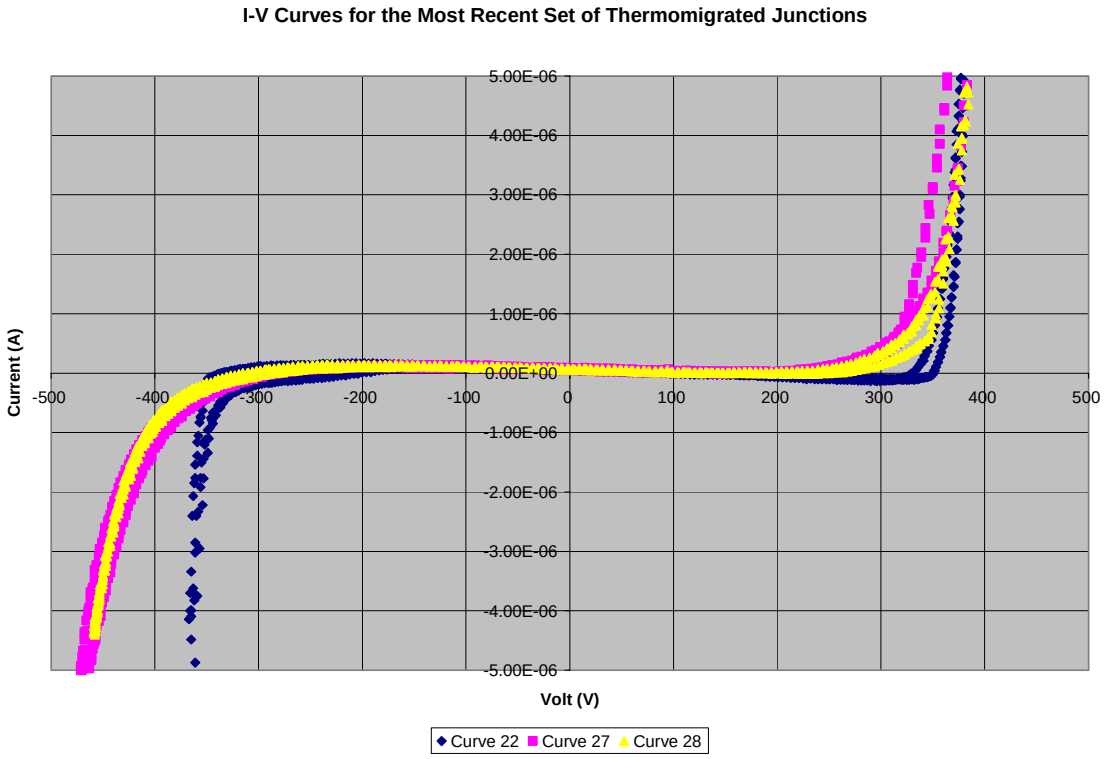

Figure 16 - I-V curve for the latest thermomigrated junctions. This is for 2 junctions in series. The overall blocking voltage averages 378V.

Table 4 - Blocking voltages and leakage currents for the latest thermomigrated junctions.

	Vbr(-) (V)	Vbr(+) V	Ileak(-) (uA)	Ileak(+) (uA)
Gyro1	360	365	0.07	0.07
Gyro2	420	355	0.08	0.06
Gyro3	430	340	0.06	0.07
	Vbr Ave	378.33	**Ileak Ave**	0.0683
	Vbr stdev	37.24	**Ileak stdev**	0.0075

The average breakdown voltage is 378V with a standard deviation of 37.24V. Per junction, the average blocking voltage is 189V. This exceeds the theoretical maximum of 184V, but remains within one standard deviation. The average leakage current is 0.0683μA with a standard deviation of 0.0075. The average "equivalent resistance" is 2.76GΩ. The average power dissipated just below breakdown is 25.83μW.

The leakage currents are on the order of $6x10^{-8}$A, which is about 10 times larger than the theoretical calculation (discussed in chapter 3) for the current, i.e. on the order of $5x10^{-9}$A. It should be noted that these curves were not obtained in darkness, and therefore the number of optically generated carriers may be significant. For the purposes of this thesis, the leakage current is sufficiently low to operate micro-electro-mechanical devices, and attention was turned to other isolation technology issues. However, the effects are noted, and for future research, should be investigated.

Compatibility with other micromachining technologies

The fabrication of MEMS devices cannot be done with thermomigration alone. It must be used in conjunction with a number of other MEMS technologies. The thermomigrated junction isolation scheme is, in many ways, a technological response to

deep reactive ion etching. If thermomigration is incompatible with this technology, many of the motivations for developing thermomigrated junctions are lost.

The same could also be said about the two other large categories of microsystems fabrication: surface micromachining and CMOS microelectronics. The compatibility of thermomigrated junctions with these two technologies, would allow TGZM electrically isolated devices to leverage the capabilities of these two well-developed and powerful technologies. Although thermomigrated junction isolation's compatibility with these two technologies is not as critical, the ability to fabricate MEMS devices with all four technologies, thermomigration, DRIE, surface micromachining, and CMOS, is compelling.

TGZM with DRIE – The Demonstration Actuator

The application of thermomigration to MEMS devices complements the high aspect ratio, deep reactive ion etching technologies by enabling electro-mechanical function. To demonstrate the compatibility of these two fabrication technologies, a simple electro-mechanical device, an electrostatic actuator, is fabricated and operated.

The fabrication of the demonstration actuator is shown in figure 17. First the aluminum to be thermomigrated is deposited and patterned. It is then thermomigrated, and finally, the bulk silicon is deep reactive ion etched.

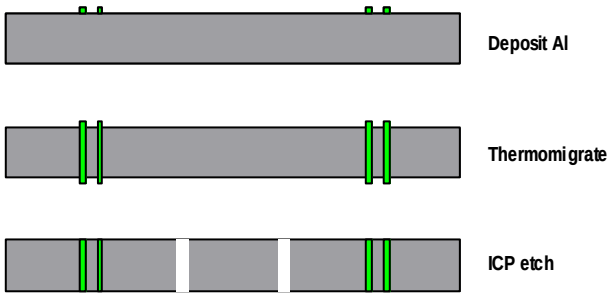

Figure 17 - Fabrication flow for the blocking voltage/leakage current sample and the demonstration actuator.

Etching thermomigrated silicon is possible, however, the etch rate is slower. Figure 18 shows masked and unmasked thermomigrated regions of silicon. The unmasked thermomigrated silicon is etched (the top surface is out of focus), but not completely gone. The thermomigrated silicon is highly doped with aluminum forms aluminum fluoride in the fluorine plasma which has a low vapor pressure. Fortunately, the ratio of silicon to aluminum is approximately 10^4:1, which allows the fluorine plasma to etch the silicon around the aluminum.

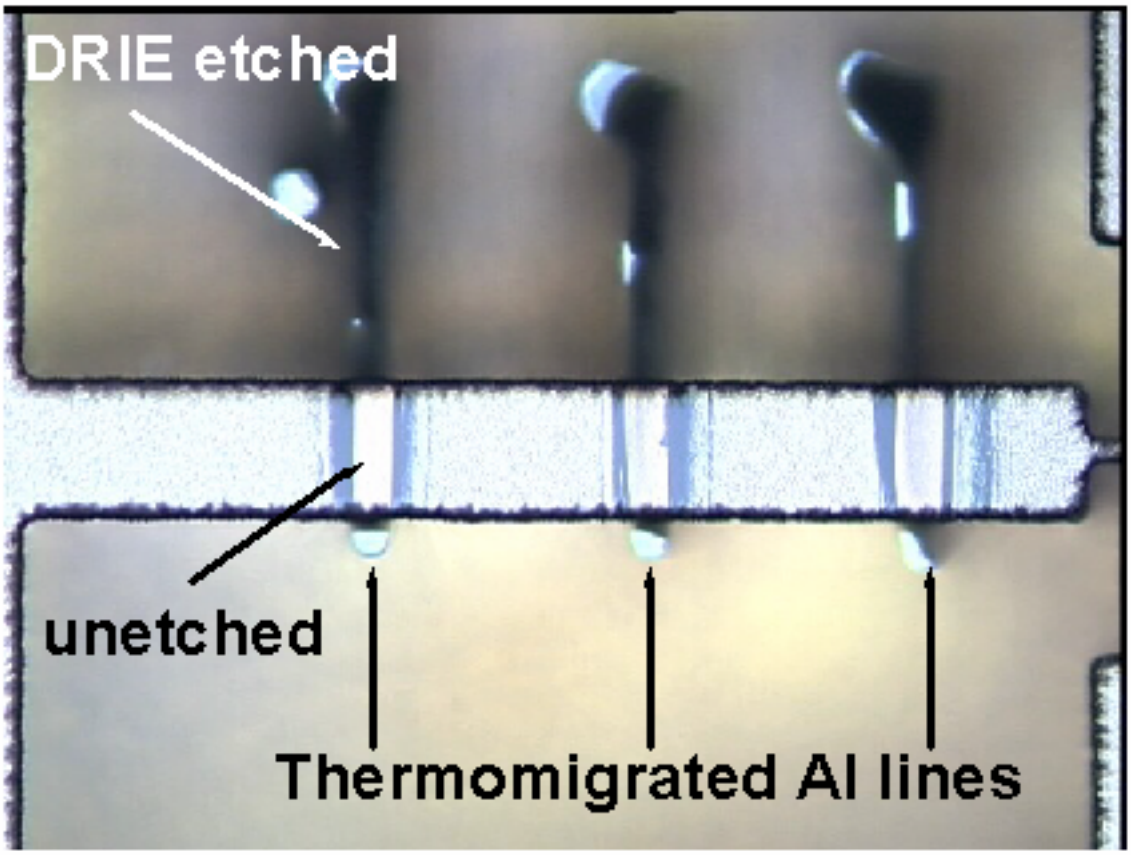

Figure 18 - Photomicrograph of a deep reactive ion etched and thermomigrated silicon. The thermomigrated silicon etches slower than the undoped silicon at approximately half the rate. The silicon surrounding the thermomigrated region is completely etched away, while the thermomigrated silicon is partially etched.

Figure 19 shows the front and back of the completed demonstration actuator. The thermomigrated aluminum junction can be seen to penetrate through the wafer, illustrating that the aluminum doped silicon extends through the wafer (since on these wafers the lapping step after the thermomigration was omitted).

In the fabrication of the actuator, the final ICP etch was used to form the spring and comb drive electrodes of a simple electrostatic actuator. The width of the aluminum-doped silicon region is 100μm. The length of the device is 2 mm overall and the fingers of the comb drive are 40 μm in width.

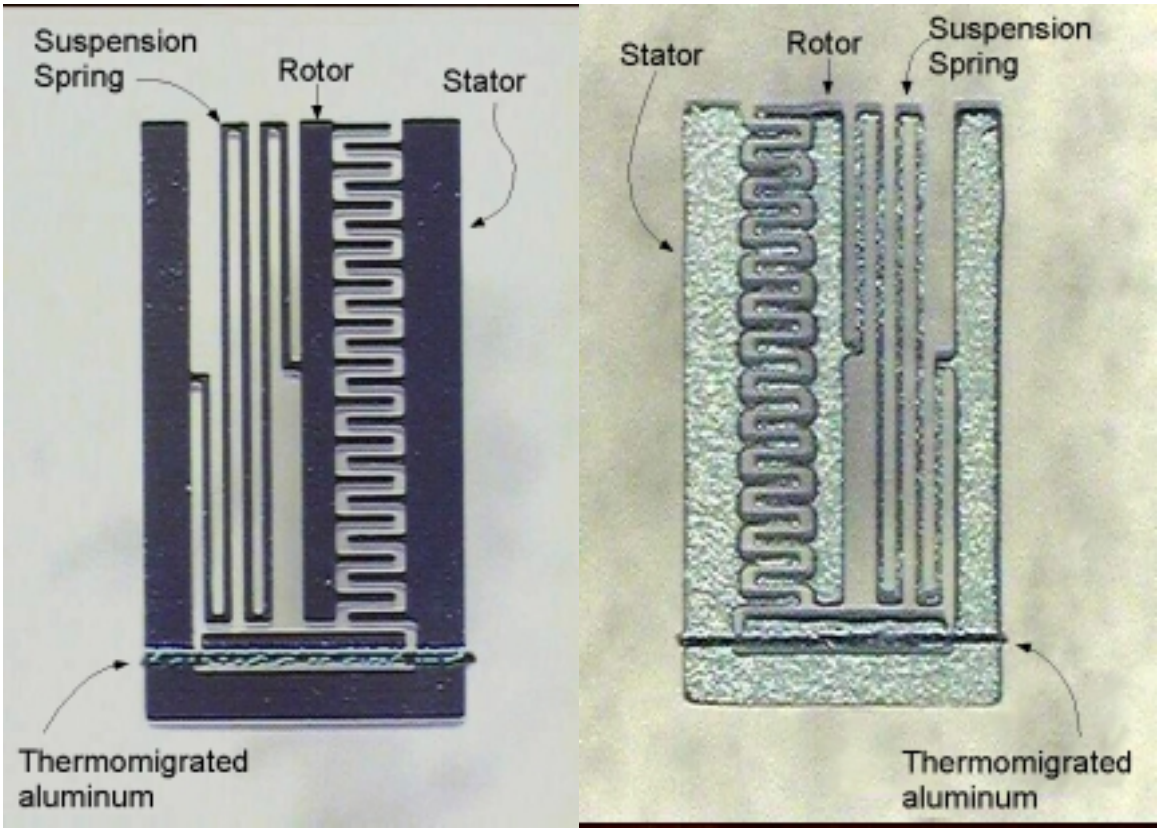

Figure 19 - The front and back of the demonstration actuator. The width of the device is 1mm. The demonstration actuator consists of a comb drive and a support spring. The thermomigrated line can be seen on both sides, indicating through-wafer penetration.

The demonstration actuator was placed on a probe station, with a tungsten probe contacting the stator and another probe contacting the rotor. The probes were driven by a Trek 50/750 high voltage amplifier at 300:1 voltage amplification. The amplifier, in turn, was driven by an HP 33120A function generator with a sinusoidal signal output. A Tektronix 2221 oscilloscope was connected in parallel to the probes to monitor the voltage across the demonstration device. The actuator was driven with an AC signal just under breakdown at 162 Vpp and 60 Hz with an 84 V DC offset. At this voltage, the actuator displaced by approximately 10 microns.

A close up of one of the fingers of the interdigitated electrostatic actuator is shown in figure 20. In figure 20, the finger is shown with no voltage applied. In figure 21, the finger is shown moving at 60Hz (note that the stator remains focused, while the finger of the rotor is blurry), demonstrating electrical isolation, electro-mechanical function, and compatibility of the TGZM and DRIE technologies towards the fabrication of MEMS devices.

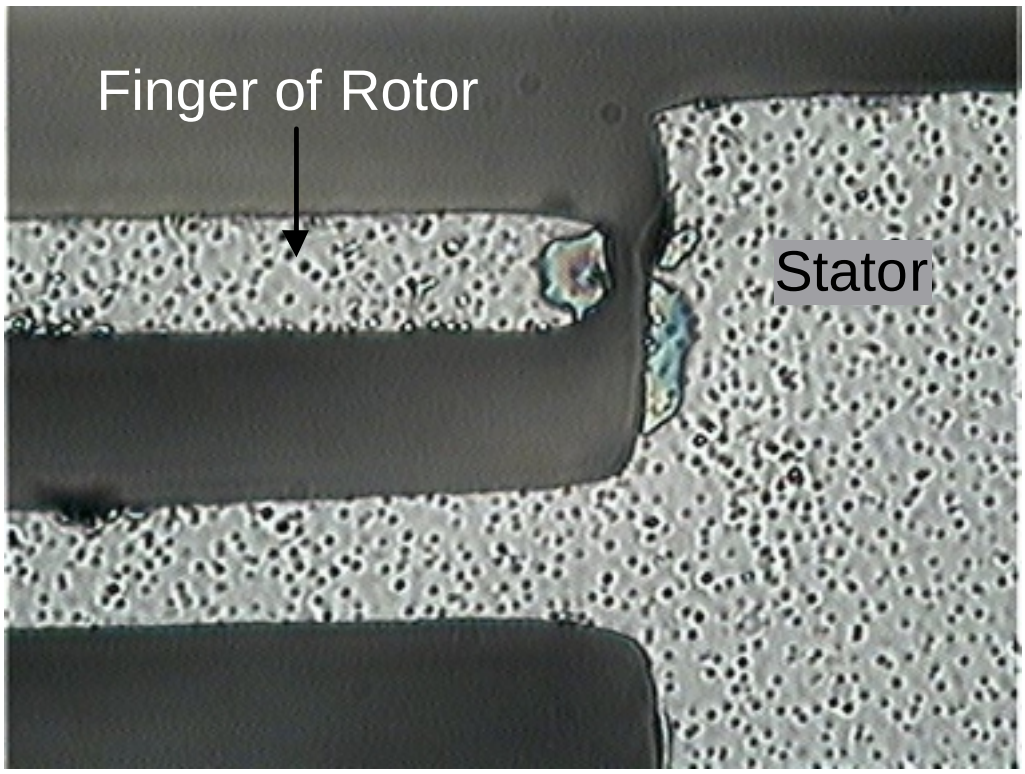

Figure 20 - Photomicrograph of one finger of the demonstration actuator. Zero voltage is applied.

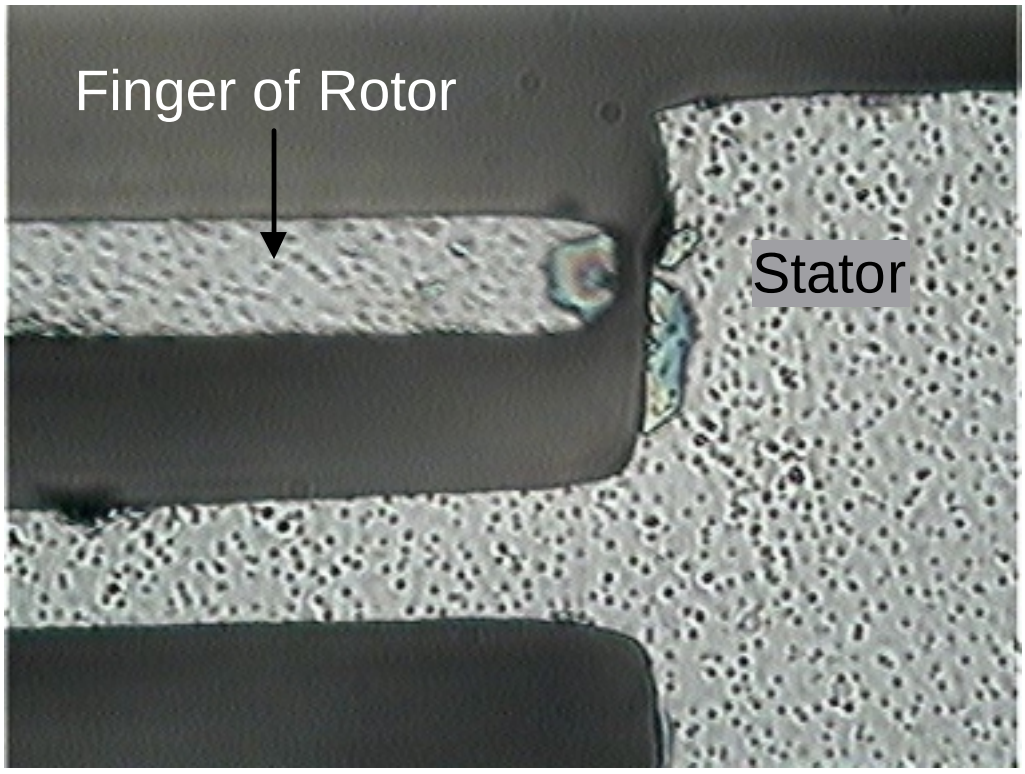

Figure 21 - Photomicrograph of one finger of the demonstration actuator with 162Vpp drive voltage with a DC offset of 81V at 60Hz. Note that the stator remains in focus, while the finger is blurry.

Other micromachining technologies

The TGZM and DRIE combination can fabricate thick, high-aspect ratio, single crystal silicon electro-mechanical devices. However, other microfabrication technologies such surface micromachining and microelectronics integration would complement the TGZM + DRIE combination. The main difficulty is the high processing temperatures of the thermomigration, which may alter or destroy other features on the wafer. In addition, after the thermomigration process, the excess aluminum and heat damaged silicon are removed either by lapping or by an etch, which can also damage any previously fabricated structures.

Given the high temperatures of the thermomigration and the destructive post-processing, the thermomigration is usually done first, and all other processes done afterward. For most aspects of microfabrication, a thermomigrated wafer acts simply as a n-type silicon wafer with a few regions of p-doped silicon. As a result, after the thermomigration post processing, most microfabrication may proceed normally. It should be noted that if the thermomigration was performed poorly, in such a way as to induce non-uniform heat induced stress effects, the wafer can become highly strained, resulting in a fragile wafer.

Surface Micromachining

Surface micromachining after the thermomigration is a straightforward process since the thermomigrated wafer acts mechanically as an unprocessed wafer. Surface micromachined structures made of polymers, metals, sacrificial layers have been demonstrated with this technique. A general process flow for integrating surface micromachined structures into a thermomigrated and deep reactive ion etched wafer is shown in figure 22.

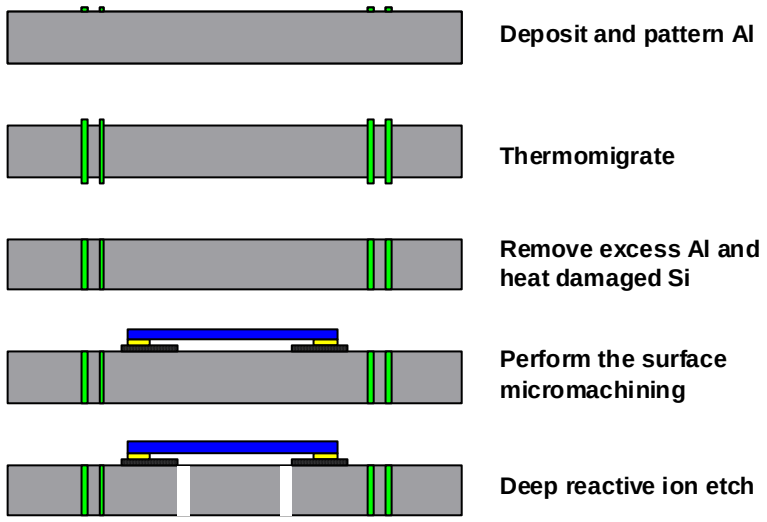

Figure 22 - Fabrication flow for integrating surface micromachined features onto a thermomigrated/DRIE wafer.

Capacitive electrodes have been integrated onto a wafer with thermomigrated junction isolation and with deep reactive ion etched features. A photomicrograph of a device is shown in figure 23.

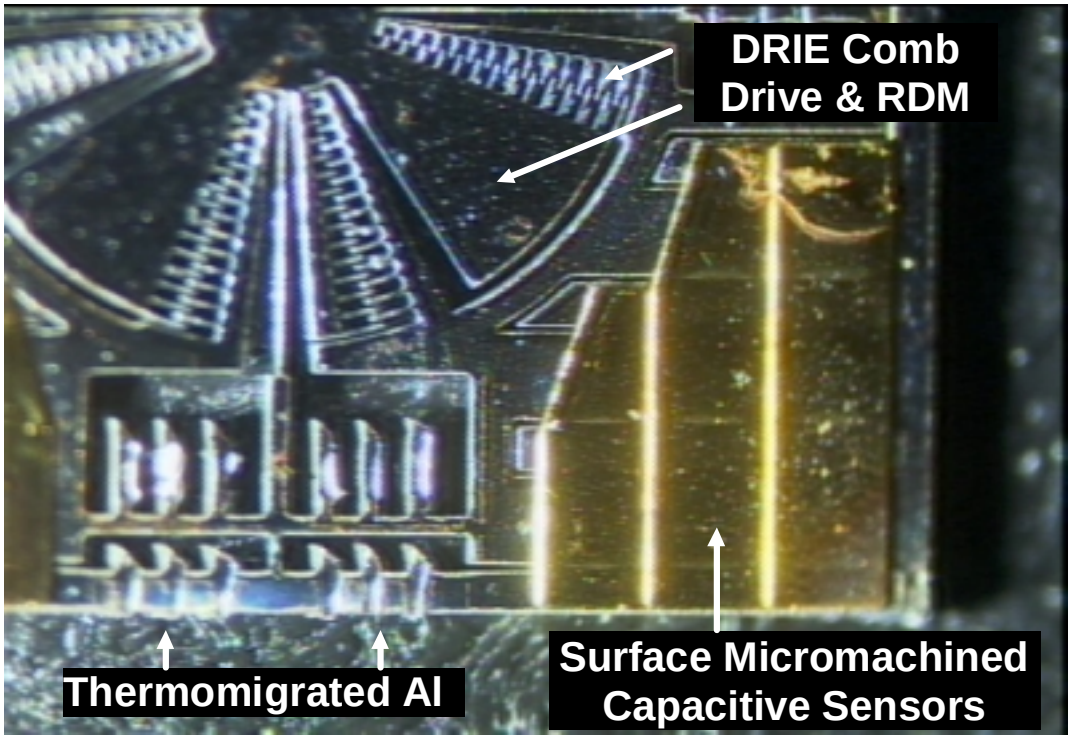

Figure 23 - Photomicrograph of a device showing thermomigrated, DRIE, and surface micromachined structures.

CMOS

To integrate CMOS devices, there are two possible methods: thermomigrate before CMOS fabrication or thermomigrate afterwards. Technologically, the most straightforward method is to thermomigrate first. After thermomigration, as in the case of surface micromachining, the wafer acts as a n-type wafer with some p-type regions. Typical CMOS fabrication after this step may proceed without alteration.

However, while it is technologically straightforward to integrate circuitry after the thermomigration process, it may not be economically feasible. Very few accessible microelectronics fabrication lines allow specially treated silicon wafers containing

foreign materials to enter the line. Integrating microelectronic circuitry after the thermomigration step would therefore require a specialized fabrication facility for post-Al thermomigrated wafers. Such a facility can cost hundreds of millions of dollars. A more economically attractive approach is to leverage existing microelectronic fabrication lines and perform the thermomigration process with wafers that have the integrated circuitry already fabricated.

The biggest concern with this approach is that the high processing temperatures of the thermomigration will cause dopants to diffuse; however, given the very short thermomigration processing time, this problem may be avoidable by selecting dopants with low diffusivities. More problematic is that after the thermomigration, the heat-damaged Si and the excess Al must be removed to prevent a short across the npn junction. These layers are usually removed by lapping the top 50μm of silicon or so from both sides of the wafer, which precludes microelectronics since most microelectronic devices reside in the top few micrometers of silicon.

To make the post-thermomigration treatment compatible with microelectronic circuitry, in lieu of lapping, a chemical etch approach is developed. Chromium is used to mask the wafer, with windows that expose only the areas around the npn junctions to a diluted HNO_3:HF:H_20 etch for 3 minutes. This etch removes both silicon and aluminum, albeit it preferentially etches the Al, then n- or p-type silicon doped in excess of $10^{19}cm^{-3}$, and finally the more lightly doped silicon.

To demonstrate the compatibility of thermomigration with pre-existing microelectronic devices, thermomigration was performed on a wafer with PMOS devices from the microelectronics teaching lab at the Georgia Institute of Technology. A diagram

of the fabrication flow is shown in figure 24 and the processing specifics of the PMOS devices are detailed in appendix A. The minimum gate length of the smallest operating transistor was 40μm.

First, 5μm of aluminum was deposited and patterned for the thermomigrated aluminum. This process also removed the Al interconnects between transistors, since they would also thermomigrate. The TGZM process was then performed until the aluminum thermomigrated to the opposite face of the wafer. Then Cr was deposited and patterned to serve as a mask for the thermomigrated areas. The excess Al and heat-damaged Si were removed in the dilute HNO_3:HF etch while the Cr protected the rest of the wafer. Afterwards, Al was redeposited and repatterned for the interconnects.

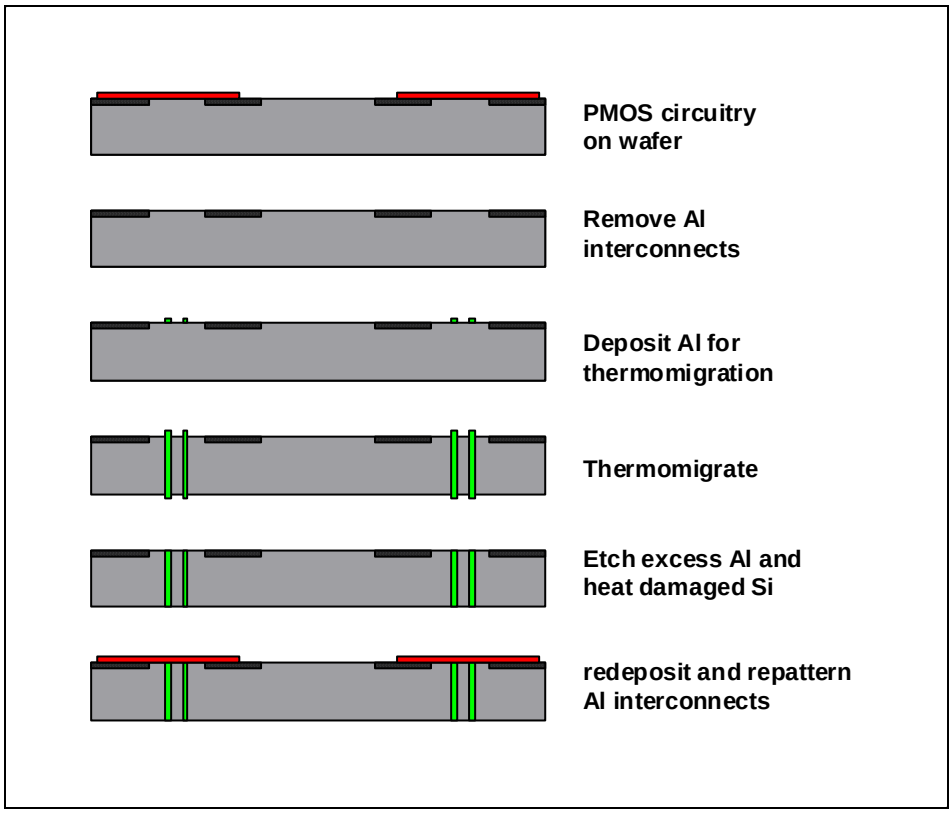

Figure 24 - Fabrication flow for thermomigration of a wafer with PMOS devices.

I-V curves of the transistors taken before and after the thermomigration are shown in figure 25 and figure 26. It is found that the 40μm PMOS transistors function nearly identically after the thermomigration is performed. The only observed change is that the breakdown voltage of the transistor increased from about 50 to 60V.

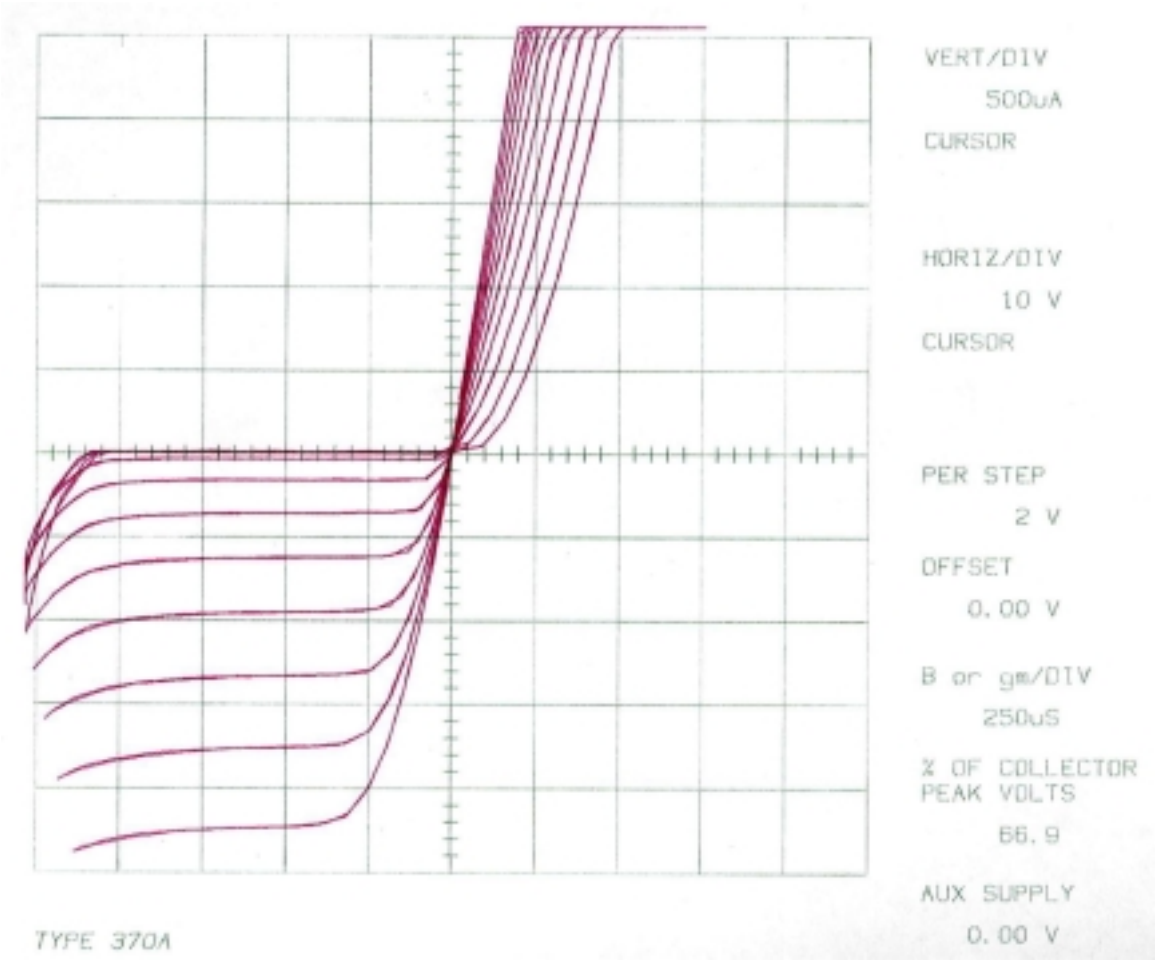

Figure 25 - I-V curves of a 40μm transistor before thermomigration.

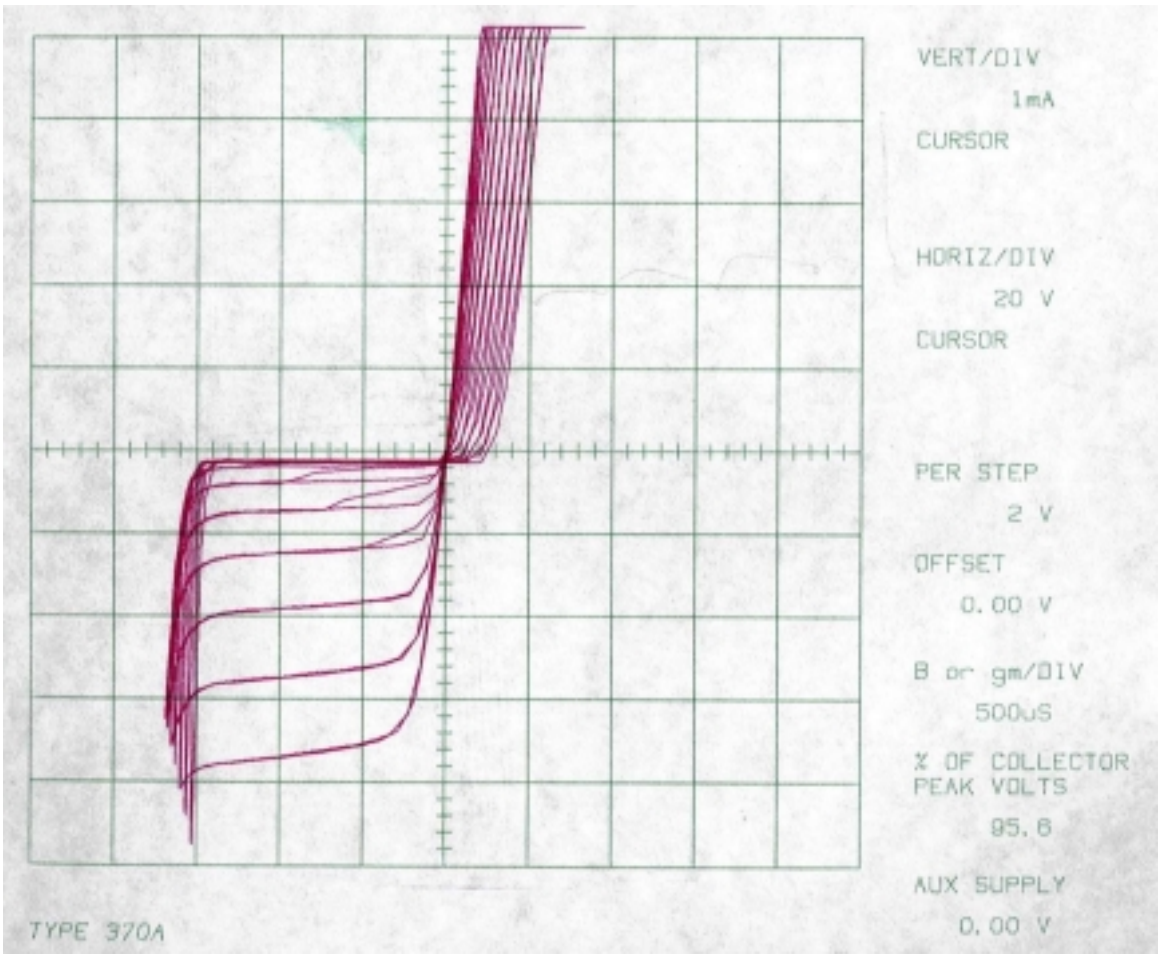

Figure 26 - I-V curves of a 40µm transistors after thermomigration. Note that the scales of the two graphs are different. The first I-V curve has a vertical scale of 500µA and a horizontal scale of 10V. The second I-V curve has a vertical scale of 1mA and a horizontal scale of 20V.

The demonstration of the compatibility of 40µm transistors with the thermomigration process ensures that simpler circuits, such as amplifiers, oscillators, and sense electronics, may be integrated with MEMS devices using the thermomigration/DRIE technique. This guarantees that at least some of the benefits of microelectronic integration may be gained with the TGZM/DRIE technique without incurring the costs of a specialized microelectronic fabrication facility.

Conclusion

The compatibility of thermomigrated pn junctions with the deep reactive ion etching has been established. This compatibility insures that thermomigrated junctions may enable electro-mechanical function in thick, high-aspect ratio, deep reactive ion etched single crystal silicon structures. The blocking voltages are adequately high, and the leakage currents are sufficiently low. Moreover, higher blocking voltages may be enabled by using higher resistivity n-type wafers and/or by arranging multiple npn junctions in series.

In addition to compatibility with DRIE, the thermomigration technique can also be integrated with surface micromachined and CMOS devices. This insures that the TGZM/DRIE devices are not restricted to being fabricated by solely these two technologies, but may also access the full fabrication envelope enabled by surface micromachining and microelectronic fabrication technologies.

Thermomigrated junction isolation shows a great deal of promise. Its compatibility with such a wide range of fabrication technologies indicates that many of the high-performance, complex micro-systems already developed by other fabrication technologies may be leveraged and enhanced by the addition of junction isolated, deep reactive ion etched, single crystal silicon structures.

Chapter 4

Design of an Angular Rate Sensor with Thermomigrated Junction Isolation and Deep Reactive Ion Etching

Design is strongly directed by the possibilities of fabrication technology. Given how strongly design and fabrication are coupled, to some degree it is disingenuous to discuss them separately. Moreover, design/fabrication tends to be an iterative process, with each new design being influenced by each previous fabrication attempt, and vice-versa.

With microfabricated devices, the design-fabrication relationship is even more tightly coupled. Compared with conventional machining technologies, micromachining entails a number of additional difficulties, which poses tighter constraints on the possible design space. One of the most defining constraints is the fact that assembly is virtually impossible with microscopic parts. As a result, the great challenge for microfabricated designs is not only to form very small features, but to also simultaneously form them in their final place.

Despite the entwined nature of the fabrication-design process, for this thesis, it is possible to discuss the design to first order detail with a rough concept of the fabrication path. Once the design is described, the fabrication is discussed in more detail in the next chapter.

This chapter first discusses the primary application for gyroscopes, i.e. navigation. Then, the basic operating principle of gyroscopes is discussed. After that, the design

arguments for each component of the gyroscope are detailed. Finally, simulations are presented to verify and optimize the design.

Inertial Navigation

Every rigid body has 6 spatial degrees of freedom, 3 for position, and 3 for orientation. For general navigational applications, it is necessary to know all 6 degrees of freedom. Inertial navigation systems often employ 6 sensors, 3 that measure translational changes (accelerometers) in each direction, and 3 that measure rotational changes (angular rate sensors) in each direction.

Since these sensors measure changes, time integration of the kinematic equations allows one to calculate the position or heading relative to an initial point. For changes in linear momenta, the acceleration may be locally measured, and integrated over time to calculate position and velocity:

$$\vec{v}(t) = \int \vec{a}(t)dt + \vec{v}_o$$

$$\vec{x}(t) = \iint \vec{a}(t)dt^2 + \int \vec{v}_o\, dt + \vec{x}_o$$

Rotation has a similar set of relations; however, the first derivative of angular position is a directly and locally measurable quantity. If one is in a rotating system, coriolis and/or centripetal forces may be measured to find the rotation rate. Once the rate has been determined it may be time integrated once to find angular position. The relation is:

$$\theta(t) = \int \dot{\theta}(t) dt + \theta_o$$

The fact that only a single time integration is needed, has implications for the error behavior of these systems. Because all of these relations are accumulative, i.e. quantities are integrated, the error also accumulates. If the error is assumed to be uncorrelated for each measurement, then successive additions of the error results in a random walk of the measured value about the true value.

If the error is integrated yet one more time, as is the case for calculating position from acceleration, the effect of error is amplified. Because angular rate measurements may avoid this second integration the translational and rotational components of inertial navigation are often separated.

It is possible to use accelerometers instead of angular rate sensors to measure angular rate. This approach has a number of attractive features, namely that already existing high performance accelerometers may be used in lieu of developing angular rate sensors. If the accelerometers are placed a known distance apart, then:

$$a_1 = m\omega^2 r_1$$
$$a_2 = m\omega^2 r_2$$

$$\frac{1}{m}\frac{(a_2 - a_1)}{(r_2 - r_1)} = \frac{1}{m}\frac{\Delta a}{\Delta r} = \omega$$

By measuring the difference in accelerations and dividing by the known separation distance between the two accelerometers, one may obtain ω, the rotation rate.

The difficulty with this approach is that the relative error in the measurement becomes a function of the radius of the turn. For example, if the two accelerometers happen to be close to the origin of the turn, then for a given rotation rate, there should be a large signal in the acceleration. However, if the two accelerometers happen to be far away from the origin of the turn, then the output signal of the two accelerometers is small, and therefore the relative error is larger. As a result, the overall error in the navigation becomes path dependent. This could be compensated for if there was a way to measure the radius of the turn. However by the edicts of relativity, this is physically impossible without some sort of external reference

Gyroscopic Angular Rate Sensors

There are a number of operating principles around which to design angular rate sensors. However, gyroscopic sensors have a number of attractive features. Gyroscopes are distinguished from other angular rate sensors by the fact that gyroscopes employ gyroscopic torque to measure angular rate. This means that the sensor uses the moment-of-inertia of the proof body, as opposed to a proof mass, that is used in many other sensor designs. In both proof mass and proof moment-of-inertia designs, the sensitivity depends on the ratio of inertias along the sense and drive axes. For linearly vibrating sensors, the mass in both directions is the same or almost the same, and the ratio is nearly unity. However, gyroscopes operate on the moment of inertia, which unlike mass, is highly anisotropic, i.e. a strong dependence on the radial dimension. This asymmetry allows a

large moment of inertia along the drive axis, while simultaneously allowing a small moment of inertia along the sense axis. As a result, the ratio may be much larger than unity.

Despite this inherent advantage, gyroscopes remain relatively rare among micromachined designs. The primary difficulty is that gyroscopes entail more fabrication complexity, mostly due to the fact that many of the components of a gyroscope must be gimbaled, i.e. allowed to rotate. In addition to the rotating proof body, it is necessary to have a second electro-mechanical system that allows the rotating body to turn about a sense axis, so that the device is allowed to respond to the generated gyroscopic torque. Supports that allow rotation are termed gimbals.

The need for a gimbaled proof body complicates the fabrication of a MEMS-based gyroscope because the entire electro-mechanical subsystem, including the moving mass, the electrostatic actuators, and the electrical connections, must be rotationally free. This means that at least two voltage distinct regions must defined on the gimbal to electro-mechanically drive the proof body. This also means that the electrical signals to and from the proof body must route through the gimbal itself, while imposing a minimum of torque on the gimbal. These problems are rather straightforwardly solved with a macroscopic device given the relative dimensions and masses of the mechanical and electrical subsystems, however, on a microscopic device, the electrical and mechanical system may be of comparable dimension and mass, and therefore the mechanical design of the electrical system may not be decoupled from the mechanical portion of the device.

Some designs have attempted to ease the requirements of incorporating an electromechanically functional subsystem on a rotating platform by placing the stator for

the proof body off the gimbal, thus avoiding many of the on-gimbal electrical isolation and connection necessities. This, however, compromises the performance of the gyroscope. As the gyroscope responds by rotating along its sense axis, the off-gimbal drive stator and the on-gimbal rotor move out of alignment with respect to one another. The electrostatic forces between the stator and rotor will exert a restoring torque along the sense axis to re-align the stator and rotor that is many times larger than the signal itself. Given the magnitude of torque necessary to appreciably drive the proof body, such a gyroscope will be unable to meet tactical grade navigation specifications. This problem is elegantly sidestepped by placing both the stator and rotor on the gimbal, thus insuring alignment of the RDM stator and rotor at all times.

For this thesis, an angular rate sensor based on a gyroscopic operating principle is chosen to illustrate the utility of thermomigrated junction isolation. The thermomigrated junction electrical isolation can straightforwardly enable electro-mechanical function on a rotating platform without the need for performance compromising substrate wafers, as with the bond/etch electrical isolation approach, and without the need for reliability compromising backfill materials, as with the etch/backfill approach.

Moreover, this electro-mechanical functionality may be achieved while preserving the benefits from deep reactive ion etching of single crystal silicon, i.e. the increased mass of the proof body, and the increased torque from thick, high-aspect ratio electrostatic actuators.

Principle of Operation

The easiest way to conceptualize the operating principle of gyroscopic sensors is to first imagine a spinning mass called the "proof body." Because of conservation of angular momentum, the spin axis of that mass points along a consistent direction. The spin axis of the mass is termed the "drive axis." If the spinning mass is free to rotate about all axes, then as the observer turns, in the observer's frame, the proof body continues to point along one direction and may thus act as a directional reference.

If the spinning mass is instead allowed to only rotate along certain axes, then the spinning mass cannot, in general, continue to point in one direction. As it turns, a gyroscopic torque is exerted on the mass. Gyroscopic torque is the cross product of the spinning mass's angular momentum and the rotation rate of the constraining axis. The axis along which the gyroscopic torque exerts is called the "sense axis." In the observer's local frame, it appears that the spin axis is rotating about the sense axis. The motion along the sense axis is proportional to the input rotation rate, and therefore one's rotation rate may be calculated from the gyroscopic torque and the angular momentum of the proof body.

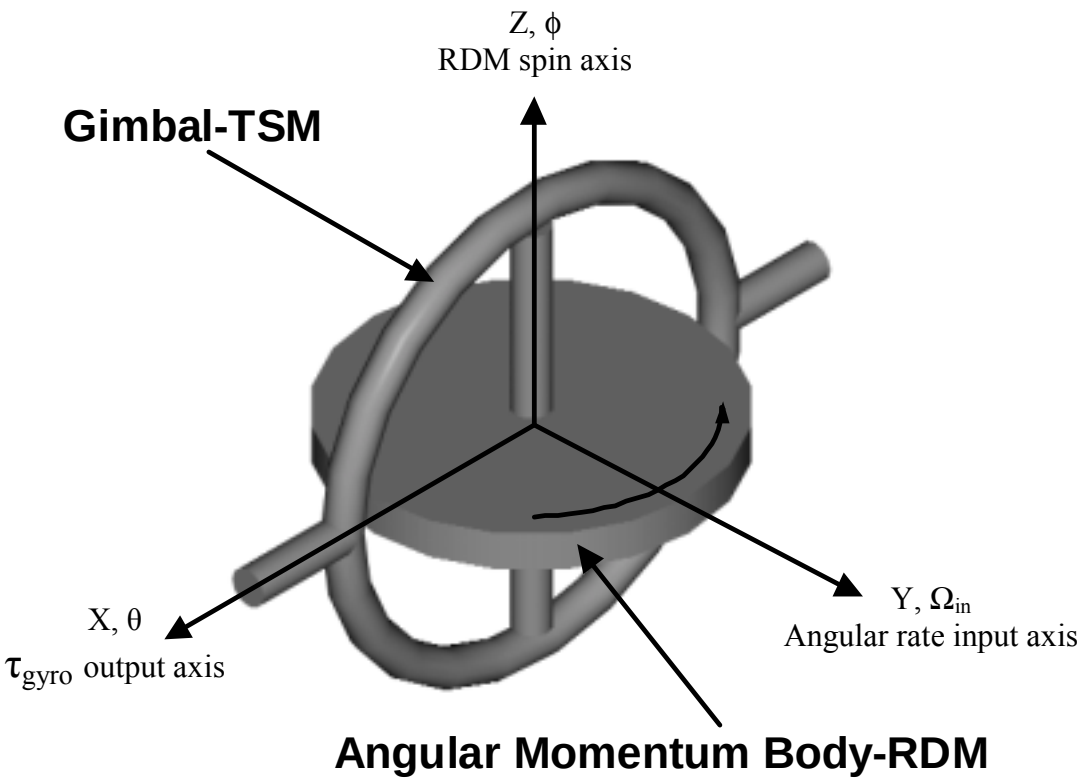

Figure 27 - Schematic of the operating principle of a gyroscope. The direction and axes conventions are shown.

The basic equation of motion for a gyroscope is the rotational analog of Newton's 3rd law, i.e., the time change of angular momentum is equal to the input torque. The input torque is the gyroscopic torque, i.e., the input angular rate, Ω_{in}, crossed with the angular momentum of the spinning mass, L_ϕ. The conventions and directions of each variable are illustrated in figure 27.

$$\vec{\tau}_{gyro} = \dot{\vec{L}}_\theta = I_\theta \ddot{\vec{\theta}}$$

$$\vec{\tau}_{gyro} = \vec{\Omega}_{in} \times \vec{L}_\phi$$

Assuming that $\vec{L}_\theta$, $\vec{L}_\phi$, and $\vec{\Omega}_{in}$ are all perpendicular to each other, the above relations may be equated and rearranged to calculate the input angular rate

$$\frac{d}{dt}\left(\dot{\vec{\theta}}\right) = \Omega_{in}\frac{\vec{L}_\phi}{I_\theta} = \Omega_{in}\frac{I_\phi\dot{\phi}}{I_\theta}$$

This relation indicates for a given input angular rate, Ω_{in}, the output, i.e. the change in the direction of the spinning mass ($\dot{\vec{\theta}}$), may be amplified by increasing the rotational momentum in the ϕ-direction($I_\phi\dot{\phi}$) and minimizing the moment-of-inertia about the θ-axis (I_θ).

From this relation, the advantage of thick gyroscopes starts to become clear. The output response of the gyroscope is directly proportional to the angular momentum, which in turn, is linear with moment-of-inertia. For a disc, the moment-of-inertia, I, is:

$$I = \frac{\rho\pi r^4 z}{2}$$

where ρ is the mass density of the disc, r is the radius and z is the thickness. Since moment-of-inertia is such a strong function of radius, it is assumed that for both bulk and surface micromachined structures, the radial dimension lies in the plane of the surface of the wafer so that its extent may be maximized as large as the die allows (on the order of millimeters). However, surface micromachined structures are typically on the order of

tens of micrometers, whereas bulk-micromachined structures may be hundreds of micrometers thick. As a result, for a given area, moment of inertia of a bulk-micromachined proof body may be increased by orders of magnitude for a given area compared to its surface micromachined counterparts.

The above relationship also points out that the output response is proportional to a ratio of the moment of inertia along the drive and sense axes. As discussed before, in linear, vibratory angular rate sensors, the relationships are largely the same, except that translational quantities are used. For linear vibratory sensors, the input rate is amplified by the ratio of the masses, instead of moments-of-inertia, along the sense and drive directions. Because mass is an isotropic quantity, this ratio is usually close to unity. But, moment of inertia is strongly anisotropic, and this ratio may be made to be hundreds of times larger in a gyroscopic sensor.

Oscillatory Version

With microscopic devices, freely rotating parts suffer from a number of disadvantages. Rotating parts suffer from the fabrication and control complexity of a rotationally free mechanical support, such as a bearing (mechanical, air, or magnetic). Moreover, rotating parts experience wear, which for micrometer scale parts, erosion of a few micrometers can quickly change the behavior of the device.

Given these difficulties, the micromachined version of this device is an oscillatory analog, i.e., instead of rotating continually, all parts oscillate, rotating a few degrees in one direction and back again. Through the few degrees the proof mass is actually rotating, it has an angular momentum whose conservation ensures the spin axis points in

a constant direction. It is rather straightforward to design an oscillating part that rotates for a few degrees and then reverses direction. Many micromechanical devices do this by suspending the oscillating mass with beams. The beams lift the mass to allow it to freely oscillate, and also provide the restoring force for a simple harmonic oscillator. For a gyroscope, the beams serve the additional function of the springs that transfer the gyroscopic torque from the proof body to the support gimbal.

However, the oscillatory version of this design seems somewhat problematic in that at some point during the oscillation, the angular momentum becomes small, allowing the spin axis to easily change direction. However, if the time scale for the change of the angular rate is large compared with the oscillation period of the sensor, then the measurement of angular rate is sampled frequently enough to minimize the error introduced when the mass is not rotating. For inertial navigation purposes, this approximation is usually valid, since changes in direction may occur on time scales of seconds, while the proof body oscillates on a time scale of milliseconds.

Like the rotational device described above, the oscillatory gyroscopic device has two main mechanical components. The first is the proof body that generates the angular momentum of the device. This component is historically labeled the "Rotor Driven Member" or "RDM" because it is driven to induce the rotation about the drive axis. The second mechanical component is the gimbal that allows the proof mass to rotate about the sense axis when gyroscopic torque is induced. This component is historically termed the "TSM" or "Torque Summing Member" referring to the fact that the TSM's rotation results from the gradual accumulation of torques.

For both the RDM and the TSM, the fundamental equation of motion is the well known forced, damped, simple harmonic oscillator. In the case of the RDM, the driving term is from an electromechanical actuator. Assuming the RDM rotates about the ϕ-direction, the equation of motion is:

$$I_\phi \ddot{\vec{\phi}} + b_\phi \dot{\vec{\phi}} + k_\phi \vec{\phi} = \vec{\tau}_{actuator}$$

where I_ϕ is the moment of inertia of the RDM about the ϕ-axis, ϕ is the angular position of the mass, b_ϕ is the damping constant, k_ϕ is the spring constant, and $\tau_{actuator}$ is the torque supplied by the actuator.

The TSM is modeled as another damped, forced, simple harmonic oscillator, however, for this body, the driving term is the gyroscopic torque resulting from the cross-product of the input angular rotation rate and the RDM angular momentum. Because the angular momentum of the RDM is an oscillatory term, and since Ω_{in} changes slowly over one cycle of the RDM, the resultant gyroscopic torque on the TSM is also an oscillatory term. It is assumed that the TSM rotates about the θ-direction, and that θ and ϕ are perpendicular:

$$I_\theta \ddot{\vec{\theta}} + b_\theta \dot{\vec{\theta}} + k_\theta \theta = \Omega_{in} \times \vec{L}_{RDM}$$

I_θ is the moment of inertia of the TSM, θ is the angular position of the mass, b_θ is the damping constant, k_θ is the spring constant, Ω_{in} is the input angular rate of the sensor, and L_{RDM} is the angular momentum of the RDM.

The TSM and RDM are coupled by the beams that suspend the RDM. One end is attached to the RDM and the other is anchored to the TSM. These beams also act as springs, albeit very stiff springs compared to the RDM and TSM springs.

RDM Design

The RDM's main function is to provide the angular momentum that drives the TSM. A larger generated angular momentum results in a higher performance gyro. This is the criterion used to optimize the RDM mechanical, electrical, and electro-mechanical designs.

RDM Mechanical Design-Moment of Inertia

The oscillatory angular momentum for the RDM is defined by

$$L_{RDM} = I_{RDM}\dot{\phi}$$

where L_{RDM} is the angular momentum of the RDM in the ϕ-direction, I_{RDM} is the moment of inertia of the RDM in the ϕ-direction and, $\dot{\phi}$ is the time rate of change of ϕ. If we assume that ϕ is a harmonic quantity, then the time derivative is

$$\dot{\phi} \equiv \frac{d\phi}{dt} = \frac{d}{dt}\left(\phi_o e^{j\omega t}\right) = j\omega\phi_o e^{j\omega t}$$

where ϕ_o is the amplitude of the oscillation in the ϕ-direction and ω is the angular frequency. Naively, $\dot{\phi}$ may be increased by increasing the oscillation frequency and by increasing the amplitude.

To determine the optimal orientation, consider the moment-of-inertia for parallelepiped. Assume a symmetric proof mass and alignment of the mass to the plane of the wafer. To avoid off axis elements in the moment of inertia tensor, only the 3 spin directions aligned with the sides of the parallelepiped are considered:

$$I_x = \frac{1}{12}\rho xyz\left(y^2 + z^2\right)$$

$$I_y = \frac{1}{12}\rho xyz\left(x^2 + z^2\right)$$

$$I_z = \frac{1}{12}\rho xyz\left(x^2 + y^2\right)$$

where ρ is the mass density of the body, *x* and *y* are the in-plane directions of spatial extent for the parallelepiped, and *z* is the out-of-plane extent, i.e. the thickness, of the parallelepiped. Since microfabrication in the early part of the 21st century is largely a planar technology, the *x* & *y* dimensions can be made much larger than the *z* dimension. Assuming *x, y* >> *z*, a parallelepiped rotating about the z-axis has a moment of inertia than can be as much as a factor of 2 greater than rotating in either the x or y directions.

There are several other advantages that argue for the out-of-plane direction. One is that this mode of oscillation has less squeeze film damping, thus resulting in higher amplitudes at resonance for a given input torque. Another is that the electrostatic actuators for this mode are easily made symmetric about the spin axis, resulting in a pure rotation. Rotating bodies about the x or y axes would require actuators above and below the body in order to establish symmetry, which introduces fabrication difficulties in releasing the rotating body. Finally, the actuators are naturally aligned in plane with the proof body, since both are etched out of the same piece of silicon.

For the RDM body, since a body rotating about the z-axis is chosen, a cylindrical proof geometry is chosen. The moment of inertia for this is:

$$I_{cylinder} = \frac{1}{2}\rho r^4 z$$

where ρ is the mass density of the cylinder, r is the radius, and z is its thickness.

RDM Mechanical Design-Rotational Oscillation

As stated before, the equation of motion for the RDM is a driven harmonic oscillator:

$$I_\phi \ddot{\phi} + b_\phi \dot{\phi} + k_\phi \phi = \vec{\tau}_{actuator}$$

The general solution for the amplitude of this equation is:

$$\phi = \frac{\tau_{actuator} / k_{RDM}}{\sqrt{\left(1 - \omega_{act}^2 / \omega_o^2\right)^2 + \left(\frac{\omega_{act} / \omega_o}{Q}\right)^2}}$$

where Q is the Q-factor for the damped harmonic oscillator and is equal to $Q = I\omega_o / b$, ω_{act} is the driving frequency of the actuator, and ω_o is the natural resonant frequency of the spring/moment-of-inertia RDM oscillator. Assuming that the RDM is being driven at resonance in order to benefit from the resonant amplification of the RDM displacement, then $\omega_{act} = \omega_o$, and the maximum displacement to this differential equation is:

$$\phi_{\max} = Q_{RDM} \frac{\tau_{actuator}}{k_{RDM}}$$

where k_{RDM} is the spring constant for the RDM mass. This result intuitively appeals, since the max amplitude is simply the DC displacement of the RDM $\left(\tau / k\right)$ multiplied by the Q-factor.

This result may be used to find the angular momentum of the RDM, which is:

$$L_{RDM} = I_{RDM}\dot{\phi} = I_{RDM}\phi_{\max}\omega_{RDM} = \left[\frac{1}{2}\rho r^4 z\right]\left[Q_{RDM}\frac{\tau_{actuator}}{k_{RDM}}\right]\omega_{RDM}$$

The resonant frequency is chosen to be that which maximizes the angular momentum. The angular momentum of the RDM as a function of resonant frequency is calculated to be:

$$L_{RDM} = I_{RDM}\dot{\phi}_{res} = I_{RDM}\, j\omega_{RDM}\, \frac{\tau_{act}}{k_{RDM}} Q_{RDM} = I_{RDM}\, j\omega_{RDM}\, \frac{\tau_{act}}{I_{RDM}\omega_{RDM}^2} Q_{RDM} = j\frac{\tau_{act}}{\omega_{RDM}} Q_{RDM}$$

This indicates that the lower the resonant frequency, the higher the angular momentum of the RDM. This is counter-intuitive to what one would expect, since a higher oscillation frequency would indicate faster motion of the proof body. However, for constant torque generation, this relation holds. Because the resonance condition links oscillation frequency to moment of inertia and spring constant, a higher oscillation frequency implies a stiffer spring constant, which in turn, means a smaller amplitude of motion.

The minimum resonant frequency is set by beam fabrication realities. A longer, thinner beam is more pliable, but the beams can only be so long and so thin. The thinness is set by the reproducible aspect ratio of the deep reactive ion etch for a 300μm thick silicon wafer. This is about 30:1 given optimal conditions, and for practical conditions with an undedicated and therefore unoptimizable ICP, 20:1 is more realistic. Given these constraints the minimum width is 15μm.

The length can be extremely long, since the beam may be folded an odd number of times within a given area (the odd number condition is necessary so that the beam's two ends connect on opposite sides). For example, the beam may be folded three times

so that its overall length is triple the original length. Given a 15μm wide beam, this requires a 105μm wide space, which is feasible.

Although the length of the beam is not restricted by fabrication concerns, beams of such length and geometry start to introduce another problem: unwanted resonant modes. These beams start to lose their vertical stiffness and twisting modes in the RDM start to become introduced.

Given the dimensions of the RDM, the available space, and the distribution of modes in frequency space, a 2kHz resonant frequency is chosen for the RDM. This is the lowest easily achieved oscillation frequency given the constraints of the fabrication technology.

RDM Spring Design

Having selected the out-of-plane geometry for the RDM, the springs that support the RDM and provide the restoring force are considered. The RDM springs have the seemingly contradictory functions of simultaneously needing to be pliable in one direction and stiff in another perpendicular direction. In order to allow a large angular displacement, the springs for the RDM must be pliable in the direction of rotation. Assuming parallelepiped beams, since they are the easiest to microfabricate, the expression for spring constant in terms of the beams geometry are

$$k_{\phi} = 4E\frac{w^3 t}{L^3}$$

where E is the Young's modulus of the beams, w is the extent of the beam tangent to the direction of rotation, L is the length of the beam, which is radial to the rotational axis, and t is the thickness of the beam, i.e., the thickness of the wafer. The factor of 4 in front corresponds to the number of beams supporting the RDM.

In addition to allowing rotation of the RDM, the beams/springs have a secondary function to transfer the gyroscopic torque to the TSM, which requires that the springs be stiff in a direction parallel to the gyroscopic torque:

$$k_\theta = 4E\frac{t^3 w}{L^3}$$

k_θ is the stiff of the beam in the θ-direction, and the remaining constants are the same as above.

Looking at these two expressions, the two spring constants are naturally decoupled. Because of the cubic relation, the spring constants in each direction are largely determined by the beam's extent in each respective direction, i.e. w strongly determines the k_ϕ spring constant and t strongly determines the k_θ spring constant.

This is in contrast to the case for rotation about in-plane axes, where the beams must be pliable in torsion, but stiff out-of-plane. The torsional spring constant for a parallelepiped beam is described by:

$$k = 2\left(\frac{G}{12}\right)\left(\frac{wt}{L}\right)\left(w^2 + t^2\right)$$

where G is the shear modulus, which is related to the Young's modulus, E, by:

$$G = \frac{E}{2(1+\nu)}$$

where ν is the Poisson ratio for the beam material. The out-of-plane spring stiffness is described by:

$$k = 2E\frac{t^3 w}{L^3}$$

The spring constants are not as cleanly decoupled for torsional springs for the two motions. If we make the approximation that $t>>w$, then the two expressions are distinguished by a cubic dependence on L in one case and a linear dependence on L in the other. Unlike the situation where the rotational axis is out-of-plane, i.e. the two spring constants are distinguished by two different design parameters, in this case, the spring constant in each direction is largely distinguished by different power relationships of the same design parameter.

RDM Electrical Design

To make an electromechanical RDM, we must include an actuator to drive the RDM into oscillation. There are a number of actuator designs based on a number of operating principles, however, electrostatic comb actuators are chosen for their relative ease of fabrication. All that is needed for an electrostatic actuator are two conductive

surfaces that move relative to each other. As a voltage is applied, the electric field draws one surface towards the other.

As discussed before, for inertial grade angular rate sensors, it is necessary that the stator of the RDM reside on the gimbal, i.e. on the TSM. This creates a number of other difficulties, since it requires that the RDM actuator be fabricated on a moving part, i.e. the TSM. The wafer bonding approaches are difficult to implement since they require an extra bonded wafer on the TSM. This would add a great deal of mass and volume, which initially seems advantageous, however because the bonded wafer only holds the moving parts in relative position to one another, it is a static body that does not add any angular momentum to the RDM. It does, however, add great deal of inertia to the TSM, reducing its response to the gyroscopic torque. Moreover, this mass is lop-sided, affecting the symmetry of the device, making it sensitive to inputs other than rotation, such as acceleration.

The other major approach, backfilling, would require a 300μm deep trench filled with either poly-silicon or silicon dioxide, which invokes a number of fabrication problems with internal stress, adhesion, and keyholing. Moreover, backfilling the silicon trench with another, non-crystalline material mitigates many of the inherent mechanical reliability advantages of single crystal silicon.

The TGZM technique coupled with the DRIE technology sidesteps the above difficulties and also naturally allows several features, such as electrical connections and thick, high-aspect ratio proof masses, actuators, and beams. The npn junctions electrically separate the bulk silicon into several regions to allow actuation. These regions may be continuous from the RDM to TSM to the edge of the die, so as to act as

conductors that electrically connect the actuator to the edge of the chip. The bulk of the TSM itself acts as the electrical connection from the RDM to the edge of the die, thus integrating the electrical subsystem into the mechanical bodies themselves, insuring that the electrical connections do not affect the mechanical design.

Both the RDM stator and rotor are entirely placed on the TSM, insuring no error torques from actuator misalignment. Also, since the actuator electrodes are carved through the bulk silicon, 300μm tall electrostatic comb drives are possible, allowing a large area between electrodes, capable of generating large torques per unit chip area. Since the electrodes are fabricated from the same piece of silicon, the electrodes are naturally aligned and the generated torque is symmetrical.

The actuator equation for an electrostatic drive is the angular derivative of energy of a capacitor:

$$\tau \equiv \frac{dE}{d\theta} = \frac{d}{d\theta}\left(\frac{1}{2}CV^2\right)$$

where τ is the torque produced by the drive, E is the energy of the capacitor, θ is the angle about which the capacitors move, C is the capacitance of the electrostatic drive, and V is the applied voltage. A radial, interdigitated comb drive is chosen since it has the greatest torque for a given area. [Kaiser2000]. The torque may expressed as:

$$\tau_{perDrive} = \frac{1}{2}\varepsilon_0 \frac{hr_i}{g} V^2 N_F$$

where ε_o is the free space permittivity, h is the height of the fingers (the thickness of the silicon), r_i is the radius of the innermost finger, g is the gap between the stator and rotor, V is the voltage on each capacitive plate, and N_F is the number of fingers on the drive. This is the torque due to interdigitated drive. The total torque is summed over all comb drives:

$$\tau = \frac{1}{2}\varepsilon_0 \frac{hr_i}{g} V^2 N_F N_D$$

where N_D is the number of drives.

This relation indicates that the torque increases with increasing height, h, and with decreasing gap, g. This points out some of the inherent advantages of deep reactive ion etched, bulk-micromachined structures. The thickness of the bulk-micromachining allows orders of magnitude increase in generated torque compared to surface micromachined counterparts, while the high-aspect ratios preserve the narrow gaps. Since the RDM angular momentum is linear with torque, these possible geometries with DRIE, bulk-micromachined silicon allow for large increases generated angular momentum, and in turn, improved gyroscope performance.

TSM Design

The primary function of the TSM is to allow rotation about the sense axis to detect the gyroscopic torque due to an angular rate. The TSM also serves the secondary function of carrying the entire RDM, i.e. the mechanical, electrical, and electro-

mechanical components. Finally, the TSM serves as the electrical conduit through which the RDM's electrical connections to the frame must route.

TSM Mechanical Design

Like the RDM, the TSM's equation of motion may also be modeled as a damped, driven harmonic oscillator, but with the gyroscopic torque as the driving force.

$$I_{TSM}\ddot{\theta} + b_{TSM}\dot{\theta} + k_{TSM}\theta = \Omega_{in} \times \vec{L}_{RDM}$$

Assuming that the input angular rate and the RDM angular momentum are normal to each other, the solution to this equation is:

$$\theta = \frac{\Omega_{in} L_{RDM} / k_{TSM}}{\sqrt{\left(1 - \omega_{RDM}^2 / \omega_{oTSM}^2\right)^2 + \left(\frac{\omega_{RDM} / \omega_{oTSM}}{Q_{TSM}}\right)^2}}$$

Examining this expression, the angular motion of the TSM is maximized with increasing input angular rate, increasing angular momentum of the RDM, and increasing Q-factor of the TSM, and decreasing spring constant. Also, the angular motion is increased when the oscillation frequency of the RDM is matched to the resonant frequency of the TSM.

TSM Spring Design

The TSM springs are torsional flexures to allow the TSM to rotate about an axis that lies in the plane of the wafer. The torsional spring constant as a function of geometry for a parallelepiped beam is:

$$k = 2\left(\frac{G}{12}\right)\left(\frac{wt}{L}\right)\left(w^2 + t^2\right)$$

For DRIE beans, the thickness of the spring, ~250μm, is much larger than the width, ~15μm.

It is desirable to suppress the other modes of oscillation for the TSM. This can be arranged by increasing the resonant frequency for all other modes. Because the width of the beam is so small compared to the beam's other dimensions, the main motion of concern is the translational motion of the TSM that is parallel the width of the beam.

To suppress this motion, the width may be increased, but the beam must remain torsionally pliable. Since the thickness of the beam is so much greater than the width, the width may be increased to some extent without appreciably affecting the spring constant in the torsional direction. The spring constant is unaffected to first order as long as the w^2 is on the order of 10% of t^2. This allows the width of beam to be approximately 30% the thickness. For a 200μm thick beam, this allows for a width of 60μm. This adequately shifts the remaining modes of motion for the TSM to above 6100Hz, which is well above the operating frequency of the RDM at 2000Hz. Such a separation in frequency space ensures suppression of the undesired modes.

TSM Electrical Design

Capacitive sensors are chosen to sense the TSM motion because of their ease of fabrication. All that is needed for a capacitive sensor are two conductive surfaces that move relative to each other. As one surface moves, the capacitance between them changes, resulting in an electrical method of motion detection.

The relationship between the motion and the capacitance change (to first order) for a parallel plate capacitor is

$$\Delta C = \frac{dC}{dg}\Delta g = \frac{d}{dg}\left(\varepsilon_o \frac{area}{g}\right)\Delta g = \varepsilon_o \frac{area}{g^2}\Delta g$$

where Δg is the change in the gap between the two plates, g is the separation gap, ε_o is the dielectric constant of the material between the two conductive surfaces (air in this case), and *area* is the area of the parallel plates.

Further sensitivity may be extracted by forming pairs of capacitive sensors. This allows differential measurement, which allows the sensors to be insensitive to many undesired modes of TSM motion. For example, translational displacement along the z-axis (the axis perpendicular to the plane of the wafer) may occur from linear acceleration of the sensor. With a pair of sensors, one on each side of the TSM, rotational motion can be distinguished from linear translation. Linear translation would result in capacitive changes on both sensors in the same direction, whereas rotation would be distinguished as capacitance changes in opposite directions.

RDM-TSM Coupling

Mechanical Design

The springs that support the RDM also transfer the gyroscopic torque from the RDM to the TSM. The interaction between the two bodies is modeled as two coupled simple harmonic oscillators. There are a number of ways to couple energy from one simple, harmonic oscillator to another; however the most direct way is to simply have a stiff spring between the two. Anything other than this scheme requires careful control of the spring constants and moments of inertia to allow efficient energy transfer between the two bodies.

If the springs are fabricated from the bulk silicon, then they will have a thickness the same as the wafer thickness, yet another advantage of bulk-micromachined silicon gyros. Such a thick beam makes for a very stiff spring between the RDM and TSM. This results in a complete and immediate transfer of gyroscopic torque to the TSM.

TSM-RDM Coupling - Electrical Design

The primary electrical requirement of the RDM-TSM springs is that they carry the electrical signals from the frame of the gyro to the TSM to the RDM. However, there is the additional requirement that the electrical connections do not mechanically affect the gyro. With the TGZM process, it is possible to use the bulk silicon itself as a conductor, and an electrically conductive passage may be formed through the TSM. A map of the voltage-distinct regions of the gyro is shown in figure 28.

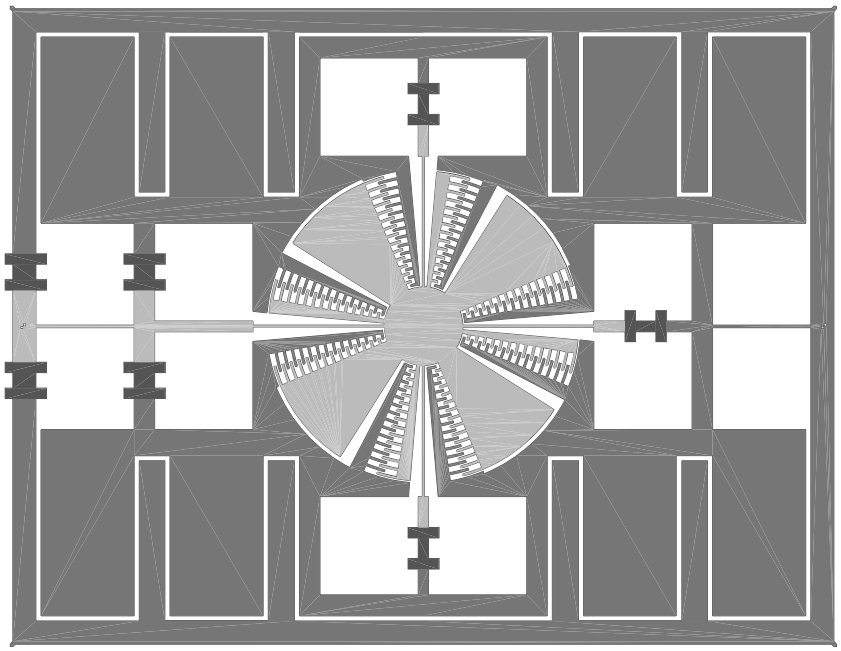

Figure 28 - Map of the voltage distinct regions defined by the thermomigrated pn-junctions. The light areas denote one region and the dark areas denote a second region. The device remains mechanically one monolithic piece of silicon, but electrically is divided into 2 regions.

Contact is made to the gyro at the frame in the light area for the charged region and in the darker area for the ground. Most of the TSM is grounded which acts as the ground plane for the capacitive sensors. This approach does not affect the symmetry nor the mechanical behavior of the gyro, while requiring one mask step for the aluminum definition, and one process step for the thermomigration.

TSM-RDM Coupling - Resonant frequency match

Resonant amplification of both the RDM and TSM motion can increase the sensitivity of the gyro by orders of magnitude. In order to take advantage of this amplification, the resonant frequencies of the two oscillators must match. Because the RDM and TSM are both simple harmonic oscillators, in general, they will each have different resonant frequencies.

Resonant frequency matching is, perhaps, the outstanding, unsolved problem with coupled oscillators in MEMS devices. Since Q-factors can be in the tens of thousands, many MEMS devices would improve performance by orders of magnitude with a solution to this problem. Unfortunately, a satisfactory solution has yet to be found.

The main difficulty is that although the absolute variation in micromachining technologies is small, the relative error may be very large. Consequently, one may design spring constants and moments-of-inertia to have matching resonant frequencies, but manufacturing variation will, in general, shift these frequencies away from each other. For example, the process variation for a 20μm wide spring may be ±5μm. Although a 5μm variation is small, this is a 25% variation in beam widths. This variation may be further amplified by factors such as the cubic dependence of the spring constant. Overall, a 25% variation in beam width results in a 40% variation in resonant frequency.

Several approaches to this problem have been proposed, but none present a complete solution. One approach is to design wider beams so that for constant absolute error, the relative error is reduced. However given the limited area, this approach has limited application in microsystems. This may work for beams of certain geometries and certain bending modes, but for the RDM, to half the percent error, the width must be doubled. This doubling, in turn, is cubed in the calculation of the spring constant, resulting in an overall increase in spring constant by a factor of 8. This may be compensated for by lengthening the beam by a factor of 8, but then folded beams must be considered, and this begins to introduce unwanted resonant modes.

Another suggestion is to arrange process variation such that the effects cancel. For example, if manufacturing variation decreases a beam's spring constant, then arrange

for the proof body to also decrease in mass/moment-of-inertia. Usually this is not possible since the beam is 20μm wide while the proof body may be millimeters in size, so the relative error is vastly different. However, the effect of relative error may be increased in the proof body by constructing the body with many 20μm wide lines. Thus if the beam decreases in width by 25%, then all the 20μm beams that make up the proof body also decrease by 25%. However, the dependence of width to spring constant is cubic, whereas the dependence of beam width to proof body mass is quadratic. Thus a 25% shift in beam width still results in a 25% shift in resonant frequency, which for reasonable Q-factors, disallows any resonant amplification effects for coupled oscillators.

Yet another alternative approach is to "tune" the resonant frequency. One could approach this by either changing the spring constant or the moments-of-inertia by adding or removing material. However, changing the geometrical parameters of either the springs or the masses requires uniform and precision machining of tiny, mechanically-free parts. This is neither straightforward, nor batch-fabrication compatible.

Alternatively, one could externally apply an electrostatic field to shift the resonant frequency. [MacDonald1995] By adding a DC field to the TSM's surface micromachined actuators, another term is added to the damped simple harmonic oscillator equation:

$$I\ddot{\theta} + b\dot{\theta} + k\theta = \Omega_{in} \times \vec{L} + \frac{1}{2}\varepsilon_o C(\phi) V_{DC}^2$$

where the additional driving term is the electrostatic force due to the applied DC field.

Examining the Taylor expansion of the DC electrostatic tuning term, the first order term is linear with angular displacement, and therefore acts like a spring with a negative, voltage-dependent spring constant:

$$I\ddot{\theta} + b\dot{\theta} + \left(k - 2\varepsilon_o \frac{x^3 y V_{DC}^2}{z_o^3} \right) \theta = \Omega_{in} \times \vec{L}$$

By applying a DC voltage, the spring constant is effectively decreased, and the resonant frequency is lowered. This approach is feasible, however in practice, it only results in a resonant frequency tuning range on the order of 5-10%. This is inadequate since the expected resonant frequency shift due to manufacturing variability is on the order of ±40%.

Finally, another way to approach this problem is to purposefully mismatch the two resonant frequencies. This abandons the attempt to employ resonant amplification, and instead, to optimize the condition when the two resonant frequencies are unmatched. The first oscillator is driven in resonance, and the second oscillator has very pliable springs. The pliability of the springs allows the second oscillator to respond as much as possible to the first oscillator. Off resonance, the maximum displacement for a simple harmonic oscillator is:

$$\phi_{\max} = \frac{\tau}{k}$$

This approach is unable to take advantage of any resonant amplification, but optimizes the unmatched resonant frequency case.

Overall Design

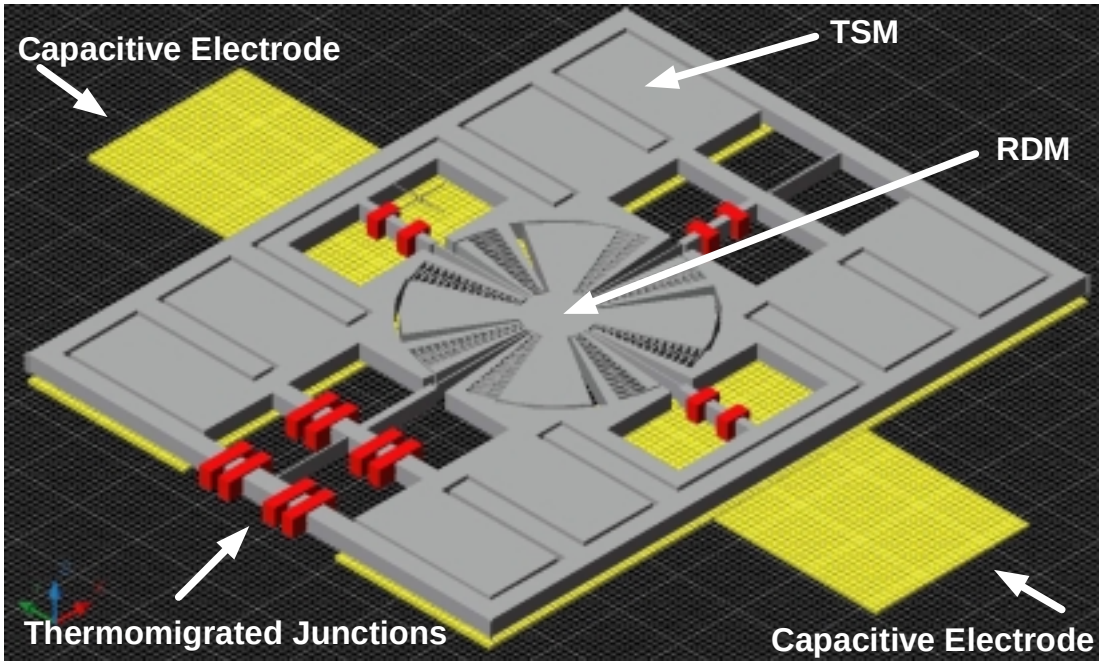

Figure 29 - Overall design of the micro-gyroscope. The design represents a number of ways that the device benefits from thermomigrated junctions, including preservation of the single crystal material, avoidance of bulky substrate wafers, batch-fabrication compatibility, a thick & massive angular proof body, and high-aspect ratio, electrostatic comb drives.

A general layout of the angular rate sensor is shown in figure 29. The grey is the bulk silicon etched portion of the angular rate sensor. The central, cylindrical part is the RDM, and the outer parallelepiped is the TSM. Both mechanical bodies are designed to allow 5 degrees of rotation.

The 8 sets of angular comb drives are visible on the RDM. The outer circular part of the RDM is the stator and is both electrically and mechanically part of the TSM. The inner part of the RDM is the rotor and is electrically isolated from the rest of the bulk silicon by the 4 red aluminum thermomigrated junction isolation areas radially arranged around the RDM.

Design Simulation

Simulation of the gyroscope is used to verify the design and to also guide optimization of design parameters. The gyroscope is simulated in Mathematica and in ANSYS.

Mathematica Simulation

Mathematica, a program developed by Wolfram Corporation, is capable of manipulating equations symbolically. A model accurate to first order is constructed in Mathematica for the gyroscope design. The Mathematica code is included in appendix E.

The simulation has several purposes. One is to verify the analytical solutions discussed in the design section. Another is that the analytical relations are often overly cumbersome for exploration of the multidimensional parameter space. Computer simulation facilitates that exploration by providing a graphical understanding of the relationships between the various design parameters and the operational characteristics.

As discussed above, both the RDM and the TSM are modeled as forced, damped, simple harmonic oscillators. Electromechanically, the RDM is modeled as an electrostatic comb drive actuator that drives the RDM. The rotational amplitude of the

TSM is translated into a capacitance by the electrostatic sensors. Given these relations and the inputted values listed in table 5, the response of the gyroscope may be modeled.

Table 5 - Input parameters for the Mathematica simulation of the microgyroscope.

Theoretical Gyroscope Response

Inputted Values

Parameter	Value	Units
Fundamental Constants		
permittivity of free space	8.85E-12	F/m
Material		
Si density	2330	kg/m^3
Si Young's Modulus	1.60E+11	Pa
Si Poisson's Ratio	0.22	
Device Parameters		
Entire Device		
Thickness	200	um
RDM		
Resonant Frequency	1806	Hz
Q-Factor	40	
Radius	1.5	mm
Gap of the Drive	20	um
Number of Drives	8	
Number of Fingers/Drive	14	
Drive Voltage	200	V
TSM		
Resonant Frequency	574	Hz
Q-Factor	1	
Width	7	mm
Length	5	mm
Capacitance gap	15	um

The gyroscope response, i.e. the capacitance change, expected for a given inputted angular rate is shown in figure 30. To first order, the expected output of the

gyroscope is linear. The model predicts a capacitance change of 6.48fF for a 10 deg/s input.

```
Plot[deltaCapGyroOut[omegaInV, rhoSi,
  lengthTSM, widthTSM, tSi,
  capGapTSM, 0, wT, gT, rhoSi, rRDM,
  tSi, driveGap, nFingers,
  nDrives, driveVolt, wR, gR],
    {omegaInV, 0, 30 Pi / 180}, Frame → True,
 FrameLabel → {"Angular Rate (rad/s)",
   "Capacitance Change (F)"}]
```

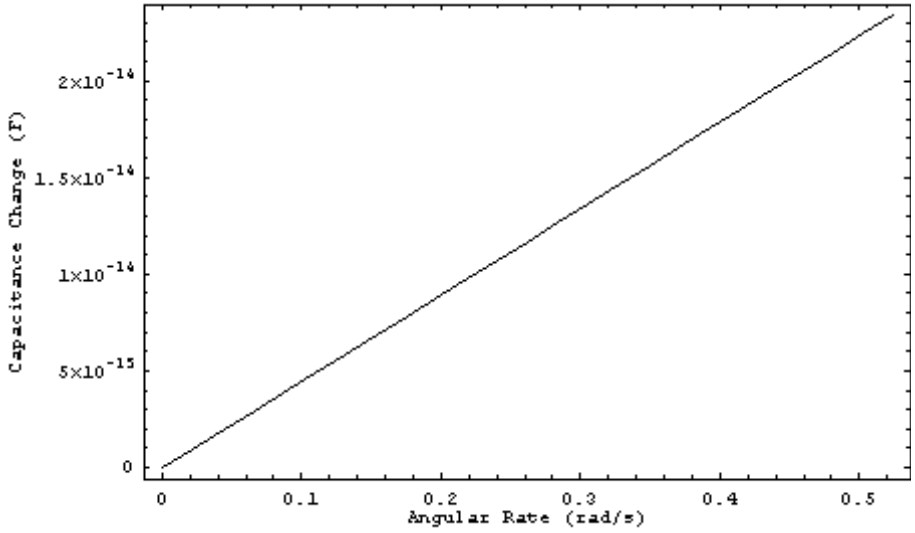

Figure 30 - Expected response of the micro-gyroscope to angular rate.

To find optimal design parameters, the output capacitance change is plotted as a function of RDM radius and TSM length, shown in figure 31. The model predicts that there is a line of RDM radii and TSM lengths that have the same optimal capacitance change. This is easier to see in the contour plot shown in figure 32. As a result, holding all other design parameters constant, there is no optimal RDM radius/TSM length combination.

```
Plot3D[
    deltaCapGyroOut[omegaIn, rhoSi,
  lengthTSMV, widthTSM, tSi,
   capGapTSM, 0, wT, qT, rhoSi, rRDMV,
  tSi, driveGap, nFingers,
   nDrives, driveVolt, wR, qR],
    {lengthTSMV, 3 10^-3 , 10 10^-3},
    {rRDMV, 1 10^-3, 3 10^-3},
    ViewPoint -> {-1.557, -2.141, 2.108},
 AxesLabel → {"TSM Length (mm)",
   "RDM radius (mm)",
"Capacitance Change (F)"}]
```

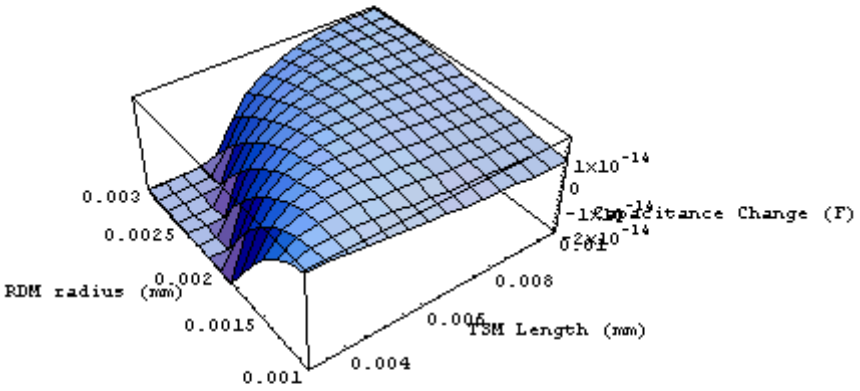

Figure 31 - Plot of the sensitivity of micro-gyroscope to RDM radius and TSM length.

```
ContourPlot[
    deltaCapGyroOut[omegaIn, rhoSi,
  lengthTSMV, widthTSM, tSi,
   capGapTSM, 0, wT, gT, rhoSi, rRDMV,
  tSi, driveGap, nFingers,
   nDrives, driveVolt, wR, gR],
 {lengthTSMV, 3 10^-3 , 10 10^-3},
    {rRDMV, 1 10^-3, 3 10^-3},
 Frame → True,
 FrameLabel → {"TSM Length (mm)",
   "RDM Radius (mm)"}]
```

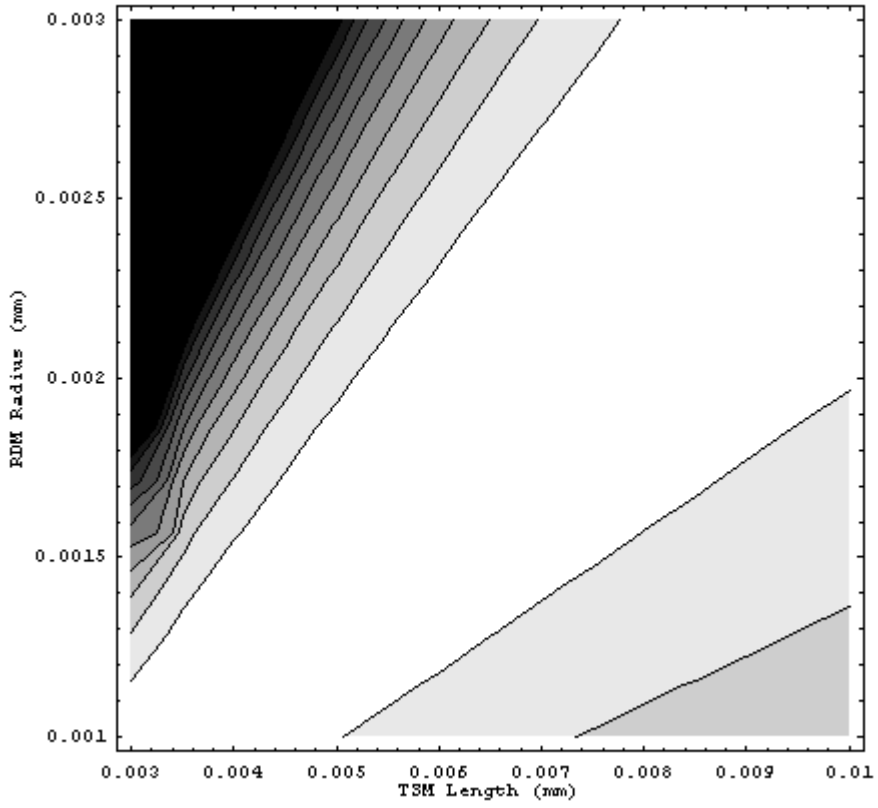

Figure 32 - Contour plot of sensitivity of the gyroscope as a function of RDM radius and TSM length. An optimal line of RDM radii and TSM lengths exists, but no optimal point.

However, for a given RDM radius there is an optimal TSM length. A RDM radius of 1.5mm is chosen because a 1.5mm radius RDM results in a cylinder that is 3mm diameter and 300μm thick. Because the cylinder is an order of magnitude wider than thick, it is likely to favor rotational modes of motion around the cylinder's z-axis rather than wobbling modes. Using this value for the RDM radius, the Mathematica model predicts that for a 1.5mm radius RDM, the optimal TSM length from the rotation axis is 5.06mm. This plot is shown in figure 33. An optimal length exists, because a longer TSM increases the capacitive sensing area, but also increases moment of inertia of the TSM.

```
Plot[{deltaCapGyroOut[omegaIn, rhoSi, lengthTSMV,
      widthTSM, tSi,
      capGapTSM, 0, wT, qT, rhoSi, 1.5 * 10^-3,
      tSi, driveGap, nFingers,
      nDrives, driveVolt, wR, qR]},
  {lengthTSMV, 3.5 10^-3, 10 10^-3},
  Frame → True, FrameLabel → {"TSM Length (mm)",
"Capacitance Change (F)"}]
```

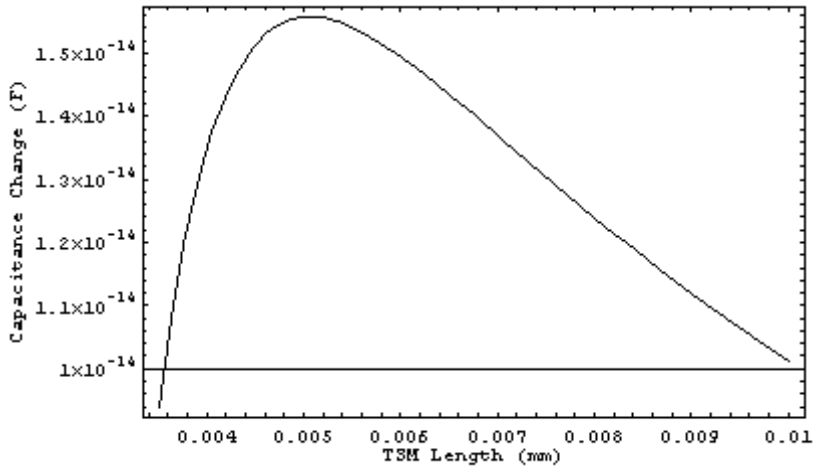

Figure 33 - Sensitivity of the microgyroscope as a function of TSM length for a RDM radius of 1.5mm.

How does TSM length parallel to the rotation axis affect capacitive response? The plot of capacitance change versus TSM width is shown in figure 34. To 1st order, the sensitivity of the gyroscope is constant with respect to TSM width. This is because although a longer TSM increases the moment of inertia linearly, the area available to capacitive sensing also increases linearly. As a result, these two effects cancel, and the sensitivity remains constant with respect to the TSM dimension parallel to the axis of rotation.

```
Plot[
    deltaCapGyroOut[omegaIn, rhoSi,
  lengthTSM, widthTSMV, tSi,
   capGapTSM, 0, wT, qT, rhoSi, rRDM,
  tSi, driveGap, nFingers,
  nDrives, driveVolt, wR, qR],
    {widthTSMV, rRDM + 0.5 10^-3 , 20 10^-3},
 Frame → True,
 FrameLabel → {"TSM Width (mm)",
"Capacitance Change (F)"}]
```

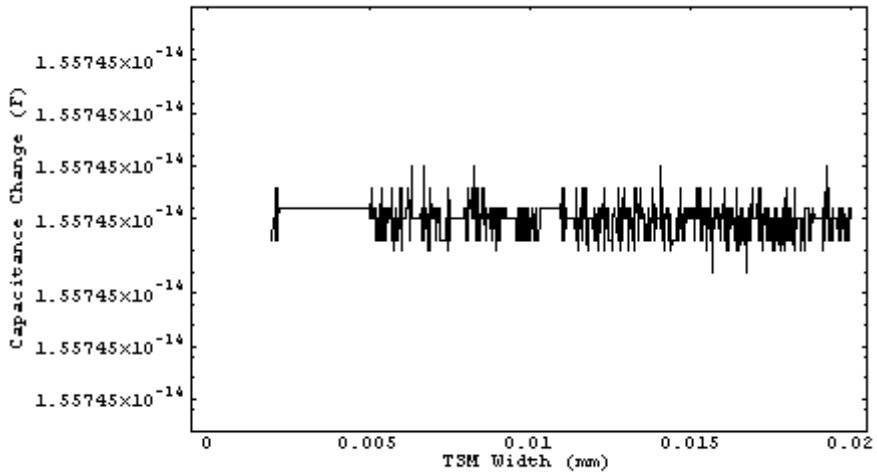

Figure 34 - Sensitivity of the gyroscope to TSM width. To first order, sensitivity is not a function of TSM width.

Studying the response of the device as a function of resonant frequencies of the RDM and TSM, the lower resonant frequencies result in higher capacitance changes to a given input angular rate. This plot is shown in figure 35.

```
Plot3D[
deltaCapGyroOut[omegaIn, rhoSi, lengthTSM,
  widthTSM, tSi,
  capGapTSM, 0, wTV, qT, rhoSi, rRDM,
  tSi, driveGap, nFingers,
   nDrives, driveVolt, wRV, qR],
{wRV, 10^2, 10^4},
{wTV, 10^2, 10^4},
 ViewPoint -> {2.893, 1.311, 1.168},
 AxesLabel →
  {"RDM resonant frequency (Hz)",
   "TSM resonant frequency (Hz)",
"Capacitance Change (F)"}]
```

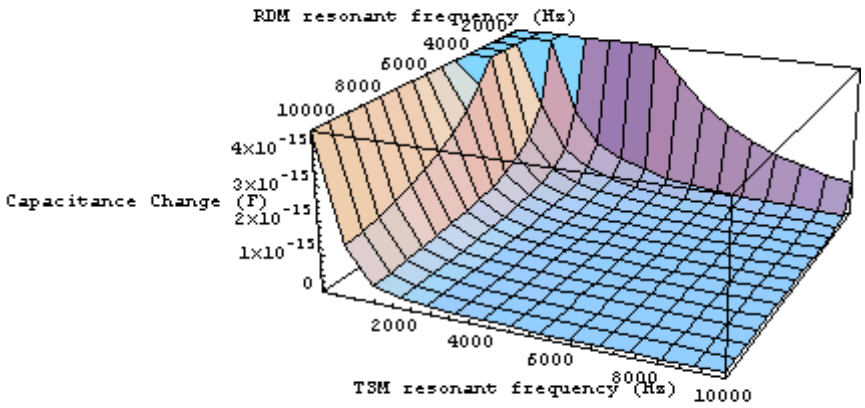

Figure 35 - Plot of device sensitivity as a function of RDM and TSM resonant frequencies. Lower resonant frequencies indicate a higher performing device.

The performance of the gyroscope turns out to be a strong function of the drive voltage. A log-log plot of the expected capacitance change to the drive voltage is shown in figure 36.

```
LogLogPlot[
    deltaCapGyroOut[omegaIn, rhoSi,
  lengthTSM, widthTSM, tSi,
   capGapTSM, 0, wT, qT, rhoSi, rRDM,
  tSi, driveGap, nFingers,
   nDrives, driveVoltV, wR, qR],
{driveVoltV, 10, 1000},
 FrameLabel → {"Drive Voltage (V)",
   "Capacitance Change (F)"},
 Frame → True]
```

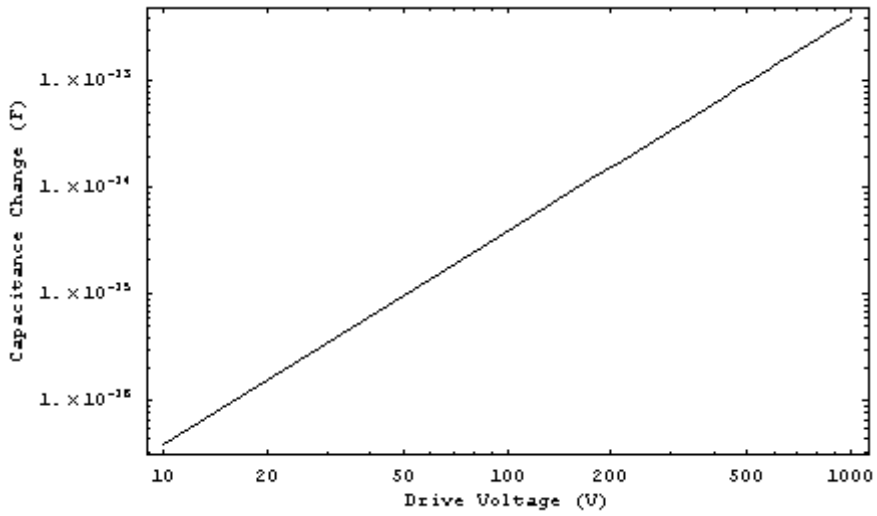

Figure 36 - Device sensitivity as a function of drive voltage.

ANSYS Finite Element Simulation

Candidate mask designs were defined in AutoCAD and a 3D model built by extruding the masks. These 3D models were then directly imported into ANSYS.

Adding material property data, the ANSYS was used to verify design and to visualize and calculate the resonant modes and frequencies.

There are a number of element types available in ANSYS. Solid elements are chosen because they allow 3D analysis of objects. Among solid elements, a tetrahedral element is chosen because of the complex shape of the imported model allows for a free mesh to be constructed automatically.

Among 3D, solid, tetrahedral elements there are SOLID72, SOLID92, and SOLID187. All of these elements are similar, and differ mostly by the number of nodes and the degrees of freedom. Like so many other analyses, there is a basic tradeoff between time and accuracy. For ANSYS, this tradeoff is determined by the number of degrees of freedom, both in the number of elements as well as the degrees of freedom within each element.

SOLID72 is a 4 node element with one node at each corner of the tetrahedron. In addition to translational degrees of freedom, each node also has rotational degrees of freedom. SOLID72 consistently predicts resonant frequencies are well above results from experiment. This indicates that there are not enough degrees of freedom with SOLID72, and the element acts overly stiffly for accurate resonant frequency calculations. The manual for ANSYS recommends SOLID72 for testing purposes, and does not recommend its use for actual calculations.

SOLID187 is a 10 node tetrahedral element that has quadratic displacement behavior and is particularly well suited for non-linear simulations. However, since the gyroscope is anticipated to work within the linear, elastic region of the material, this

element is overly complex, requiring larger memory spaces and greater simulation times, without offering greater accuracy.

SOLID92's number of degrees of freedom lies somewhere between SOLID72 and SOLID187. Like SOLID187, SOLID92 is also a 10 node tetrahedral solid element but does not calculate each node's motion to second order. Many of its degrees of freedom assume linear behavior from both the materials as well as the geometry. As a result, this element avoids the unnecessary complexity of SOLID187, but still provides adequately accurate simulation results.

The gyroscope is constructed from single crystal silicon, which is an anisotropic material. However, to simplify analysis, an isotropic material was assumed. [Bouwstra1993] The material constants are shown in table 6.

Table 6 - Material constants used for the ANSYS finite element simulation.

Young's Modulus	150GPa
Poisson's Ratio	0.17
Density	2330 kg/m^3

The gyroscopic model in ANSYS is slightly modified to remove the comb drive teeth. The absence of the teeth is found to adjust the resonant frequency by about 5%. To verify the size of the shift, the RDM with and without the comb drive is modeled. The results of the modeling are shown in figures 37 and 38.

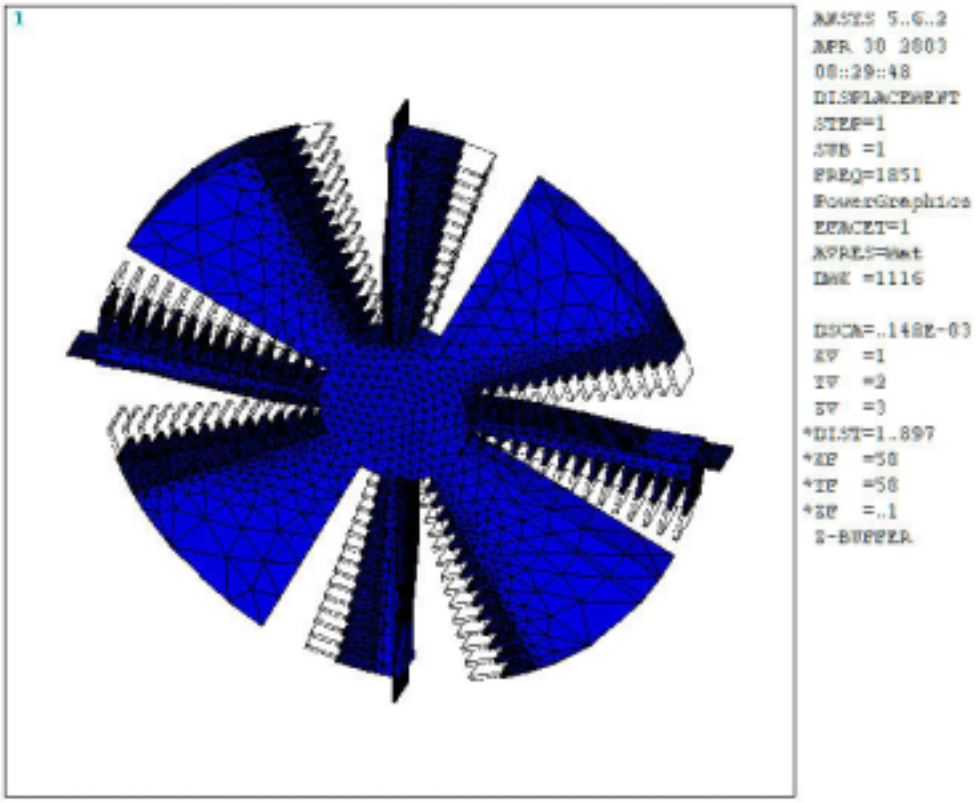

Figure 37 - 1st mode of the RDM with the teeth of the comb drive. The calculated resonant frequency is 1851Hz.

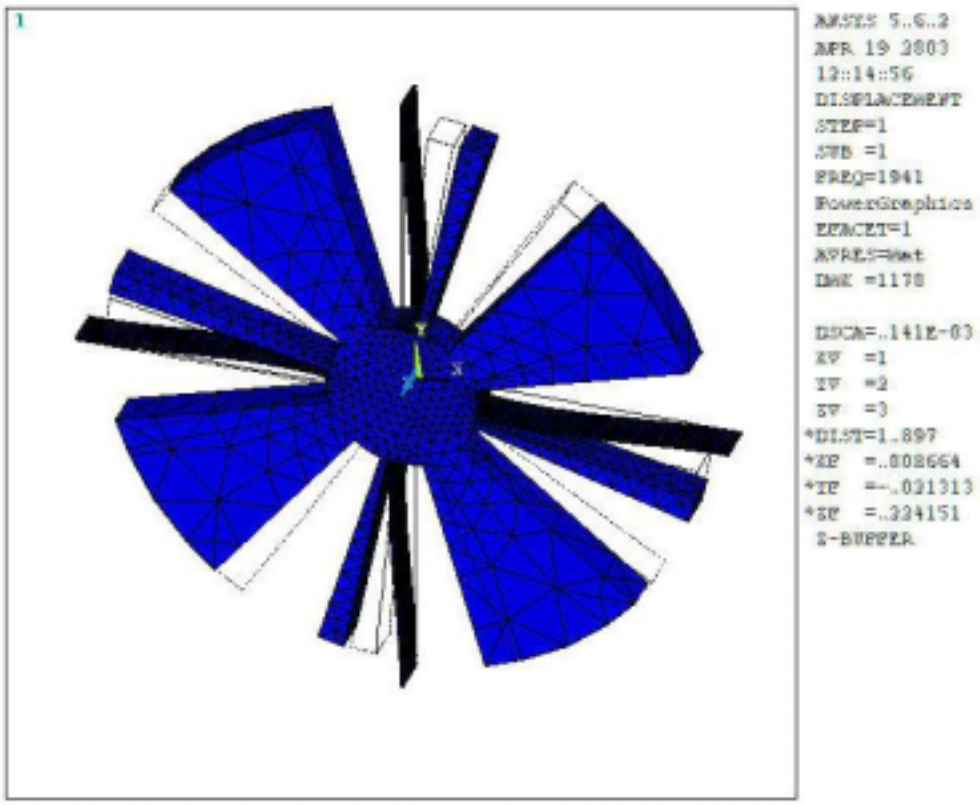

Figure 38 - 1st resonant mode of the RDM without the comb drive teeth. The calculated resonant frequency is 1941Hz, which differs by 5.7% from the model with the teeth. This simulation, however, completes in hours versus days for the model with the teeth.

ANSYS predicts that the resonant frequency is 1851Hz with the comb teeth and 1941Hz without. This is a 5.7% difference. But, because of level of detail needed to capture the geometric features of the comb fingers, the difference in computation time on a 1.8GHz Pentium 4 with 512MB of RDRAM is 3 days versus 4 hours. As a result, for the purposes of verification of the model, modeling the comb drive is unnecessary, and a small 5% difference is assumed. It is known that given the realities of microfabrication, a greater than 5% shift in resonant frequency is probable from fabrication variation alone.

For the entire device, the first 8 resonant frequencies are computed. The first three are shown here. The remaining 5 are in appendix B.

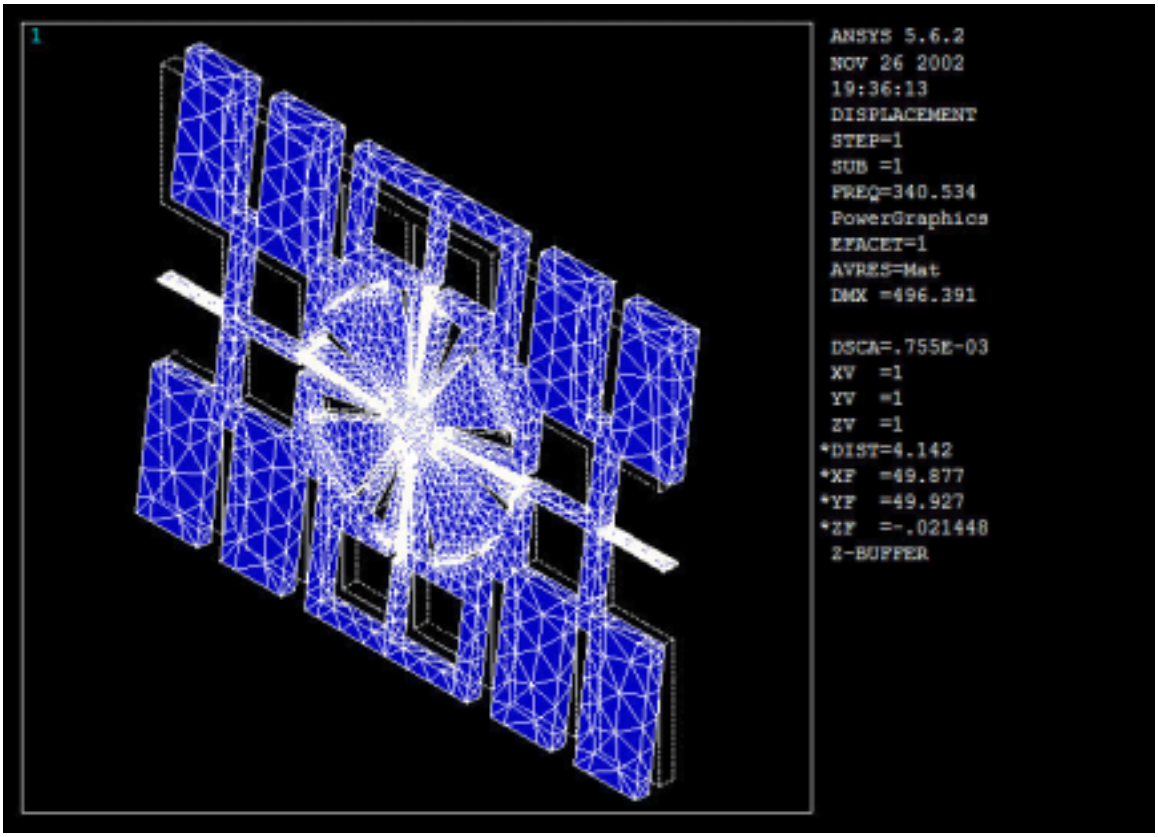

Figure 39 - 1st resonant mode for the gyroscope: TSM rotation about the sense axis. The calculated resonant frequency is 340Hz.

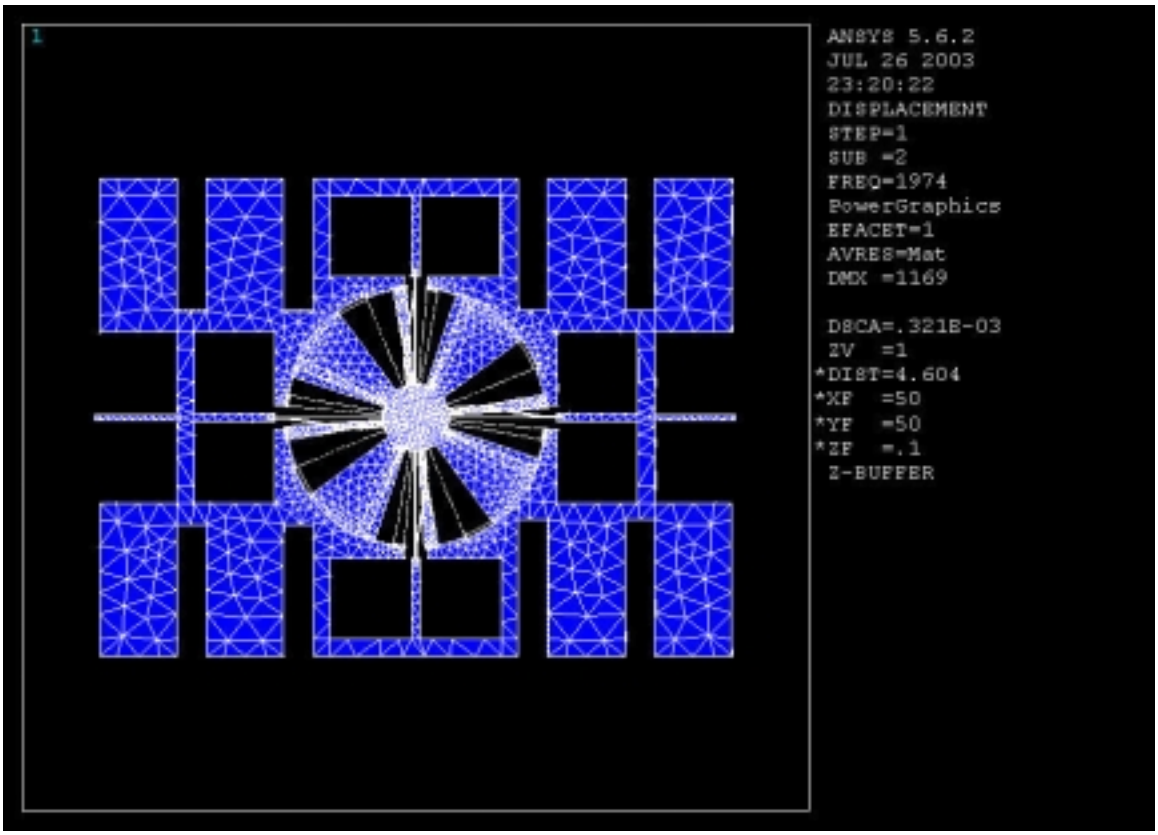

Figure 40 - 2nd resonant mode for the gyroscope: RDM rotation about the drive axis. Calculated resonant frequency is 1974Hz.

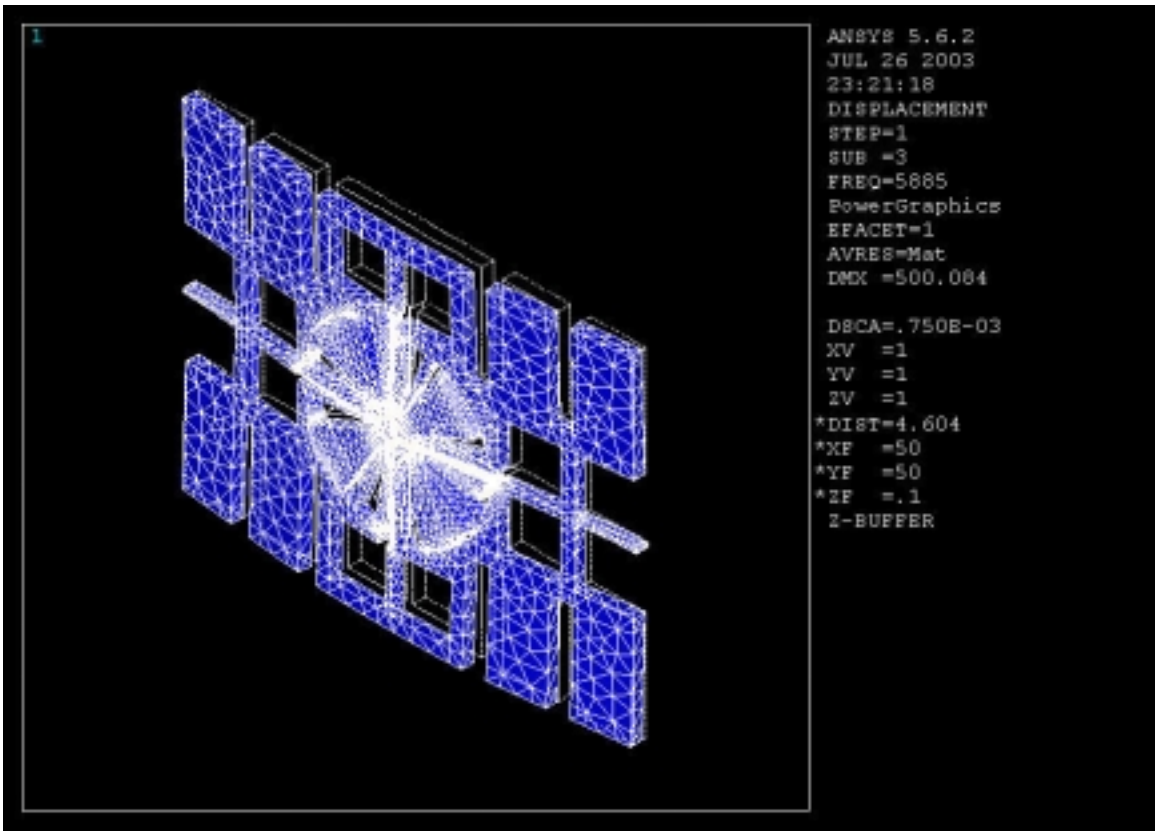

Figure 41 - 3rd resonant mode for the gyroscope: TSM bending. Calculated resonant frequency for this mode is 5885Hz, which well above the two desired modes. All other modes of motion may therefore be rejected by driving the gyroscope below 5885Hz.

The first two modes are the desired TSM and RDM motions. The TSM has a resonant frequency of 340Hz and the RDM rotation resonant frequency is at 1974Hz. The next resonant mode is the TSM bending back and forth. The bending is done about the y-axis and has a resonant frequency of 5885Hz. This mode is adequately separated in frequency space so as to avoid excitation of any other modes other than the two desired modes. A summary of the ANSYS modal simulation is shown in table 7, and all 8 modes and the ANSYS simulation conditions are listed in Appendix B.

Table 7 - A listing of the predicted modes and resonant frequencies for the ANSYS simulation of the microgyroscope.

ANSYS Modal Simulation Results Summary

mode number	Frequency (Hz)	mode
1	340	TSM Rotation-Y axis
2	1974	RDM Rotation-Z axis
3	5885	TSM bending-about Y axis
4	6103	TSM translation-along y axis
5	7252	TSM Rotation-Z axis
6	7446	TSM twist-X axis
7	12607	TSM Bend-X axis
8	13263	TSM Twist-about X&Y axis

Chapter 5

Fabrication of an Angular Rate Sensor with Thermomigrated Junction Isolation and DRIE

Because of the interrelatedness of design and fabrication, many of the larger points with regard to the fabrication of the device are made in Chapter 4, where the design of the gyroscope is discussed. This chapter focuses on the fabrication of the microgyroscope, and discusses its manufacture in detail.

The fabrication of the micro-gyroscope is 90% of the time and effort of the second part of this thesis. Despite the fact that fabrication is the vast majority of the work, this is the shortest chapter. Fabrication work is largely Edisonian, in that many different possibilities must be eliminated before a viable path is identified. Given this reality, most of the fabrication results are negative, and even though they account for the bulk of the results, they are discussed minimally. The final, positive results that lead to working devices are reported fully, and the negative results are partially enumerated in the troubleshooting section.

General Fabrication Flow

The general flow of the fabrication is illustrated in figure 42.

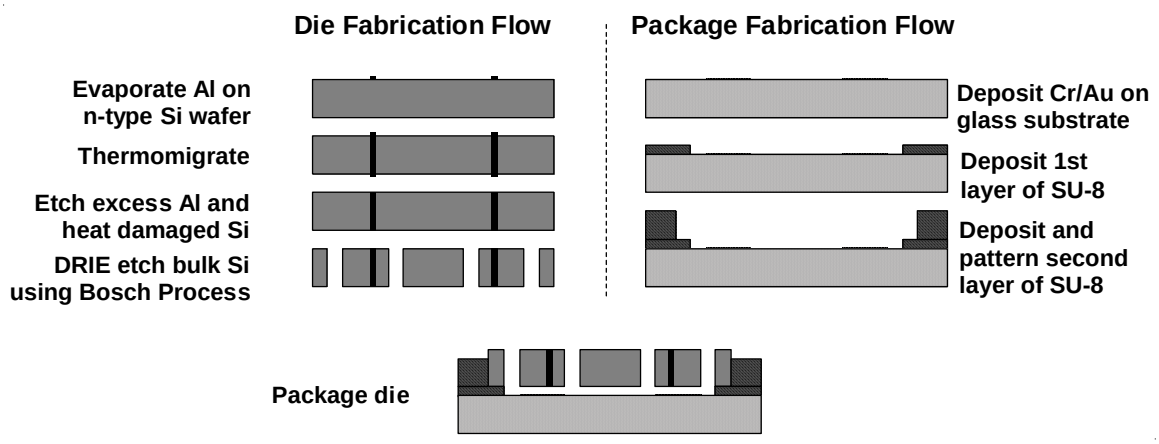

Figure 42 - Fabrication flow for the TGZM/DRIE micro-gyroscope and the package.

The general fabrication flow for the gyroscope is that the RDM and TSM are fabricated on a single silicon wafer using only the TGZM and DRIE fabrication steps. In parallel, a package for this device is fabricated on a glass substrate. The package integrates the capacitive electrodes underneath the TSM to detect its motion. A side view of the packaged device is shown in figure 43. The mask designs are shown in appendix C.

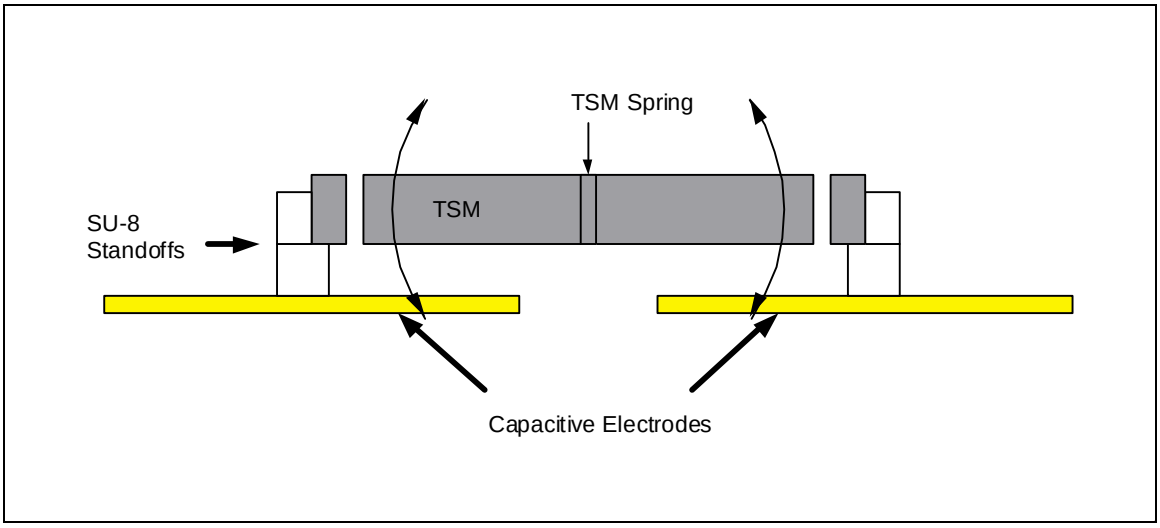

Figure 43 - Side view schematic of the packaged die. The die is held above the bottom surface of the package, which has integrated capacitive electrodes to detect the TSM motion.

Silicon Die Processing

The aluminum thermomigration and deep reactive ion etching are done on the first wafer. The wafer selection is important, since, as discussed in chapter 3, the blocking voltages depend strongly on its properties. For the gyroscope, a n-type, 1Ω-cm, <100>, prime grade wafer is obtained. The wafer is cleaned using the RCA clean process, and 5μm of Al is deposited. The deposition method is inconsequential, as electron beam evaporation, filament evaporation, and DC sputtering are all suitable.

After deposition, the Al is patterned using standard photolithography and PAN etch. Because the Al to be etched is so thick, a heated solution of PAN etch is used to accelerate the etch. A hot plate temperature of 60C is used. Above this temperature, the PAN etch erodes the photoresist before the Al is completely gone.

The PAN etch is somewhat difficult because small bubbles evolve during the etch. These bubbles mask the aluminum and create small islands of Al all over the wafer. It is possible to simply wait for these islands to etch away, but while waiting, the masked aluminum may undercut to an unacceptable degree. To prevent this, constant agitation is necessary during the etch. Ultrasonic agitation works well.

Once the silicon and aluminum are prepared, the substrate undergoes the thermomigration process. Given the equipment and the wafer (discussed in chapter 2), at maximum power, the entire process requires 1.5 hours for complete thermomigration. The heat of the thermomigration process is so intense that it damages components of the filament evaporator. To minimize the damage, the wafer is thermomigrated for 15 minutes and then the apparatus is allowed to cool for 30 minutes, vented with N_2. The

actual thermomigration time is approximately 1.5 hours, but the entire process time is 4.5 hours.

Afterwards, the excess aluminum and heat damaged silicon are etched using a solution of $HF:HNO_3:H_2O$ in a ratio of 15:35:50 for 2 minutes. This etch also produces a great deal of bubbles and light agitation is recommended.

As discussed in chapter 2, large lateral thermal gradients in the silicon raise a number of practical problems for fabrication. First, if the lateral thermal gradients are very large, differential thermal expansion will cause the wafer to warp and become non-planar. Almost all microfabrication tools assume a flat wafer. Even small deviations from flatness can cause problems. For example, a warped wafer on a vacuum spin chuck may allow small leaks in the vacuum, making spinning photoresist impossible. Or, an uneven wafer when placed in contact with the mask will fracture the substrate.

A second problem is even when lateral gradients are not so large as to cause warping, they still may be large enough to induce significant internal stress. This makes the wafer prone to fracture, and makes microfabrication immensely more difficult. For example, just pinching the wafer incorrectly at the edge with tweezers can cause the wafer to fracture along crystal planes.

As discussed in chapter 2, to avoid loss of the wafer from these problems, the lateral thermal gradients may be mitigated by ensuring uniform thermal gradients with heat sources that are large relative to the thermomigrated substrate and with thermal compensation structures. Finally, slow ramp times for the temperature both up and down are necessary. A 5 minute temperature ramp is used in this work to fabricate the gyroscope.

After thermomigration and post-processing, the wafer is then prepared for the deep reactive ion etch. Both photoresist and silicon dioxide may be used as a masking layer for the Bosch process. Photoresist is chosen because of its convenience and speed. Thick photoresist is used, Clariant AZ4620, and is spun at 1000rpm for a 17μm layer. The photoresist is then aligned, exposed, and developed in standard fashion. Because the p-type silicon etches at a different rate than the n-type silicon, alignment to the thermomigrated regions is straightforward.

If the wafer is lapped instead of etched to remove the heat damaged silicon and excess aluminum, then the thermomigrated areas are indistinguishable from the field of the wafer. In this case, a stain made of dilute HNO_3:HF:H_2O in a ratio of 5:5:90 may be used to darken the p-doped areas to allow accurate alignment.

Through-Wafer Deep Reactive Ion Etching

Because the thermomigrated wafer will be etched completely through, it is necessary to mount the thermomigrated wafer to another wafer. During the etch, some parts of the wafer will inevitably complete first. While waiting for the remaining sections to etch, the plasma will also react with whatever is below the thermomigrated wafer. Without another wafer underneath, the electrode may be etched by the plasma. To prevent this sort of damage, a second wafer is placed underneath the thermomigrated one.

The bond between these two wafers has two purposes. First, it transfers heat so that the etched wafer is adequately cooled. Second, the bond holds the two wafers together during the etch, but must cleanly release the etched wafer without damaging the mechanically fragile MEMS structures etched by the DRIE step.

For the heat exchange, it is found that any sufficiently thin material may transfer heat via conduction. As a result, the thinner this layer, the better the heat transfer. However, the thinner the layer, usually, the more difficult it is to separate the two wafers.

The second requirement, a reliable, releasable bond, took some time to identify. Typical silicon bonding techniques, such as fusion bonding, are difficult to separate afterwards, as is the intent of those techniques. Alternatively, organics may be used like a glue, such as photoresist. However, any volatiles between the two wafers, such as photoresist solvent, outgas during the etch, causing the wafers to separate. Organics without solvent, such as silicone, may be used, but many of these organics cross link when exposed to the plasma, and become difficult to remove cleanly.

In the end several non-solvent containing thermosets were found to work. Both paraffin wax and black wax work well. Paraffin is preferred, mainly because black wax is a mixture of organics, and each molecule's interaction with the plasma chamber is unknown.

To bond the two wafers, a small amount of paraffin is placed between the two wafers, and set on a hotplate to melt the paraffin. When liquefied, paraffin is quite thin, and so an extremely thin layer of paraffin may be arranged between the two wafers. The melting point of the paraffin must be less than the soft bake temperature of the photoresist, otherwise, the photoresist will reflow. For the particular paraffin chosen, the melting point is 65C. After the paraffin cools and resolidifies, the wafers are adequately bonded together for the deep reactive ion etch. To separate the wafers, a heated bath of Shipley 1112 photoresist stripper is used. The heat melts the wax, and the stripper

dissolves both the wax as well as the photoresist used to mask the thermomigrated wafer during the deep reactive ion etch.

Aluminum Thermomigrated Junction Deep Reactive Ion Etching

As discussed in chapter 3, the Bosch process etches the non-thermomigrated silicon slower than the thermomigrated silicon, at a ratio of about 2:1. This is probably due to the fact that the vapor pressure of aluminum fluoride is quite low, so the aluminum is likely sputtering off, instead of being etched. The etch probably proceeds because the ratio of Al to Si is on the order of 10^4:1 in the p-doped regions, allowing the silicon to etch around the aluminum.

To minimize this etch rate difference, RIE lag may be taken advantage of. [Jansen1997] RIE lag is mostly a geometric phenomenon where thinner trenches etch slower than wider trenches. This is mostly a function of the aspect ratio of the trenches. The bottom of a thin, high-aspect ratio trench sees a small solid angle of incoming reactive ions. The bottom of a wider, low-aspect ratio trench sees a larger solid angle of incoming reactive ions. The result is that the wider trenches etch more rapidly than the thinner ones.

To take advantage of this phenomenon the etched areas around the thermomigrated junctions have an aspect ratio of 1:1. For most of the wafer, the etch gaps are small. The minimum feature size is 15μm and trenches have 20:1 aspect ratio. However, around the thermomigrated regions, the etched region is comparatively large. At an aspect ratio of 1:1, any ion incoming at an angle of 45 degrees or less will etch the silicon. The number of ions with incoming angles larger than 45 degrees is relatively few.

So, any further increase in aspect ratio does not appreciably increase etch rates. As result, to avoid unnecessarily large areas devoted to this purpose, the areas around the thermomigrated regions have an aspect ratio of 1:1. This improves the etch rate difference, but does not completely eliminate it. For the purposes of fabricating the gyroscope, this is not a crucial issue, however for the purposes of general application of the thermomigrated junction isolation technique, this phenomenon may require more investigation.

Dicing

Dicing a wafer that contains micro-mechanical components is more problematic than that for conventional microelectronic die. At the dicing stage, most, if not all, of the components are mechanically free and due to their size, unable to withstand the forces induced during dicing with a saw. After the silicon etch, the wafer is extremely fragile and requires great care. At this point, only non-accelerative processes are possible.

To dice the devices, the deep reactive ion etch is used to almost completely separate individual die. Only small tangs in the corners of each device remain to hold the wafer together. After the deep reactive ion etch post-processing, the tangs in the corners are ablated with a laser to release each device.

The deep reactive ion etch could be used to completely separate the dice, and forgo the tang/laser ablation step. However, several steps must still be taken after deep reactive ion etch. The wafer must be separated from the paraffin wax and substrate wafer. The photoresist mask must be removed. The wafer must be cleaned. And finally, the wafer must be dried. All of these steps may be done by individual die, but this is labor

intensive, and diminishes the benefits of batch compatible processing. To preserve batch processing, a workable tang/laser ablation process is identified.

An infrared laser at 1026nm is used to ablate the remaining silicon. The parameters for the laser are shown in Table 8. The laser is manually targeted to fire at each tang, and only one or two shots are required to eliminate each tang.

Table 8 - Laser settings used to cut the tangs for dicing the wafer.

Laser Settings for Dicing	
Wavelength	1026nm
Transmission	80%

Packaging

Once the devices are diced and separated, it is necessary to package the device such that electrical connections may be made without exerting damaging mechanical forces on the die.

In this case the package also has the secondary function of providing the capacitive electrodes to sense TSM motion. For this particular purpose, the only necessary features are the electrodes themselves and spacers to set the distance between the electrodes and the TSM. Additional, optional structures are holders that position the first wafer correctly relative to the second.

The fabrication of the package begins with a glass wafer. Glass is a good dielectric that is cheap, readily available, and is easily diced. The wafer is RCA cleaned and a layer of Cr/Au is evaporated to a thickness of 500Å/3000Å. The Cr/Au is patterned using standard lithography techniques to define the capacitive sensing electrodes.

A layer of SU-8 is spun and patterned to serve to define the gap between the two electrodes of the capacitive sensor. SU-8 2 is used to define a 10μm layer. Finally, a thick, 100μm, layer of SU-8 is defined to simply hold the thermomigrated/DRIE wafer in correct alignment to the Cr/Au electrodes.

Once the thermomigrated/DRIE wafer is diced and the glass wafer is also diced, one die and one package are brought together, aligned, and bonded using a thin layer of SU-8. SU-8 2 is used to bond the two die together. The SU-8 2 is spun and pre-baked to get rid of solvent. The places where the bond is to form are exposed to UV light. The silicon die and the glass die are brought together, aligned, and contacted. Then, the silicon and glass are heated on a hotplate to crosslink the SU-8. The two die are now bonded.

Wirebonding

Wirebonding for this prototype is done directly to the lightly doped silicon. This is not an easy process and requires multiple attempts to form a reliable bond. However, it can be done. A wedge bonder is used with gold wire. It is easier to bond to the smoother side of the silicon wafer than the rough side. Finally, a number of broken die may result from the pressure exerted by the bonder.

Completed Fabrication

After the silicon die is fabricated, packaged, and wirebonded, the device is complete. A photomicrograph of the completed device is shown in figure 44. The central, cylindrical RDM can be seen. Both the rotor and the stator of the RDM reside

completely on the TSM. The TSM itself is supported by two beams at the 3 o'clock and 9 o'clock positions that allow the TSM to rotate about an in-plane axis going from east to west. Underneath the die, the gold TSM electrodes can be seen on top of the glass at noon and 6 o'clock. Finally, the wirebonds to the die edge can be seen at 3 and 9 o'clock. The two voltage-distinct regions can be seen. From the two wirebond leads on the left, a conductive path may be found from the die edge, through the left TSM beam to the TSM, and finally to outside stators of the RDM. From the right, a wirebond contacts the die frame, and is prevented from shorting by the two thermomigrated junctions above and below the wire bond. The conductive path continues through the right TSM beam and prevented from shorting through the TSM bulk by another pair of thermomigrated junctions above and below where the beam contacts the TSM. Through the eastern RDM beam, this region continues to the inside of the RDM and the rotor side of the actuators. Finally, the conductive path continues through the other 3 RDM beams that connect to the TSM. Shorting is prevented by the 3 thermomigrated junctions that lie north, west, and south of the RDM.

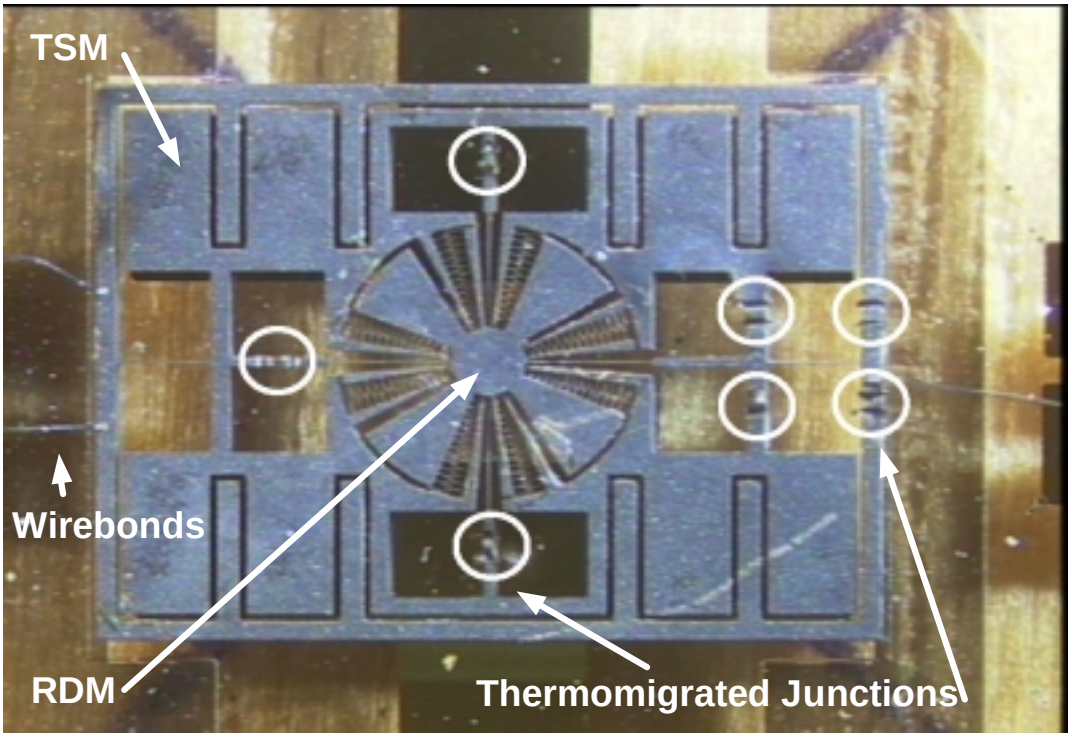

Figure 44 - Photomicrograph of fabricated, diced, packaged, and wire bonded device. The thermomigrated junctions may be seen at the noon, 3 o'clock, 6 o'clock, and 9 o'clock positions on the die. The capacitive electrodes on the package may be seen on the glass substrate at the noon and 6 o'clock positions.

SEM of the completed device is shown in figure 45. The central cylindrical RDM may be seen. Both the stator and rotor are mechanically integrated into the TSM. The 5 points at which the thermomigration is performed to define the voltage-distinct regions may be seen at the noon, 3 o'clock, 6 o'clock, and 9 o'clock positions on the die.

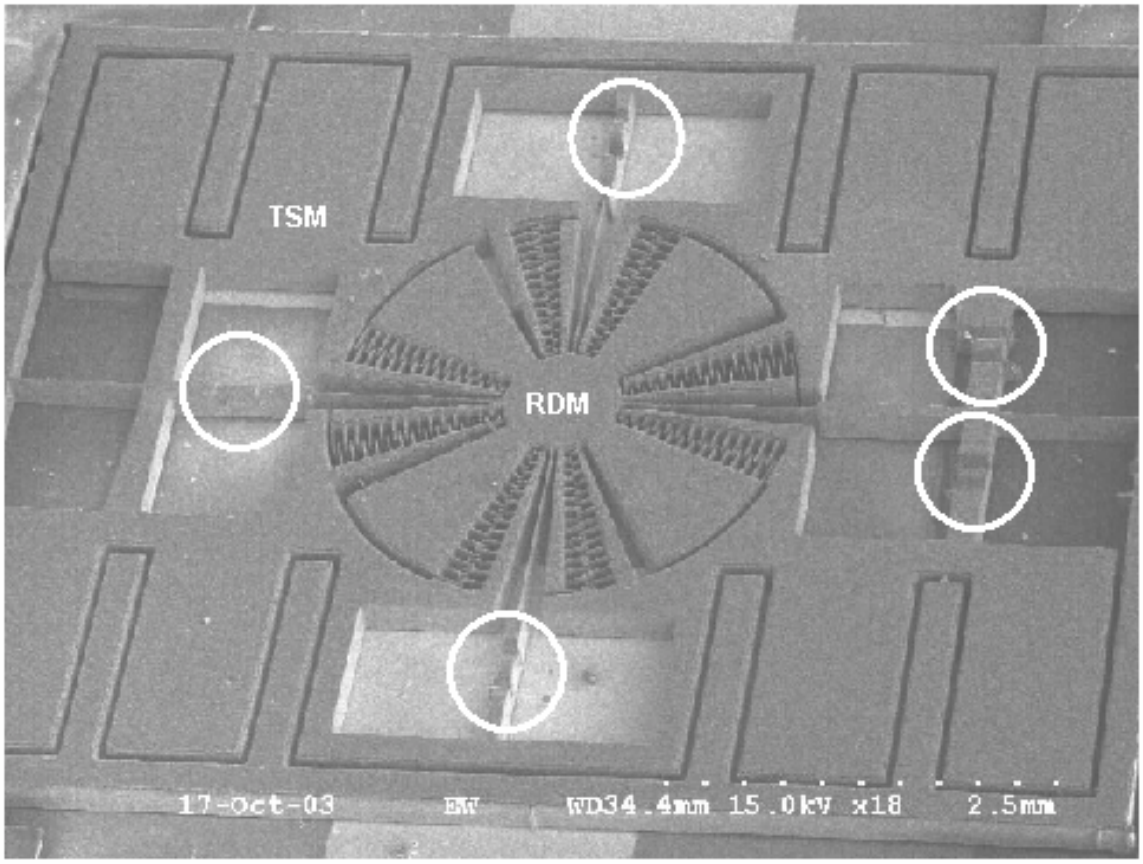

Figure 45 - SEM of the completed micro-gyroscope.

Figure 46 shows the RDM in greater magnification. The 4 springs that support the RDM and provide the restoring force may be seen at the noon, 3 o'clock, 6 o'clock, and 9 o'clock positions. The 8 comb drives are also visible.

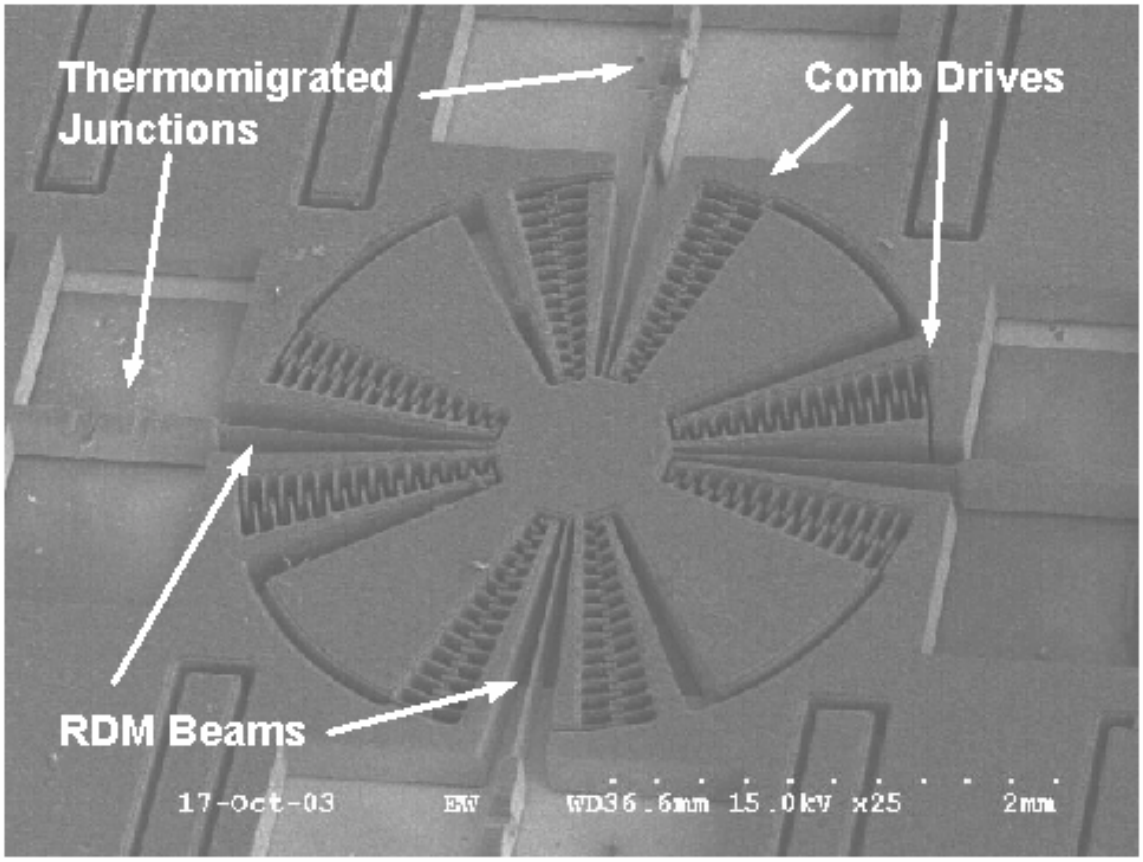

Figure 46 - SEM of the RDM. The 4 beams that support the RDM can be seen going in the north, south, east, and west directions. The 8 comb drives can also be seen.

Figure 47 shows the one set of comb drives and one beam in greater detail. All of the features are nicely defined by the deep reactive ion etching step. The tops of the combs and the beams show some roughness. This is due to "notching" or "toeing," an ion etch phenomenon. The comb fingers are underetched by about 35μm from the wafer surface.

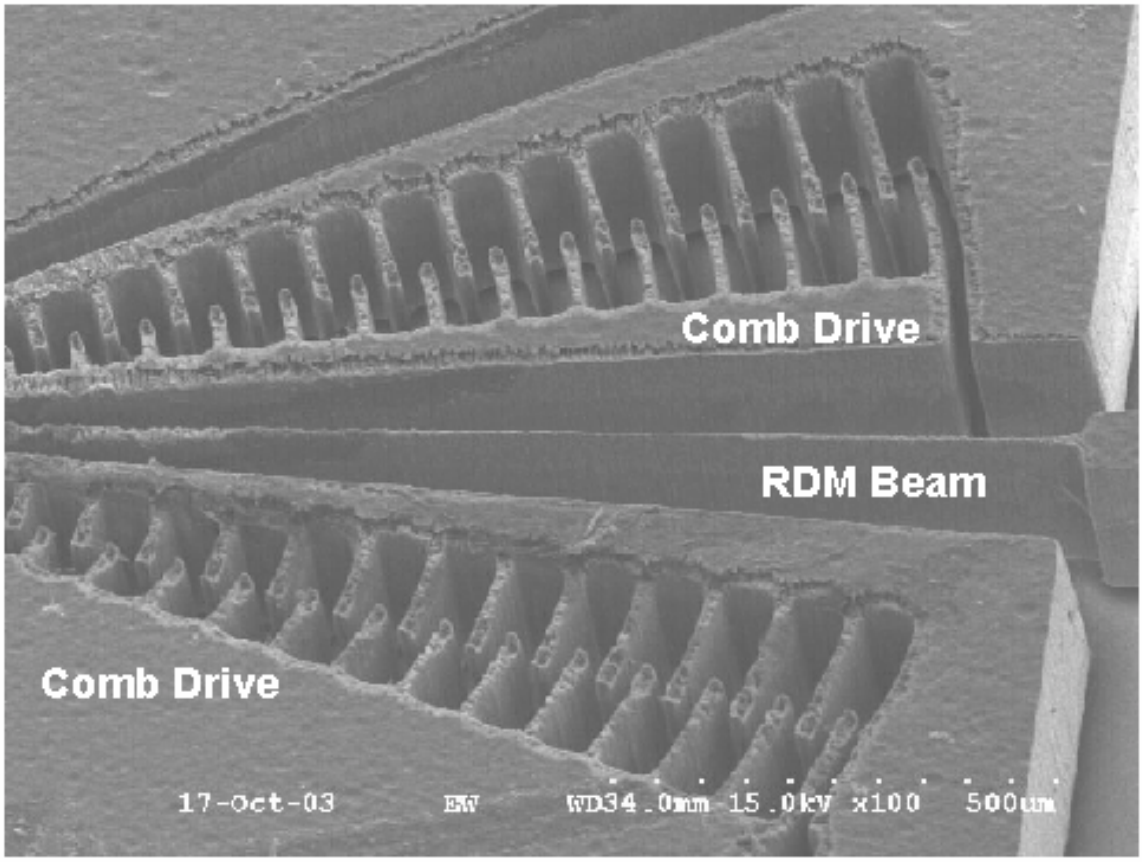

Figure 47 - SEM of one set of comb drives and one beam. The roughness on top of the comb drive and beam is due to toeing during the plasma etch.

In the ICP and plasma etching systems in general, if there is an insulating layer, then charge accumulates upon it. These charges tend to deflect the path of incoming ions, forcing them to deviate from an ideal straight path. If that insulating layer is at the bottom of a trench, for example, to function as an etch stop, then the scattered incoming ions are redirected laterally, causing lateral etching at the bottom of the trench. An illustration of toeing is shown in figure 48. A number of papers in the literature suggest methods to minimize toeing, ranging from using a conductive etch stop layer to changing the frequency of the plasma chamber. This problem is solvable, but not addressed in this thesis, since it is not essential to the fabrication of a working micro-gyroscope.

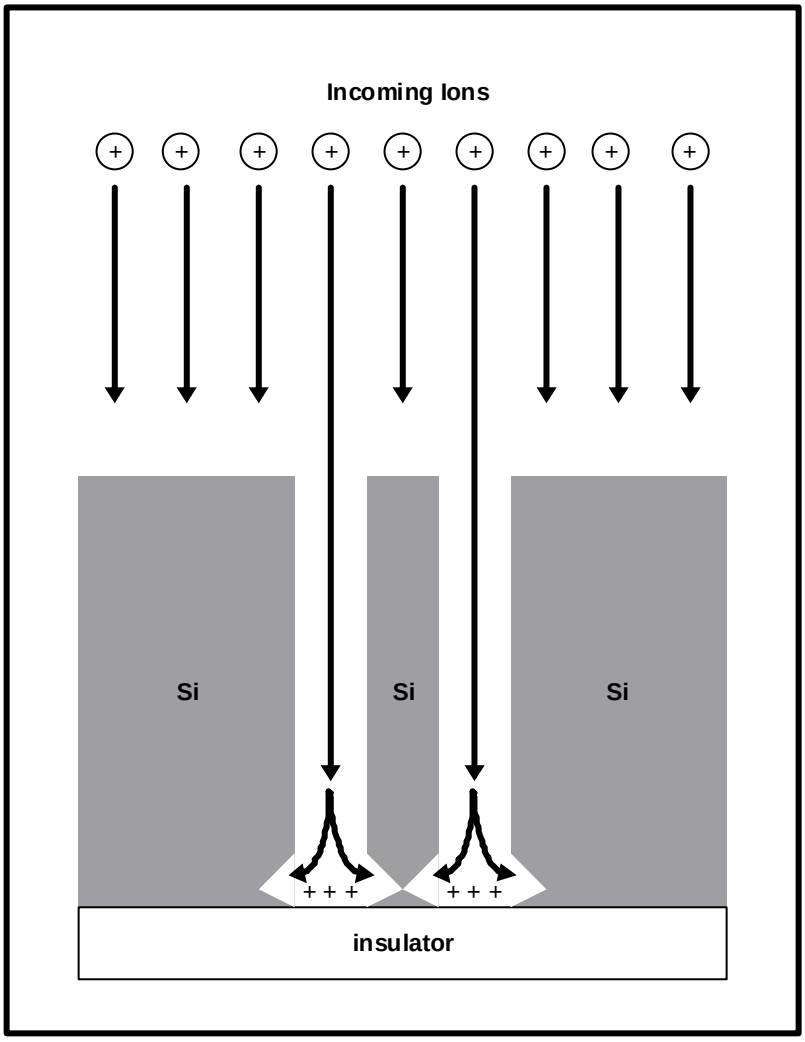

Figure 48 - Illustration of toeing or notching phenomenon in reactive ion etching.

Figure 49 shows one corner of the micro-gyroscope to show the RDM and TSM in greater detail. A thermomigration-defined electrically conductive path from the die edge to the center of the RDM can be seen. Fingers from the die edge that go into the TSM can also be seen. This is a remnant feature from attempts to integrate surface-

micromachined electrodes onto the TGZM/DRIE die, which is discussed later in this chapter.

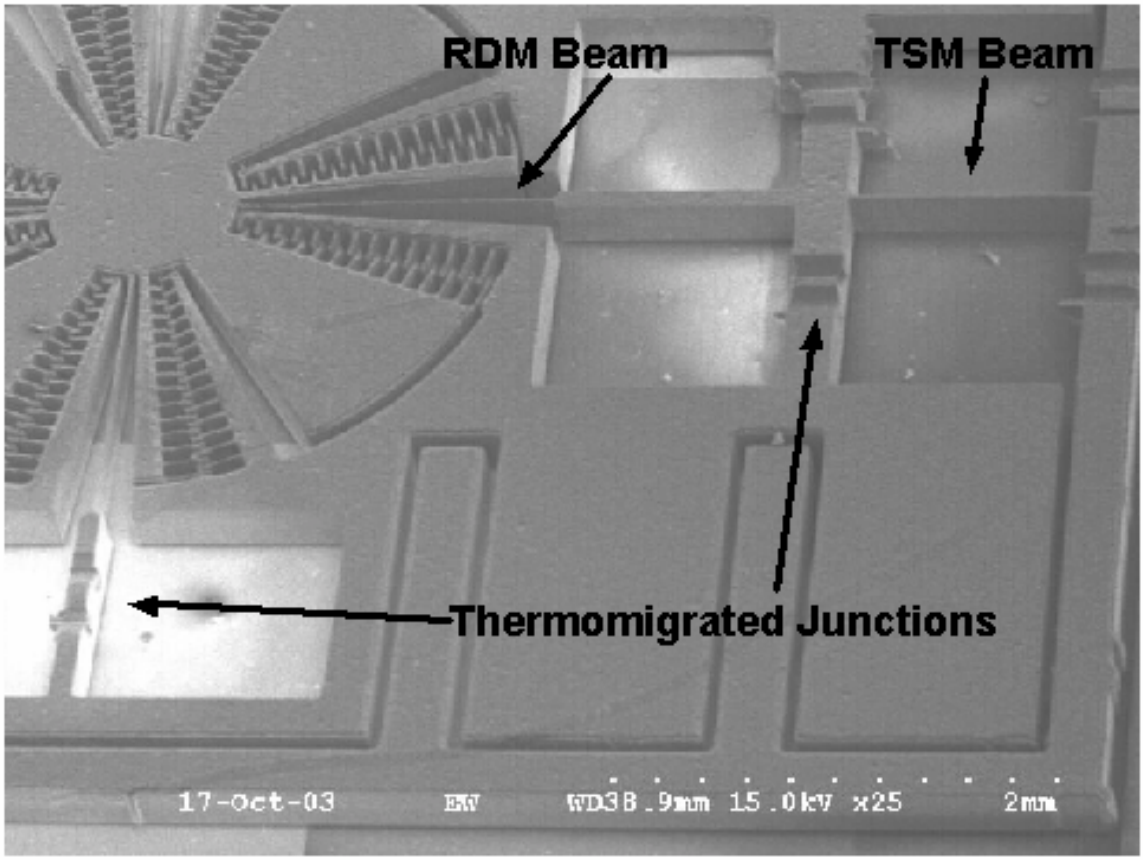

Figure 49 - SEM of one quarter of the gyroscope. The two voltage distinct regions can be seen. From the die edge, the voltage is connected to the inner part of the RDM by the TSM beam and then by the RDM beam. The voltage is prevented from connecting to the rest of the TSM by the thermomigrated junctions.

Figure 50 shows the thermomigrated regions and a wire bond in greater detail. The overhang from the differential ion etch rates of the n- and p-type silicon can be seen.

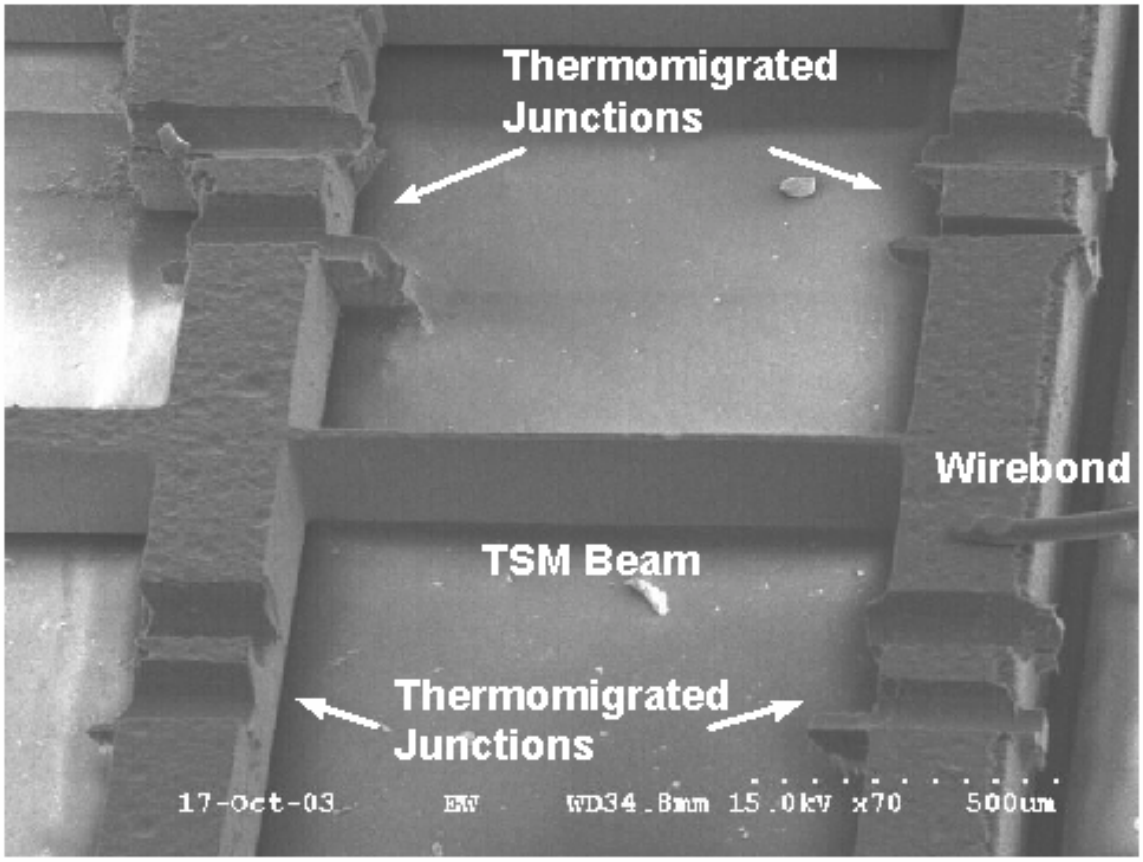

Figure 50 - SEM of thermomigrated junctions. The unetched doped silicon can be seen, extending from the junction into the removed silicon areas.

Figure 51 shows an effect of the aluminum and heat damaged silicon post-processing step for the thermomigration. The p-doped silicon is preferentially etched. This may be avoided by lapping the wafer rather than etching it. And this effect may be minimized by etching in the dark.

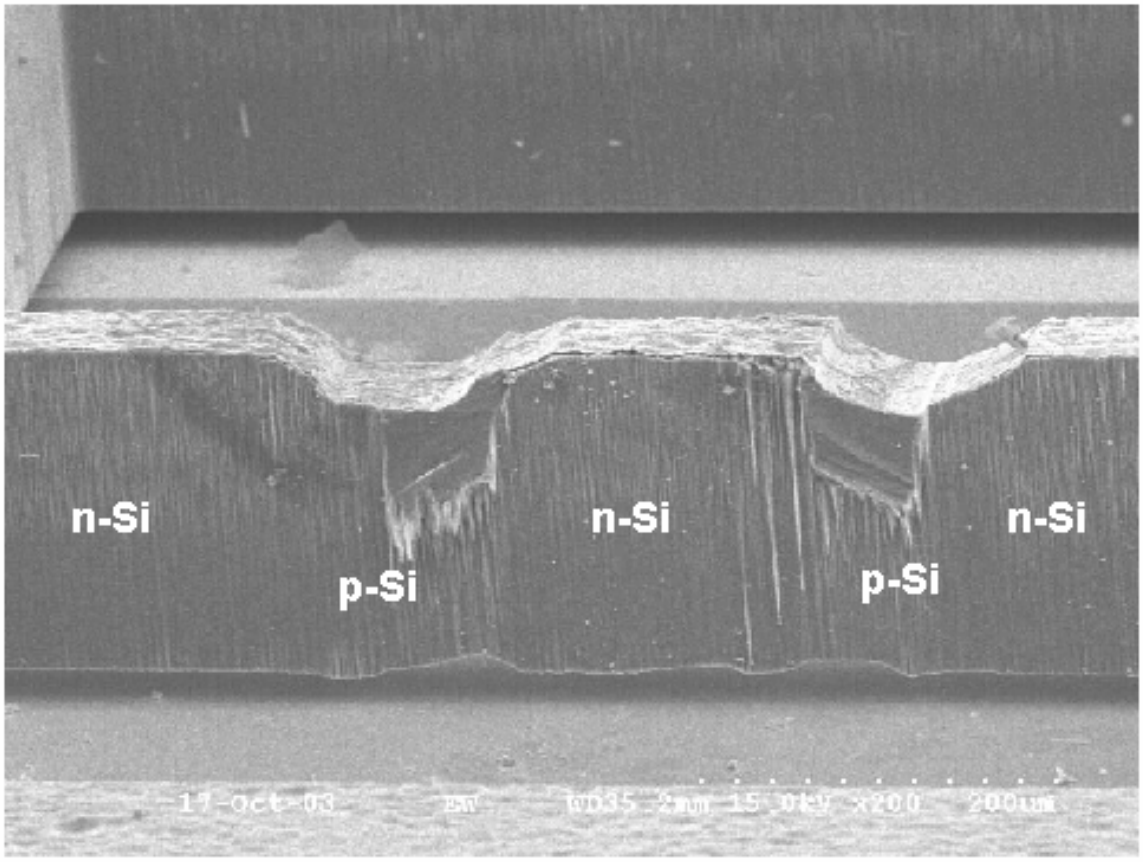

Figure 51 - Side view SEM of thermomigrated junctions. The figure shows the preferential etch of the p-type silicon.

Surface Micromachined TSM Electrodes

As an alternative to the TSM electrodes integrated into the package, a great deal of time and effort went towards the development of surface micromachined TSM electrodes. The integration of this feature would demonstrate the compatibility of thermomigration/deep reactive ion etching approach with surface-micromachining. However, because this is unnecessary towards the demonstration of the TGZM/DRIE method of fabricating MEMS, and because this reduced yields, this integration was left for the next prototyping stage.

Surface micromachined electrodes are a natural choice for fabricating the TSM electrodes, since this approach would take advantage of many of the inherent characteristics of surface micromachining. The primary argument for surface micromachined TSM electrodes is that the sensitivity of capacitive electrodes varies as the inverse of the gap distance squared between the silicon TSM and the electrodes. For surface micromachined structures, the thickness of each layer is straightforwardly controlled, since the deposition rate can be very slow. As a result, gaps less than 1μm can be easily fabricated.

In these cases, the minimum gap is usually set not by deposition method, but by other constraints, such as the necessary amplitude of motion that the gap must accommodate or the ability to sacrificially etch a thin layer for the gap.

Indeed, completed devices that incorporated all of the steps, i.e. the thermomigrated pn-junctions, the deep reactive ion etched silicon, and the surface micromachined electrodes, have been fabricated. A photomicrograph of one of the devices is shown in figure 52. Furthermore, every permutation where 2 of the 3 steps (TGZM/DRIE/Surface micromachined electrodes) were satisfactory, was seen at some point. However, a die where all three steps were working was not fabricated. The photomicrograph in figure 52 shows a device where the DRIE and surface micromachining both were satisfactory, but the pn junctions thermomigrated laterally far enough to leave undoped silicon in the electrical isolation region so that the micro-gyro was shorted.

A more thorough discussion of the surface micromachined electrodes is in the appendix F, where a copy of a paper on the subject that is currently under review is located.

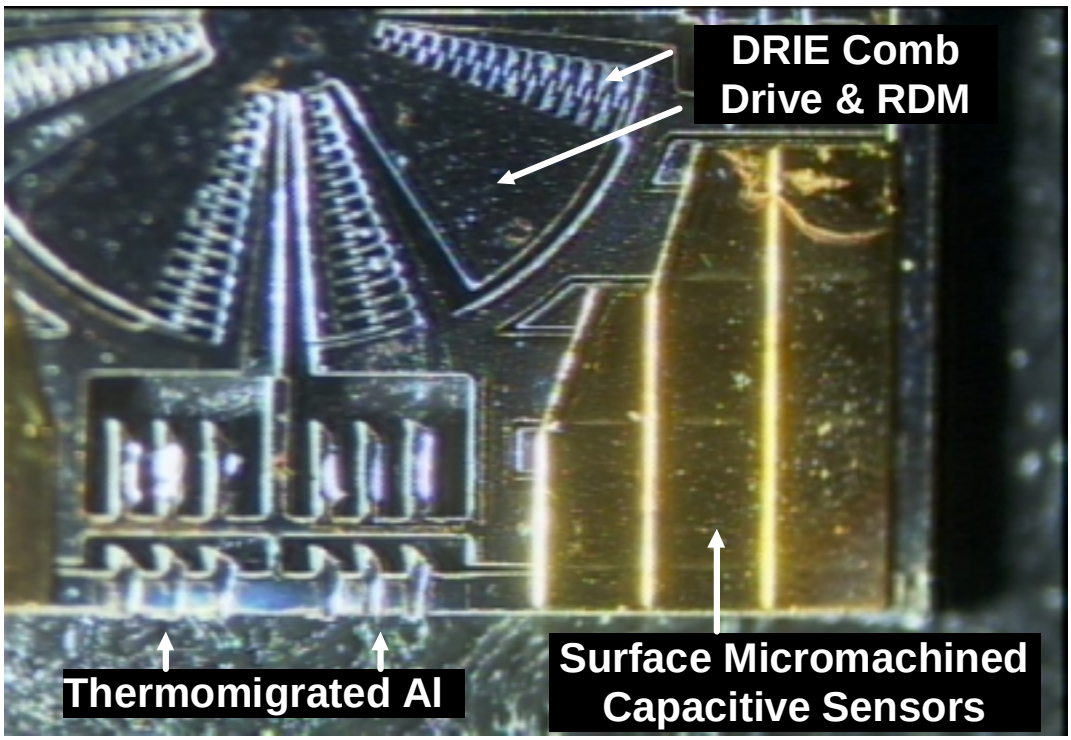

Figure 52 - Photomicrograph of a die with TGZM, DRIE, and surface micromachined structures. On this particular die, the DRIE and surface micromachined features are working. However, the RDM is shorted due to lateral thermal gradients. The thermomigrated junctions shown have displaced slightly, thus incompletely blocking current flow between the two voltage regions of the microgyroscope.

The integration of surface micromachined TSM electrodes is clearly technically feasible, and the production of a working device is simply a matter of yield. Given enough attempts, a working device would eventually be produced. However, the yields for this overall sequence of fabrication steps never rose above zero after a year of work. The most yield restrictive step is the first one, i.e. the thermomigration. The ability to

produce a sufficiently large and uniform thermal gradient for the thermomigration that is greater than approximately a 1" diameter area was not possible given the resources. Given the ability to thermomigrate 4" wafers, in my opinion, would make the integration of surface micromachined electrodes achievable is a shorter amount of time. A number of other, smaller problems also arose, and a partial list is enumerated in the "troubleshooter" section below.

Since yield drops probabilistically with each additional sequential microfabrication step. One way to increase yield, then, is to decrease the number of sequential steps. As a result, it was decided that the surface micromachined electrodes, although nice to have, were unnecessary to the demonstration of the TGZM + DRIE technique. The surface micromachined electrodes were consequently moved to the package where their fabrication could proceed in parallel, thus dividing the number of sequential fabrication procedures.

Fabrication Sequence

The final fabrication sequence for the thermomigrated gyroscope:

I. Wafer Selection and Preparation
   A. Acquire silicon wafers with the following characteristics:
   B. Type: n-type
   C. Resistivity: >1Ω-cm
   D. Quality: Prime Grade
   E. Orientation: <100>
   F. Diameter: 2". Smaller or larger wafers can be done depending on the fabrication capabilities available. 2" wafers were chosen because of the thermomigration apparatus' limits.
   G. Thickness: as needed. Standard thickness for 2" wafers is 280μm, however, thicker wafers may be used. Silicon as thick as 10,000μm (1cm) has been demonstrably thermomigrated.
   H. single side polished (double side polished are better, but are more expensive)
   I. Float zone silicon is preferred to Czochralski silicon, but not necessary, due to fewer oxygen contaminants. Professor Huber, formerly of University of Utah, now retired, surmised that blocking voltages would increase, and lateral random walk of the thermomigrated junctions is minimized with fewer oxygen contaminants.

II. Clean wafers
   A. 1st, Solvent clean: TCE/Acetone/Methanol/DI Water
   B. Followed by RCA Clean

III. Thermomigration and Post-Processing
   A. Aluminum processing
      i. Deposit >5μm of Aluminum. Electron beam evaporation, filament evaporation, and DC sputtering are all fine.
      ii. Pattern aluminum using standard photolithography. Minimum feature size demonstrated in literature is 30μm. This is a function of alignment accuracy, thermomigration time, junction depth, average temperature, thermal gradient steepness.
      iii. Etch aluminum in PAN etch. Etching through 5μm of aluminum is time consuming, and often the photoresist will begin to degrade before completion of the etch. Heat the PAN etch to 60C (according to hotplate setting) and agitate. A lot of bubbles are generated during this etch and bubbles adhered to the surface also act as a mask. Agitation removes these bubbles. Ultrasound is better than stirring.
   B. Thermomigrate. This may be done any number of ways, as long as an adequately uniform and hot temperature gradient can be established through the silicon. Here are the relevant parameters for an adapted filament evaporator:
      i. Place filament in between evaporator leads. A 50mm wide, 125μm thick, 60mm long tantalum filament was used for this purpose.
      ii. Place the silicon wafer to be thermomigrated as close as possible to the tantalum filament without touching it. Contact results in the silicon

melting. However, if the wafer is too far away, the aluminum may never thermomigrate through.

iii. Allow the cool side of the silicon wafer to trade photons with a cool body. The glass bell jar was used for these experiments, although a water cooled plate would be superior.

iv. Place a thermal compensation structure around the silicon wafer to enhance uniformity.

v. Close the bell jar around the filament and silicon wafer. Either an inert atmosphere or a vacuum can be used. For the fabricated device, a vacuum of 2μTorr was employed. At this pressure, most of the hydrogen is pumped out. Tantalum is not cheap, and hydrogen contamination of the tantalum filament makes the filament brittle, significantly shortening its lifetime.

vi. A 2000W filament evaporator. A high current/low voltage setting results in hotter filaments, and therefore faster thermomigrations. For the filament geometry used, 5V and 350A were used.

vii. Run the power through the filament for about 1.5 hours. The filament evaporator is damaged by long runs at the power and current levels used. As a result, 15 minute runs with 30 minute cool downs were employed. Cool with the bell jar vented with an inert gas, e.g. nitrogen. The heat exchange is much more efficient.

viii. One may check to see if the thermomigration of the aluminum has penetrated through the thickness of the wafer, by simply pulling the wafer out and visually checking the opposite side for aluminum

C. After thermomigration is completed, the excess aluminum and heat damaged silicon must be removed. These materials may be lapped off. However, for CMOS compatibility (the surface CMOS structures would get lapped off), an etch is used. A solution of HF:HNO3:H2O was used in a ratio of 15:35:50. The wafer is etched for 2 minutes. This etches aluminum very quickly and preferentially etches silicon doped in excess of $10^{19}cm^{-3}$. The difference in etch rate may be varied by changing the etchant ratio. [Runyan&Bean1994a] Chromium may be used to mask this etch to protect other features, such as CMOS devices.

IV. ICP/Bosch Process silicon Etching

A. Pre-Processing

i. Prepare photoresist mask for ICP etching.
   1. Photoresist: AZ4620
   2. Spin: 1000rpm/30s
   3. Rest: 5 minutes
   4. Bake at 105C for 8 minutes
   5. Expose: $5mW/cm^2$@365nm for 8 minutes
   6. Develop in AZ400K diluted 3:1 for ~3 minutes

ii. Mount 2” wafer to 4” for ICP etching
   1. spin photoresist mask on 4” substrate wafer and hard bake
   2. bond 4” and 2” wafers using melted paraffin wax (melts at 50C)

B. Etch in ICP/Bosch Process chamber

1. Temperature: 15C
2. Pressure: 10mTorr
3. Power1: 800W
4. Power2:
5. Gas Flows
   A. For deposition: 50sccm C_4F_8/40sccm Ar
   B. For etch A: 50sccm SF_6/50sccm Ar
   C. For etch B: 100sccm SF_6/50sccm Ar
6. Etch times
   A. For deposition: 3s
   B. For Etch A: 2s
   C. For Etch B: 8s
7. Total number of cycles: ~600

C. Post process:
   i. Remove photoresist and paraffin using photoresist stripper Shipley 1112 heated to 70C (according to hotplate setting).
   ii. Rinse in DI H_2O.

V. Dicing
   A. Dice wafers using IR Laser, which has low mechanical energy transfer. A dicing saw destroys the fragile mechanical structures
      i. Wavelength: 1026nm
      ii. Reflectivity: Transmission=20:80
      iii. Slew rate: 0.75mm/s
      iv. Pulse/s: 1000
      v. Pulses: 100
   B. Optional: remove excess thermomigrated silicon. The heavily doped thermomigrated silicon etches slower than the lightly doped n-type silicon. Removing the excess thermomigrated silicon increases breakdown voltage some.
      i. Use the same conditions as above
      ii. Use laser to blast off excess thermomigrated silicon

VI. Packaging and Wire Bonding
   A. Package Fabrication
      i. Use a glass wafer. Silicon wafers with oxide do not work, since the high voltages will breakdown through the oxide and the current will pass through the silicon
      ii. Clean with solvent and RCA clean
      iii. Dehydrate: 10 minutes at 120 degree oven
      iv. Deposit Cr/Au at a thickness of 100Å/3000Å.
      v. Pattern TSM electrodes using standard lithography
      vi. Spin SU-8 15 on wafer at 3000rpm for 10μm thick standoffs
      vii. Bake 100C, 1hour. Ramp from room temperature.
      viii. Expose: 50s@20mW/cm^2
      ix. Postbake: 90C for 4h.
      x. Filament evaporation of 500Å of Cr- this step is to protect unexposed SU-8 from further crosslinking and facilitate alignment

xi. Spin SU-8 25 1000rpm for structures that hold silicon device
xii. Bake: 90C for 1h. Ramp from room temperature.
xiii. Expose: 50s@20mW/cm^2
xiv. Develop all SU-8 in PGMEA
xv. Dice into separate packages using saw. Protect structures with photoresist before dicing.
xvi. Rinse each individual package.

B. Attachment
   i. Use SU-8 2 for adhesive
   ii. Swab a small amount of SU-8 2 on contact area
   iii. Expose to release acid in the chemically amplified SU-8 resist
   iv. Place silicon die
   v. Bake to crosslink SU-8 2 epoxy.

C. WireBonding
   i. Direct wirebonding to silicon is possible. It's not easy, but can be done with patience. Reza Abdovold in Farrokh Ayazi's group is "da man" when it comes to doing this. There is a small Schottky diode that is broken down due to the high voltages used. The right way to do this is the following: heavily N+ dope contact region then cover with Cr/Au contacts. Wirebond to the Au. Be careful that the deposited metal does not short the thermomigrated junctions. A shadow mask can be used to protect these areas.

VII. Optional: Surface micromachined TSM electrodes. This step goes after the thermomigration and before the DRIE.

A. Clean surface with RCA clean. This is unnecessary if the next step immediately follows the Al/Si etching.

B. Optional: Deposit Cr adhesion layer. Use shadowmask to prevent Cr shorting thermomigrated junction areas.

C. SU-8 standoff and sacrificial layer processing.
   i. HMDS adhesion promoter may be useful here.
   ii. Spin SU-8 15. 3000rpm, 30s. 15μm final thickness.
   iii. Bake 100C, 1hour. Ramp from room temperature.
   iv. Expose: 50s@20mW/cm^2
   v. Postbake: 90C for 4h.

D. Filament evaporate Cr/Cu/Cr at 500Å/2500Å/500Å to protect uncrosslinked SU-8 sacrificial layer from further exposure and to provide seed layer for electroplating. Must use filament evaporator. Electron beam evaporation and DC sputtering will crosslink unexposed SU-8.

E. Photoresist electroplating mold processing.
   i. Photoresist: AZ4620
   ii. Spin: 1000rpm/30s
   iii. Rest: 5 minutes
   iv. Bake at 105C for 8 minutes
   v. Expose: 5mW/cm^2@365nm for 8 minutes
   vi. Develop in AZ400K diluted 3:1 for ~3 minutes

F. Dissolve protective layer of Cr with dilute HCl, diluted 3:1. Initiate dissolution with by touching Cr with a small piece of aluminum foil. Rinse in DI H_2O and immediately begin electroplating.
G. Electroplate in NiFe bath
   i. Bath Composition
      1. $NiSO_4$-$6H_2O$ – 200g/L
      2. $FeSO_4$-$7H_2O$ – 8g/L
      3. $NiCl_2$-$6H_2O$ – 5g/L
      4. H_3BO_3 – 25g/L
      5. Saccharin – 3g/L
      6. Sodium Laurel Sulfate – 0.25g/L
   ii. current density: 10mA/cm^2
H. Simultaneously remove uncrosslinked SU-8, photoresist, and seed layers using Shipley 1112 photoresist stripper for about 25 minutes (10 minutes with agitation). At the beginning, do a quick dip in an ultrasound bath to breakup the seed layer. (Each layer may be removed individually with acetone/methanol for photoresist, NH_4OH + $CuSO_4$ for copper, dilute HCl for Cr, and PGMEA for the uncrosslinked SU-8)

Fabrication Troubleshooter

- Thermomigration Challenges
    - The yield of the thermomigration step is low. This is mostly due to the fact that the thermomigratable area is small, often only accommodating 4-6 devices per wafer. Solution: a number of solutions were discussed in Chapter 2. A longer term solution is to increase the thermomigration area; however this requires significant time and money invested in getting a dedicated thermomigration tool up and running.
    - Wafers may incompletely thermomigrate, thus the voltage distinct regions are shorted. Solution: always check the wafer's opposite face to see if the aluminum has penetrated through. It is possible to thermomigrate longer without adversely affecting the process. However, the aluminum thermomigration will have some degree of non-uniformity, and some regions will thermomigrate through before others. The ones that thermomigrate first, the aluminum will pool and spread on the surface while waiting for the other regions to thermomigrate completely. So the decision of when to stop is somewhat of a judgment call.
    - pn junctions may laterally thermomigrate to some degree leaving some corner of the silicon in the junction isolation region unaffected and the device become shorted. Solution: thermal compensation ring, and increasing the thermomigrated area.

- Wafers may emerge from the thermomigration step with too much heat induced internal stress. At some point during the fabrication sequence, the wafers break. Solution: uniformly and slowly heating the silicon wafer.
- Wafers emerge from the thermomigration step slightly warped, making photolithography of the smallest features impossible. Solution: uniformly and slowly heating silicon wafer.
- pn junctions may have inadequate blocking voltages due to lateral thermomigration. Angled pn junctions have lower blocking voltages. Solution: thermal compensation ring, increase thermomigration area.
- pn junctions may have inadequate blocking voltages due to incomplete removal of excess aluminum and heat damage silicon. Solution: Overetch this step to insure complete removal. Drawback: this will thin the bulk silicon of the device, resulting in lower angular momentum generated by the RDM.
- pn junctions may have inadequate blocking voltages due to over-doped n-type silicon. Solution: check the resistivity and doping-type of the wafers upon receipt with 4-point probe. A package of 25 wafers labeled 1ohm-cm resistivity measured to have 0.0001 ohm-cm sensitivity, resulting in very low blocking voltages. This was discovered after 2 months of fabrication…

- Deep reactive ion etching challenges:

- The wafer may be underetched through the wafer, such that the moving parts would be unreleased. Solution: inspect wafer before debonding wafer from substrate and check whether or not to continue etch. Drawback: Non-uniform etching may result in some areas underetching while other area overetching. This becomes a judgment call as to the optimum time to stop the etch. Also, visual inspection of 20:1 aspect ratio trenches (300μm deep x 15μm wide) of every finger of every drive is often difficult, time consuming and patience demanding.
- The wafer may be overetched. The TSM or RDM beams would be so thin that they would break. Solution/drawback: similar to the underetching point above, i.e. always time the initial etch to slightly underetch so that the status can be checked as the etch nears completion.
- The bonding of the thermomigrated wafer to the second wafer would fail during the etch, causing inefficient heat transfer and uneven etching. Solution: use bonding materials free of solvents. Black wax, vacuum grease, thermal grease, paraffin wax, and crystal bond avoided de-bonding during etch.
- Bonding material cross-links, making complete removal impossible. Solution: use materials unlikely to cross-link. Paraffin wax works well, and removes easily. A second solution is to put a layer of photoresist between the thermomigrated wafer and the bonding material.

However, the solvent in the photoresist must be completely baked out. One way to do this with the photoresist sandwiched between two wafers is to "paint" with a q-tip type brush passages in the photoresist for the solvent to escape. The photoresist removes easily.

- Release of the thermomigrated wafer from the substrate wafer breaks the thermomigrated wafer. Solution: be patient and use non-accelerative processes. Debonding at this step emphasized processes such as dissolution and heating. Paraffin wax dissolves and melts in heated Shipley 1112 photoresist remover. Black wax, vacuum grease, and thermal grease remove well in TCE, although no method for removing cross-linked material has been identified.
- Drying of the wafer broke the fragile mechanical components. Solution: do not dry with nitrogen gun! (duh). Rinse gently and dry in oven.
- ICP performance is inconsistent, usually after maintenance of the tool. Drastic changes in the ICP behavior would result in the destruction of the wafer. Solution: always run a test wafer immediately before etching the wafer in which 4 weeks of work has already been invested. Drawback: this solution requires uninterrupted time on the ICP.
- Numerous problems with cleanroom policy, ICP availability, ICP consistency, and user courtesy affected yields from this shared tool. Solution: no known solution found. This seems to be the nature of the necessity of sharing a $600,000 tool.

- Surface Micromachining Challenges
    - Adhesion of the surface micromachined structures to the silicon is poor due inadequate cleaning of the silicon wafer. Solution: Do the RCA clean (organic step only) and dehydrate the surface. Drawback: no real drawback. This is more time consuming than a simple solvent clean, but you can either choose to save an hour by doing the solvent clean instead of the RCA clean, or save a month by not losing the wafer to poor adhesion. Note: piranha etch is better than solvent clean, but vastly inferior to the organic step of the RCA clean.
    - Poor adhesion due to the temperature/length of the baking of the epoxy. Solution: Independently check the temperature of the hotplate with a thermometer/thermocouple. Always use a timer. Once you find a set of parameters that works, do not change it.
    - Poor adhesion due to inadequate UV exposure of the SU-8. Solution: independently check the intensity of the UV source before exposure.
    - Poor adhesion due to overdevelopment of the SU-8. Solution: Dilute developing solution, agitate lightly (do not ultrasound), and monitor the development continuously.
    - Blistering of the uncrosslinked SU-8 sacrificial layer during electroplating. This problem occurred intermittently. A solution was never found. Seems to be a function of immersion time. One possible solution is to increase electrodeposition rate to minimize this time.

- Loss of adhesion of electroplated metal to SU-8. Solution: deposit Cr/Cu/Cr seed layer for the electroplating as quickly as possible after SU-8 processing.
- "Wrinkling" of the uncrosslinked SU-8 during photoresist softbake. Solution: long SU-8 post bake and minimize the area of continuous regions of uncrosslinked SU-8.
- Inadequate removal of uncrosslinked SU-8 sacrificial layer. This leaves SU-8 between the silicon and the TSM electrode, which prevents TSM motion. Solution: Long removal times with agitation (stirring or ultrasound) of uncrosslinked SU-8 in solvent. This solution is mutually-exclusive to the overdevelopment problem. A second solution: introduce holes in the upper electrode to allow solvent to transport into the uncrosslinked SU-8. This also increases the Q-factor of the TSM due to reduced squeezed film damping.

Chapter 6

Characterization of the Angular Rate Sensor

After the development of the thermomigrated junction isolation technology and the design/simulation/fabrication of the device, the final step is the measurement of the micro-gyroscope's characteristics as an operating sensor.

For the purposes of this thesis, the following tests are applied. First, the electrical characteristics of the device are tested. In particular, the I-V characteristics of the junction isolation of the completed device is measured. Second, electro-mechanical behavior is tested. The primary question here is whether or not input power results in actuated motion of the RDM, and whether or not deflection of the TSM results in the expected capacitance change. Third, the mechanical behavior of the device is characterized. The primary question at this stage is whether or not the mechanical resonances of the device are at the correct frequencies and in the correct modes, and whether or not there is proper energy transfer from the RDM to TSM.

Finally, the performance of the sensor is measured. The two primary questions the gyroscope's response to angular rate, and its noise characteristics.

Electrical Measurements

The microgyroscope is a four terminal device. A photomicrograph of the completed, packaged, and wirebonded sensor is shown in figure 53. The four contacts for the terminals can be seen on the north, south, east, and west sides of the package.

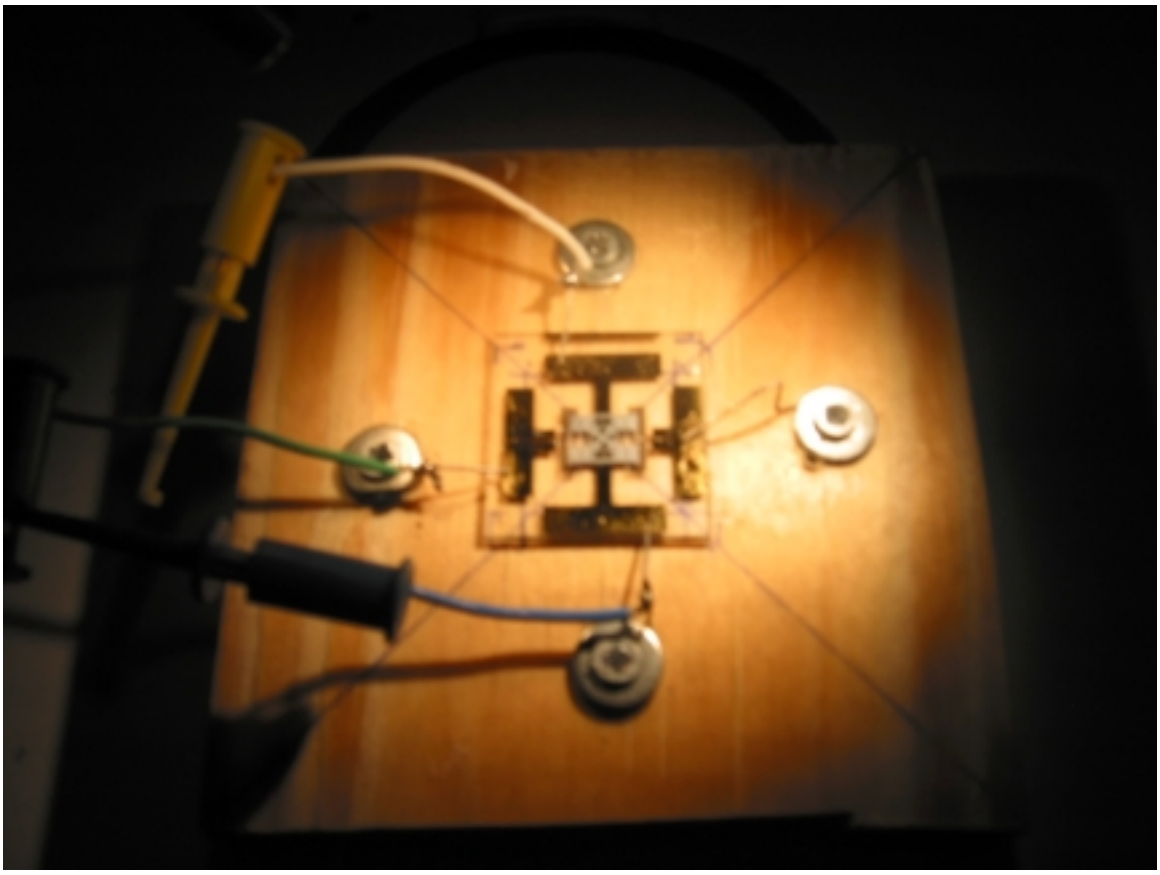

Figure 53 - Photograph of the completed device. Note the 4 contacts for this 2 port device.

Figure 54 shows an electrical schematic for the testing. The input terminal, P1, is a power signal that drives the RDM. It is electrically connected to the interior, i.e. rotor, of the RDM. The GND connection is electrically connected to the TSM and the exterior, i.e. the stator, of the RDM. The output terminal is connected to the capacitive electrodes

that measure the TSM motion. The capacitance is measured across C1 & GND and across C2 & GND.

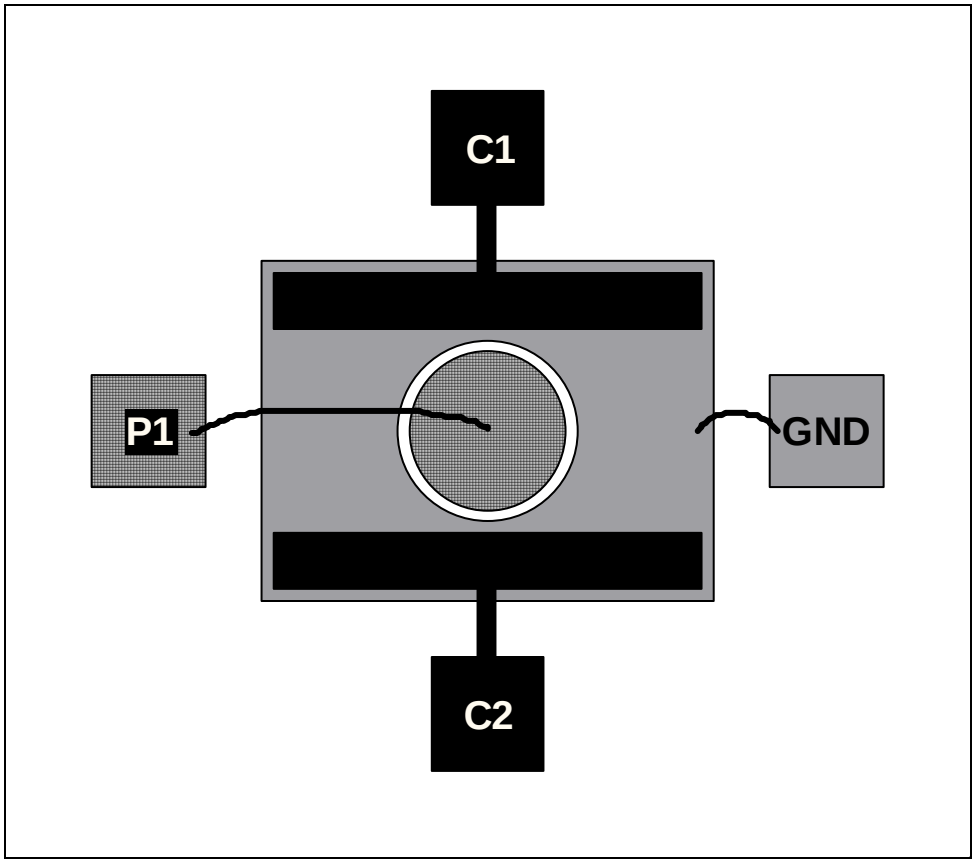

Figure 54 - Electrical schematic for the packaged device. The drive voltage has one contact, P1. The differential capacitive measurements are taken at contacts C1 and C2. There is a common ground for the P1, C1, and C2 points.

Application of a Keithley 3322 LCZ multimeter across the GND and output terminal, C1, measures a capacitive load of 5.0pF. Across the GND and C2 terminal, a capacitive load of 7.6pF. Between terminals C1 and C2, there is a capacitive load of 2.9pF. And finally, between the input power P1 and GND, a resistive load of 21MΩ.

The electrical characteristics of the junction isolation is characterized, and the I-V curve is shown in figure 55. The breakdown voltage of the junction isolation is

approximately -400V on one side and +350V on the other. The leakage current is on the order of 0.2μA. The equivalent resistance of the junction at breakdown is about 2GΩ. In comparison, the nearly vertical line that looks superimposed on the y-axis is the resistance of the silicon without junction isolation, and has a resistance of about 2kΩ.

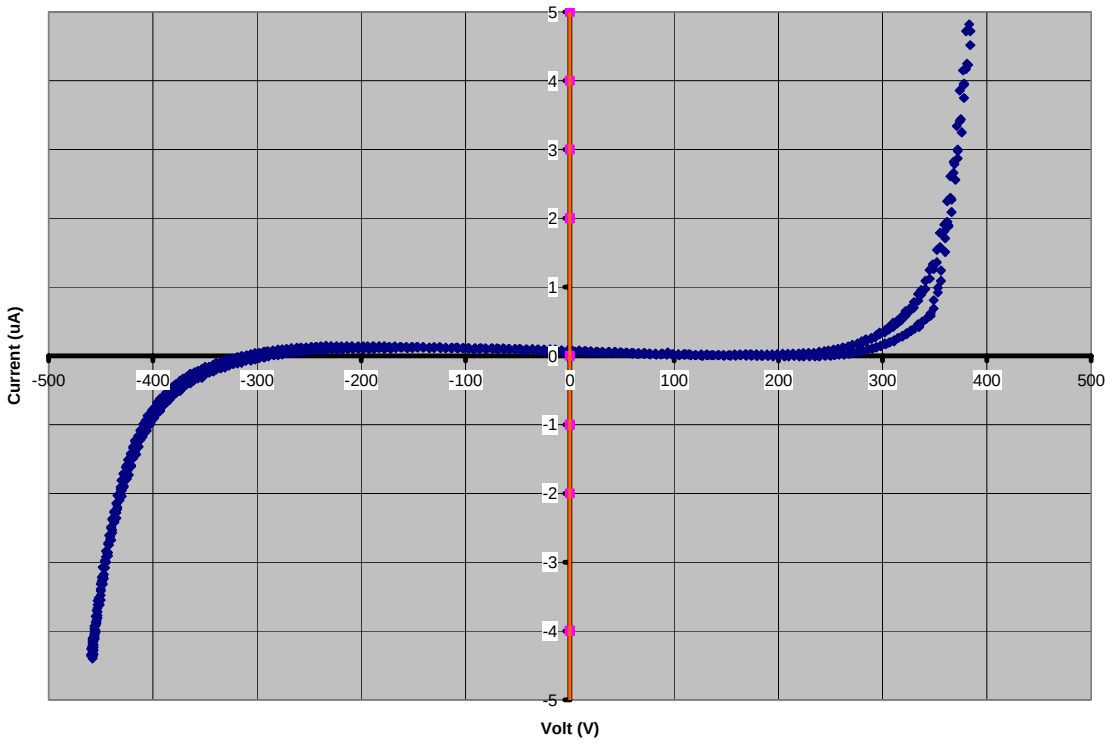

Figure 55 - I-V curve of the electrical isolation for the completed micro-gyroscope. Blocking voltages are in excess of 350V. In comparison, the nearly vertical line overlaying the y-axis is the resistance seen by two points on the silicon without an intervening npn junction.

Electro-Mechanical Tests

Once the device is known to be electrically sound, the basic electro-mechanical tests are applied. The two electro-mechanical elements are the RDM actuator and the TSM sense electrodes.

RDM Electromechanical Measurements

To test the RDM actuators, a voltage is applied across the GND and P1 terminals. The voltage is an AC signal generated by a HP33120A function generator. The signal has an amplitude of 250mV and a DC offset of 125mV. The AC signal is offset so that the signal is not frequency doubled by the electrostatic actuator. After the DC offset is added, this signal is amplified by a Trek 50/750 amplifier, which boosts the amplitude by a factor of 300, producing a 75Vpp sinusoidal wave. Higher voltages could be applied given that the blocking voltages of the pn junctions are over 350V. However, this voltage is adequate for conducting the RDM drive electromechanical tests without excessively risking the device in case of a catastrophic short.

The function generator is set to sweep the frequency from 100Hz to 2500Hz in a span of 1minute. While the signal is being swept, the RDM is monitored optically through a microscope. Within this frequency span, one resonance mode for the RDM is noted at 1806Hz. The maximum amplitude of the RDM displacement is approximately 25μm at 1.5mm. This corresponds to an angular displacement of approximately 1 degree.

TSM Electromechanical Measurements

To test the electromechanical function of the TSM, the readout electronics were connected to the GND and ports C1 and C2. The TSM was then deflected manually using a probe tip.

The Readout Electronics

The capacitive output of the gyro is translated into a voltage by electronics designed by Joe Scoppotuolo of MilliSensor Systems and Actuators. A schematic of the electronics are shown in appendix D. The readout circuit has several interesting features to improve sensitivity and signal-to-noise ratio. First, the electronics take a differential measurement of the change in capacitance between the two capacitive plates to improve sensitivity. Second, the electronics use a bandwidth narrowing technique to improve the signal-to-noise ratio.

A differential detection scheme is one where the difference between two measurands, as opposed to the absolute value of each measurand, is sensed. This scheme has a number of advantages. First, since the RDM motion is rotational, it is known a priori that if the TSM is moving properly, then the capacitance on one side increases while decreasing on the other side. As a result, taking the difference in displacement currents effectively doubles the displacement current and therefore doubles the input signal to the electronics.

In addition, the differential detection scheme can distinguish between rotations and translations. If the TSM translates, then the capacitance on each side changes the same amount, therefore canceling, to first order, the input signal to the electronics. This allows the electronics to reject any translational z-direction accelerations that the micro-gyroscope may experience. If the TSM rotates, then the input, as discussed above, adds and a stronger signal is detected.

A second feature of the read out electronics is that it employs a bandwidth narrowing technique to increase the signal to noise ratio. A 333kHz, $7V_{rms}$ signal is fed into the capacitive plates via the GND connection, and the resultant displacement

currents across the TSM capacitors are inputted into the readout electronics. This scheme transforms the detected signal into an AM modulation of the 333kHz signal. Since the signal is now known to be at 333kHz, a great deal of noise may be rejected by simply filtering out all other frequencies. A *Mathematica* simulation of the signal and its expected modulation by the capacitive plate motion is in appendix G. The expected displacement current is on the order of 10μA and the AM modulation of that signal is expected to be on the order of $10 \pm 0.5\mu A$.

The bandwidth narrowing scheme has a second advantage in that the displacement current is a linear function of frequency. By boosting the signal frequency from 2kHz to 333kHz, an increase in displacement current amplitude of approximately 150:1 is gained.

The treatment of the signal by the circuit is as follows. First the two displacement currents are fed into each input side of a 1:1 transformer. The input side is center tapped to ground. This is where the subtraction of the displacement currents, i.e. the differential measurement occurs. If the two currents entering each side of the transformer are equal, then they cancel. However, if one current is entering while the other is exiting, the total current through the transformer is doubled.

The output port of the transformer is first connected to a differential amplifier, then passed on to a 10:1 amplification stage, and next, a 40:1 amplification stage. After this amplification, the signal is fed into a mixer, which demodulates the 2kHz mechanical signal off the 333kHz carrier wave. The signal then passes through an active filter to further eliminate noise, and then amplified through a 2.5:1 amplifier. Finally, the signal is passed through an output buffer to drive any electronics that may come afterwards.

The overall amplification from the amplifier stages is 1000:1. The supply voltage is ±15V. The capacitance to voltage transfer function for the readout electronics is measured using capacitance decade boxes connected to the inputs of the electronics. The overall transfer function is sigmoidal, but this over a range of hundreds of picofarads. Around zero capacitance difference, the curve is quite linear, and the slope measures to be 6.16V/pF.

TSM Electromechanical Test

To test the electromechanical function of the TSM, a 333kHz signal is fed into the GND port of the device. The C1 and C2 ports are then connected to the inputs to the subtracting transformer. The input power terminal, P1, is left unconnected. The TSM was then deflected manually using a probe tip. A schematic of the test is shown in figure 56.

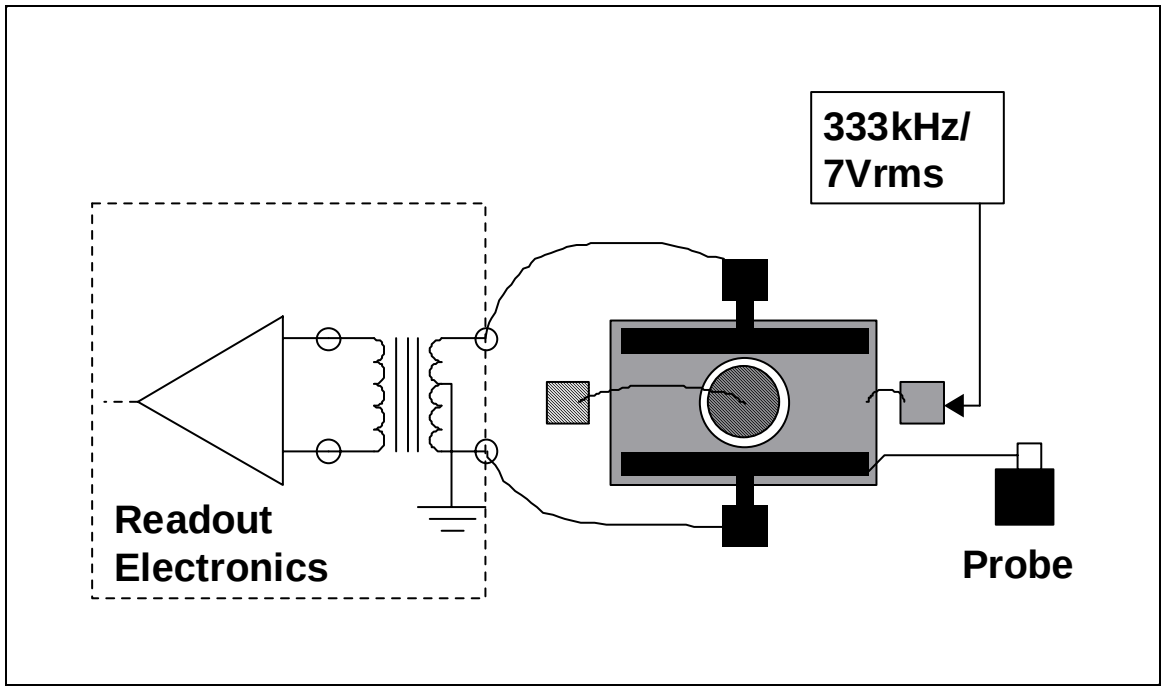

Figure 56 - Schematic of the connection between the gyroscope and the readout electronics for TSM motion detection.

The output of the readout electronics is connected to an oscilloscope. Setting the oscilloscope to 0.1V/div, the output of the readout electronics could be seen to move up and down with the deflection of the TSM. Nearly full deflection resulted in an output voltage shift of approximately 0.5V. Full deflection is not possible, since at full deflection the two capacitor plates contact which causes a short.

Mechanical Spectrum

Once an operating gyroscope is found to be electrically and electro-mechanically functional, the mechanical spectrum of the device is measured. For this measurement, the RDM is driven and the TSM motion is sensed.

A picture of the test setup is shown in figure 61. A schematic of the test setup is shown in figure 57.

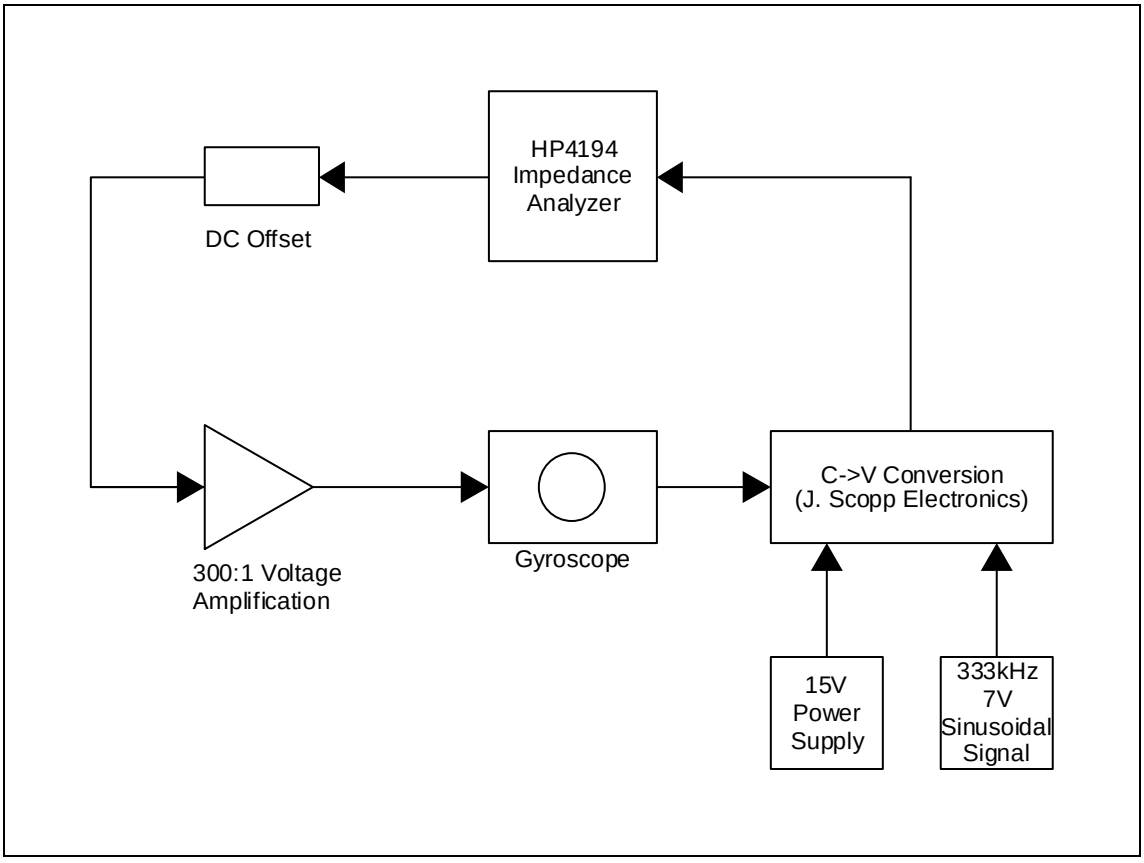

Figure 57 - Schematic of the test setup to measure the mechanical spectrum of the gyroscope.

The gyro is driven by a Trek 50/750 high voltage amplifier, which in turn, is driven by an HP 4194 impedance analyzer with a DC offset to prevent frequency doubling of the frequency at the electrostatic actuators. The impedance analyzer operates in gain-phase mode and sweeps the frequency with an output of 0.25V. The response is detected at the same frequency at the impedance analyzer's outputs. The capacitive output of the gyro is translated into an electrical voltage by the readout electronics discussed above. After conversion, the signal is fed into the input of the impedance

analyzer, which outputs the impedance response as a function of frequency. The spectrum is shown in figure 58.

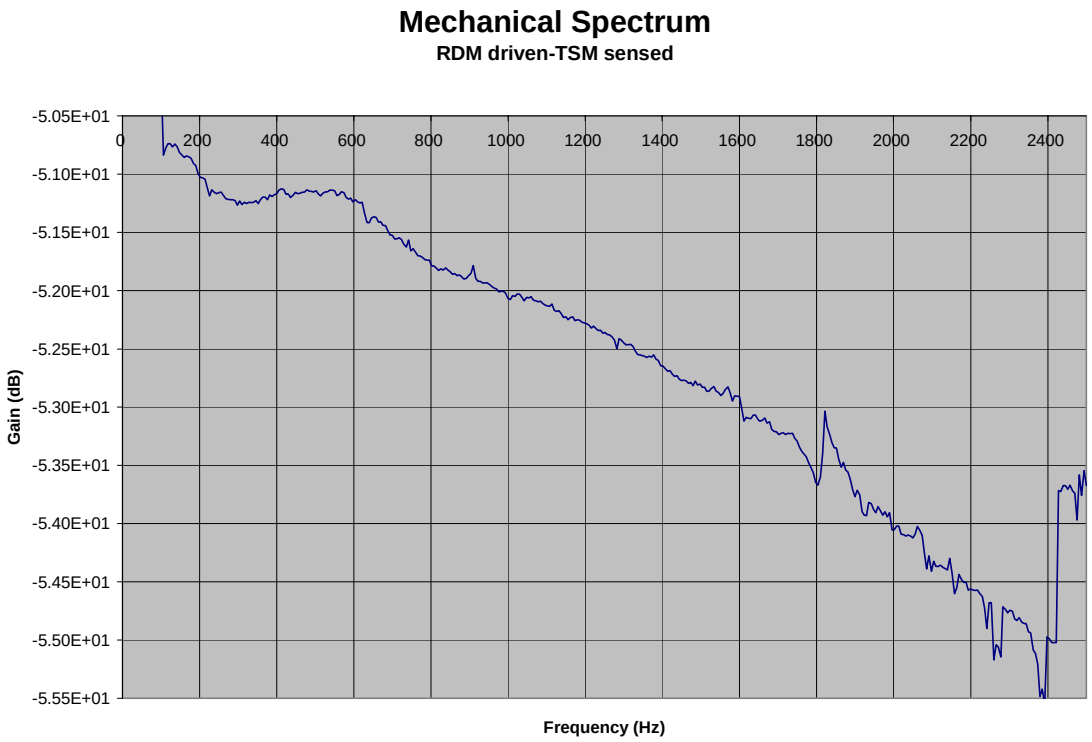

Figure 58 - Mechanical spectrum of the micro-gyroscope. There are two detected resonance peaks. One is for the TSM at approximately 400Hz and the other is for the RDM at approximately 1800Hz.

The motion of both the RDM and TSM can be seen on this spectrum. The broad peak at 400Hz is the TSM motion. The Q for the peak is 2. This peak has a low Q which may be attributable to squeezed film damping between the upper and lower electrodes. However, for the purposes of this thesis, the predominant damping mechanisms are not investigated. This is an interesting future point for investigation, however, since the sensitivity of the device may be improved by decreasing the damping.

The second, sharper peak at about 1800 is the RDM resonant frequency, confirming the previous visual measurement of the RDM resonance at 1806Hz. The Q factor for the RDM motion is 40.

Sensor Basics

The basic function of a sensor is to transduce an input to an output signal, typically an electrical voltage. The ideal sensor has an output versus input graph that shown in figure 59. The line is infinitely thin, indicating infinite precision, i.e. for any input, the output is exactly known. The output is linear with input, and the slope of the line is referred to as the sensitivity of the device.

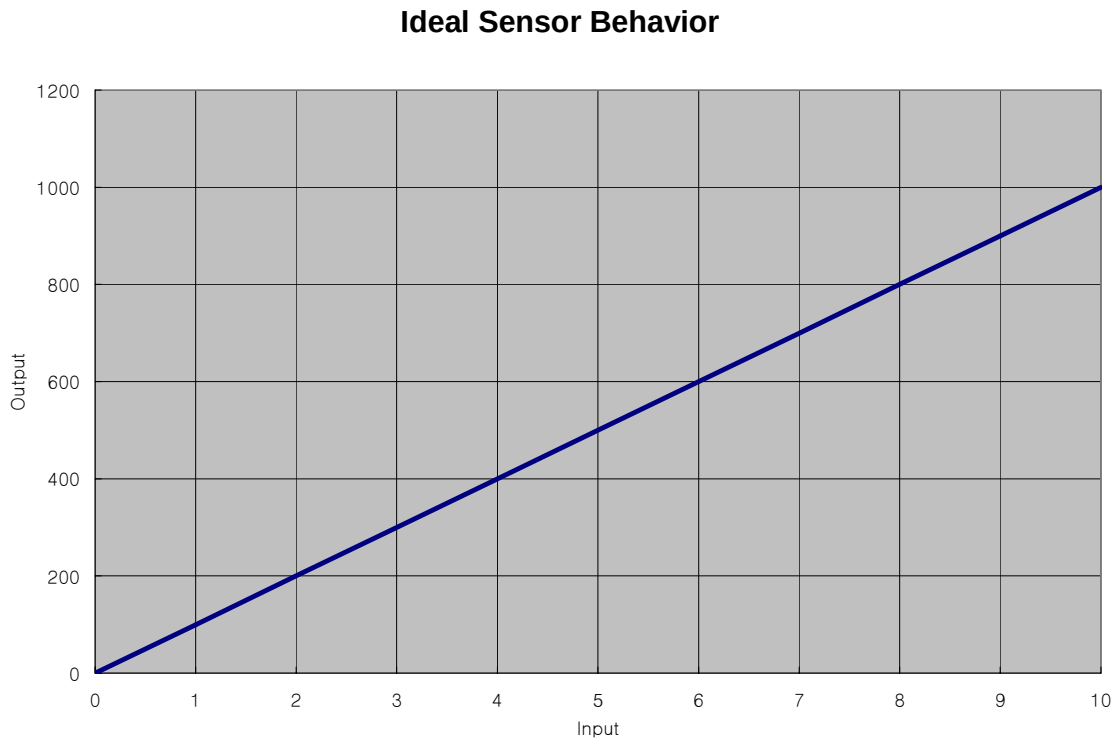

Figure 59 - The response for an ideal sensor. The behavior is linear and there is zero width to line, indicating infinite precision. The slope is referred to as the sensitivity of the device.

A more realistic sensor is seen in figure 60. The line has some spread, commonly referred to as "noise," indicating an amount of uncertainty in the input and the measurement.

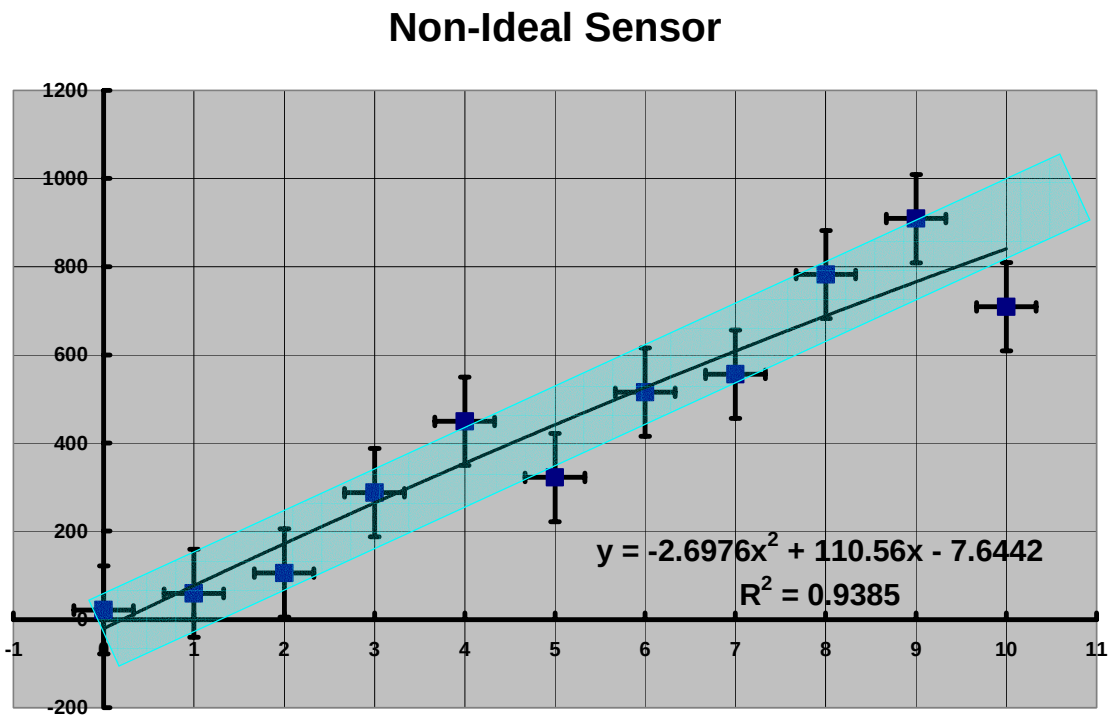

Figure 60 - The response for a more realistic sensor. There is some width to the line indicating uncertainty in the interpretation from output to input.

Gyroscope Sensitivity

To measure the sensitivity and noise, the same experiment is done as in the measurement of the mechanical spectrum. The only difference is that the gyro is placed on a rate table, i.e. a platform with a controllable rotation rate. The output (capacitance change) is measured as a function of the input (angular rate). We place the packaged

angular rate sensor on the rate table. The capacitance change is measured by measuring the displacement current of the changing capacitance.

The drive voltage is still 0.25V at the HP4194A impedance analyzer, which is DC offset by 0.125V to avoid frequency doubling. This signal is once again amplified by the Trek 50/750 300:1 amplifier, resulting in a 75Vpp signal at the micro-gyroscope.

A photograph of the test setup is shown in figure 61.

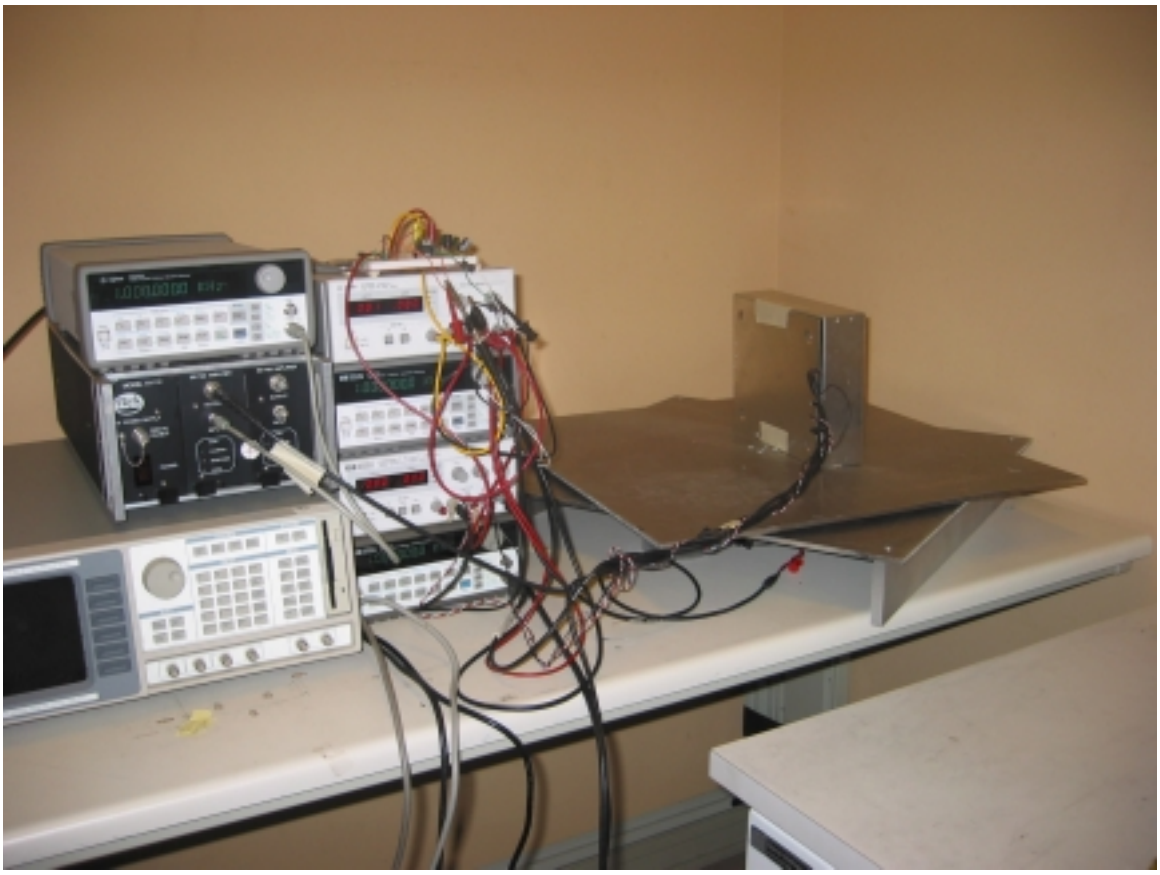

Figure 61 - Photograph of the test setup. The rate table is seen on the right. The gyroscope and the readout electronics are inside the shielded, grounded aluminum box that is set on its side on the table. The Trek 50/750 amplifier is the middle black box seen on the far left. The top two boxes on the right stack of electronics are the function generator and power supply to drive the rate table. The bottom two boxes are the function generator that supplies the 333kHz input signal and the power supply for the readout electronics. Not shown is the HP4194A impedance analyzer.

A schematic of the test setup is in figure 62.

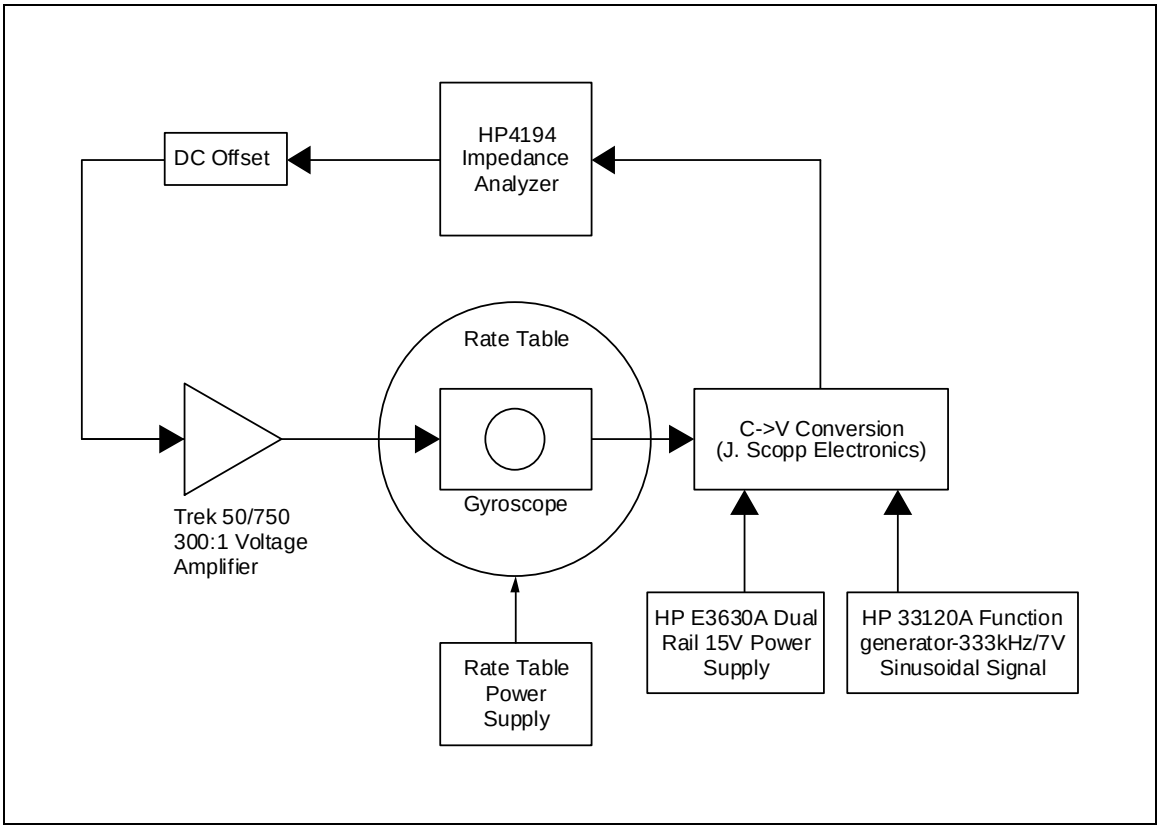

Figure 62 - Schematic of the test setup for the gyroscope response. An angular rate is inputted by the rate table. The gyroscope transduces this rotation into a capacitance change. The surrounding electronics drive and read the gyroscope response.

Although this is the preferred approach, the test setup required several modifications to meet practical constraints. First, instead of a constant rotation, the rate table oscillated back and forth at a frequency of 0.25Hz. This was chosen in order to prevent the connecting cables from twisting about each other. Despite this, the output of the gyroscope ought to vary with the rotational speed, since a counter-rotation does not result in a negative output, but rather a phase shift in the signal. Since an energy transfer from the RDM to the TSM occurs regardless of the direction of rotation of the table, an

increased capacitance change is measured, even though it is averaged over the oscillation of the rate table.

If the amplitude is averaged on time scales large compared to the frequency of the gyroscope as well as the rotational motion of the rate table, then the phase shifts do not affect the output. The amplitude of the TSM motion is recorded and averaged to remove as much noise as possible. The recording period is 6 hours.

The motion of the table is recorded and the rotation rate is a series of step functions. The rate table motion is taken by attaching a potentiometer to the center of the table. As the table rotates, the resistance varies with angular position. The position of the table for an 8V drive input is shown in figure 63. The angular position of the rate table as a function of time is a triangular wave. Taking the first derivative with respect to time, the angular velocity may be calculated, which for a sawtooth is a square wave.

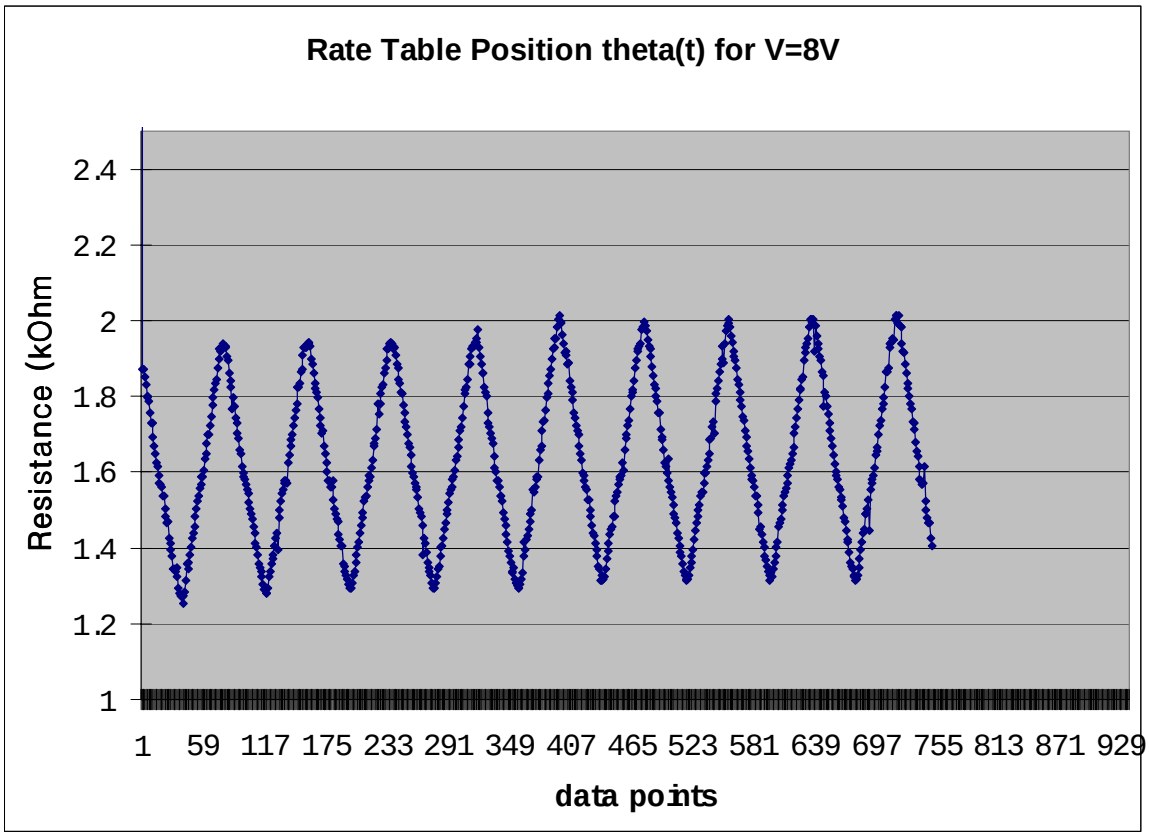

Figure 63 - Rate table behavior as function of time. Note that this is angular position versus time. The first derivative of this is angular rate, which is a square wave.

The RDM is driven, and the motion of the TSM is monitored by the capacitive displacement sensors. The unprocessed data for the spectra as a function of rotation rate is shown in figure 64. Each curve corresponds to a different angular rate.

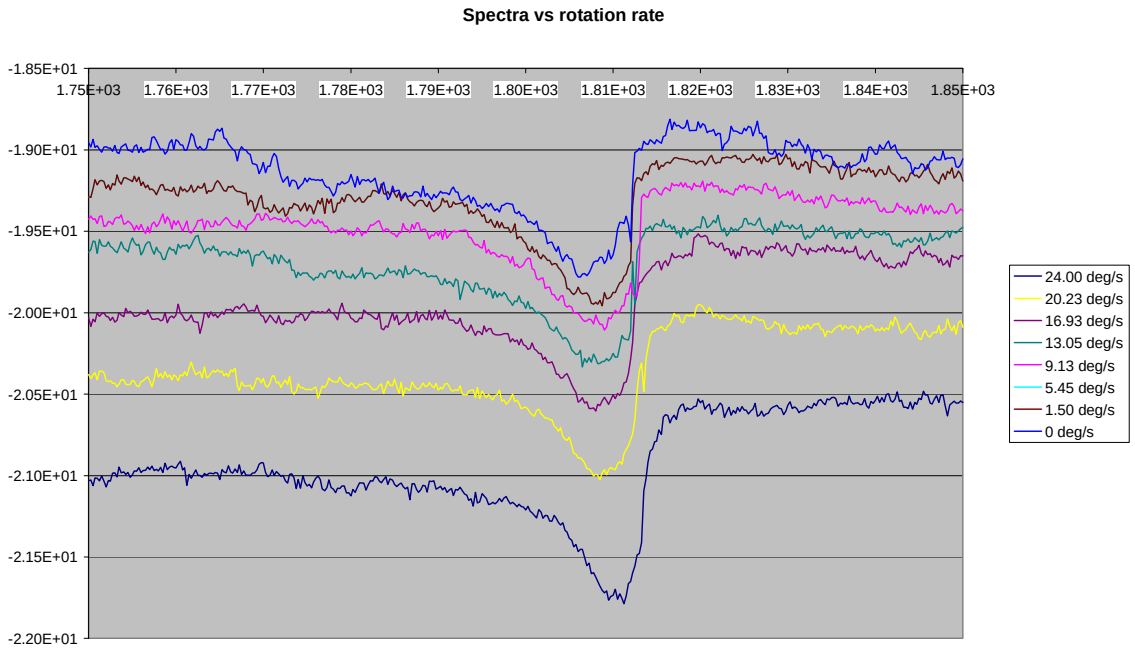

Figure 64 - Unprocessed data from the impedance analyzer as a function of various input angular rates. The angular rate information is encoded in the height of the resonance peak.

The gain at resonance is higher compared to the gain off resonance for a higher angular rate. However, because of signal drift, the absolute off resonance gain changes over time from -19dB to -21dB. This change in gain corresponds to a 5.77mV shift.

One way to conceptualize drift is to realize that the device plus test setup is not only sensitive to angular rate. Like any other physical object, it is also sensitive to temperature, fluctuations in power supply, stray fields, etc. Drift may be considered as the device's response to all other inputs.

There are a number of ways to compensate for drift. One way is called "chopping". [Van Putten2001] This method allows the system to drift and takes measurements relative to a zero input. This assumes that to first order, the device response to drift changes slowly relative to the time between measuring the zero level and

the measurand. A simple example is a spring scale. The spring's length may be a function of temperature. As a result, the measurement of a mass will drift with temperature. To compensate for this, a relative measurement is taken. A zero level is set by placing a zero mass on the scale. The measurement is the relative displacement of the spring when a mass is added.

For the angular rate sensor, the signal is encoded in the resonant peak height relative to the off resonance gain. Like the spring scale, the zero input may be determined by taking the output voltage when the operating frequency is off resonance, since then the generated angular momentum in the RDM is negligible. By doing this comparison, the curves may be normalized to a point off resonance. The normalized data is shown in figure 65. The variations in height are small, but distinguishable. A greater coupling of RDM energy is expected with higher rotational inputs, which should be reflected in the height of the resonance peak detected by the TSM.

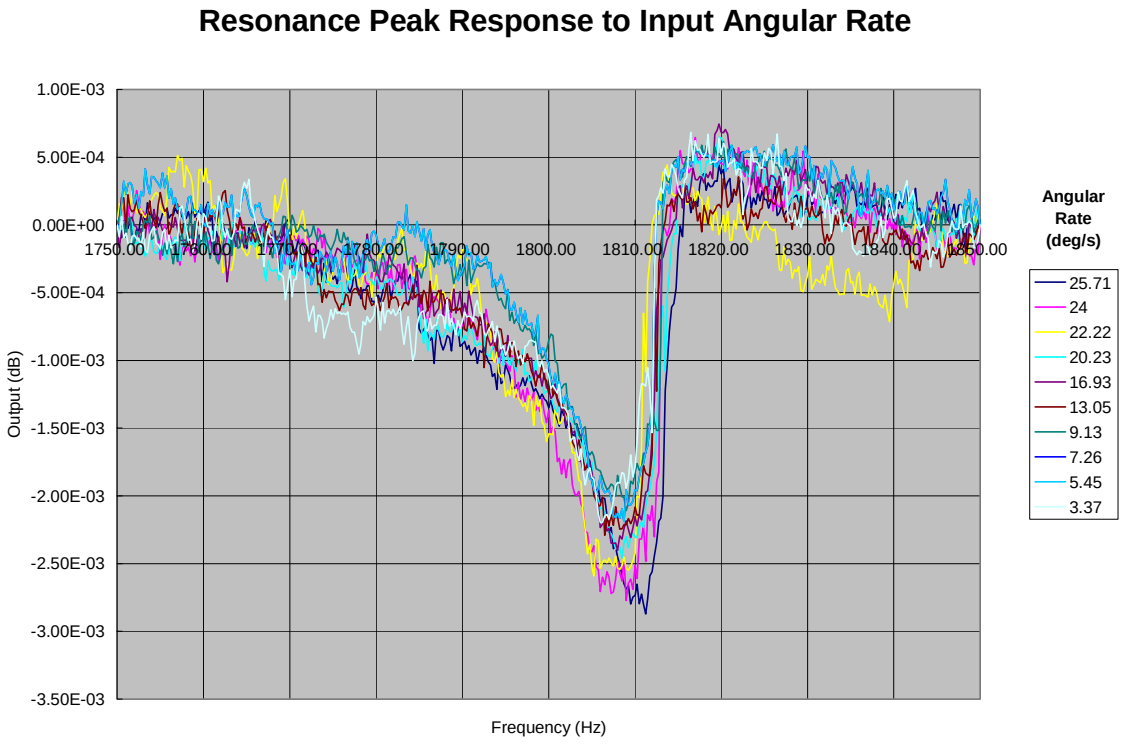

Figure 65 - Gyroscope response normalized to off-resonance to compensate for drift.

Plotting the ratio of the peak height to the off-resonance voltage output, the output-input plot for the sensor can be obtained, and is shown in figure 66.

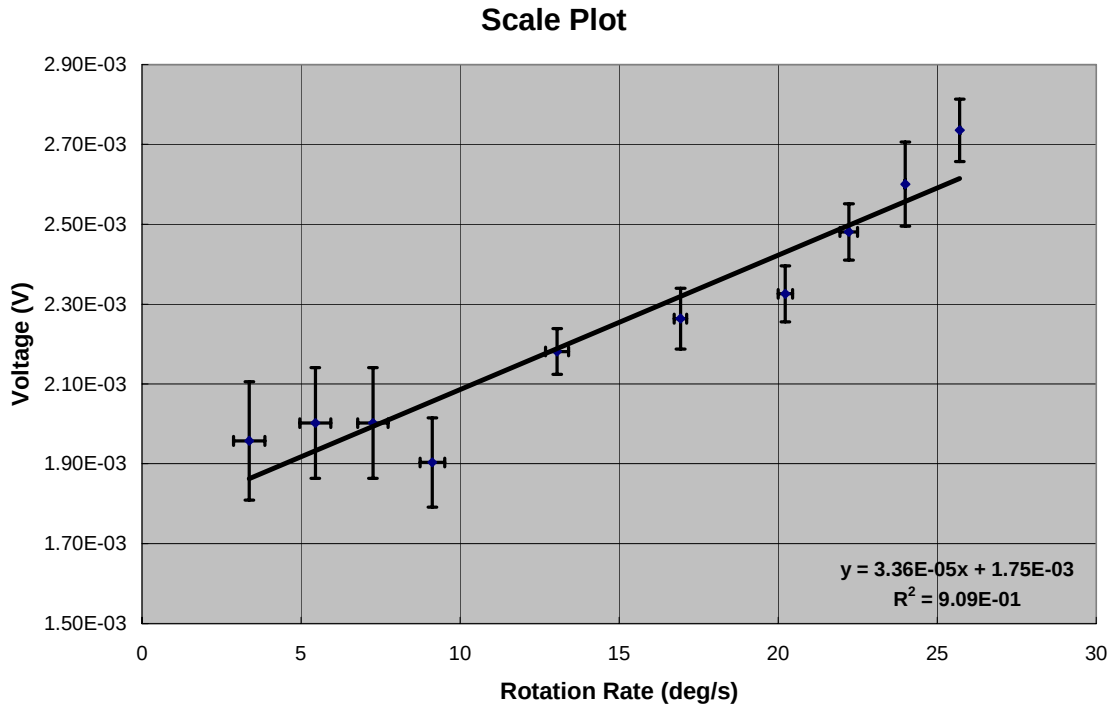

Figure 66 - Gyroscope response as a function of input angular rate. The sensitivity of the device is $3.36x10^{-5}$V/deg/s.

The plot is has a linear fit:

$$\text{Output Voltage} = 3.36x10^{-5} * (\text{Rotation Rate}) + 1.75x10^{-3}$$

$$R^2 = 0.909$$

The second order polynomial fit has a quadratic coefficient of $1.56x10^{-6}$, which when compared to the linear coefficient of $3.36x10^{-5}$, indicates that the response of the gyroscope is linear to first order.

This result may be compared to the theoretical response calculated from the *Mathematica* simulation. A table of inputted values is shown in table 9. The theoretical

response is plotted in figure 67. The *Mathematica* simulation predicts a zero offset for the theoretical curve.

Table 9 - Input parameters for the Mathematica model of the theoretical gyroscope response is shown.

Theoretical Gyroscope Response

Inputted Values

Parameter	Value	Units
Fundamental Constants		
permittivity of free space	8.85E-12	F/m
Material		
Si density	2330	kg/m^3
Si Young's Modulus	1.60E+11	Pa
Si Poisson's Ratio	0.22	
Device Parameters		
Entire Device		
Thickness	200	um
RDM		
Resonant Frequency	1806	Hz
Q-Factor	40	
Radius	1.5	mm
Gap of the Drive	20	um
Number of Drives	8	
Number of Fingers/Drive	14	
Drive Voltage	75	V
TSM		
Resonant Frequency	574	Hz
Q-Factor	1	
Width	7	mm
Length	5	mm
Capacitance gap	15	um

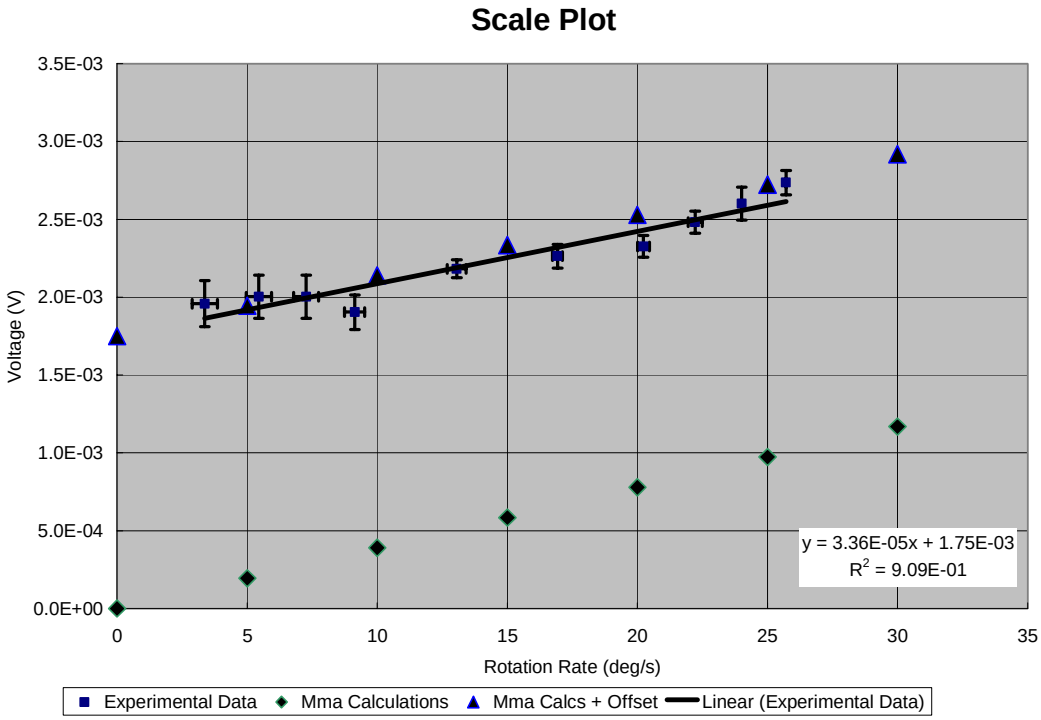

Figure 67 - Comparison of the experimental and theoretical results without the DC offset compensation.

The theoretical model does not predict a y-offset. This voltage offset is probably due to the mismatched capacitors on the TSM sensor. The electronic circuitry that reads the capacitance changes subtracts the current from one sensor from the current of the other. In theory, this subtraction ought to result in a non-zero current. However, since no pair of capacitors is perfectly matched, and since the sensitivity of the circuit is on the order of femtofarads, there is a constant, DC offset to the signal. To compensate for this, the experimentally determined y-intercept is simply added to the theoretical calculations. This plot is shown in figure 68.

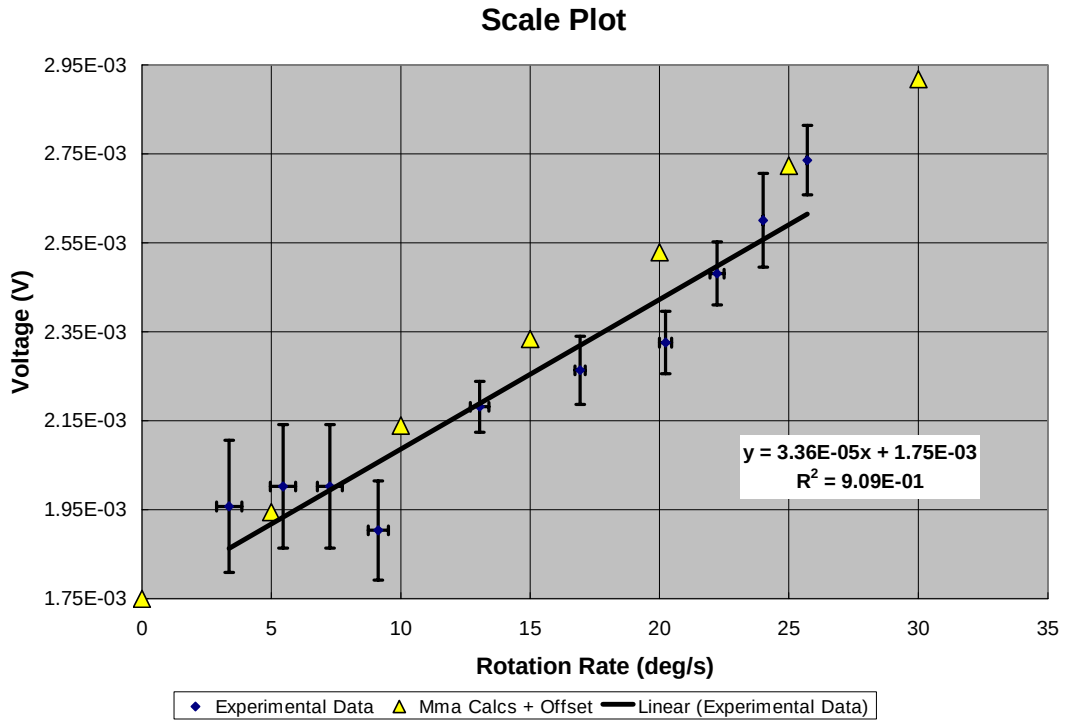

Figure 68 - Comparison of the experimental and theoretical results with DC offset compensation.

The theoretical result tends to be larger than the experimental one, but within one or two standard deviations (the error bars shown are ±1 standard deviation). A couple of factors may explain this. A number of assumptions went into the calculation of the theoretical curve. For example, the single crystal silicon is modeled as an isotropic material rather than an anisotropic one. Another is that the Q-factors and resonant frequencies are not exact and are graphically determined. Finally, the capacitance gap in the theoretical model is assumed to constant. In other words, the die and the package surfaces are assumed to be perfectly parallel. In the actual device, though, the gap is 12μm in some places and 15μm in other places, so an average gap is used as an input to the theoretical model.

Noise Characteristics

The noise of the device is measured by simply setting the input to zero, i.e. zero rotation, and monitoring the changes in the output. The drive frequency is no longer scanned, but set at the resonance. An output of the noise of the gyroscope is shown in figure 69. The averaging time is 6.75s per sample.

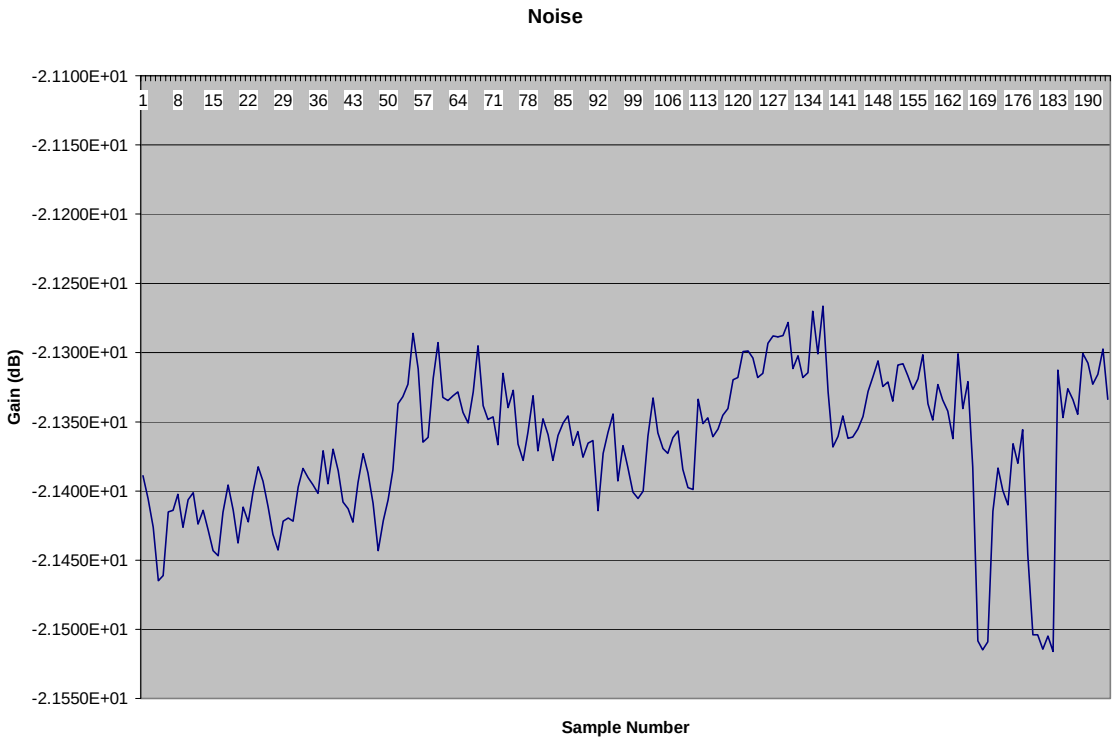

Figure 69 - Noise behavior of the gyroscope as a function of time. The device exhibits a noise floor of 8.98 deg/s/Hz$^{1/2}$.

The standard deviation of this signal is -66.7dB or 1.16x10^{-4}V, which corresponds to a rotational value of 3.45deg/s. Given a 6.75s averaging time, this corresponds to a noise floor of 3.01x10^{-4}V/Hz$^{1/2}$ or 8.96deg/s/Hz$^{1/2}$.

Discussion of Performance

Qualitatively, the performance of the device is linear to first order. Quantitatively, the sensitivity is low compared with other microgyroscopes. A table of the sensitivity and noise characteristics of other MEMS gyroscopes is shown in table 10.

It should be pointed out that several operating parameters may be changed to increase the sensitivity. The gyro was operated at 75Vpp, despite the fact that the blocking voltages were measured to be in excess of 350V. Simply increasing the drive voltage to 300Vpp would produce a factor of 16 increase in device sensitivity. However, this was not done, since the output of HP4194A impedance analyzer is maximized at 0.25V.

Other parameters that may be changed to increase sensitivity include electronic amplification of the signal, amplitude of the 333kHz wave, and the frequency of the carrier wave. Moreover, the device could be operated under low pressures, so that the Q-factor of the RDM motion could be boosted from 40 to thousands. This last option was not done, since a cheap, affordable gyroscope will operate at atmosphere to avoid the difficulties and cost of vacuum packaging.

The noise of the device indicates that this is not a tactical navigation grade device. However, the measured noise probably does not reflect a fundamental noise floor from the device itself. For signals at this voltage level, shielding is extremely important, and although basic shielding was implemented (all wires wrapped in grounded conductors, ground loops avoided, etc.), its realization is by no means optimized.

However, overall, as a device to demonstrate the utility of the thermomigration/DRIE method of fabricating MEMS devices, it clearly succeeds. This is a first generation prototype and the focus was on solving fabrication problems and on optimizing performance. A number of performance improving steps that were not included in this work may be taken in the next and succeeding generations, which are discussed in the next chapter.

Table 10 - Table of sensitivities and noise characteristics for various MEMS angular rate devices.

MEMS Gyroscopes-Sensitivity and Noise Characteristic

Group	Year	Sensitivity mV/deg/s	Noise deg/s/rt Hz	note	Reference
Draper Labs-Greiff	1991		4	device operated in vacuum	Greiff1996
Draper Labs-Greiff	1996		0.01		Greiff1996
Berkeley-Howe	1996		1		Howe1996
JPL-Tang	1997	24			Tang1997
Samsung-Song	1997	0.13	0.04	device operated at 10mTorr	Song1997
Bosch-Funk	1999	1.5	0.4		Funk1999
Penn State-Varada	2000	0.000091		SAW device	Varadan2000
CMU-Fedder	2001	0.12			Fedder2001
UMich-Najafi	2001	0.2	~1		Najafi2001
CMU-Fedder	2002	0.4	0.02		Fedder2002a
CMU-Fedder	2002	0.0008	0.5		Fedder2002b
ADI ADXRS150	2003	12.5	0.05		ADI2003a
ADI ADXRS300	2003	5	0.1		ADI2003b
Berkeley-Howe	2003	0.33	0.05	device operated at 70mTorr	Howe2003a
Berkeley-Howe	2003	1.5	0.01	device operated at 70mTorr	Howe2003a
Berkeley-Howe	2003		8		Howe2003b
GT-Chung & Allen	2003	0.0336	8.96	V=75Vpp	
GT-Chung & Allen	2003	0.732		V=350Vpp (predicted)	

Chapter 7

Conclusion & Future Work

The combination of aluminum thermomigration and deep reactive ion etching is a viable technique for fabricating useful MEMS devices that preserves the thickness and high-aspect ratios available from DRIE, the reliability of silicon crystal silicon, the accessible design space from surface-micromachining, the functionality of CMOS electronics, and the economics of batch fabrication.

No significant theoretical or practical obstacles lie in the path of microfabricating useful, functional devices with this technique. No expensive or unusual steps must be taken. A viable fabrication path from wafer start to die packaging has been identified.

The electrical characteristics of the junction isolation allow a large operating range for possible devices based on this technique. Overall blocking voltages increases linearly with additional npn junctions in series, thus limiting maximum blocking voltages only by available chip area. Leakage currents are practically demonstrated to be less than 0.1μA.

In comparison to trench etching/backfill techniques, thermomigration sidesteps issues such as keyholing, adhesion, and mechanical property alteration. With respect to bond/etch approaches, thermomigration avoids a substrate wafer which allows for rotating or moving platforms with electromechanical components. And, in contrast to the

SCREAM process, active electro-mechanically functional devices may reside on a moving platforms.

However, there are situations where thermomigration may be a second choice. For example, in a case where very small CMOS devices are already on substrate, the high temperature processing of thermomigration may diffuse dopants to a point where circuits become inoperable. Also, for situations where current leakage is important, there are alternatives that inherently provide zero leakage current solutions, such as the bond/etch approach.

Bulk Silicon Devices with Thermomigration and DRIE

The application of thermomigration coupled with deep reactive ion etching expands the design space for MEMS devices. No fundamental or practical difficulties towards the realization of thick, high aspect ratio, electro-mechanical silicon devices. A functioning device may be realized with a combination of thermomigration, deep reactive ion etching, surface micromachining, and/or CMOS fabrication.

However, the use of thermomigration may require some reordering of the fabrication sequence. Although the temperature of the TGZM step is high, the overall energy of the process is smaller than expected since the processing time can be short. As a result, despite the high temperatures, some fabricated structures can be on wafer even during the thermomigration, such as doped structures, polysilicon, or silicon dioxide layers. Other on-wafer structures, however, may be unable to withstand the temperature, even despite the short processing time, such as materials that may degrade, melt, change crystal structure, or materials that are CTE mismatched to the silicon substrate. These

structures can be fabricated on a thermomigrated wafer after the TGZM step, since the thermomigration is simply a doping method, and for most intents and purposes, changes in the wafer due to thermomigration are transparent to many fabrication technologies, such as surface micromachining.

However, for microelectronic integration, this may be overly restrictive. The postponement of the microelectronic fabrication after the thermomigration step can be done, however, this then requires a fabrication line that will accept thermomigrated wafers.

Currently, there is a debate about the cost-benefit of integrated microelectronic circuitry on MEMS die. Most for most applications, there is little compelling reason to have both the MEMS and the microelectronics on the same die, and the cheapest solution is usually to partition the system into two die, i.e. a microelectronic chip and a MEMS chip, each separately packaged.

However, for situations where the MEMS and microelectronics must reside on the same chip, thermomigration may still be a viable alternative. The thermomigration and the post-processing can still be done with microelectronics or other devices on the wafer. However, instead of lapping, an etchant must be used. The etchant does not affect the other structures if masked so that it only removes the heat damaged silicon and the excess aluminum in the thermomigrated areas. One such combination is a dilute solution of HF/HNO_3 for an etchant, and chromium used for a mask.

Thermomigration and Angular Rate Sensors

A prototype angular rate sensor was successfully fabricated to demonstrate a path from wafer start to packaging. Although a number of practical problems were encountered, no serious obstacles were found.

Perhaps the most difficult challenge in this work is achieving a sufficiently uniform thermal gradient across the wafer. The thermomigration step is the single most yield restricting step in the fabrication of the microgyroscope. However, an apparatus capable of uniformly heating a sufficiently large area places a number of power and thermal demands. This is not a insurmountable problem with several solutions described in the literature. [Harrison1983, Dilhac1999, Cline1976b, Normann1992b]

Future Work

This work is mostly a proof of concept. It demonstrates the applicability of thermomigrated junctions for electrical isolation of thick, bulk silicon MEMS devices. Yet a great many areas of exploration remain, and the next logical steps are to explore the thermomigration and the gyroscope fabrication individually.

With regard to thermomigration, the following things could be investigated:

1. A better thermomigration apparatus
    A. Larger area
    B. Better uniformity
    C. Higher temperature
    D. More precise control of temperature from 1300-1400C to set doping levels

2. An etch that does not preferentially remove p-type silicon
3. An investigation into the high leakage current
4. Thermomigration using float zone rather than Czochralski silicon. It is hypothesized by Huber that since float zone silicon has fewer oxygen contaminants, it may allow less random walk in thermomigrated regions, and therefore closer spacing of the p-type regions. [Huber2000]
5. Doping with other materials. Possible interesting materials are: P, As, and B for electrical properties. Ni, Co, and Fe for magnetic properties. Er for possible optical properties. Ge and C for semiconductor properties. Thermomigration is possible with all these materials since the eutectic point for two materials is always below the melting point of each material. As a result, thermomigration ought to be possible, perhaps not practical, but possible. Very large volume and high inductance inductors, for example, may be fabricated using this process.
6. Control of doping density by diluting dopant with other materials
7. Doping multiple materials simultaneously
8. ICP process - introduce Cl in the plasma to improve etch rate of the Al doped areas
9. Thermomigrating a CMOS wafer with Cu interconnects, since Cu has a higher melting point than Al.

With regard to the gyroscope, a great many topics may also be investigated:

1. Thicker silicon wafer for thicker devices

2. Surface micromachined electrodes
3. A lighter TSM
4. Rearranging the RDM & TSM so that the RDM is on the outside and the TSM is on the inside
5. Integration with microelectronics, particularly C-V conversion electronics
6. Finer features in the RDM/TSM etching, i.e. 30:1 or 40:1 aspect ratios
7. Vacuum operation
8. Resonant frequency matching
9. Decrease damping

Testing

1. A better rate table – a more precise rate table with less noise in the generated input angular rate should be acquired.
2. slip ring connections to allow continuous rotations

Final Word

This work explores both a new fabrication technology as well as device design. The demonstration of a viable path from wafer start to packaging in such a way that the advantages from deep reactive ion etching, single crystal silicon, batch fabrication, surface micromachining, and CMOS integration are preserved, points to a commercially viable means of producing high performance microscopic devices. It is my hope that this bit of knowledge advances and contributes to creating microsystem technologies that can help solve many of the challenges that humankind faces today.

Appendix A – PMOS Fabrication

1. RCA Clean
2. Oxide Mask
   A. Temperature: 1175C
   B. Time: 6 hours
   C. Gas: O_2-N_2
   D. N2 dry time: 5:50 minutes
   E. O2 dry time: 10 minutes
3. Photolithography
   A. Dehydrate oven: 200C
   B. Primer: 10s dwell
   C. Resist 1813P
   D. Spin speed: 3500rpm
   E. Time: 30s
   F. Soft bake: 5 minutes
   G. Temp: 95-100C
   H. Exposure time: 30s
   I. Energy: 6mW/cm2
   J. Developer: MF319
   K. Time: 1:15 minutes
   L. DI rinse: 10s
   M. Hard bake: 120C
   N. Time: 15 minutes
4. B.O.Etch
   A. Time: 6 minutes
   B. DI rinse: 10s
5. Photoresist Removal
   A. Chemical: 1165 Stripper
   B. Temp: 70C
   C. Time: 3minutes
   D. DI rinse: 10s
6. RCA Clean
7. P+ source/drain predeposition
   A. Solid sources: GS 126
   B. Time: 30 minutes
   C. Temp: 935C
   D. N2 flow rate: 1000sccm
8. Boron glass removal
   A. Chemical: HF
   B. Ratio: 1:50
   C. Time: 2 minutes
   D. DI rinse: 10s
9. RCA clean
10. Gate Oxidation
    A. Temp: 1000C

B. Time: 55 minutes
C. Gas: O2
D. Flow rate: 1000sccm

11. photolithography
    A. Dehydrate oven: 200C
    B. Primer: 10s dwell
    C. Resist: 1813P
    D. Spin speed: 3500rpm
    E. Time: 30s
    F. Soft bake: 5 minutes
    G. Temp: 95-100C
    H. Exposure time: 35s
    I. Energy: 6mW/cm2
    J. Developer: MF319
    K. Time: 2minutes
    L. DI Rinse: 10s
    M. Hard bake: 120C
    N. Time: 5 minutes
12. B.O. Etch
    A. Time: 1:30s
    B. DI rinse: 10s
13. Photoresist removal
    A. Chemical: 1165 stripper
    B. Temp: 70C
    C. Time: 3 minutes
    D. DI rinse: 10s
14. HF dip
    A. Time: 1 minute
    B. DI Rinse: 15s
15. Metallization
    A. Machine: Denton
    B. Metal: Al99%/Si 1%
    C. Distance: 12”
    D. Rate: 3.5-4
    E. Pressure: 3μTorr
16. photolithography
    A. Dehydrate oven: 200C
    B. Primer: 10s dwell
    C. Resist: 1813P
    D. Spin speed: 3500rpm
    E. Time: 30s
    F. Soft bake: 5 minutes
    G. Temp: 95-100C
    H. Exposure time: 35s
    I. Energy: 6mW/cm2
    J. Developer: MF319

K. Time: 2minutes
L. DI Rinse: 10s
M. Hard bake: 120C
N. Time: 5 minutes

17. PAN etch
    A. Chemical: PAN
    B. Temp: 50-55
    C. DI rinse: 10-20s
18. Photoresist removal
    A. Chemical: 1165 stripper
    B. Temp: 70C
    C. Time: 3 minutes
    D. DI rinse: 10s
19. Plasma Etch
    A. Gas: O2
    B. Time:10 minutes
    C. Pressure: 150mTorr
    D. Power: 100W
20. Sinter/Anneal
    A. Temp: 400C
    B. Time: 30 minutes
    C. Gas: N2
    D. Flow rate: 1000sccm

Appendix B-ANSYS Modal Simulation Results

Simulation Parameters:

ANSYS version: 5.6.2
Element Type: SOLID92 — 3-D 10-Node Tetrahedral Structural Solid
Material Constants: isotropic material was assumed.
Density: 2300 kg/m3
Elastic Modulus: 150GPa
Poisson's Ratio: 0.17
Meshing: Smartmesh, smartsize=6
Loads: Structural displacement loads – all degrees of freedom set to zero – applied to two ends of the TSM beams.
Analysis: Modal
Modal Extraction: Subspace

ANSYS Modal Simulation Results Summary

mode number	Frequency (Hz)	mode
1	340	TSM Rotation-Y axis
2	1974	RDM Rotation-Z axis
3	5885	TSM bending-about Y axis
4	6103	TSM translation-along y axis
5	7252	TSM Rotation-Z axis
6	7446	TSM twist-X axis
7	12607	TSM Bend-X axis
8	13263	TSM Twist-about X&Y axis

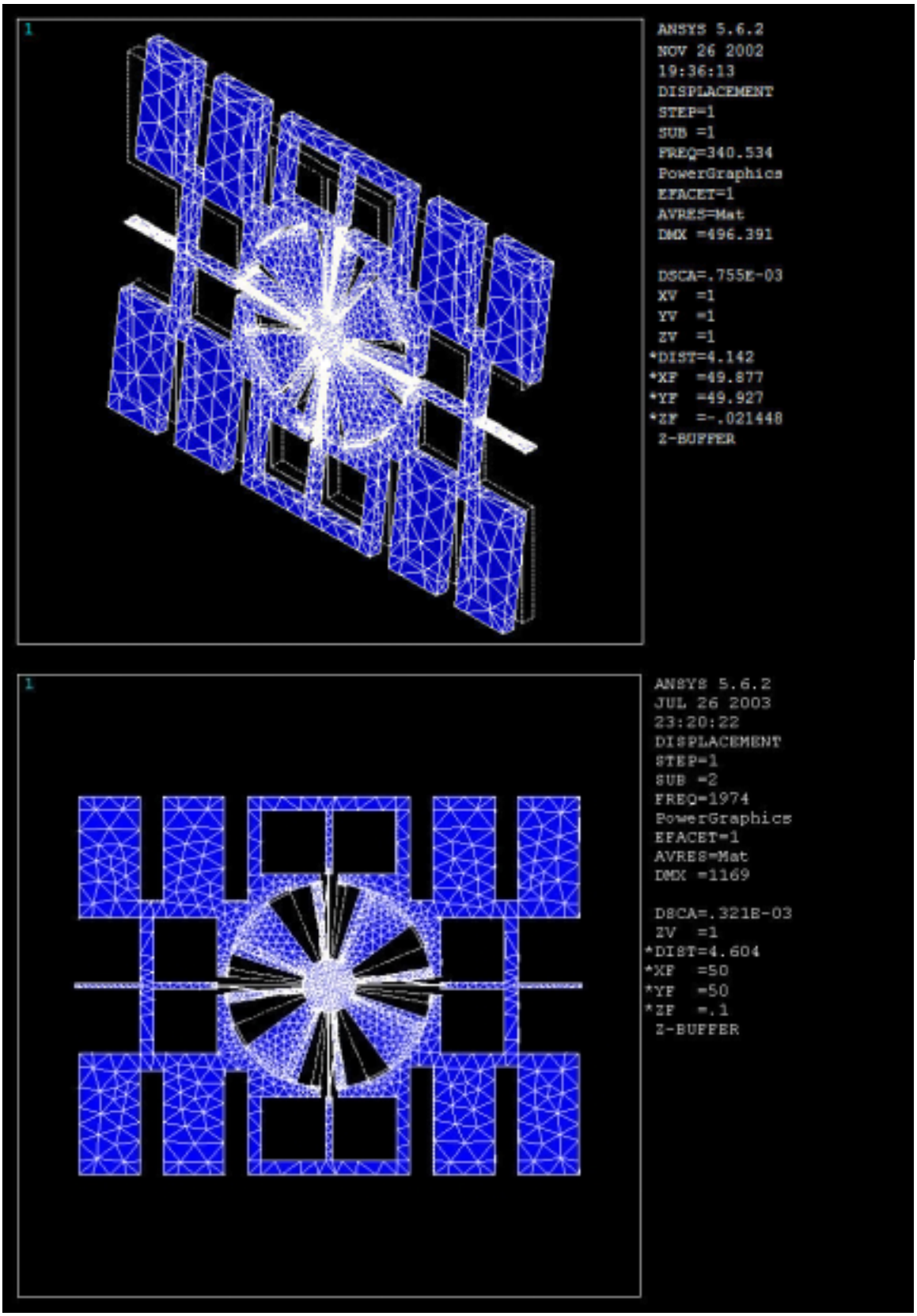
1
ANSYS 5.6.2
NOV 26 2002
19:36:13
DISPLACEMENT
STEP=1
SUB =1
FREQ=340.534
PowerGraphics
EFACET=1
AVRES=Mat
DMX =496.391
DSCA=.755E-03
XV =1
YV =1
ZV =1
*DIST=4.142
*XF =49.877
*YF =49.927
*ZF =-.021448
Z-BUFFER
1
ANSYS 5.6.2
JUL 26 2003
23:20:22
DISPLACEMENT
STEP=1
SUB =2
FREQ=1974
PowerGraphics
EFACET=1
AVRES=Mat
DMX =1169
DSCA=.321E-03
ZV =1
*DIST=4.604
*XF =50
*YF =50
*ZF =.1
Z-BUFFER

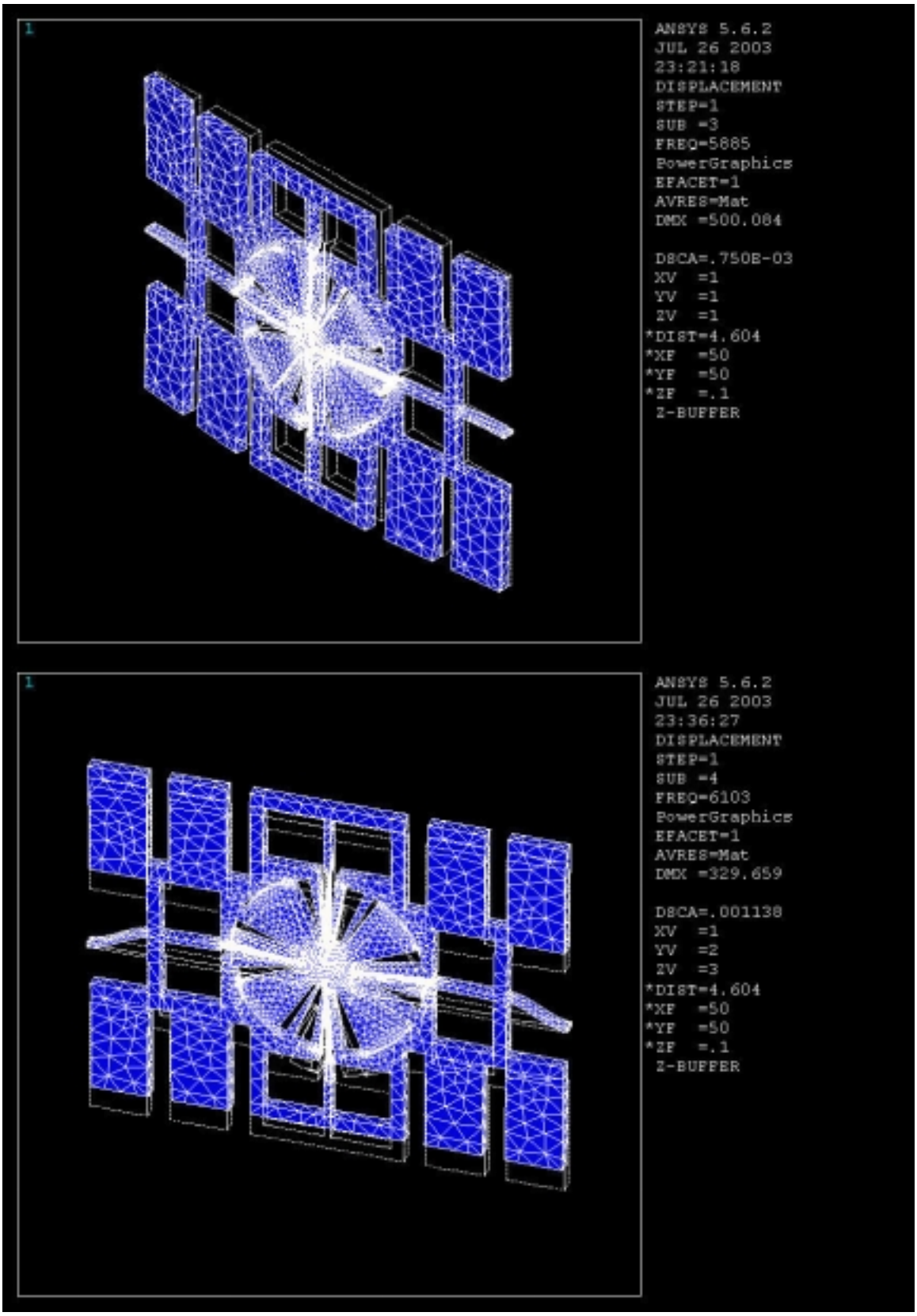
1
ANSYS 5.6.2
JUL 26 2003
23:21:18
DISPLACEMENT
STEP=1
SUB =3
FREQ=5885
PowerGraphics
EFACET=1
AVRES=Mat
DMX =500.084
DSCA=.750E-03
XV =1
YV =1
ZV =1
*DIST=4.604
*XF =50
*YF =50
*ZF =.1
Z-BUFFER
1
ANSYS 5.6.2
JUL 26 2003
23:36:27
DISPLACEMENT
STEP=1
SUB =4
FREQ=6103
PowerGraphics
EFACET=1
AVRES=Mat
DMX =329.659
DSCA=.001138
XV =1
YV =2
ZV =3
*DIST=4.604
*XF =50
*YF =50
*ZF =.1
Z-BUFFER

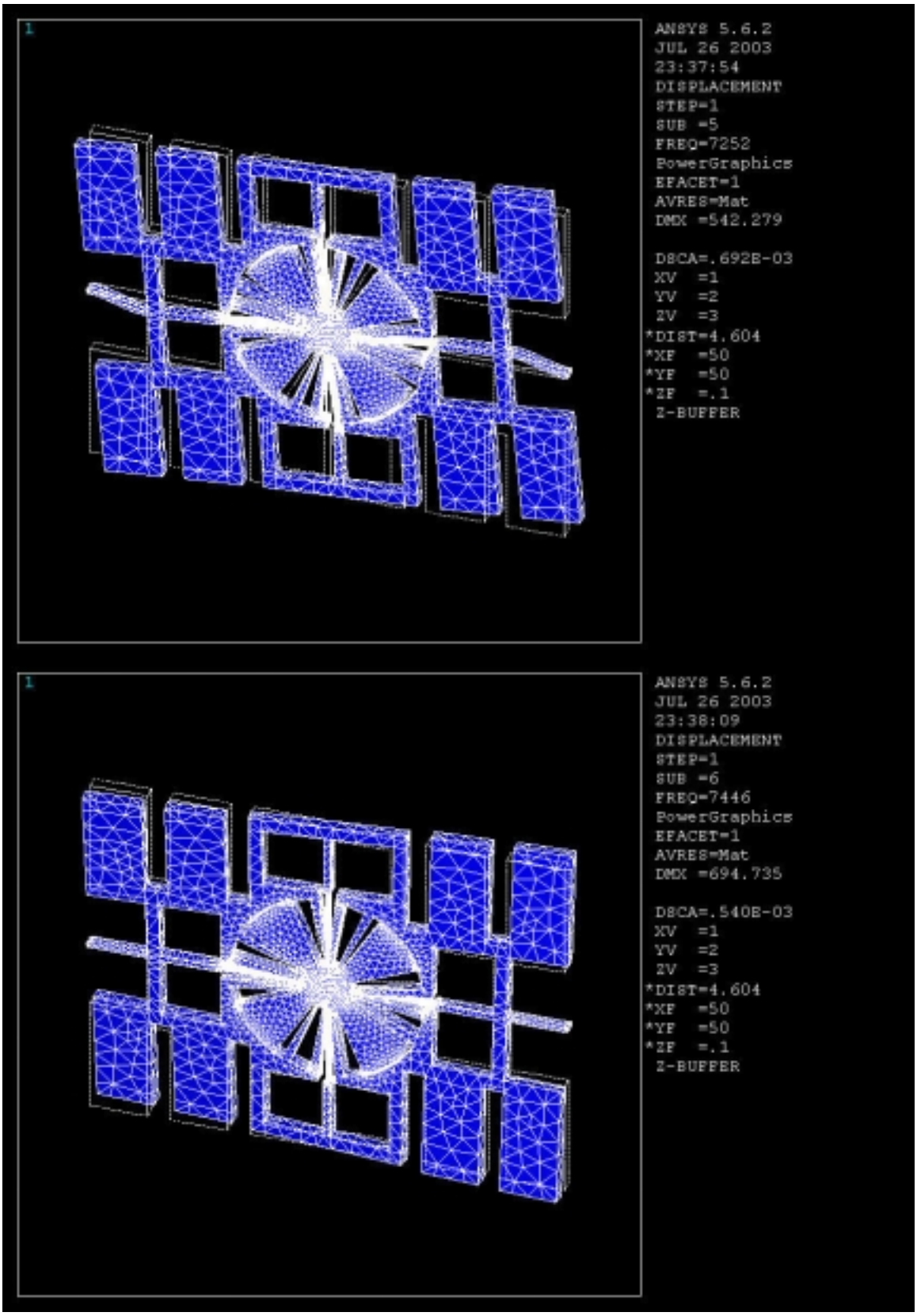
1
ANSYS 5.6.2
JUL 26 2003
23:37:54
DISPLACEMENT
STEP=1
SUB =5
FREQ=7252
PowerGraphics
EFACET=1
AVRES=Mat
DMX =542.279
DSCA=.692E-03
XV =1
YV =2
ZV =3
*DIST=4.604
*XF =50
*YF =50
*ZF =.1
Z-BUFFER
1
ANSYS 5.6.2
JUL 26 2003
23:38:09
DISPLACEMENT
STEP=1
SUB =6
FREQ=7446
PowerGraphics
EFACET=1
AVRES=Mat
DMX =694.735
DSCA=.540E-03
XV =1
YV =2
ZV =3
*DIST=4.604
*XF =50
*YF =50
*ZF =.1
Z-BUFFER

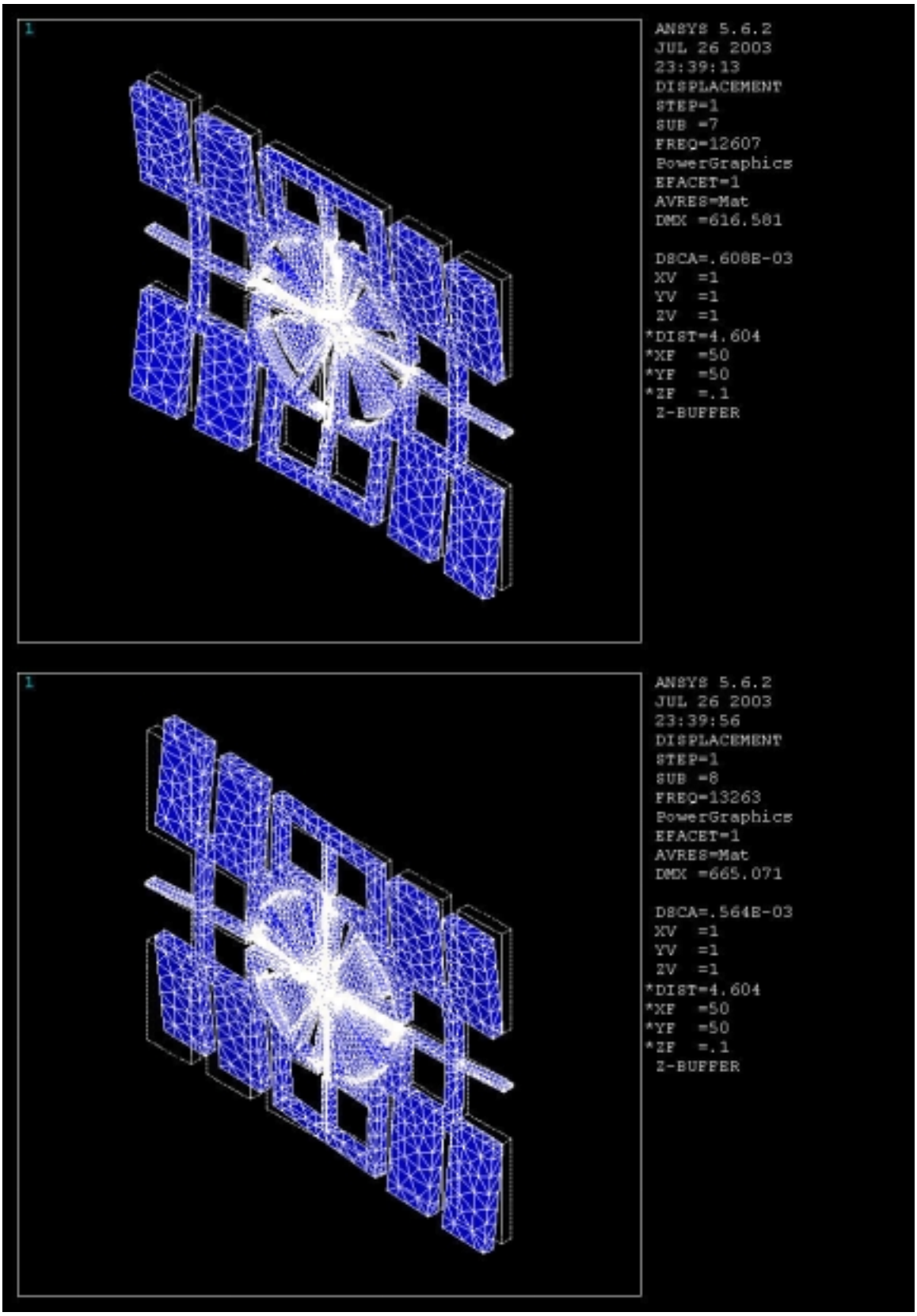
1
ANSYS 5.6.2
JUL 26 2003
23:39:13
DISPLACEMENT
STEP=1
SUB =7
FREQ=12607
PowerGraphics
EFACET=1
AVRES=Mat
DMX =616.581
DSCA=.608E-03
XV =1
YV =1
ZV =1
*DIST=4.604
*XF =50
*YF =50
*ZF =.1
Z-BUFFER
1
ANSYS 5.6.2
JUL 26 2003
23:39:56
DISPLACEMENT
STEP=1
SUB =8
FREQ=13263
PowerGraphics
EFACET=1
AVRES=Mat
DMX =665.071
DSCA=.564E-03
XV =1
YV =1
ZV =1
*DIST=4.604
*XF =50
*YF =50
*ZF =.1
Z-BUFFER

Appendix C-Mask Designs

Device and Package:

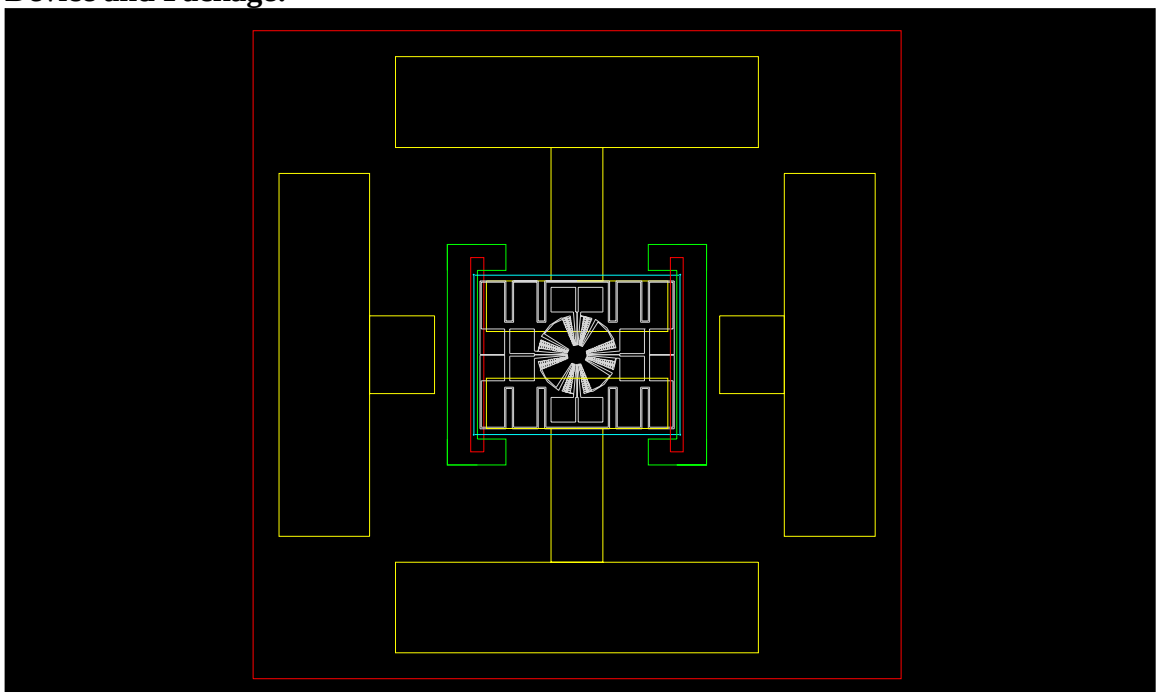

Gyroscope:

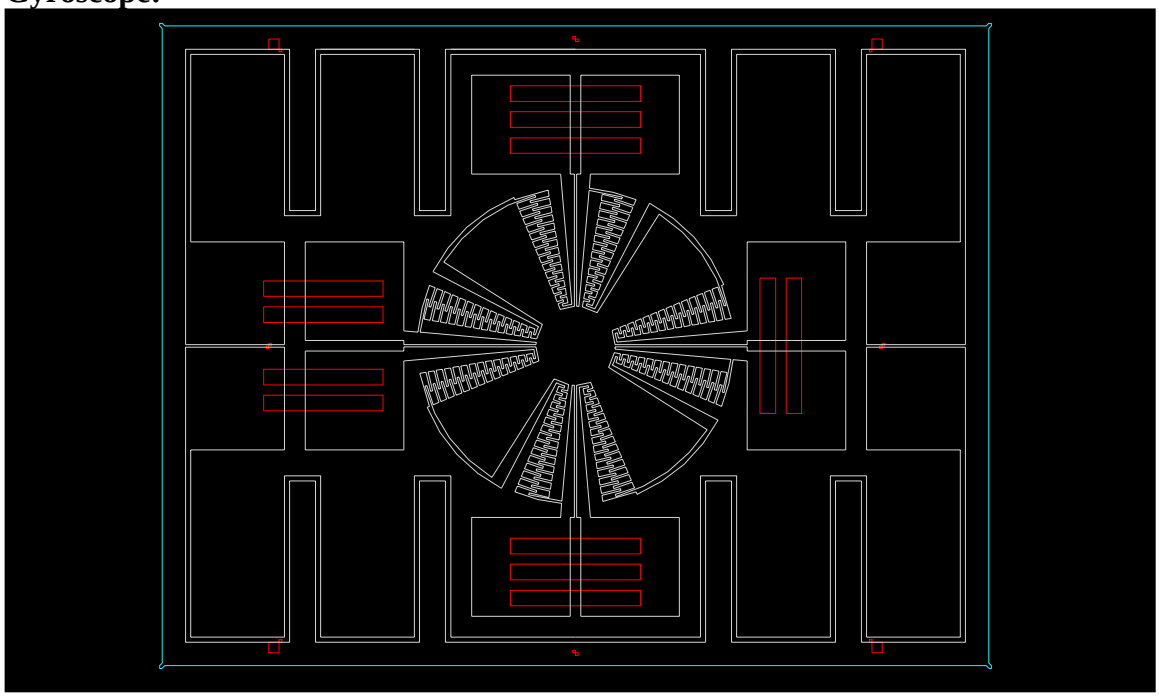

Gyroscope-Silicon Layer

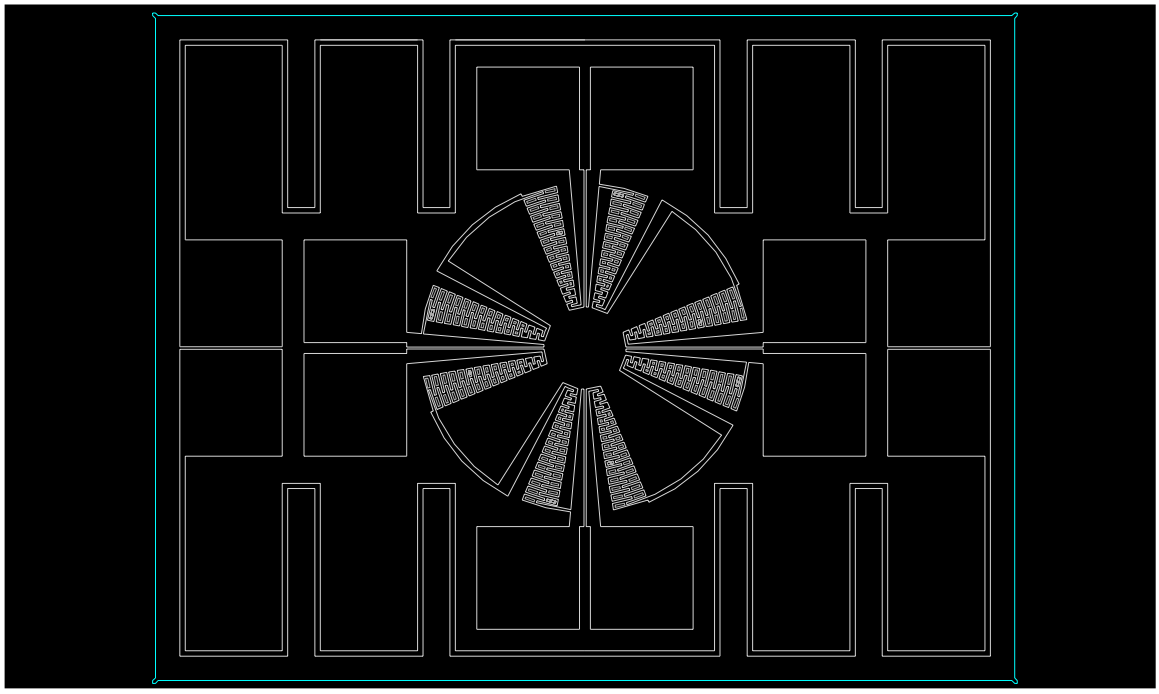

Gyroscope-Aluminum Layer:

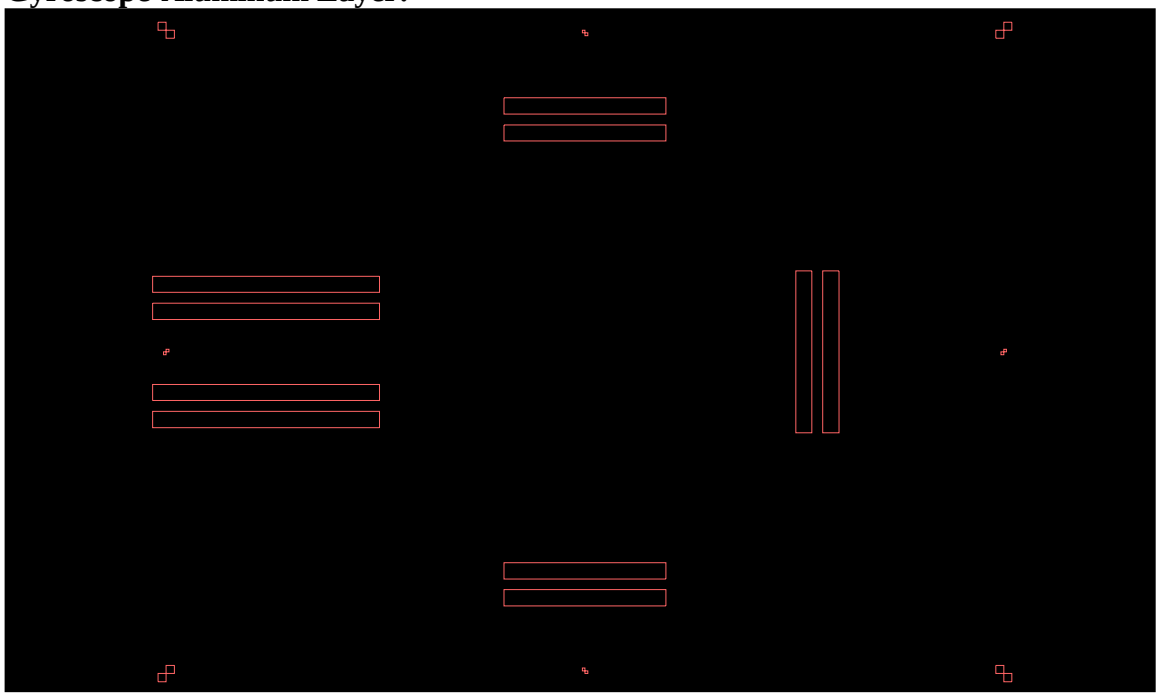

Package:

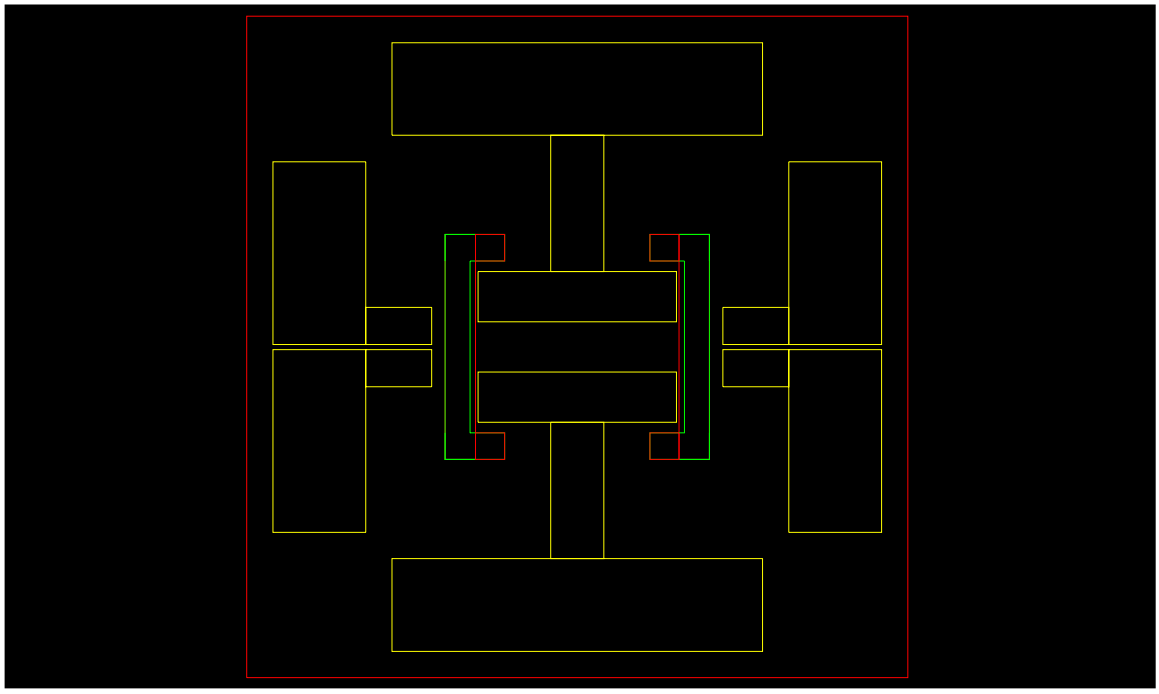

Package-Gold TSM Electrodes:

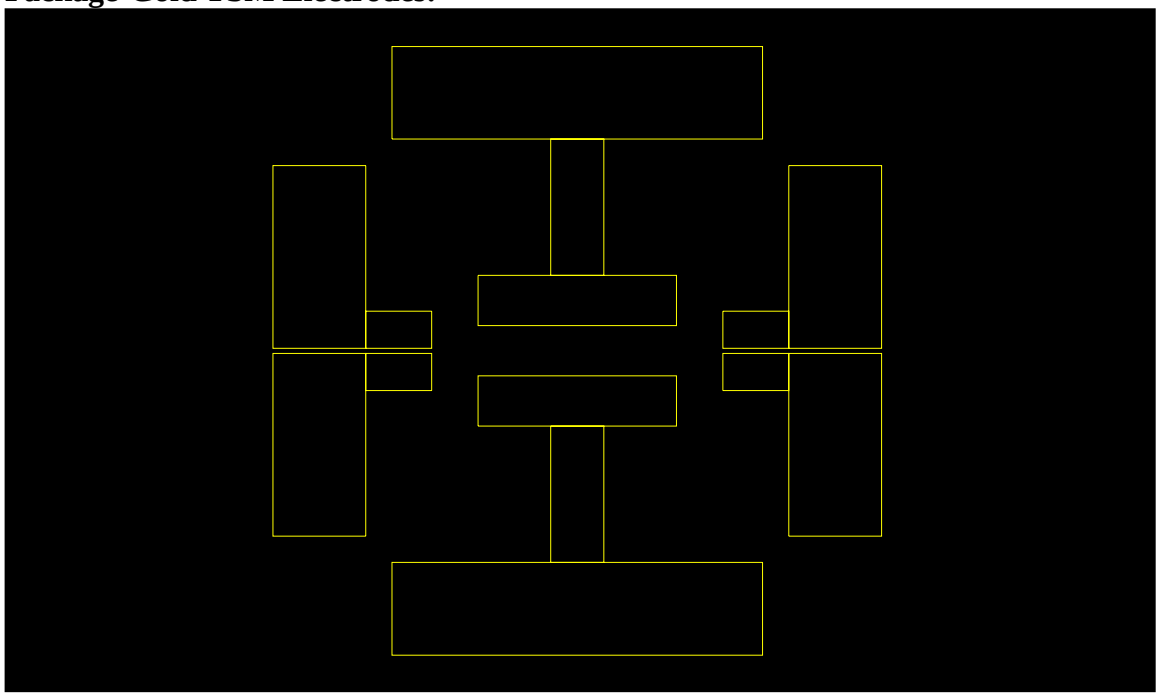

Package-Standoffs:

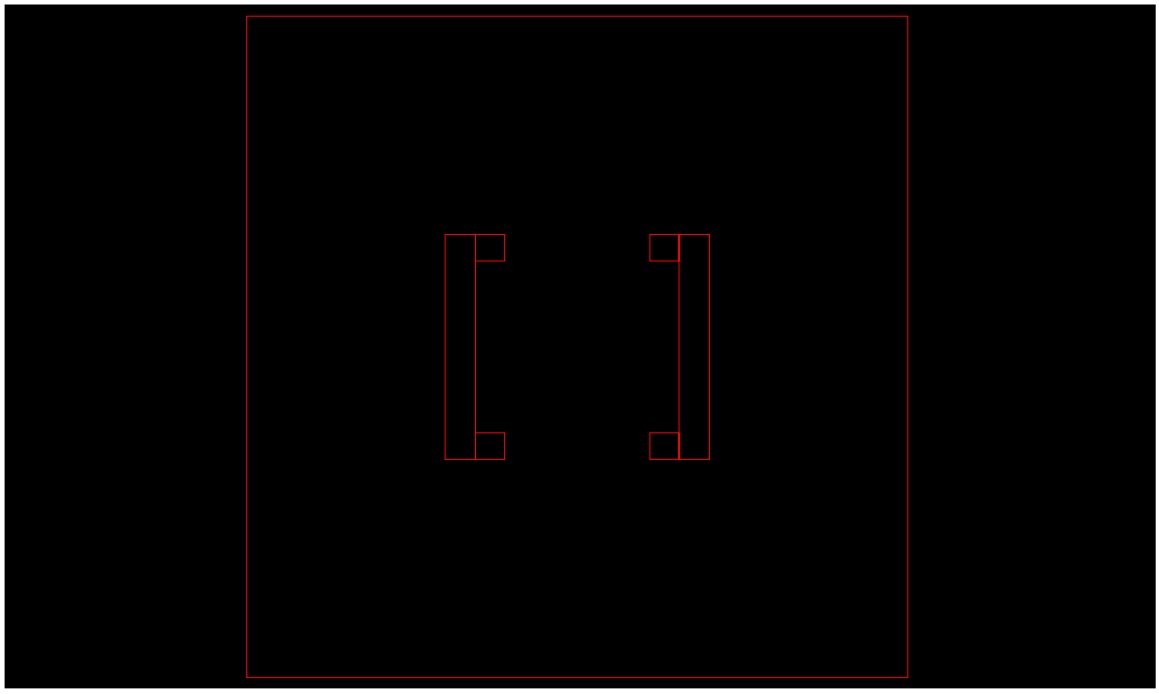

Package-Silicon Gyro Holders

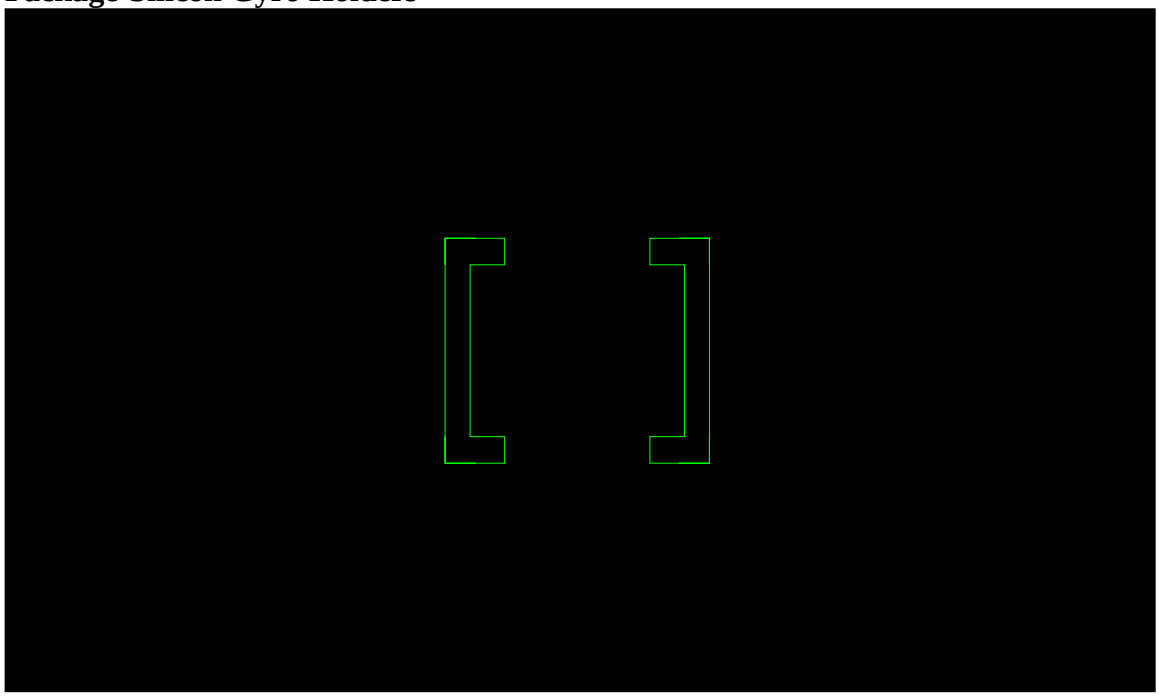

Appendix D– Capacitance to Voltage Conversion Circuit

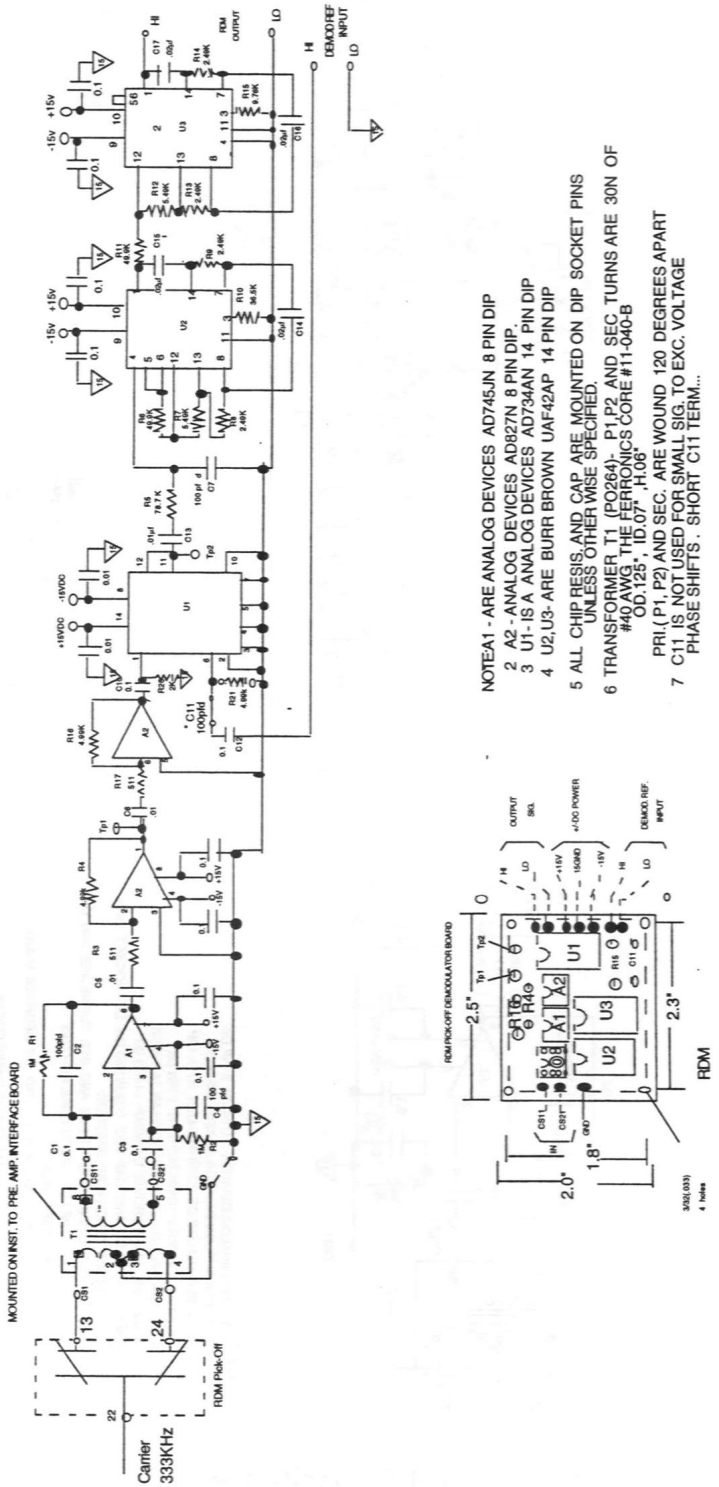

Appendix E-Mathematica Code

Open loop gyro performance calculation

C.Chung
Original: 8/99
Modified: 6/03 (RDM v34 numbers)

This notebook calculates the performance of an open loop gyro with an in-plane RDM and TSM.

eo = permittivity of free space
rhoSi = mass density of single crystal silicon
wR = resonant frequency of RDM
wT = resonant frequency of TSM
qR = Q-factor of RDM
qT = Q-factor of TSM
tSi = thickness of Si device
rRDM = radius RDM
driveGap = gap of capacitive drive of the RDM
nFingers = number of fingers per drive
nDrives = number of drives
driveVolt = drive voltage of the RDM
omegaIn = input rotation for gyro
widthTSM = width of the TSM (parallel to rotation axis)
length of TSM = length of TSM (perpendicular to rotation axis... aka radius of TSM)
capGapTSM = TSM sense capacitor gap

```
<< Graphics`Graphics`
```

Fundamental and Material Constants

```
eo = 8.85 * 10^-12;
rhoSi = 2330;
eSi = 200 10^9;
gSi = 80 10^9;
```

Design Constants

Note: qT is set to 1 since there is no Q amplification due to the resonant frequency mismatch of the coupled oscillators.

```
wR = 2 Pi 3000;
wT = 2 Pi 3000;
qR = 100;
qT = 20;
tSi = 300 *10^-6;
rRDM = 1.5*10^-3;
driveGap = 20 * 10^-6;
nFingers = 13;
nDrives = 8;
driveVolt = 300;
omegaIn = 1/57;
widthTSM = 5 *10^-3;
lengthTSM = 5* 10^-3;
capGapTSM = 10*10^-6 ;
N[nFingers, 4]
```

13.

TSM Equations

```
capPP[x_, y_, z_] := eo x y / z
capCyl[h_, alpha_, r2_, r1_] :=
 eo h / alpha Log[r2 / r1]
```

Total capacitance of the TSM is a parallel plate capacitor for when the angle is zero, in series with a angular, cylindrical capacitor:

```
capTSMTotal[x_, y_, z_, h_, alpha_,
  r2_, r1_] =
    Simplify[
        capPP[x, y, z] *
   capCyl[h, alpha, r2, r1] /
    (capPP[x, y, z] +
      capCyl[h, alpha, r2, r1])
    ]
```

$$\frac{8.85\times10^{-12}\,h\,x\,y\log\left(\frac{r2}{r1}\right)}{\text{alpha}\,x\,y+h\,z\log\left(\frac{r2}{r1}\right)}$$

```
dCapTSM[x_, y_, z_, h_, alpha_, r2_, r1_] =
    - Simplify[
        D[
            capTSMTotal[x, y, z, h,
     alpha, r2, r1], alpha
        ]
    ]
```

$$\frac{8.85 \times 10^{-12}\, h x^2\, y^2 \log\left(\frac{r2}{r1}\right)}{\left(\text{alpha}\, x\, y + h z \log\left(\frac{r2}{r1}\right)\right)^2}$$

```
deltaThetaTSM[lRDM_, qT_, omega_, iT_,
  wT_] :=
      lRDM qT omega / ( iT wT^2)
Integrate[rho (x^2 + z^2), {x, -xo / 2, xo / 2},
  {y, -yo / 2, yo / 2}, {z, -zo / 2, zo / 2}] //
 Simplify
```

$$\frac{1}{12}\, \text{rho}\, \text{xo}\, \text{yo}\, \text{zo}\left(\text{xo}^2 + \text{zo}^2\right)$$

```
iT[rho_, x_, y_, t_] :=
        rho / 12 x y t (x^2 + t^2)
```

RDM Equations

```
phiR[tau_, qR_, iR_, wR_] := tau qR / (iR wR^2)
iR[rho_, r_, t_] := 1 / 8 rho Pi / 2 r^4 t
tau[nFingers_, nDrives_, y_, z_, volt_,
  r_] := nFingers * nDrives 1 / 2 eo y / z
  volt^2 r / 2
lRDM[iR_, phiR_, wR_] := iR * phiR * wR
```

Gyro Equations

```
deltaCapGyroOut
        [omega_, rhoTSM_, lengthTSM_,
  widthTSM_, tTSM_, capGapTSM_, alphaTSM_,
  wT_, qT_,
           rhoRDM_, rRDM_, tRDM_,
  driveGap_, nFingers_, nDrives_, volt_,
  wR_, qR_] :=
       dCapTSM[lengthTSM / 2 - rRDM,
   widthTSM, capGapTSM, widthTSM,
   alphaTSM, lengthTSM / 2, rRDM] *
       deltaThetaTSM[
           lRDM[ iR[rhoRDM, rRDM, tRDM],
               phiR[
                   tau[nFingers, nDrives,
      tRDM, driveGap, volt, rRDM / 2],
               qR, iR[rhoRDM, rRDM, tRDM],
    wR],
               wR] ,
           qT, omega,
   iT[rhoTSM, lengthTSM, widthTSM, tTSM],
           wT]
```

Numerical Calculations

```
tauNum = tau[nFingers, nDrives, tSi,
  driveGap, driveVolt, rRDM]
```
4.65952×10^{-7}
```
iTNum =
 N[iT[rhoSi / 10, lengthTSM / 2, widthTSM, tSi],
  3]
```
4.61631×10^{-13}
```
iRNum = N[iR[rhoSi, rRDM, tSi], 3]
```
6.9482×10^{-13}
```
phiRNum = phiR[tauNum, qR, iRNum, wR]
```
0.188741
```
phiRNum * 180 / Pi
```
10.8141
```
deflectionRDM =
 N[phiRNum rRDM, 4] // EngineeringForm
```
283.112×10^{-6}
```
phiDotRDM = phiRNum * wR
```
3557.69
```
lRDMNum = lRDM[iRNum, phiRNum, wR]
```
2.47195×10^{-9}
```
deltathetaTSMNum =
 deltaThetaTSM[ lRDMNum, qT, omegaIn,
  iTNum, wT]
```
5.28808×10^{-6}
```
thetaNumDeg = deltathetaTSMNum * 180 / Pi
```
0.000302985
```
deflectionTSM =
 deltathetaTSMNum * lengthTSM / 2
```
1.32202×10^{-8}
```
dCapTSMNum =
 dCapTSM[lengthTSM - rRDM, widthTSM,
   capGapTSM, widthTSM, 0, lengthTSM, rRDM] *
  deltathetaTSMNum
```
2.38084×10^{-14}
```
capTSM = capTSMTotal[lengthTSM - rRDM,
  widthTSM, capGapTSM, widthTSM, 0,
  lengthTSM, rRDM]
```
1.54875×10^{-11}
```
capTSMPercentChange = dCapTSMNum / capTSM * 100
```
0.153727

Plots of TSM Capacitance change as a function of design variables

First find the optimal values for the rRDM and lengthTSM.
A plot varying both rRDM and lengthTSM shows this.

```
Plot3D[
    deltaCapGyroOut[omegaIn, rhoSi,
  lengthTSMV, widthTSM, tSi, capGapTSM,
  0, wT, qT,
            rhoSi, rRDMV, tSi, driveGap,
  nFingers, nDrives, driveVolt, wR, qR],
    {lengthTSMV, 3 10^-3 , 10 10^-3},
    {rRDMV, 1 10^-3, 3 10^-3},
    ViewPoint -> {-1.557, -2.141, 2.108}]
```

General::spell1 :
Possible spelling error: new symbol name "lengthTSMV" is similar to existing symbol "lengthTSM".

General::spell1 :
Possible spelling error: new symbol name "rRDMV" is similar to existing symbol "rRDM".

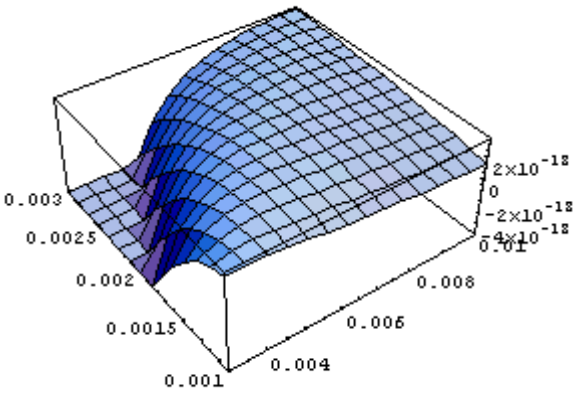

- SurfaceGraphics -

Is there a maximum? We search for one...

```
FindMinimum[
    -    deltaCapGyroOut[omegaIn, rhoSi,
   lengthTSMV, widthTSM, tSi, capGapTSM,
   0, wT, qT,
            rhoSi, rRDMV, tSi, driveGap,
   nFingers, nDrives, driveVolt, wR, qR],
    {lengthTSMV, 6 10^-3, 1 10^-3 ,
  20 10^-3},
    {rRDMV, 2 10^-3, 1 10^-3, 20 10^-3}]
```

$\{-3.29452 \times 10^{-18}, \{\text{lengthTSMV} \to 0.00809674, \text{rRDMV} \to 0.0023796\}\}$

This is deceptive because the answer changes depending on the starting coordinates. We try 3 different starting points for the rRDM

```
FindMinimum[
    -    deltaCapGyroOut[omegaIn, rhoSi,
   lengthTSMV, widthTSM, tSi, capGapTSM,
   0, wT, qT,
            rhoSi, rRDMV, tSi, driveGap,
   nFingers, nDrives, driveVolt, wR, qR],
    {lengthTSMV, 6 10^-3, 1 10^-3 ,
  20 10^-3},
    {rRDMV, 1 10^-3, 1 10^-3, 20 10^-3}]
{-3.29081 × 10^-18,
 {lengthTSMV → 0.00584669, rRDMV → 0.00173363}}
FindMinimum[
    -    deltaCapGyroOut[omegaIn, rhoSi,
   lengthTSMV, widthTSM, tSi, capGapTSM,
   0, wT, qT,
            rhoSi, rRDMV, tSi, driveGap,
   nFingers, nDrives, driveVolt, wR, qR],
    {lengthTSMV, 6 10^-3, 1 10^-3 ,
  20 10^-3},
    {rRDMV, 3.1 10^-3, 1 10^-3, 20 10^-3}]
{-3.2928 × 10^-18,
 {lengthTSMV → 0.006663, rRDMV → 0.00197485}}
Plot[
    {deltaCapGyroOut[omegaIn, rhoSi,
   3 10^-3, widthTSM, tSi, capGapTSM,
   0, wT, qT,
            rhoSi, rRDMV, tSi, driveGap,
   nFingers, nDrives, driveVolt, wR, qR],
    deltaCapGyroOut[omegaIn, rhoSi,
   4 10^-3, widthTSM, tSi, capGapTSM,
   0, wT, qT,
            rhoSi, rRDMV, tSi, driveGap,
   nFingers, nDrives, driveVolt, wR, qR],
    deltaCapGyroOut[omegaIn, rhoSi,
   5 10^-3, widthTSM, tSi, capGapTSM,
   0, wT, qT,
            rhoSi, rRDMV, tSi, driveGap,
   nFingers, nDrives, driveVolt, wR, qR]},
    {rRDMV, 0.5 10^-3 , 2 10^-3}]
```

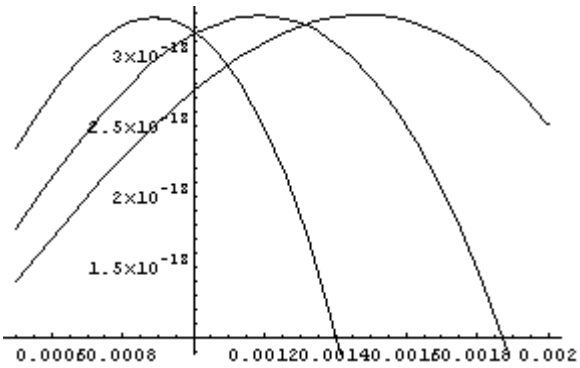

- Graphics -

So, let's set a rRDM and find the optimal lengthTSM:

```
FindMinimum[
    -    deltaCapGyroOut[omegaIn, rhoSi,
   lengthTSMV, widthTSM, tSi, capGapTSM,
   0, wT, qT,
            rhoSi, 1.5*10^-3, tSi,
   driveGap, nFingers, nDrives, driveVolt,
   wR, qR],
    {lengthTSMV, 6 10^-3, 4 10^-3 , 20 10^-3}]
```

$\{-3.28794 \times 10^{-18}, \{\text{lengthTSMV} \to 0.00506903\}\}$

```
FindMinimum[
    -    deltaCapGyroOut[omegaIn, rhoSi,
   lengthTSMV, widthTSM, tSi, capGapTSM,
   0, wT, qT,
            rhoSi, 2*10^-3, tSi, driveGap,
   nFingers, nDrives, driveVolt, wR, qR],
    {lengthTSMV, 6 10^-3, 1 10^-3 , 20 10^-3}]
```

$\{-3.29297 \times 10^{-18}, \{\text{lengthTSMV} \to 0.00675749\}\}$

```
FindMinimum[
    -    deltaCapGyroOut[omegaIn, rhoSi,
   lengthTSMV, widthTSM, tSi, capGapTSM,
   0, wT, qT,
            rhoSi, 1*10^-3, tSi, driveGap,
   nFingers, nDrives, driveVolt, wR, qR],
    {lengthTSMV, 3 10^-3, 3 10^-3 , 20 10^-3}]
```

$\{-3.27351 \times 10^{-18}, \{\text{lengthTSMV} \to 0.00340741\}\}$

```
FindMinimum[
    -    deltaCapGyroOut[omegaIn, rhoSi,
   7 10^-3, widthTSM, tSi, capGapTSM,
   0, wT, qT,
            rhoSi, rRDMV, tSi, driveGap,
   nFingers, nDrives, driveVolt, wR, qR],
    {rRDMV, 6 10^-3, 1 10^-3 , 20 10^-3}]
```

$\{-3.29262 \times 10^{-18}, \{rRDMV \to 0.00205076\}\}$

What is the optimal TSM width? On the one hand, the wider, the greater the cap change, on the other hand, the greater moment of inertia...
It seems that the capacitance change is constant relative to the TSM width. This makes sense, since the cap change is linear with width, and so is momentum of inertia. As a result, the two cancel...

```
Plot[
    deltaCapGyroOut[omegaIn, rhoSi,
  lengthTSM, widthTSMV, tSi, capGapTSM,
  0, wT, qT,
            rhoSi, rRDM, tSi, driveGap,
  nFingers, nDrives, driveVolt, wR, qR],
    {widthTSMV, 1 10^-3 , 20 10^-3}]
```

```
General::spell1 :
  Possible spelling error: new symbol name "widthTSMV" is
    similar to existing symbol "widthTSM".
```

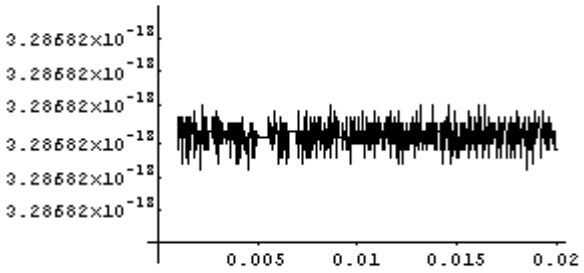

- Graphics -

Does in fact thickness make a difference?... (um... well, it depends on what you like... :-)) The idea is that a bulk micromachined RDM will generate more angular momentum and therefore be more sensitive.

If we vary the RDM and TSM thickness together, we find that thinner is better (1st plot). However, if we vary the RDM thickness but keep the TSM thickness constant, we find that thicker is better for the RDM (2nd plot). We can also see this when we keep the

RDM thickness constant, and vary the TSM thickness (3rd plot). In the 3rd plot, we see that there is a strong function of output deltaCap if the TSM thickness decreases.

```
Plot[
    deltaCapGyroOut[omegaIn, rhoSi,
  lengthTSM, widthTSM, tSiV, capGapTSM,
  0, wT, qT,
            rhoSi, rRDM, tSiV, driveGap,
  nFingers, nDrives, driveVolt, wR, qR],
    {tSiV, 10 10^-6, 500 10^-6}]
```

General::spell1 : Possible spelling error: new symbol name "tSiV" is similar to existing symbol "tSi".

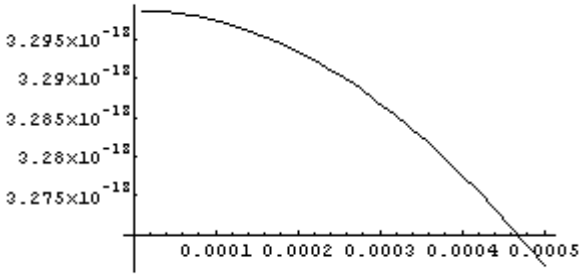

-Graphics-

```
Plot[
    deltaCapGyroOut[omegaIn, rhoSi,
  lengthTSM, widthTSM, tSi, capGapTSM,
  0, wT, qT,
            rhoSi, rRDM, tSiV, driveGap,
  nFingers, nDrives, driveVolt, wR, qR],
    {tSiV, 10 10^-6, 500 10^-6}]
```

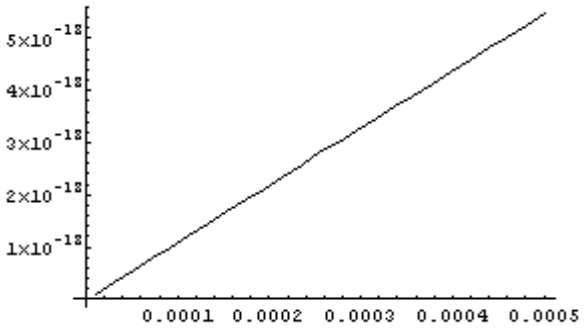

-Graphics-

```
Plot[
    deltaCapGyroOut[omegaIn, rhoSi,
  lengthTSM, widthTSM, tSiV, capGapTSM,
  0, wT, qT,
            rhoSi, rRDM, tSi, driveGap,
  nFingers, nDrives, driveVolt, wR, qR],
    {tSiV, 10 10^-6, 500 10^-6}]
```

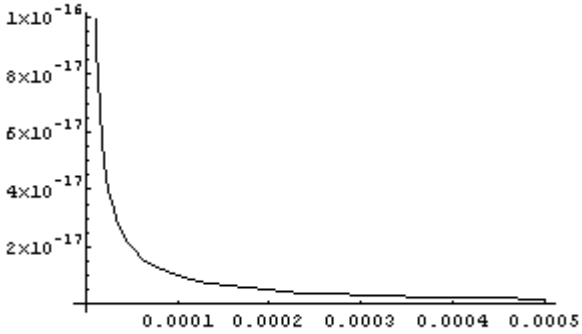

- Graphics -

```
LogLogPlot[
    deltaCapGyroOut[omegaIn, rhoSi,
  lengthTSM, widthTSM, tSiV, capGapTSM,
  0, wT, qT,
            rhoSi, rRDM, tSi, driveGap,
  nFingers, nDrives, driveVolt, wR, qR],
    {tSiV, 10 10^-6, 500 10^-6}]
```

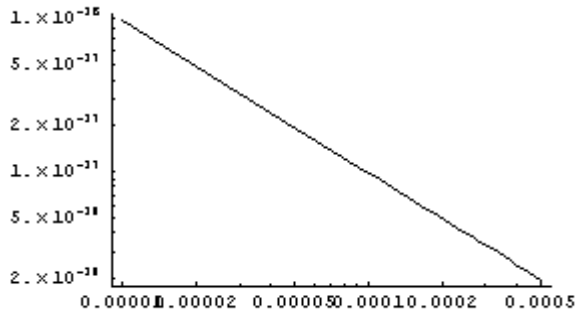

- Graphics -

Varying both the RDM and TSM thicknesses, we see that the biggest signal comes from a thick RDM, and a thin TSM.

```
Plot3D[
    deltaCapGyroOut[omegaIn, rhoSi,
  lengthTSM, widthTSM, tTSMV, capGapTSM,
  0, wT, qT,
            rhoSi, rRDM, tRDMV, driveGap,
  nFingers, nDrives, driveVolt, wR, qR],
    {tTSMV, 10 10^-6, 500 10^-6},
{tRDMV, 10 10^-6, 600 10^-6}]
```

General::spell1 : Possible spelling error: new symbol name "tTSMV" is similar to existing symbol "tTSM".

General::spell : Possible spelling error: new symbol name "tRDMV" is similar to existing symbols {rRDMV, tRDM}.

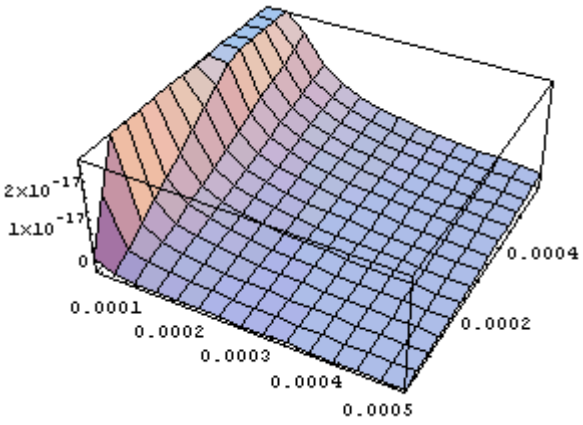

- SurfaceGraphics -

What if we do the same study, but this time vary the thickness of both the RDM and TSM, but also vary the effective density of the TSM...
From the curve, we see that a less dense TSM is certainly better. We see that the sensitivity of the gyro is a strong function of the TSM's effective density, but a weak function of the TSM/RDM thickness

```
Plot3D[
    deltaCapGyroOut[omegaIn, rhoTSMV,
  lengthTSM, widthTSM, tV, capGapTSM,
  0, wT, qT,
            rhoSi, rRDM, tV, driveGap,
  nFingers, nDrives, driveVolt, wR, qR],
    {tV, 10 10^-6, 500 * 10^-6},
{rhoTSMV, rhoSi / 10, 2 * rhoSi}]
```

General::spell1 :
Possible spelling error: new symbol name "rhoTSMV" is similar to existing symbol "rhoTSM".

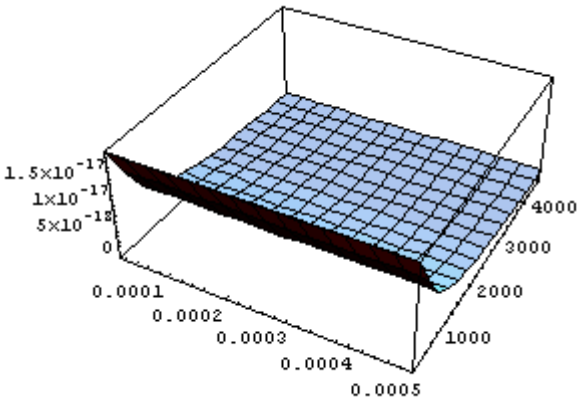

- SurfaceGraphics -

What if we vary the densities of both the RDM and TSM? Is there an optimum? We see that there is no optimum, but a less dense TSM yields the largest cap change. However, we also see that changing the effective density of the RDM affects the cap change very little. This is a bit of a surprise... It may be due to the way the TSM's moment of inertia is calculated. We should go back and change the TSM's I as the sum of the TSM's I and the RDM's I.

```
Plot3D[
    deltaCapGyroOut[omegaIn, rhoTSMV,
  lengthTSM, widthTSM, tSi, capGapTSM,
  0, wT, qT,
           rhoRDMV, rRDM, tSi, driveGap,
  nFingers, nDrives, driveVolt, wR, qR],
    {rhoRDMV, rhoSi / 10, 2 * rhoSi},
{rhoTSMV, rhoSi / 10, rhoSi}]
```

General::spell1 :
Possible spelling error: new symbol name "rhoRDMV" is similar to existing symbol "rhoRDM".

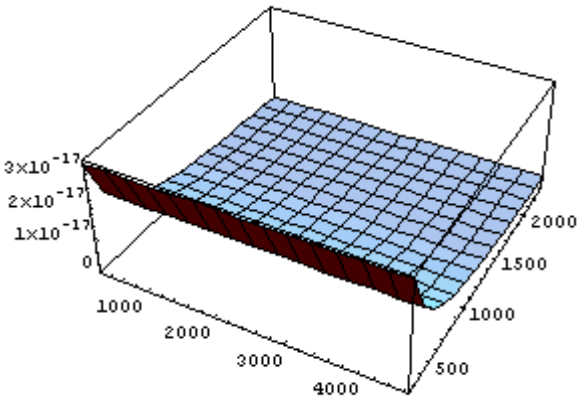

- SurfaceGraphics -

Suppose now we vary both the thickness and the effective density of the TSM...
As expected the thinnest, least dense TSM yields the largest signal. Varying both does increase the output signal by quite a bit, like an order of magnitude.

```
Plot3D[
    deltaCapGyroOut[omegaIn, rhoTSMV,
  lengthTSM, widthTSM, tTSMV, capGapTSM,
  0, wT, qT,
            rhoSi, rRDM, tSi, driveGap,
  nFingers, nDrives, driveVolt, wR, qR],
    {tTSMV, 100 10^-6, 500 10^-6},
{rhoTSMV, rhoSi / 10, rhoSi}]
```

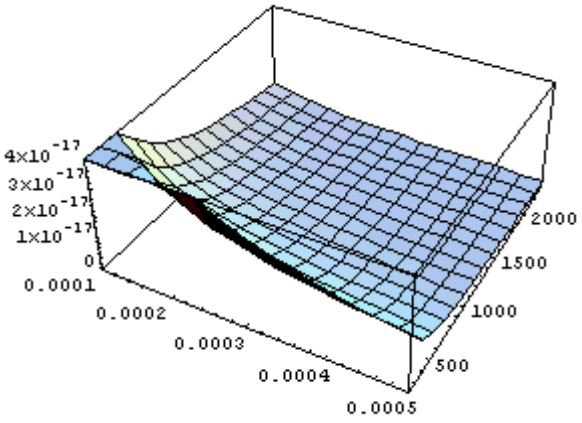

- SurfaceGraphics -

Suppose, we make the effective TSM density 1/2 of silicon, and vary the RDM/TSM thickness. We see that it's the same curve, but the capacitance change is 2x as big.

```
Plot[
    deltaCapGyroOut[omegaIn, rhoSi / 2,
  lengthTSM, widthTSM, tTSMV, capGapTSM,
  0, wT, qT,
            rhoSi, rRDM, tSi, driveGap,
  nFingers, nDrives, driveVolt, wR, qR],
    {tTSMV, 100 10^-6, 500 10^-6}]
```

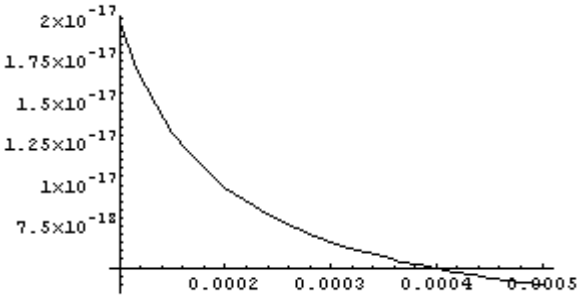

- Graphics -

So we see that a less massive TSM results in higher performace. This is all well and good, but we need to include the loss of capacitance due to the reduction of TSM surface area. (calculation assumes that the holes are significantly bigger than the TSM cap gap) We see that the two effects exactly cancel out. So to get any improvement in performance, the holes of the TSM must be approx the same size as the TSM cap gap.

```
Plot[
    deltaCapGyroOut[omegaIn, rhoSi,
  lengthTSM, areaTSM * widthTSM, tSi,
  capGapTSM, 0, wT, qT,
            rhoSi, rRDM, tSi, driveGap,
  nFingers, nDrives, driveVolt, wR, qR],
    {areaTSM, 0.1, 1}]
```

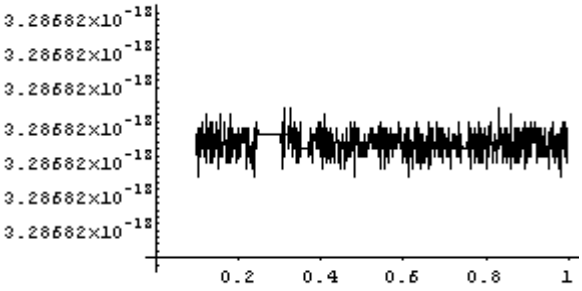

- Graphics -

Calculation of optimal operating frequency & voltage

Now let's graph sensitivity vs. operating frequency and operating voltage.

We plot the sensitivity as a function of both wR and wT, and see that increasing operating frequencies rapidly decreases sensitivity. We can offset this somewhat with higher operating voltages. Plotting this, we see that increasing operating voltage also increases sensitivity. Finally, we can see both of these effects working together in a 3D plot.

```
Plot3D[
deltaCapGyroOut[omegaIn, rhoSi, lengthTSM,
  widthTSM, tSi, capGapTSM, 0, wTV, qT,
            rhoSi, rRDM, tSi, driveGap,
  nFingers, nDrives, driveVolt, wRV, qR],
{wRV, 2 Pi 10^2, 2 Pi 10^4},
{wTV, 2 Pi 10^2, 2 Pi 10^4}]
```

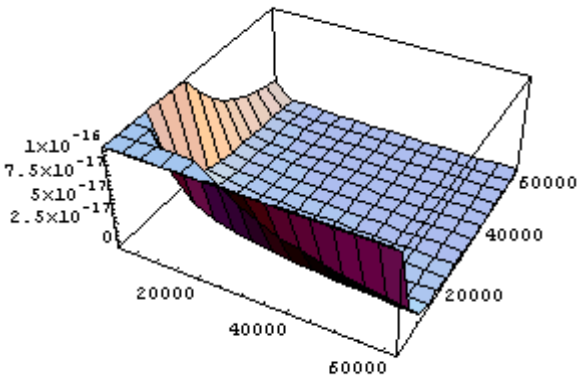

- SurfaceGraphics -

```
Plot3D[
    deltaCapGyroOut[omegaIn, rhoSi,
  lengthTSM, widthTSM, tSi, capGapTSM,
  0, wT, qT,
            rhoSi, rRDM, tSi, driveGap,
  nFingers, nDrives, driveVoltV, wRV, qR],
{wRV, 2 Pi 10^2, 2 Pi 10^4},
{driveVoltV, 10, 1000}]
```

General::spell1 :

Possible spelling error: new symbol name "driveVoltV" is similar to existing symbol "driveVolt".

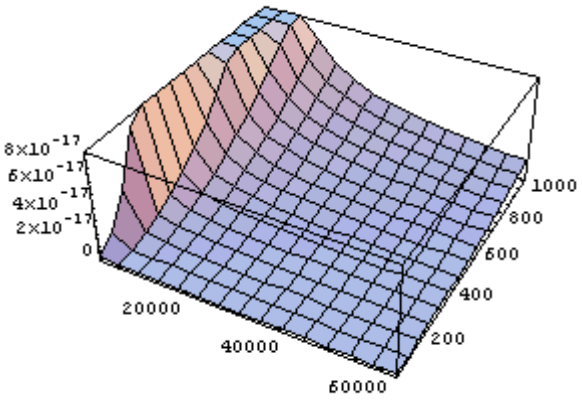

- SurfaceGraphics -

```
LogLogPlot[
    deltaCapGyroOut[omegaIn, rhoSi,
  lengthTSM, widthTSM, tSi, capGapTSM,
  0, wT, qT,
           rhoSi, rRDM, tSi, driveGap,
  nFingers, nDrives, driveVoltV, 2 Pi wR,
  qR],
{driveVoltV, 10, 1000}]
```

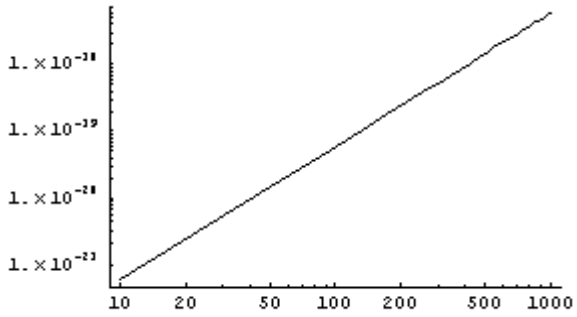

- Graphics -

Calculation of spring dimensions

```
k[i_, w_] := i w^2
N[k[iT[rhoSi, lengthTSM, widthTSM, tSi], wT],
 3]
```

0.023079

```
beamWidthTSM = 40 10^-6;
beamThickTSM = 300 10^-6;
beamLengthTorsion[g_, k_, w_, t_] :=
 2 / 12 g / k w t (w^2 + t^2)
```

```
beamlengthTSM =
 N[beamLengthTorsion[gSi,
   k[iT[rhoSi, lengthTSM, widthTSM, tSi],
    2 Pi 4000], beamWidthTSM, beamThickTSM],
  3]
```
0.000635037
```
k[iRNum, wR]
```
0.000438886
```
beamLengthDefl[e_, k_, w_, t_] :=
 (4 e / k t w^3)^(1 / 3)
beamLengthRDM =
 beamLengthDefl[eSi, k[iRNum, wR],
  50 100^-6, 300 10^-6]
```
4.08874×10^{-7}
```
beamWidthDefl[e_, k_, L_, t_] :=
 (k L^3 / (4 e t))^(1 / 3)
beamWidthRDM =
 beamWidthDefl[eSi, k[iRNum, wR],
  125 10^-3, 300 10^-6]
```
0.0000152859
```
Plot[beamLengthDefl[eSi,
  k[iR[rhoSi, rRDM, tSi], wR], w, tSi],
 {w, 10^-5, 10^-4}]
```

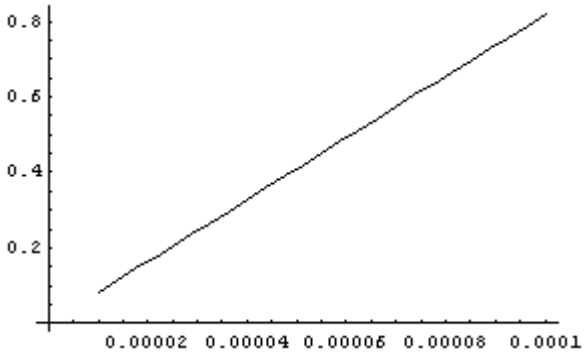

-Graphics-
```
Plot[beamWidthDefl[eSi, k[iRNum, wR],
  L, tSi], {L, 10^-3, 10^-2}]
```

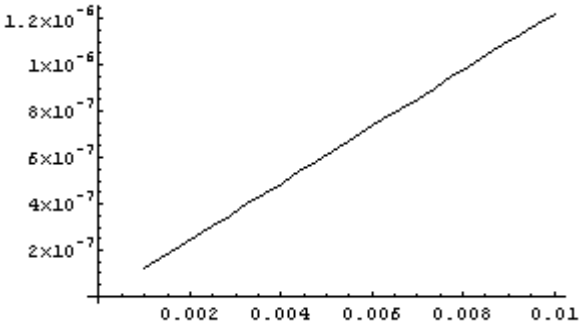

- Graphics -

```
kRayExpress[e_, v_, w_, t_, L_, r_] :=
 4 e w^3 t / L
  ( ( (r^2 / L^2) + 1 - 0.63 (w / t) ) /
    (6 (1 + v)))
Solve[k[ iR[rhoSi, rRDM, tSi], 2 Pi 7100] ==
  kRayExpress[eSi, 0.25, 40 10^-6, tSi,
   L, 0.5 10^-3], L]
```

$$\{\{L \to -0.0000803985 - 0.000487382\,i\},\ \{L \to -0.0000803985 + 0.000487382\,i\},\ \{L \to 0.00151748\}\}$$

```
Plot[
 Sqrt[kRayExpress[eSi, 0.25, wbeam, tSi,
     1.5 10^-3, 0.5 10^-3] /
    iR[rhoSi, rRDM, tSi]] / (2 Pi ),
 {wbeam, 20 10^-6, 40 10^-6}]
```

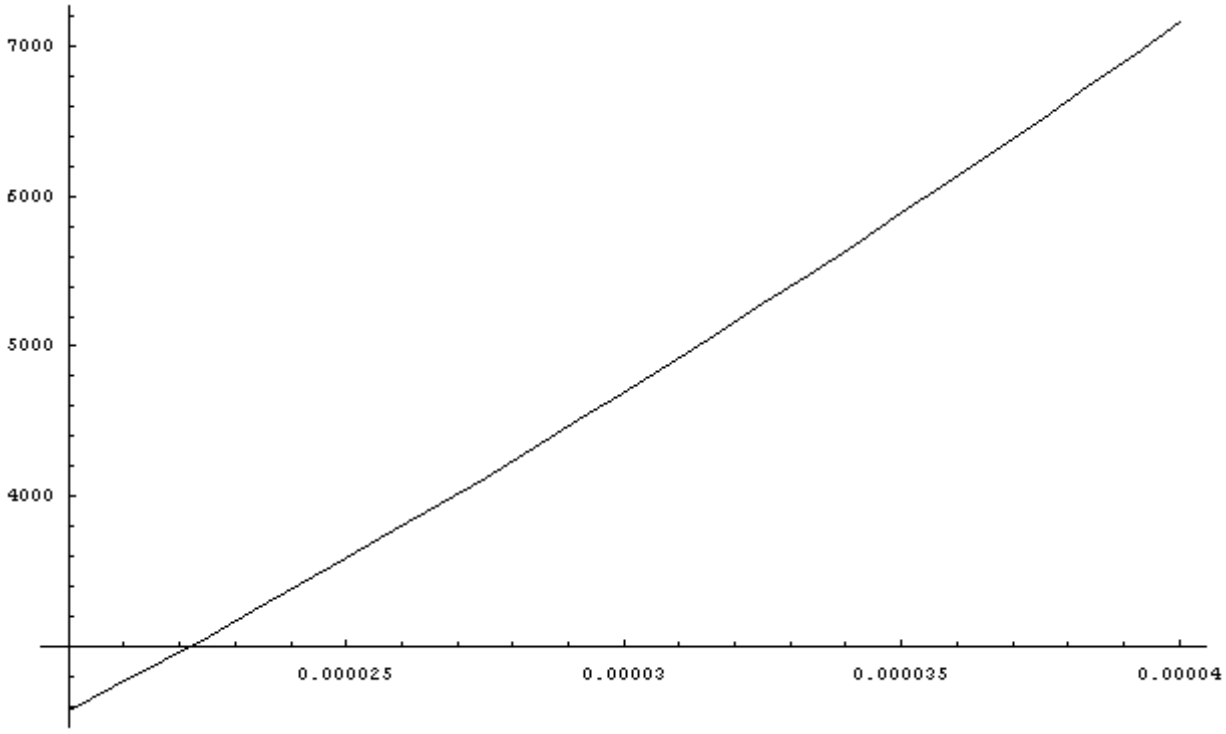

- Graphics -

Tunable Capacitor Design

This section calculates the design parameters for the tunable capacitor for the TSM

```
N[lengthTSM/2*5*Pi/180]
```

0.000218166

```
k_spring[i_, w_] := i w^2
pe_spring[ϕ_, momentOfInertia_, w_] :=
  1/2 k_spring[momentOfInertia, w] ϕ^2
pe_tuningCap[x_, y_, z_, h_, alpha_, r2_, r1_, volt_] :=
  volt^2/2
   (capTSMTotal[x, y, z, h, alpha, r2, r1] +
      capTSMTotal[x, y, z, h, -alpha, r2, r1])
pe_tuningCap[x, y, z, h, α, r2, r1, V]
```

$$\frac{1}{2} V^2$$

$$\left(\frac{8.85\times10^{-12}\, h x\, y \log\left(\frac{r2}{r1}\right)}{h z \log\left(\frac{r2}{r1}\right) - x\, y\, \alpha} + \frac{8.85\times10^{-12}\, h x\, y \log\left(\frac{r2}{r1}\right)}{x\, y\, \alpha + h z \log\left(\frac{r2}{r1}\right)}\right)$$

```
Plot[
  Evaluate[
    Table[pe_spring[ϕ, iTNum, wT] -
        pe_tuningCap[lengthTSM/2 * 2/3, widthTSM/2,
          50 10^-6, widthTSM, ϕ, lengthTSM/2,
          rRDM, volt], {volt, 0, 750, 100}]
  ],
  {ϕ, -1 π/180, 1 π/180}
]
```

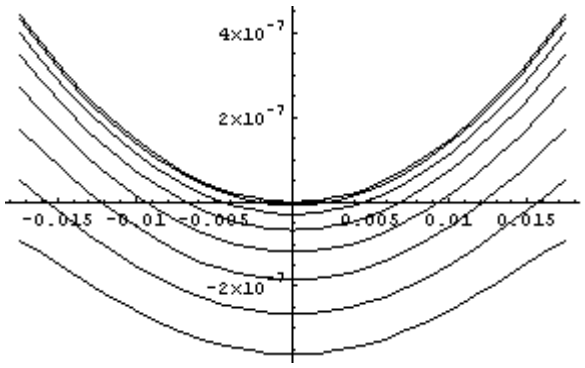

- Graphics -

$$\text{pe}_{\text{tuningCap}}[l_{TSM}/2, w_{TSM}, z_o, w_{TSM}, \phi, l_{TSM}/2, r_{RDM}, V] \text{ //}$$

FullSimplify

$$\frac{1.77\times10^{-11}\, V^2 \log^2\left(\frac{i_{TSM}}{2\, r_{RDM}}\right) l_{TSM}\, w_{TSM}\, z_o}{4\log^2\left(\frac{i_{TSM}}{2\, r_{RDM}}\right) z_o^2 - \phi^2\, i_{TSM}^2}$$

Series[$\text{pe}_{\text{tuningCap}}[l_{TSM}, \text{width}_{TSM}, z_o, w_{TSM}, \phi, l_{TSM}, r_{RDM}, V]$ // FullSimplify, $\{\phi, 0, 5\}$]

$$\frac{8.85\times10^{-12}\, V^2\, l_{TSM}\, \text{width}_{TSM}}{z_o} +$$

$$\frac{8.85\times10^{-12}\, V^2\, i_{TSM}^3\, \text{width}_{TSM}^3\, \phi^2}{\log^2\left(\frac{i_{TSM}}{r_{RDM}}\right) w_{TSM}^2\, z_o^3} +$$

$$\frac{8.85\times10^{-12}\, V^2\, i_{TSM}^5\, \text{width}_{TSM}^5\, \phi^4}{\log^4\left(\frac{i_{TSM}}{r_{RDM}}\right) w_{TSM}^4\, z_o^5} + O(\phi^6)$$

```
Solve[k == 8.849999999999999`*^-12 V^2 l^3 widthTSM/z_o /.
    {V → 200, z_o → 50 10^-6, k → iTNum wT^2},
  l]
```

$$\left\{\left\{l \to -\frac{0.372007 + 0.644334\,i}{\sqrt{\text{width}_{\text{TSM}}^3}}\right\},\right.$$

$$\left.\left\{l \to -\frac{0.372007 - 0.644334\,i}{\sqrt{\text{width}_{\text{TSM}}^3}}\right\}, \left\{l \to \frac{0.744013}{\sqrt{\text{width}_{\text{TSM}}^3}}\right\}\right\}$$

```
Plot[
  Evaluate[
    Table[pe_spring[ϕ, iTNum, wT] - 1/(50 10^-6
        (2.2124999999999997`*^-12 volt^2 lengthTSM
          widthTSM) -
        (5.531249999999999`*^-13 volt^2 lengthTSM^3
            widthTSM ϕ^2)) /
        (Log^2(lengthTSM/(2 rRDM)) (50 10^-6)^3),
      {volt, 0, 500, 50}]
  ],
  {ϕ, -1 π/180, 1 π/180}
]
```

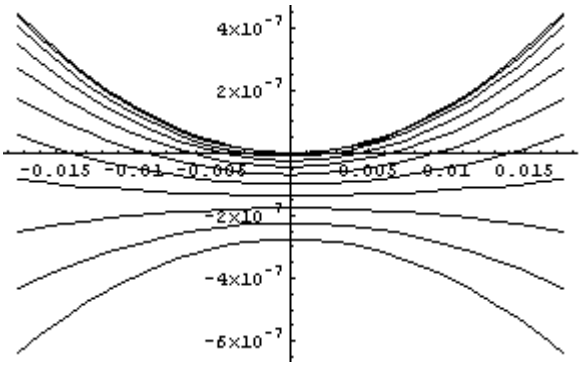

- Graphics -

$$\text{Plot}\Big[\text{Evaluate}\Big[\text{Table}\Big[pe_{spring}[\phi, iTNum, wT] - \frac{1}{50\,10\,\hat{}\,-6}(2.2124999999999997\hat{}*\hat{}-12\ volt^2\ lengthTSM\ widthTSM) - (5.531249999999999\hat{}*\hat{}-13\ volt^2\ lengthTSM\hat{}\,3\ widthTSM\,\phi^2)\Big/\Big(\log^2\Big(\frac{lengthTSM}{2\,rRDM}\Big)(50\,10\,\hat{}\,-6)\hat{}\,3\Big) - (1.3828124999999998\hat{}*\hat{}-13\ volt^2\ lengthTSM\hat{}\,5\ widthTSM\,\phi^4)\Big/\Big(\log^4\Big(\frac{lengthTSM}{2\,rRDM}\Big)(50\,10\,\hat{}\,-6)\hat{}\,5\Big), \{volt, 0, 500, 50\}\Big]\Big], \{\phi, -1\,\pi/180, 1\,\pi/180\}\Big]$$

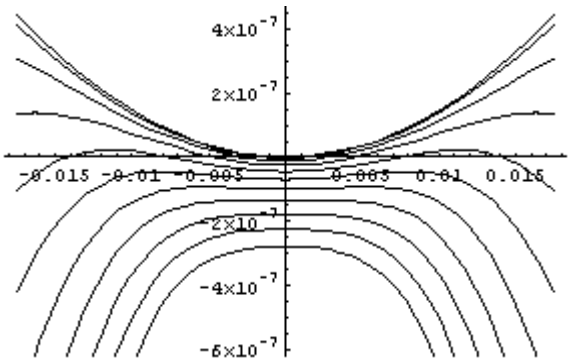

- Graphics -

Miscellanea

Clamped-Clamped Beam analysis for the design of the TSM electrodes

The upper electrodes must fulfill the following requirements:
1. must not deflect under load such that they distort the output measurement
2. must be able to actuate the TSM
3. must be able to tune the TSM's resonant frequency

The following would be nice:

1. easy to fabricate, i.e. SU-8 sac layer
2. be wirebondable (i.e. made of Al)

Physical Constants:

$e_{Al} = 70\,10\text{^}9$
$\rho_{Al} = 2710$
$e_{NiFe} = 210\,10\text{^}9$
$\rho_{NiFe} = 8800$
70000000000
2710
210000000000
8800

Deflection of a clamped-clamped beam with an applied pressure (electrostatic field) has the following form:

v = q x^2 (L - x)^2/24 E I

which means that the max deflection is at the center, x=L/2, due to symmetry:

delta = q L^4/384 E I

where I for a beam of rectangular cross section is:

I=wt^3/12

and so the final expression for delta is:

$$\delta = q \frac{1}{32 E_{Young's\,Mod}} \frac{L^4}{w t^3}$$

$$\text{deflectionTSMElectrode[eYM\_, L\_, w\_, t\_, q\_] := } q \frac{1}{32\,\text{eYM}} \frac{L^4}{w t^3}$$

$$\text{kTSMElectrode[eYM\_, w\_, t\_, L\_] := } \frac{32\,\text{eYM}\, w t^3}{L^4}$$

We require that the TSM electrode's deflection due to an actuation voltage be an order of magnitude greater than the translational deflection of the tip of TSM due to the torsional spring:

$$k_{torsion}[g\_, w\_, t\_, L\_] := 2 \frac{g}{12} w t \frac{(w^2 + t^2)}{L}$$

$$\text{forceAtTip} = k_{torsion}[gSi,\ 20\,10\text{^}-6,\ 300\,10\text{^}-6,\ 10\text{^}-3]\ (5\,Pi/180) / (lengthTSM/2)\ //\ N$$

```
0.252444
deflectionTSMElectrode[e_NiFe, 250 10^-6, 250 10^-6,
    20 10^-6, forceAtTip / (250 10^-6)] // N //
  EngineeringForm
293.485 × 10^-9
Solve[0.25 10^-6 ==
    deflectionTSMElectrode[e_NiFe, L, 10^-3,
      25 10^-6, forceAtTip / L], L]
{{L → -0.000235121 - 0.000407241 i},
  {L → -0.000235121 + 0.000407241 i}, {L → 0.000470242}}
```

Converted by *Mathematica* August 4, 2003

Appendix F –
Surface Micromachining of TSM Electrodes

Uncrosslinked SU-8 as a Sacrificial Material

Charles Chung* and Mark Allen**

*cccatl@hotmail.com, (404) 894-9908, Microelectronics Research Center, 791 Atlantic Drive, Georgia Institute of Technology, Atlanta, Georgia USA 30332-0269

**mark.allen@ece.gatech.edu, (404) 894-0000, Microelectronics Research Center, 791 Atlantic Drive, Georgia Institute of Technology, Atlanta, Georgia USA 30332-0269

Abstract

SU-8 has gained wide popularity as a surface micromachining material, mostly due to characteristics of the epoxy in the crosslinked state. However, uncrosslinked SU-8 also has interesting properties, particularly as a sacrificial layer in surface micromachined processes. Uncrosslinked SU-8 can maintain a flat, stable surface for subsequent surface micromachining; it is chemically resistant to subsequent surface micromachining; and, uncrosslinked SU-8 can be removed selectively in the presence of a wide range of materials, including metals, semiconductors, oxides, ceramics, and many polymers. The processing of uncrosslinked SU-8 as a sacrificial layer is mostly unchanged from the conventional method. Care must be taken to not expose the SU-8 to the UV radiation used in subsequent layers and to avoid significant movement of the uncrosslinked SU-8 when taken above the glass transition temperature (~65C). In this paper, uncrosslinked SU-8 as a sacrificial layer is demonstrated, the fabrication details are described, and an application is shown.

Introduction

Surface micromachined, mechanically free microstructures often utilize a sacrificial layer to release the mechanically free part. Sacrificial layers have several necessary characteristics. They must provide a stable, flat platform for subsequent surface micromachining. They must be chemically resistant to subsequent processing. And, finally, they must remove easily, cleanly, and selectively to release the mechanically free structure. Only a few materials fulfill these requirements, the most widely used in the MEMS field being SiO_2, poly-silicon, and copper.

The introduction of high aspect ratio microfabrication technologies, such as SU-8 epoxy, has greatly expanded the accessible design space for micrometer scale systems. These micromachining technologies extend MEMS designs into the 3rd dimension by tens or even hundreds of micrometers. However, above a certain thickness, approximately several tens of micrometers, the commonly used sacrificial materials become more difficult to use. It becomes difficult to deposit SiO_2 and poly-Si to these thicknesses, and the deposition and selective removal of copper becomes more and more time intensive the thicker the sacrificial layer. Additionally, these materials impose significant fabrication constraints, e.g. SiO_2 and poly-Si require elevated temperatures for deposition, and copper is often selectively removed with strongly basic or acidic etchants for appreciable removable rates. Moreover, electrodeposited copper requires significant additional fabrication complexity, which entails deposition of an insulating layer,

deposition of a seed layer, patterning the electrodeposition mold, establishment of electrical contact to the seed layer, and finally selective removal of all of the above materials.

An alternative sacrificial material may be found upon closer examination of SU-8. SU-8 is a negative resist and its characteristics in the crosslinked state make it highly suitable for a number of structural purposes that has been widely discussed in the literature. However, uncrosslinked SU-8 also has a number of interesting properties. Below the glass transition temperature, ~65C, SU-8 is highly chemically resistant, maintains a flat, stable surface for subsequent photolithography, and because uncrosslinked SU-8 is developed with solvents, it may be easily and selectively removed in the presence of a wide range of materials, such as semiconductors, metals, ceramics, and certain polymers. Finally, since uncrosslinked SU-8 is deposited simultaneously with the crosslinked SU-8, a significant amount of fabrication complexity may be avoided.

Fabrication Process

The typical method for SU-8 processing is to spin, pre-bake, expose, post-bake, and immediately develop. However, if the development step is postponed, then the uncrosslinked SU-8 remains and may be used as a sacrificial layer. The general process flow for using uncrosslinked SU-8 as a sacrificial material is shown in figure 1. For the most part, the SU-8 process remains unaltered, however the key changes are the long post-exposure bake and the chromium deposition.

The long post exposure bake minimizes amount of reflow that the uncrosslinked SU-8 undergoes, if taken above the glass transition temperature, T_g~65C. Without this step, if the uncrosslinked SU-8 is taken to a high enough temperature, e.g. to softbake photoresist, then it flows, which may move or deform structures above the uncrosslinked SU-8. A long post-exposure bake, on the order of several hours, depending on the thickness of the layer, suppresses this flow. This displacement may also be mitigated by having small areas of uncrosslinked SU-8. Large continuous areas allow greater displacements in the uncrosslinked SU-8, thus smaller areas prevent this movement.

The purpose of the chromium deposition is to prevent exposure of the uncrosslinked SU-8 sacrificial layer from subsequent lithography. At least 250Å of chromium must be deposited for a sufficiently opaque layer. It should be noted that this thin film of Cr may also conveniently serve as an excellent adhesion layer. SU-8 is crosslinked by the release of protons by exposure to photons of UV energy or greater. As a result, no metal deposition technologies that expose the uncrosslinked SU-8 to photons of these energies may be used. Both sputtering and electron beam metal deposition technologies emit high energy photons that can crosslink the unexposed SU-8. However, filament evaporators vaporize metal by resistively heating a crucible. If the temperature of the evaporated metal and crucible is low enough such that the emitted blackbody radiation has a sufficiently low amount of energy in the UV or above, then metal may be deposited on uncrosslinked SU-8 without affecting it. Fortunately, at a pressure of 1μTorr, Cr sublimates at approximately 977C. At this temperature, the peak of the blackbody radiation is theoretically calculated to be approximately 4μm, well in the infrared range, and therefore, virtually no crosslinking photons are generated. Observing

the metal and crucible during deposition, the color is a dull orange-red, corroborating low energy photon radiation.

Once the SU-8 has metal deposited on it, subsequent lithography is possible since the crosslinked versus uncrosslinked SU-8 differs in appearance. The Cr on top of the crosslinked SU-8 appears smoother and more reflective. It is easily visually distinguished both by the naked eye as well as under magnification. Subsequent surface micromachining may then be continued on top of the SU-8.

Application

The motivation for this exploration was to fabricate capacitive electrodes for a bulk-machined, torsional silicon oscillator. The electrodes function as both sensors and actuators. The requirements are that the electrodes must be conductive, mechanically stiff compared to the motion of the oscillator, and electrically insulated from the silicon oscillator.

In addition to these requirements, the performance of the device benefited from a large separation between the silicon and the metal electrode. The electrode gap needed to be on the order of 125μm to allow the oscillator sufficient amplitude in its motion. Parasitic capacitance needed to be minimized, which implied that the anchors for the capacitive electrodes should be separated from the silicon substrate as widely as possible. Finally, large actuation voltages were needed, on the order of hundreds of volts, which a large gap facilitated by increasing the dielectric breakdown voltage.

A mechanically stiff, yet conductive upper electrode was fabricated using electroplated metal. The electrodeposition process enables a thick, relatively stress-free conductive layer to be deposited. Given the dimensions of the electrode, 3mm long and 250μm wide, a 25μm thick layer was sufficiently stiff to be an order of magnitude stiffer than the torsional springs that supported the oscillating silicon body.

The typical way that our group would fabricate these electrodes would be to use a Cu sacrificial layer. A comparison of the two methods is illustrated in table 1.

The SU-8 sacrificial layer reduces the processing time and complexity significantly. Moreover, the plating time necessary to deposit and subsequently remove 125μm of copper would be on the order of two days (optimistically) and is avoided. With the 125 micrometer separation between the silicon oscillator and the upper electrode, the parasitic capacitance is reduced by two orders of magnitude, since the only alternative was thermal silicon dioxide which may be grown to approximately 1μm. The detailed account of how the electrodes were fabricated is described in table 2.

A view of the electrodes from overhead is shown in figure 2. A side view is shown in figure 3. The removed SU-8 underneath the NiFe electrodes is clearly seen. A close-up of the one of the standoffs is shown in figure 4. The height of the SU-8 standoff is approximately 125μm, and the thickness of the NiFe is approximately 35μm.

This fabrication technique may be additionally used in conjunction with deep reactive ion etching. Once the electrodes were fabricated and the uncrosslinked SU-8 was removed, the photoresist mask for the oscillator was patterned on the back side of the wafer. The silicon was then etched from the back side through the wafer using deep reactive ion etching. A picture of the electrodes with the bulk-machined silicon is shown in Figure 5.

Conclusion

Uncrosslinked SU-8 as a sacrificial material has been demonstrated. The process is mostly unchanged from the typical SU-8 process, however there are a few changes to which attention must be paid, i.e. a long post-exposure bake and filament evaporation of chromium. When applicable, uncrosslinked SU-8 may reduce fabrication time and complexity. This technique seems particularly well suited for applications that require sacrificial layers on the order of tens or hundreds of micrometers thick. Finally, an application of this technique was illustrated and its compatibility with deep reactive ion etching of silicon is demonstrated.

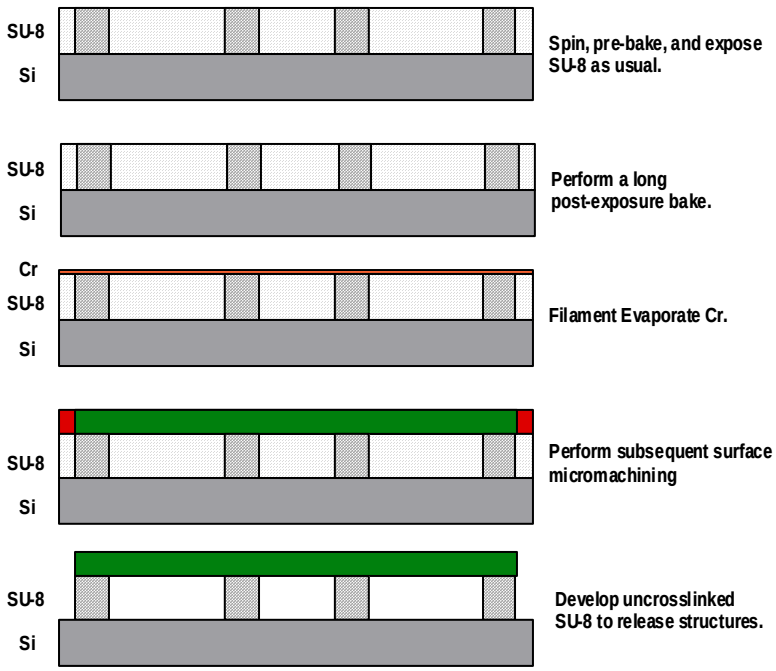

Figure 1: General process flow for using uncrosslinked SU-8 as a sacrificial layer.

Processing with Cu sacrificial layer

1. Deposit insulator to separate silicon substrate from electrode
2. Deposit electroplating seed layer
3. Deposit photoresist plating mold for Cu sacrificial layer
4. Electroplate copper
5. Remove photoresist mold
6. Deposit another photoresist plating mold for NiFe electrode
7. Electroplate NiFe
8. Remove photoresist mold
9. Selectively remove copper
10. Remove electroplating seed layers
11. Remove insulator

Processing with SU-8 sacrificial layer

1. Spin, pre-bake, expose, and post-bake SU-8
2. Deposit seed layer for NiFe electrodeposition
3. Deposit and define photoresist plating mold
4. Electroplate NiFe
5. Simultaneously remove uncrosslinked SU-8, seed layers, and photoresist via liftoff (selective removal of each layer is also possible)

Table 1: Comparison of SU-8 sacrificial layer technique with Cu sacrificial layer

1. Clean silicon wafer using RCA clean
2. Spin Microchem SU-8 2025 (1000rpm/30s)
3. Softbake SU-8 on hotplate (ramp from room temperature to 100C/hold at 100C for 1 hour)
4. Expose (50s@20mW/cm^2)
5. Post-bake SU-8 on hotplate(100C/~12 hours)
6. Deposit Cr/Cu/Cr electroplating seed layer with filament evaporator (500Å@3Å/s for Cr and 2500Å@3Å/s for copper)
7. Spin Clariant AZ4620 photoresist for plating mold (1000rpm/30s)
8. Allow AZ4620 to rest for 5 minutes
9. Softbake photoresist on hotplate (100C/8min)
10. Expose photoresist (8min/5mW/cm^2@365nm)
11. Develop photoresist in AZ400 (diluted 3:1) for ~3 minutes
12. Dip wafer in dilute HCl to remove protective layer of Cr
13. Electroplate NiFe (35um)
14. Simultaneously remove SU-8, photoresist, and seed layers using Shipley 1112 photoresist stripper for about 25 minutes (10 minutes with agitation). At the beginning, do a quick dip in an ultrasound bath to breakup the seed layer. (Each layer may be removed individually with acetone/methanol for photoresist, $NH_4OH + CuSO_4$ for copper, dilute HCl for Cr, and PGMEA for the uncrosslinked SU-8)

Table 2: Detailed account of fabrication of the NiFe electrodes

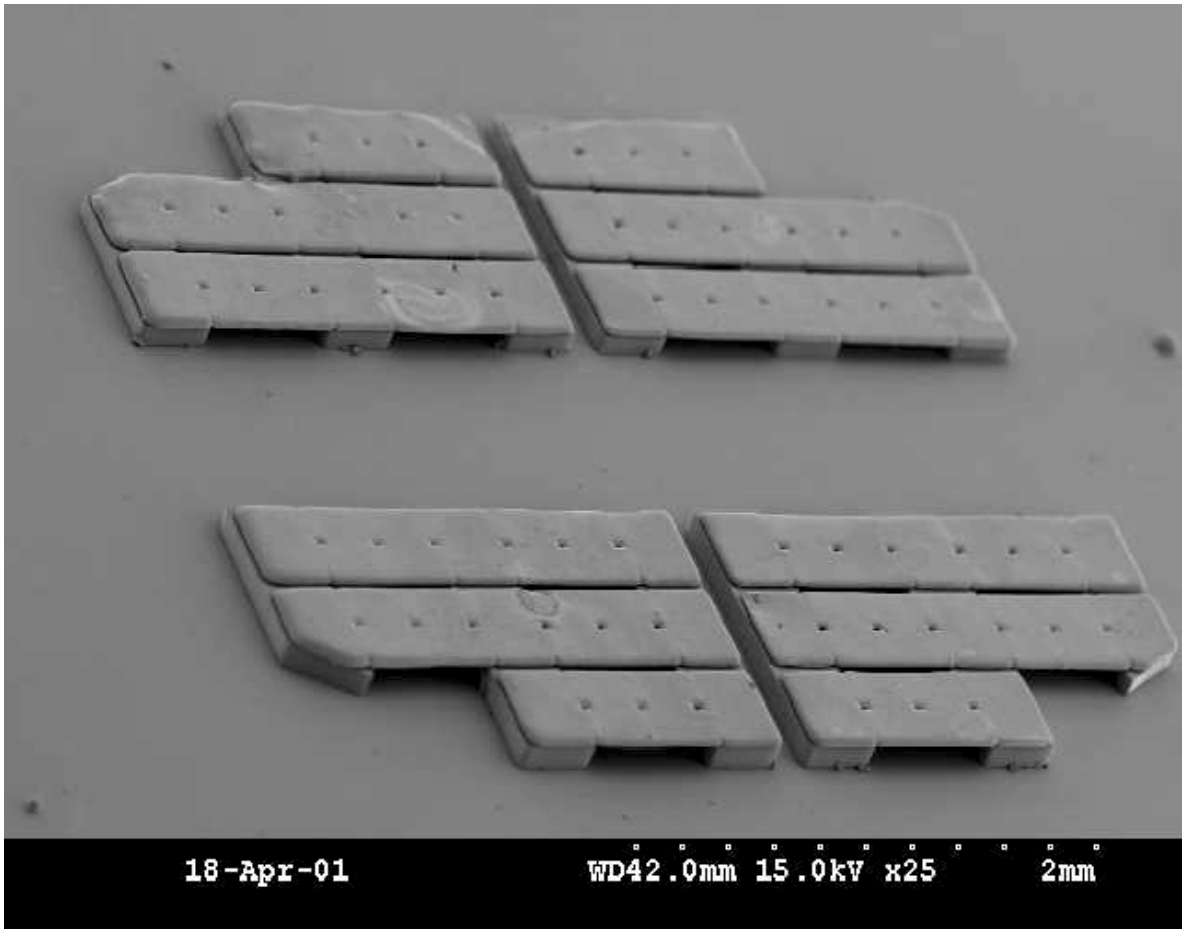

Figure 2: Overview of upper NiFe electrodes for silicon oscillator. The uncrosslinked SU-8 has been removed. Multiple electrodes are fabricated so that some may serve as actuators and others as capacitors.

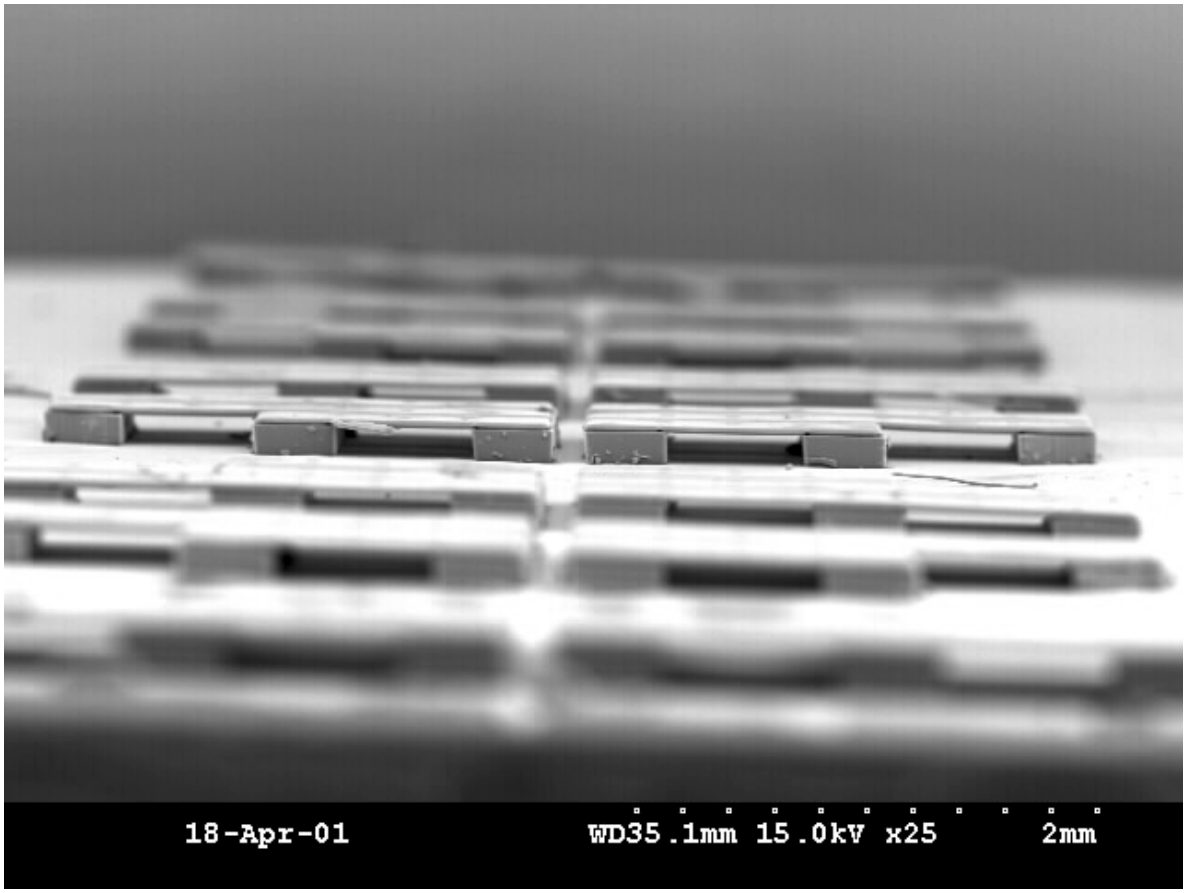

Figure 3: Side view of the electrodes. The uncrosslinked SU-8 is clearly removed, since it is possible to see through, underneath the NiFe electrodes.

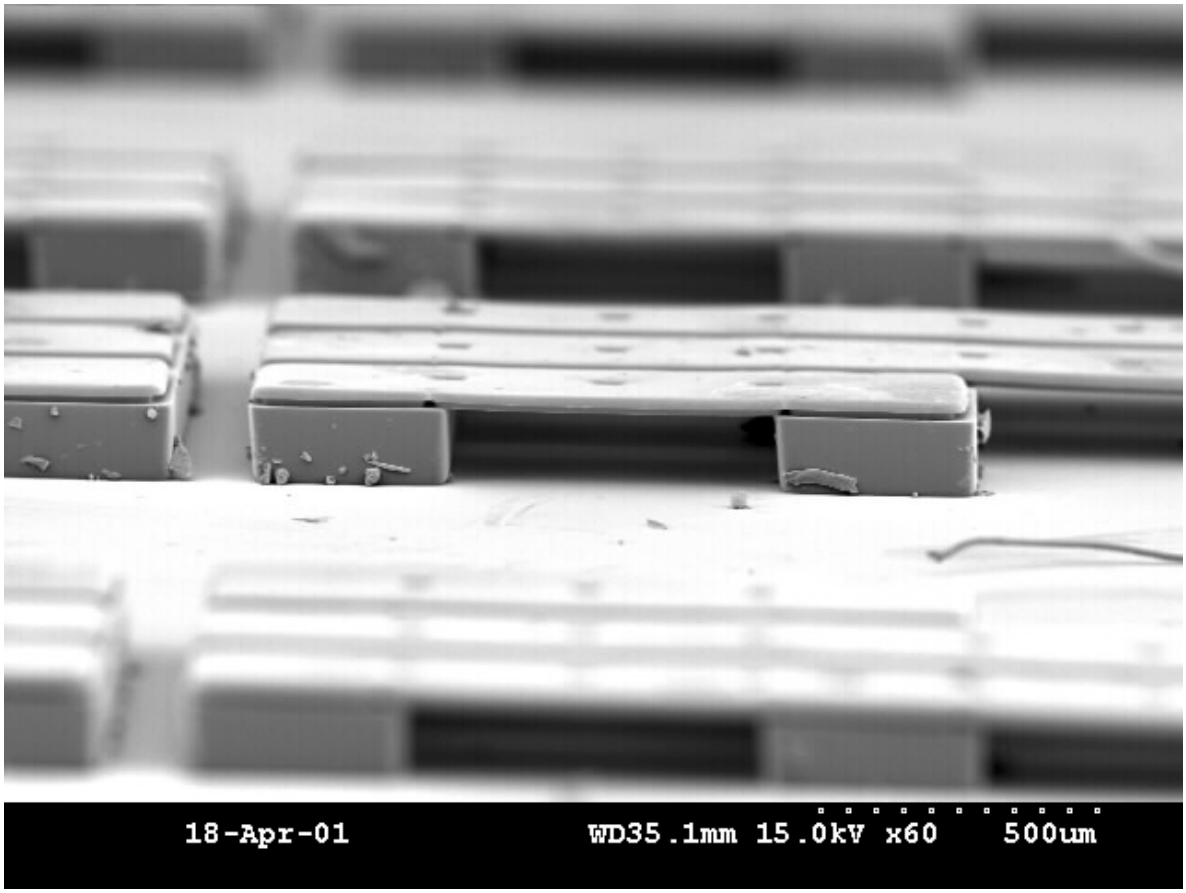

Figure 4: Close up of the SU-8 standoff that insulates the upper electrode from the silicon substrate. The SU-8 structure is 125μm thick and the electroplated NiFe is approximately 35μm thick. The thickness of the SU-8 layer allows for a minimum parasitic capacitance and a maximum actuation voltage.

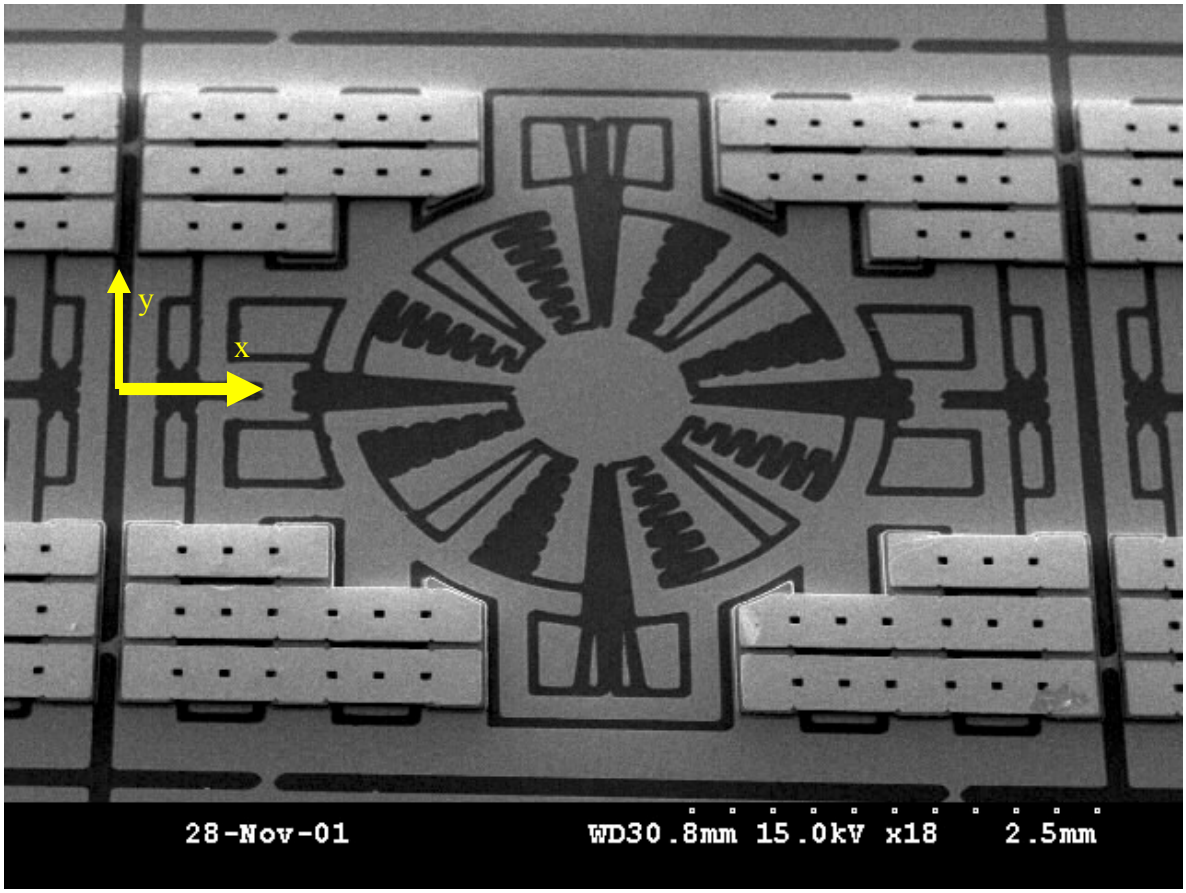

Figure 5: The silicon oscillator is etched out of the bulk silicon using deep reactive ion etching. The center rotates about an axis perpendicular to the surface, and its movement induces oscillations in the outer oscillator, which rotates about the x-axis. The motion of the outer member is allowed by the removal of the uncrosslinked SU-8 underneath the electrodes. The NiFe electrodes serve as both capacitive sensors and electrostatic actuators, and they are insulated from the Si substrate by 125μm of crosslinked SU-8.

Appendix G
Mathematica Code for Electronic Output

```
In[1]:= << Graphics`Graphics`
In[2]:= capo1 = 5 10^-12;
        capo2 = 5 10^-12;
        dcap = 50 10^-15;
        vo = 7;
        wC = 1.8 10^3;
        wT = 333 10^3;
In[8]:= cap1[t_] := capo1 + dcap Exp[I wC t]
        cap2[t_] := capo2 - dcap Exp[I wC t]
        vtest[t_] := vo Exp[I wT t]
In[11]:= current1[t_] =
          Evaluate[D[cap1[t] * vtest[t], t]]
         current2[t_] =
          Evaluate[D[cap2[t] * vtest[t], t]]
         currentTot[t_] = current1[t] - current2[t]
```

Out[11]= $$6.3\times10^{-10}\, i\, e^{334800.\, i\, t} + 2331000\, i\, e^{333000\, i\, t}\left(\frac{1}{200000000000} + \frac{e^{1800.\, i\, t}}{20000000000000}\right)$$

Out[12]= $$-6.3\times10^{-10}\, i\, e^{334800.\, i\, t} + 2331000\, i\, e^{333000\, i\, t}\left(\frac{1}{200000000000} - \frac{e^{1800.\, i\, t}}{20000000000000}\right)$$

Out[13]= $$1.26\times10^{-9}\, i\, e^{334800.\, i\, t} - 2331000\, i\, e^{333000\, i\, t}\left(\frac{1}{200000000000} - \frac{e^{1800.\, i\, t}}{20000000000000}\right) + 2331000\, i\, e^{333000\, i\, t}\left(\frac{1}{200000000000} + \frac{e^{1800.\, i\, t}}{20000000000000}\right)$$

```
In[14]:= currentTot[t] // N // Expand
```

Out[14]= $$(0. + 0.\, i)\, 2.71828^{(0. + 333000.\, i)\, t} + (0. + 2.3436\times10^{-7}\, i)\, 2.71828^{(0. + 334800.\, i)\, t}$$

```
In[15]:= Plot[Im[currentTot[t]], {t, 0, 20 / wC}]
```

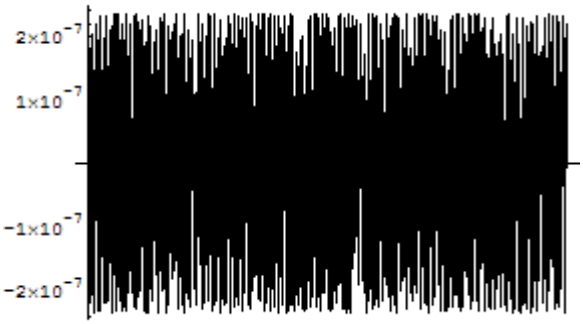

Out[15]= - Graphics -

In[16]:=
```
Im[current[t] * 1 / (1 + I rfilt wf capfilt)]
```

Out[16]= $\text{Im}\left[\frac{\text{current}[t]}{1 + i\ \text{capfilt}\ \text{rfilt}\ \text{wf}}\right]$

In[29]:=
```
Plot[
 Re[currentTot[t] *
   1 / (1 + I rfilt wT capfilt)], {t, 0, 20 / wC},
 PlotRange → All]
```

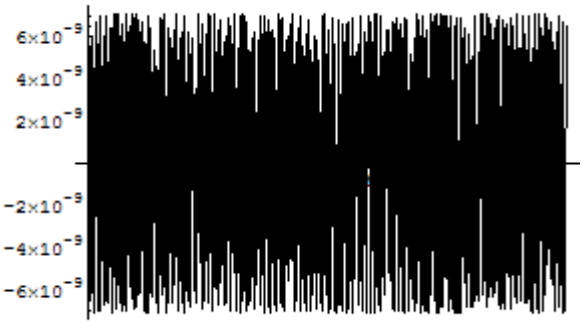

Out[29]= - Graphics -

In[18]:=
```
vfilt[w_, t_] = vo * Exp[I wf t]
capfilt = 10^-12
rfilt = 10^8
vo = 10
```

```
General::spell1 :
 Possible spelling error: new
   symbol name "vfilt" is similar
   to existing symbol "rfilt".
```

Out[18]= $7\, e^{i\,t\,wf}$

Out[19]= $\frac{1}{1000000000000}$

Out[20]= 100000000

Out[21]= 10

In[22]:=
```
voutfilt[w_, t_] =
  vfilt[w, t] * rfilt I wf
   capfilt / (1 + rfilt I wf capfilt)
```

Out[22]=
$$\frac{7\, i\, e^{i\, t\, wf}\, wf}{10000\left(1+\frac{i\, wf}{10000}\right)}$$

In[23]:=
```
rfilt wf capfilt / (1 + rfilt wf capfilt)
```

Out[23]=
$$\frac{wf}{10000\left(1+\frac{wf}{10000}\right)}$$

In[24]:=
```
LogLogPlot[1 / (1 + rfilt wf capfilt),
  {wf, 0, 10^6}]
```

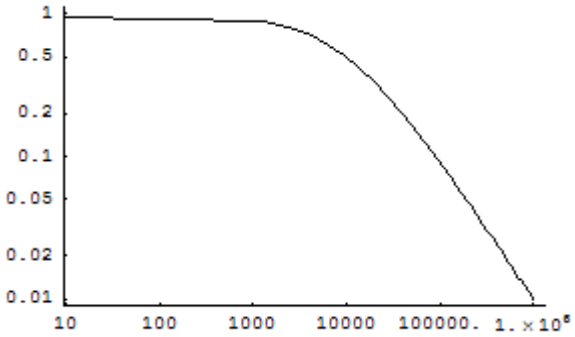

Out[24]= - Graphics -

References

[ADI2003a] Analog Devices. ADXRS150 Specification Sheet.

[ADI2003b] Analog Devices. ADXRS300 Specification Sheet.

[Anceau2002] Morillon, B.; Dilhac, J.-M.; Ganibal, C.; Anceau, C. "Power device insulation by Al thermomigration." 6th International Seminar on Power Semiconductors. ISPS'02. Proceedings p.145-9. 2002

[Bouwstra1993] Spiering, V.L., Bouwstra, S., Spiering, R., "On chip decoupling zone for package-stress reduction." Sensors and Actuators, A.39, 1993, 149-156. (http://bell.mma.edu/~jmcent/siliconprop.htm)

[Cline1976a]T.R. Anthony and H.E. Cline. "Deep-Diode Arrays." J. Appl. Phys. Vol. 47, no. 6, p.2550-2557. June, 1976.

[Cline1976b] T.R. Anthony, J.K. Boah, M.F. Chang, H.E. Cline. "Thermomigration Processing of Isolation Grids in Power Structures." IEEE Transactions on Electron Devices. Vol. ED-23, no. 8, p. 818-823. August, 1976.

[Cline1976c] H.E. Cline and T.R. Anthony. "Thermomigration of Aluminum Rich Liquid Wires through Silicon." Journal of Applied Physics. V74, n6, p2332-2336. 1976.

[Dilhac1999] Dilhac, J.-M.; Cornibert, L.; Morillon, B.; Roux, S.; Ganibal, C. "Industrial relevance of deep junctions produced by rapid thermal processing for power integrated circuits." 11th International Symposium on Power Semiconductor Devices and ICs. ISPSD'99 Proceedings (Cat. No.99CH36312) p.237-40. 1999.

[D'Altroy1985] D.J. Lischner, H. Basseches, and F.A. D'Altroy. "Observations of the Temperature Gradient Zone Melting Process for Isolating Small Devices." Journal of the Electrochemical Society. v132, n12, p2997. 1985.

[Elwenspoek1997] C. Gui, H. Jansen, M. de Boer, J. Berenschot, J. Gardeniers, M. Elwenspoek. "High Aspect Ratio Crystalline Silicon Microstructures Fabricated with Multi Layer Substrates." Tranducers '97. Chicago, USA. pp. 633-636. June 16-19, 1997.

[ESPI] ESPI Metals Tantalum Reference Sheet. http://www.espimetals.com/tech/tantalum.pdf

[Fedder2001] Huikai Xie and Gary K. Fedder. "A CMOS-MEMS Lateral Axis Gyroscope." Proceedings of the IEEE Micro Electro Mechanical Systems. p162. 2001.

[Fedder2002a] Huikai Xie and Gary K. Fedder. "A DRIE CMOS-MEMS Gyroscope." Proceedings of the IEEE Micro Electro Mechanical Systems. p1413. 2002.

[Fedder2002b] H. Lao, H. Lakdawala, L.R. Carley, and G.K. Fedder. "A Copper CMOS-MEMS Z-axis Gyroscope." Proceedings of the IEEE Micro Electro Mechanical Systems. p631. 2002.

[Funk1999] K. Funk, H. Emmerich, A. Schilp, M. Offenberg, R. Neul, F. Larmer. "A Surface Micromachined Silicon Gyroscope Using a Thick Polysilicon Layer." Proceedings of the IEEE Micro Electro Mechanical Systems. p57. 1999.

[Greiff1996] Paul Greiff, Bernard Antkowiak, James Campbell, and Anthony Petrovich. "Vibrating Wheel Micromechanical Gyro." Proceedings of the Ninth Annual International workshop on Micro Electro Mechanical Systems. p31. 1996.

[Harrison1983] Harrison, H.B.; Johnson, S.T.; Cornish, B.; Adams, F.M.; Short, K.T.; Williams, Narayan, J.; Brown, W.L.; Lemons, R.A. "Applications of a continuous wave incoherent light source (CWILS) to semiconductor processing." Laser-Solid Interactions and Transient Thermal Processing of Materials p.393-9. 1983.

[Howe1996] W.A. Clark, R.T. Howe and R. Horowitz, Surface micromachined *Z*-axis vibratory rate gyroscope. In: *Solid-State Sensor and Actuator Workshop* (2–6 June, 1996), pp. 283–287.

[Howe1997] T. Brosnihan, J. Bustillo, A. Pisano, R. Howe. "Embedded Interconnect and Electrical Isolation for High-Aspect-Ratio, SOI Inertial Instruments." Transducers '97. Chicago, USA. pp. 637-640. June 16-19, 1997.

[Howe2003a] M. Palaniapan, R.T. Howe, J. Yasaitis. "Performance Comparison of Integrated Z-Axis Frame Microgyroscopes." Proceedings of the IEEE Micro Electro Mechanical Systems. p 482. 2003.

[Howe2003b] S. Bhave, J. Seeger, X Jiang, B, Boser, R. Howe, and J. Yasaitis. "An Integrated, Vertical-Drive, In-Plane-Sense Microgyroscope." Proceedings of the IEEE Micro Electro Mechanical Systems. p 171. 2003.

[Huber2000] Discussion at Hilton Head 2000 conference.

[Jansen1997] Jansen, H. (MESA Res. Inst., Twente Univ., Enschede, Netherlands); De Boer, M.; Wiegerink, R.; Tas, N.; Smulders, E.; Neagu, C.; Elwenspoek, M. "RIE lag in high aspect ratio trench etching of silicon." Microelectronic Engineering, v 35, n 1-4, Feb. 1997, p 45-50.]

[Kaiser2000] Todd J. Kaiser. A Micromachined Pendulous Oscillating Gyroscopic Acclerometer. Ph.D. Thesis. Georgia Institute of Technology. 2000.

[Laermer1999a] US Patent #6,284,148. "Method for anisotropic etching of silicon."

[Larmer1999b] F. Laermer, A. Schilp, K. Funk, M. Offenberg. "Bosch deep silicon etching: Improving uniformity and etch rate for advanced MEMS applications." Proceedings of the IEEE Micro Electro Mechanical Systems. p 211-216. 1999.

[Little1989] M. J. Little, R. D. Etchells, J. Grinberg, S. P. Laub, J. G. Nash, and M.W. Yung. "The 3-D Computer." International Conference on Wafer Scale Integration,1989, pp. 55-64.

[Lord1988] H.A. Lord. "Thermal and stress analysis of semiconductor wafers in a rapid thermal processing oven." IEEE Transactions on Semiconductor Manufacturing, v 1, n 3, Aug. 1988, p 105-14

[MacDonald1994] Shaw, K.A.; Zhang, Z.L.; MacDonald, N.C. "SCREAM I: a single mask, single-crystal silicon, reactive ion etching process for microelectromechanical structures." Sensors and Actuators A. vol.A40, no.1, p.63-70. January, 1994.

[MacDonald1995] Capacitance based tunable micromechanical resonators Adams, S.G.; Bertsch, F.M.; Shaw, K.A.; Hartwell, P.G.; MacDonald, N.C.; Moon, F.C. 8th International Conference on Solid-State Sensors and Actuators and Eurosensors IX. Digest of Technical Papers. pt. 1, p 438-41 vol.1. 1995.

[Najafi1995] Y. Gianchandani, K. Ma, K. Najafi. "A CMOS Dissolved Wafer Process for Integrated p++ Microelectromechanical Systems." Tranducers '95. Stockholm, Sweden. Pp. 79-82. June 25-29, 1995.

[Najafi2001] F. Ayazi and K. Najafi. "A HARPSS Polysilicon Vibrating Ring Gyroscope." Journal of Microelectromechanical Systems. v10, n2, p169. June, 2001.

[Normann1991] Campbell, P.K.; Jones, K.E.; Huber, R.J.; Horch, K.W.; Normann, R.A. "A silicon-based, three-dimensional neural interface: manufacturing processes for an intracortical electrode array." IEEE Transactions on Biomedical Engineering vol.38, no.8 p.758-68. 1991.

[Normann1992a] Johansson, T.; Abbasi, M.; Huber, R.J.; Normann, R.A. "A three-dimensional architecture for a parallel processing photosensing array (silicon retina application)." IEEE Transactions on Biomedical Engineering vol.39, no.12 p.1292-7. 1992.

[Normann1992b] M. Abbasi, R Johansson, R. Normann. "Silicon-carbide-enhanced thermomigration." J. Appl Phys. V.72, n.5, p.1846-1851. September, 1992.

[Norskog1981] Norskog, A.C.; Warner, R.M., Jr. "A horizontal monolithic series-array solar battery employing thermomigration." Journal of Applied Physics. V52, n3, pt1, pp1552-4. 1981.

[Pfann1955] U.S. Patent 2,770,761 (November 13, 1956)

[Pfann1978] W. Pfann. Zone Melting. Huntington, NY: Robert E. Krieger Pub., 1978.

[Ru2000] Ru, C.Q. "Thermomigration as a driving force for instability of electromigration induced mass transport in interconnect lines." Journal of Materials Science vol.35, no.22 p.5575-9. 2000

[Runyan&Bean1994] W.R. Runyan and K.E. Bean. Semiconductor Integrated Circuit Processing Technology. Addison-Wesley Publishing Company. 1994. p63.

[Runyan&Bean1994a] W.R. Runyan and K.E. Bean. Semiconductor Integrated Circuit Processing Technology. Addison-Wesley Publishing Company. 1994. p257.

[Schmidt1995] L Parameswaran, C. Hsu, M. Schmidt. "A Merged MEMS-CMOS Process using Silicon Wafer Bonding." International Electron Devices Meeting. pp. 613-616. Washington, DC. December 10-13, 1995.

[Song1997] Y. Oh, B. Lee, S. Baek, H. Kim, J. Kim, S. Kang, and C. Song. "A Surface-Micromachined Tunable Vibratory Gyroscope." Proceedings of the IEEE Micro Electro Mechanical Systems (MEMS). p272. 1997.

[Streetman1990] B. Streetman. Solid State Electronic Devices. Englewood Cliffs, New Jersey:Prentice Hall, 1990.

[Sze1981] Sze. Physics of Semiconductor Devices. New York: John Wiley and Sons, 1981.

[Sze2002a] S.M.Sze. "Semiconductor Devices" 2nd edition. John Wiley & Sons. 2002. p.49-51.

[Sze2002b] S.M Sze, "Semiconductor Devices." John Wiley & Sons, Inc. New York. 2002. p.110.

[Tang1997] T Tang, R. Gutierrez, C. Stell, V. Vorperian, G. Arakaki, J. Rice, W. Li, I Chakraborty, K. Shcheglov, J Wilcox, W. Kaiser. "A Packaged Silicon MEMS Vibratory Gyroscope for Microspacecraft." Proceedings of the IEEE Micro Electro Mechanical Systems (MEMS). p500-505. 1997.

[van Putten2001] M.J.A.M. van Putten and M.H.P.M van Putten. "Facing Drift: a Comparison of Three Methods." Sensors and Actuators A. v.90, pp. 172-180. 2001.

[Varadan2000] V.K. Varadan, W.D. Suh, P.B.Xavier, K.A. Jose, and V.V. Varadan. "Design and Development of a MEMS-IDT Gyroscope." Smart Material Structures. v9, p898. 2000.

[Whitmann1926] W.G. Whitmann, Amer. J. Sci., 211, 126 (1926)

VITA

Charles Choi Chung was born in Washington, D.C. on May 17, 1969. He received a Bachelor of Arts from the University of Pennsylvania in Physics and Environmental Studies, a Master of Arts from Duke University in Physics. He has worked at NASA and at the National Solar Observatory. And, he has been the national co-chair for Student Pugwash USA (SPUSA).

In his personal life, Charles holds two black belts, one in Chishin-ryu karate and another in Yoshinshinto-ryu Jiu Jitsu. He plays in the Atlanta Ultimate Frisbee league. He also enjoys cooking and learning new languages.